

**Development of Recycling Compatible Pressure-Sensitive Adhesives and Coatings**

**Final Scientific Report for Project DE-FC36-04GO14309**

**Project Period: October 1st, 2004 – November 30th, 2009**

**By**

**Steven J. Severtson (Principal Investigator)**

**Department of Bioproducts and Biosystems Engineering, University of Minnesota  
2004 Folwell Avenue, St. Paul, MN 55108**

**Jihui Guo, Jinfeng Wang and Gang Pu**

**Department of Bioproducts and Biosystems Engineering, University of Minnesota  
2004 Folwell Avenue, St. Paul, MN 55108**

**Larry E. Gwin (Contact)**

**Franklin International, 2020 Bruck Street, Columbus, OH 43207**

**Carl J. Houtman**

**USDA Forest Service, Forest Products Laboratory, One Gifford Pinchot Drive  
Madison, WI 53705**

**Executive Summary**

The objective of this project was the design of new water-based pressure-sensitive adhesive (PSA) products and coatings engineered for enhanced removal during the processing of recycled fiber. Research included the formulation, characterization, and performance measurements of new screenable coatings, testing of modified paper and board substrates and the design of test methods to characterize the inhibition of adhesive and coating fragmentation and relative removal efficiencies of developed formulations. This project was operated under the requirements that included commercially viable approaches be the focus, that findings be published in the open literature and that new strategies could not require changes in the methods and equipment used to produce PSA and PS labels or in the recycling process. The industrial partners benefited through the building of expertise in their company that they would not, and likely could not, have pursued if it had not been for the partnership.

Results of research on water-based PSAs clearly identifies which PSA and paper facestock properties govern the fragmentation of the adhesive and provide multiple strategies for making (pressure-sensitive) PS labels for which the PSA is removed at very high efficiencies from recycling operations. The application of these results has led to the identification of several commercial products in Franklin International's (industrial partner) product line that are recycling compatible. Several new formulations were also designed and are currently being scaled-up. Work on recycling compatible barrier coatings for corrugated containers examined the reinforcement of coatings using a small amount of exfoliated organically modified montmorillonite (OMMT). These OMMT/paraffin wax nanocomposites

demonstrated significantly improved mechanical properties. Paraffin waxes containing clay were found to have significantly higher Young's moduli and yield stress relative to the wax matrix, but the most impressive finding was the impact of the clay on the elongation at break; a nearly 400% increase was observed for a clay concentration of 0.5 wt.%. These coatings also demonstrate a number of other property enhancements, which make them a good candidate for continued research. Another approach explored in this research was the use of structured and self-cleaning surfaces. If the amount of coating utilized can be significantly reduced, the environmental impact is diminished.

# CONTENTS

<b>1. Introduction.....</b>	<b>1</b>
<b>2. Background .....</b>	<b>3</b>
<b>3. Research Results. ....</b>	<b>6</b>
3.1 Description of Section Layout .....	6
3.2 Optimizing the Monomer Composition of Acrylic Water-based Pressure Sensitive Adhesives to Minimize their Impact on Recycling Operations .....	7
3.3 Affect of Amphiphilic Additives on the Behavior of Water-based Acrylic Pressure Sensitive Adhesives during Paper Recycling .....	25
3.4 Significant and Concurrent Enhancement of Stiffness, Strength, and Toughness for Paraffin Wax through Organoclay Addition.....	37
3.5 Brittle–Ductile Transitions and the Toughening Mechanism in Paraffin/Organoclay Nanocomposites.....	44
3.6 Dynamic Rheological Study of Paraffin Wax and its Organo-Clay Nanocomposites.....	60
3.7 Investigation of Wax Removal Mechanism during Mechanical Pulping of Wax Coated Old Corrugated Containers (OCC) .....	71
3.8 Properties of Paraffin Wax/Montmorillonite Nanocomposite Coatings .....	79
3.9 Dependency of Contact Angle Hysteresis on Crystallinity for <i>n</i> -Alkane Substrates at Various Temperatures.....	84
3.10 Mechanical Pinning of Liquids through Inelastic Wetting Ridge Formation on Thermally Stripped Acrylic Polymers.....	96
3.11 Characterization of Dynamic Stick-and-Break Wetting Behavior for various Liquids on the Surface of a Highly Viscoelastic Polymer .....	106
3.12 Variety of Wetting Line Propagations Demonstrated on Viscoelastic Substrate.....	120
3.13 Characterizing the Distribution of Nonylpheno Ethoxylate Surfactants in Water-based Pressure-Sensitive Adhesive Films using Atomic-Force and Confocal Raman Microscopy .....	127
3.14 Modifications of Surfactant Distributions and Surface Morphologies in Latex Films due to Moisture Exposure.....	141
<b>4. Accomplishments. ....</b>	<b>153</b>
4.1 Publications.....	153
4.2 Presentations.....	154
4.3 Commercialized Technology .....	155
<b>5. Conclusions.....</b>	<b>156</b>
<b>6. Recommendations .....</b>	<b>158</b>
<b>7. Literature Cited. ....</b>	<b>158</b>

## List of Tables

Table 1. Removal efficiencies, performance and surface properties for commercial series of acrylic water-based PSAs .....	14
Table 2. Structure of monomers used in the model water-based PSA formulations .....	18
Table 3. Monomer compositions of model acrylic water-based PSA formulations.....	19
Table 4. Removal efficiencies, performance properties, glass transition temperatures and surface energies for model acrylic water-based PSA formulations.....	19
Table 5. Monomer compositions of model water-based PSA formulations.....	28
Table 6. Performance properties, wet tensile strengths and removal efficiencies (RE) measured at 50°C for the model PSAs.....	28
Table 7. Effect of wetting agent on the surface energies, surface energy components and work of self adhesion in water of model PSA films. ....	31
Table 8. Effect of tackifier dispersion on the loop tack value, glass transition temperature, wet tensile strength, self work of adhesion in water of model PSA1 and PSA2. ....	34
Table 9. Mechanical and surface properties of 3 paper facestocks used in the study and the removal efficiencies at 50 °C of model PSAs laminated onto these facestocks.....	35
Table 10. Tensile properties of pure paraffin wax and wax composite with various OMMT loadings.....	42
Table 11. Image analysis results. ....	73
Table 12. Soxhlet extraction of wax-coated board.. ....	74
Table 13. Reject weight of wax-coated and uncoated board: Chevron wax 128, repulping 35 °C.....	78
Table 14. Calculated crystallinity for paraffin waxes using XRD and DSC data .....	89
Table 15. Dynamic contact angles for paraffin waxes .....	90
Table 16. Physical properties of tested liquids .. ....	110
Table 17. Dynamic CAs (degree) and vertical surface tension components (mN/m) at the interfaces.. ....	123
Table 18. Experimental pinning values from Fig. 63 and values calculated with Eq. 12 .....	124
Table 19. Chemical and physical properties of surfactants .. ....	131
Table 20. Properties of model PSAs .....	131
Table 21. Parameters from fit with exponential decay model.....	138
Table 22. Parameters from fit with exponential decay model for surfactant distributions of model PSA films at 22 °C and relative humidity of 0 and 100%.....	146
Table 23. Enrichment factors for PSA films.....	147
Table 24. Enrichment factors for PSA films aged at 22 °C and cycled between 0% and 100% RH.....	147

## List of Figures

Figure 1. Schematic description of iterative research approach used by the research team to develop new commercial PS labels that are recycling compatible .....	1
Figure 2. Composition of water-based acrylic latex dispersion and formulated PSA and coalescence of latex particles .....	4
Figure 3. Typical composition of water-based acrylic PSA film.....	4
Figure 4. Dynamic mechanical properties for a commercial wax and wax particle deposition and screening removal efficiency data. ....	5
Figure 5. (a) $\tan \delta$ values measured for a commercial hot-melt PSA as a function of temperature. Also shown are the experimental SAFT and the $\Delta T$ determination method. (b). Removal efficiencies (points) as a function of temperature for the commercial hot-melt PSA labels produced with untreated paper facestock.....	10
Figure 6. (a). 180-degree peel strengths, (b.) loop tacks, (c.) shear values and (d.) surface energies of the commercial water-based PSAs. ....	15-16
Figure 7. Maximum dry tensile force values for the model water-based PSA films and after soaking in water for 1 minute at 22 °C and 50 °C .....	22
Figure 8. Maximum tensile force values for model water-based PSAs 1, 5 and 8 as a function of soaking time at 22 °C. (b). Removal efficiency of model water-based PSA 8 at 50 °C as a function of soaking time prior to repulping. ....	23
Figure 9. a.) Surface tension and polar and dispersive components of PSA3 with variable levels of wetting agent; b.) Spreading coefficient of PSA3 and the contact angle of this emulsion on release liner with variable levels of wetting agent.....	30
Figure 10. Morphology of adhesive particles after repulping.....	32
Figure 11. Removal efficiency at 50 °C of model PSAs as a function of the wetting agent concentration used in their formulation... ..	33
Figure 12. Removal efficiencies for PSA2 coated on EDP and C1S as a function of the emulsifier content. ....	36
Figure 13. Wide angle x-ray scattering (WAXS) scans of OMMT, pure paraffin wax, and wax/clay nanocomposites with 1, 2, 3, 4, and 5 wt.% clay loading .....	39
Figure 14. Bright field TEM micrographs of wax nanocomposite with 2 wt.% (a, b), and 4 wt.% (c, d) OMMT.....	40
Figure 15. DSC thermograms of pure paraffin wax and wax composite.....	41
Figure 16. Typical engineering stress-strain curves for pure paraffin wax and wax nanocomposite.. ..	42
Figure 17. DSC scan of the commercial paraffin wax.....	47
Figure 18. Comparison of engineering stress-strain curves of the pure paraffin wax at 20, 25 and 30 °C.....	48
Figure 19. Comparison of engineering stress-strain curves of the paraffin wax nanocomposite containing 2 wt.% organo-clay at 20, 25 and 30 °C. ....	49
Figure 20. SEM images showing the fracture surfaces .....	50
Figure 21. Temperature dependencies of (a) Young's modulus, (b) maximum stress and (c) elongation at break for pure paraffin wax and wax nanocomposite with 2 wt.% OMMT.....	51
Figure 22. Polarized optical images for pure paraffin wax .....	53

Figure 23. Optical micrographs of pure wax and wax-clay nanocomposites .....	54
Figure 24. WAXS patterns of 4 wt.% OMMT-wax nanocomposites .....	56
Figure 25. SAXS patterns of the wax and wax nanocomposites .....	57
Figure 26. TEM micrographs of 4 wt. % OMMT-wax nanocomposites .....	58
Figure 27. DSC scan of a commercial paraffin wax.....	62
Figure 28. X-ray Diffraction plots of paraffin wax at various temperatures. ....	63
Figure 29. Temperature dependence of $G'$ and $G''$ for a commercial paraffin wax.....	65
Figure 30. Temperature dependency of $G'$ and $G''$ for pure wax and wax nanocomposites. ....	66
Figure 31. Dynamic stress sweep for wax nanocomposites with three different clay concentrations at 70 °C and 1 rad/s frequency. ....	67
Figure 32. Frequency dependency of complex viscosities, $\eta^*$ , for wax nanocomposites at three different clay concentrations... ..	68
Figure 33. Frequency dependency of storage moduli, loss moduli and complex viscosities for wax/clay nanocomposites at 3 wt% clay concentration prepared via sonication and stirring.....	69
Figure 34. XRD scans of wax-clay composites prepared by stirring and sonication. ....	70
Figure 35. Frequency dependence of dynamic moduli for three wax/clay nanocomposites..	71
Figure 36. Temperature dependence of wax removal efficiency for wax-coated board .....	75
Figure 37. The fragments of wax-coated board after running .....	77
Figure 38. SEM image of repulping fragments .....	78
Figure 39. a.) Differential scanning calorimetry thermoscan of the commercial paraffin wax. b.) Mechanical properties including the Young's modulus, tensile/yield strength and elongation at break for the pure paraffin wax and its nanocomposites at various temperatures.....	80
Figure 40. Relative thermal expansivity of paraffin wax and its nanocomposite with 2 wt.% organoclay .....	81
Figure 41. SEM image on clay/wax morphology .....	82
Figure 42. Molten heating time dependence of the advancing and receding contact angle for pure wax and wax/clay nanocomposite at 2 wt.% clay concentration .....	83
Figure 43. GC-MS analysis of the paraffin samples.....	87
Figure 44. X-ray diffraction analysis of the paraffin samples carried out at room temperature .....	88
Figure 45. DSC thermograms of the paraffin samples. ....	89
Figure 46. AFM surface analysis of the paraffin wax samples.....	90
Figure 47. Raman confocal microscopy analysis of the paraffin wax before and after heat treatment. ....	91
Figure 48. AFM surface analysis of the paraffin wax samples.....	92
Figure 49. Schematic showing the multiple effects of smoothing wax surfaces via pressing. ....	95
Figure 50. The progression of the evaporation for a 5 $\mu$ L sessile water drop placed on the surface of the polymer film. ....	99
Figure 51. The addition of water to the sessile drop .....	100
Figure 52. The wetting ridge pattern formed on the coated plate during advancing .....	102
Figure 53. Optical profilometry image of a single wetting ridge formed on the plate during wetting experiments. ....	103

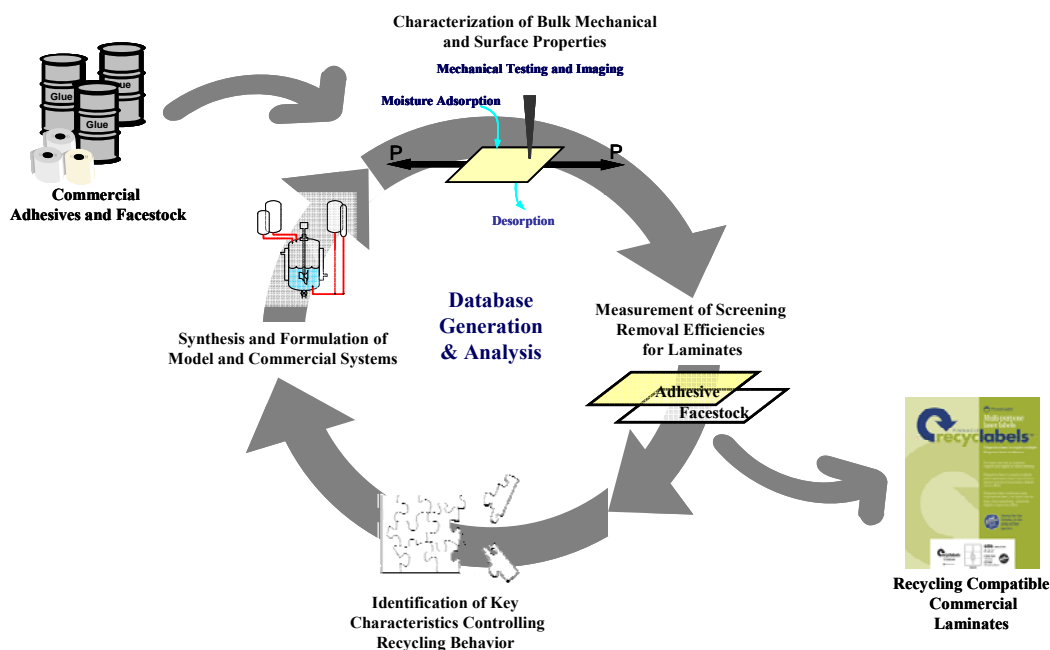
Figure 54. (Top) Force-displacement curve for a complete wetting-dewetting cycle obtained at the speed of 0.15 mm/minute. (Bottom) Schematic cartoons describing the proposed wetting-dewetting behavior of water on the acrylic adhesive substrate. ....	105
Figure 55. Schematic representation of a viscoelastic film being deformed by the vertical force component due to the surface tension of the liquid .....	106
Figure 56. Sessile drop experiment for water (a), paraffin oil (b) and water surrounded by paraffin oil (c) on the acrylic polymer film. ....	109
Figure 57. The force-displacement curves for the liquids used in the Wilhelmy plate measurements. ....	110
Figure 58. The wetting ridge patterns on the surface of the acrylic polymer film surface resulting for advancing rates of 0.1 mm/minute (a) and 1 mm/minute (b) with water and 0.1 mm/minute (c) and 1 mm/minute (d) with paraffin oil. ....	112
Figure 59. Force-displacement curves for the polymer coated plate in water for 3 advancing rates ranging from 0.1 to 100 mm/minute. ....	113
Figure 60. Optical profilometry profiles of wetting ridges produced on the polymer coated plate by water with advancing rates of 0.1 mm/minute and 0.5 mm/minute. ....	113
Figure 61. Relationships between the pinning force and pinning distance for water at various advancing rates. ....	115
Figure 62. Master curve for the acrylic polymer at using a reference temperature of 27 °C. ....	116
Figure 63. Typical force-displacement curves for the different interfaces studied. ....	122
Figure 64. Schematic showing the meniscus height difference between the calculated change and the measured change in meniscus height. ....	125
Figure 65. The relationship of the thickness of the silicone oil layer and the maximum pinning distance in receding. ....	126
Figure 66. Schematic showing the water-silicone oil interface (a) in advancing, (b) in receding for a thin silicone oil layer and (c) in receding for a thick silicone oil layer. ....	127
Figure 67. (a) AFM phase image of film-air interface of model PSA 2, and (b) film-air interface after soaking in solvent for 5 minutes. ....	133
Figure 68. (a) Atomic force microscopy phase images of film-air interfaces for drawdown coatings .....	135
Figure 69. (a) Basic Raman spectra of (a) anionic surfactant, (b) nonionic surfactant, and (c) soap-free latex .....	136
Figure 70. Surfactant distribution profile over the entire thickness of a film cast from PSA 1. ....	136
Figure 71. Surfactant distribution profile over the entire thickness of a film cast from PSA 2. ....	137
Figure 72. Fit of surfactant distribution for PSA 2 at (a) the film-air and (b) film-substrate interfaces using exponential decay model .....	137
Figure 73. Surfactant distribution profile over the entire thickness of a film cast from PSA 3. ....	139
Figure 74. AFM phase images of film-substrate interface of drawdown coatings .....	140
Figure 75. Surfactants distribution profile of original model PSA film, which was stored at 22 °C and 50% RH. ....	144

Figure 76. Surfactants distribution profiles of PSA film after being aged for 2 months at 22 °C and a.) 0% RH and b.) 100% RH.....	145
Figure 77. AFM height images of the surface of a.) a PSA film showing its residual latex structure and b.) a film produced by first dissolving the latex in THF .....	148
Figure 78. Enrichment factors at both interfaces for PSA films aged at 22 °C under various humidity conditions.....	149
Figure 79. AFM images of model PSA film surface obtained at (a.) 22 °C and 25% RH, (b.) 22 °C and 90% RH, and (c.) dry back from 90% RH to 25% RH at 22 °C .....	149
Figure 80. AFM phase images acquired for the model film subsequent to rinsing with solvent at 22 °C and (a.) 3% RH and (b.) 90% RH .....	150
Figure 81. Compatibility of nonionic surfactant (a) and anionic surfactant (b) with polymer phase in the dialyzed model PSA film .....	151



## 1. Introduction

Current pressure-sensitive (PS) labels are designed to eventually be landfilled. In their disposed form, they are typically attached to paper products, which render the paper non-recoverable. This is because the presence of pressure-sensitive adhesive (PSA) in recycled paper creates problems that reduce the efficiency of papermaking operations and diminish product quality. Control of PSA contamination is arguably the central technical challenge in expanding the use of recycled fiber. From 2000, the University of Minnesota, USDA Forest Products Laboratory and a number of industrial partners, the most prominent being H.B. Fuller Company (St. Paul, MN) and Franklin International (Columbus, OH), teamed up to address this problem. The team adopted an iterative approach (described schematically in Fig. 1) in which commercial products were characterized and their recycling behavior tested. Industrial partners supplied glues for analysis along with performance properties and basic characteristics and, more importantly, market support to help identify commercially feasible approaches to the problem. This information and test results were pooled and used to create a database from which theories were developed. These theories guided the synthesis of new model adhesives, which were characterized and their recycling behavior tested under various laminate designs. By going through these iterations, the team not only developed theories for the fragmentation behavior of films and coatings, which were published, we also assembled several formulations that were scaled-up to commercial products.



**Figure 1.** Schematic description of iterative research approach used by the research team to develop new commercial PS labels that are recycling compatible.

As will be discussed in this final report, the primary objectives for this project with regard to recycling compatible PSAs were met. Recycling compatible glues were identified from our industrial partners' current product lines and new formulations and laminate designs were developed. Further work included the examination of complex issues that appear to diminish recycling performance such as surfactant migration and storage for water-based acrylic systems.

It is also important to point out that the emphasis on sustainability has greatly intensified over the past 2 years and the ideal solution appears to be recycling compatible products, which are also compostable and/or generated from renewable resources. The results of this project address the recycling compatibility aspect, which will provide guidance in the development of such products from alternative raw materials.

As part of this project, studies were also carried out on the recycling performance, wetting and barrier performance of paraffin coatings. As with PSAs, wax creates severe production problems during paper recycling and subsequent papermaking operations and diminishes the appearance and quality of produced paper. Although petroleum has properties that make it a serious problem for recyclers, it has the advantage of being inexpensive. In fact so inexpensive that replacing it with a polymeric material is not cost effective. In this project, the development of a means for formulating wax-based coatings such that their negative impact on recycling operations is significantly reduced was examined. As will be described, attempts to formulate a recycling compatible barrier coating included a modification to both mechanical and surface properties. Modifications of bulk mechanical properties were accomplished through the dispersion and exfoliation of organically modified montmorillonite (OMMT) in paraffin wax using ultrasonic compounding. Tensile test results showed that the nanocomposites had significantly improved stiffness, tensile strength, and an elongation at break several fold that of the pure paraffin wax. Unfortunately, this modification appears to provide minimal benefits for the recycling behavior of the paraffin-based coatings. However, the new coatings do demonstrate a significantly lower tendency to form defects or cracks. This led to a second approach of significantly reducing coatings weights while maintaining the same level of performance through modifications to the wetting behavior of coated surfaces.

The reason for undertaking this research can be found in the benefits. Adopting recycling compatible coatings for paper products provides energy, environmental as well as economic benefits. The energy savings estimate by the Agenda 2020 Task Group for the substitution of current adhesive and coating technology with screenable formulations is 10 trillion BTUs per year (1.71 million barrels of oil). For the annual market production of 47.6 million tons,<sup>1</sup> this gives an energy savings value of approximately 210,000 BTUs/ton. The environmental impacts are tied to enhanced recovery of secondary fiber. Recovery of paper and paperboard for 2002 was 47.6 million tons (a recovery rate of 48.1%), with approximately 33 million tons being landfilled. The target recovery rate for the U.S. for year 2012 from the American Forest and Paper Association is 55% (of paper consumed).<sup>1</sup> To achieve this, contaminants will have to be redesigned to eliminate their negative impact on the recycling and papermaking process and on the quality of products produced containing recycled fiber. By introducing technology for making wax coatings screenable, an extra 1.3 million tons will be recycled rather than landfilled. This alone would increase the recovery rate of old corrugated containers by approximately 6%. It will also reduce or eliminate many of the problems that restrict the use of secondary fiber in production. Similar arguments can be made for the use of screenable PSAs. Their widespread use will improve the quality of all grades of recycled paper allowing for greater consumption. In general, the development and introduction of screenable PSAs and coatings should significantly increase recycling rates. With regard to the economic impact, one study claims losses of approximately \$700 million annually due to the impact of PSA contamination on repulping and papermaking operations for United States paper producers.<sup>2</sup> The economic impact of stickies

results from the downgrading of raw materials, mill production problems and landfilling costs. By replacing existing water-based PSAs and wax coatings with recycling compatible versions, most of these problems will be eliminated.

The layout of this report includes a Background section, which describes the current state of PSA and paraffin wax coating technology, followed by a section, Research Results, that provides detailed information on the studies carried out as part of this project. Also included is a summary of the publications and presentations associated with the project and a review of the new technology developed. The Conclusions section attempts to provide an overview of the research, connecting the different issues that were addressed in the Research Results section. The report ends with a Recommendations section in which future steps are suggested for this area of research emphasizing that the results of this project should be considered one of several crucial steps in the process of replacing current technologies with those that are both produced from sustainable materials and possess a closed life cycle.

## 2. Background

The dominant type of PSA utilized to produce today's label products are water-based acrylics, comprising more than 80% of the market.<sup>3</sup> This provides strong incentive to focus on these systems initially. The terminology water-based derives from this PSA being formulated and processed as an aqueous dispersion. The adhesive polymer is produced via emulsion polymerization, which requires the emulsification of reacting monomers and generates a latex dispersion (Fig. 2a). This colloid can serve as the basis for numerous PSAs produced through the addition of different types and concentrations of tackifying dispersions and additives that facilitate coating operations including wetting agents, defoamers and rheology modifiers. The adhesive polymers in water-based acrylics combine so-called soft, hard and functional monomers to achieve a variety of performance properties. The homopolymers of the soft monomers have a glass transition below about -40 °C. The most common are 2-ethylhexyl acrylate, *n*-butyl acrylate and *iso*-octyl acrylate. Hard monomers such as methyl methacrylate, vinyl acetate and styrene produce homopolymers with glass transitions above about 30 °C. Functional monomers such as acrylic acid, methacrylic acid, maleic acid and acrylamide stabilize the latex and provide the PSA polymer chain with functional groups where additional chemical reactions can occur.

Pressure sensitive labels are commonly manufactured with water-based PSA by a process known as transfer coating in which formulated adhesive latex is applied to a release liner and dried. During the drying process, latex particles undergo a film-forming mechanism where water removal draws particles into close proximity and then deforms them into a closely packed layer as shown using cryogenic scanning electron microscopy at equal magnification in Fig. 2b. At temperatures above the glass transition of the polymer, the adhesive particles fuse together to form a continuous film. This liner-backed film is then pressed onto facestock to produce the label stock. The composition of a typical multi-purpose PSA film is shown in Fig. 3. It can be seen that the most prevalent component is the adhesive polymer. Thus it is assumed that the properties of this component must be manipulated to achieve the behavior sought. However, the other components can have a significant impact on recycling behavior as will be discussed.

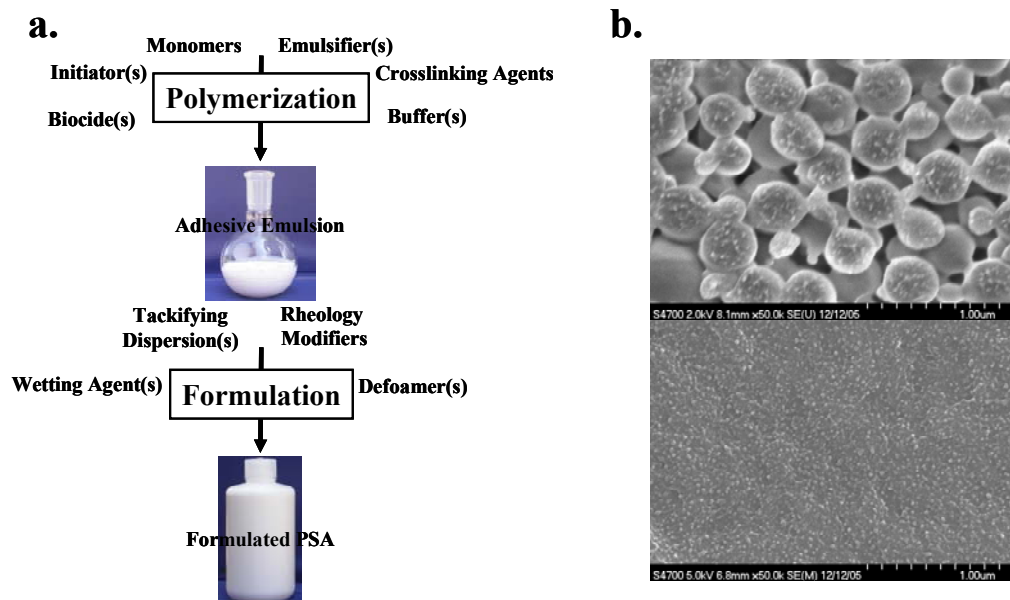


**Figure 2.** a.) Composition of water-based acrylic latex dispersion and formulated PSA and b.) the coalescence of latex particles (top) with drying to form a continuous film (bottom).

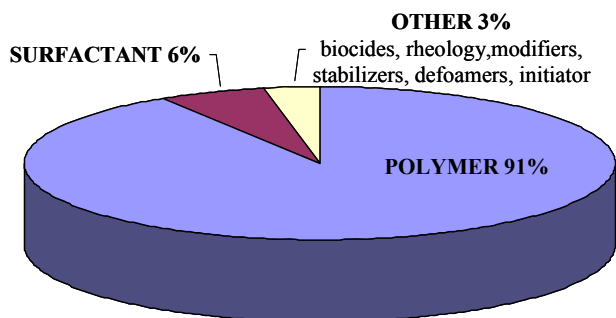


**Figure 3.** Typical composition of water-based acrylic PSA film.

An objective of research outlined in this report was to construct PSAs and more specifically PS label designs that would promote the efficient removal of the adhesive via screening. It was found that this is best accomplished by limiting the fragmentation of PSAs. The results outlined within clearly identify properties govern the fragmentation of the adhesive and provide clear strategies for making PS labels for which the PSA is removed at very high efficiencies from recycling operations. The project was operated under the requirements that included commercially viable approaches be the focus, findings be published in the open literature and new strategies could not require changes in the methods and equipment used to produce PSA and PS labels or in the recycling process. The industrial partners benefited through the building of expertise in their company that they would not, and likely could not, have pursued if it had not been for the partnership. Given the highly secretive nature of the adhesives and label manufacturing industry, the full participation of industrial partners was critical. The success of this project shows how academic and government research institutions and the research and

business components of industrial corporations can collaborate on long term initiatives that benefit the entire industry.

The other component of research in this project is the development of recycling compatible wax coatings. A large fraction of the paraffin wax refined in the United States is sold for use as a low-cost, protective coating on boxes used to ship agricultural products. The drawback of this application is that wax-coated boxes are non-recyclable. The presence of wax coatings in recycle systems hinders production and diminishes product quality.<sup>4</sup> The ineffectiveness of conventional techniques at removing wax and the underlying mechanisms via which it interferes with recycling processes are not well understood, but are believed to be tied to their unique mechanical properties. Macrocrystalline or paraffin waxes used to coat corrugated boxes are refined from paraffinic petroleum distillates that are often doped with polymeric structures such as polyethylene. The properties of these mixtures are very similar to those of n-alkanes and n-alkane blends. Bracketed between their isotropic liquid state and highly ordered crystalline phase, coating waxes possess a series of weakly structured mesophases in which molecules in the crystals have gained a rotational degree of freedom while retaining their positional order. These states are referred to as plastic crystalline or rotator phases, and they occur at temperatures just above ambient where wax coatings are recycled (Fig. 4a). To date, five unique rotator phases have been identified for n-alkanes, denoted R<sub>1</sub> through R<sub>V</sub>.<sup>5</sup> Waxes will pass through at least one of these prior to melting.

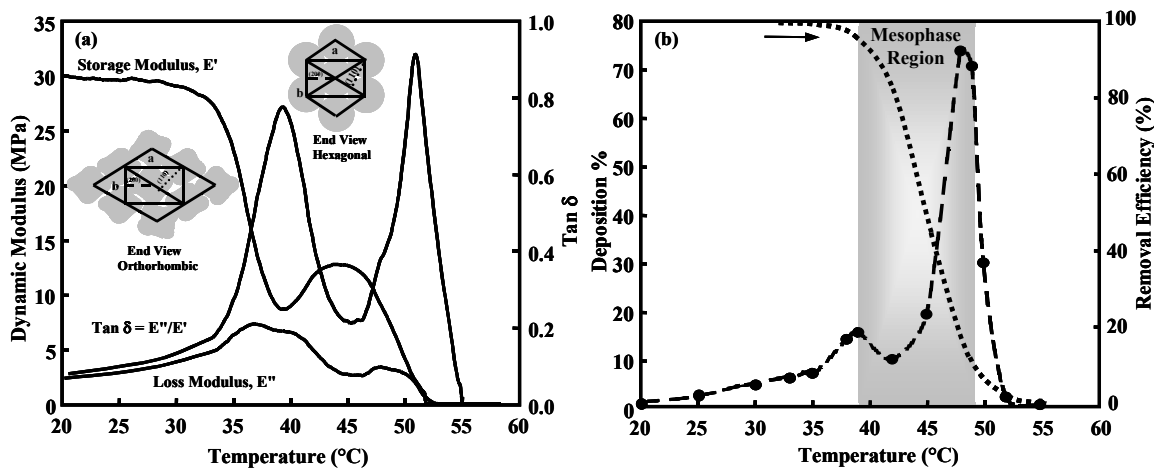


**Figure 4.** a.) Dynamic mechanical properties for a commercial wax. b.) Wax particle deposition and screening removal efficiency data estimated from repulping measurements for the same wax. The mesophase region is superimposed on Fig. 4b to indicate the temperatures that would provide problematic contaminants for this wax coating during recycling.

Figure 4b shows the deposition of the commercial wax onto Teflon™ coupons. Similar results were found for hydrophobically modified gold-coated, quartz crystals (QCM gravimetry). Deposition of waxes on process equipment, felts and the wire are one of the major problems associated with the recycling of wax-coated corrugated containers.<sup>6-9</sup> As indicated in the plot, significant deposition only occurs over the mesophase region of the wax coating.

Two approaches explored as part of this research were the manipulation of wax coating properties through the incorporation silica nanoparticles and formation of superhydrophobic surfaces allowing for the use of greatly reduced coatings weights. Results of research involving these modifications are outlined in the subsequent section, which outlines all research results.

### **3. Research Results**

#### ***3.1 Description of Section Layout***

This section provides detailed information on the most significant findings from research conducted for this project. The section is divided into 13 separate units describing work on specific topics. The overall goal of research was to develop new coatings that can be easily controlled in paper recycling operations, so-called recycling compatible formulations. As can be seen from sections 3.2 and 3.3, great progress was made on the materials of primary interest, water-based, pressure-sensitive adhesive. This includes identification of the variables controlling the fragmentation of water-based PSA films, as well as guidelines on how coating additives and laminate design (e.g., selection of label facestocks) impact recycling behavior. This component of the project nicely complements the research completed for project DE-FC07-00ID13881, which was focused on thermoplastic or hot-melt technology. The combination of findings from that project and those presented below provide clear guidelines to adhesive producers on the design of recycling compatible emulsion and thermoplastic PSA technology, covering nearly all of the commercial label market. As will be discussed in greater detail in the Accomplishments section, ideas and technology from this research are already being utilized and marketed, however much work remains. As outlined in the Recommendations section, the paradigm has shifted significantly in the past couple of years and a great emphasis is now being placed on the use of raw materials from renewable resources and the design of products with closed life cycles. The results of work presented here will hopefully help steer such future efforts to provide recycling compatibility as well as sustainability, i.e., truly environmentally benign adhesive technology.

Subsections 3.4 through 3.9 discuss research on designing recycling compatible paraffin wax barrier coatings for corrugated containers. This work focused on modifying the mechanical properties of coatings and the identification of the mechanism involved in the fragmentation of coating materials during recycling operations. The most promising approach from this effort was the development of nanoclay composite coatings. As described in detail below, modified coatings were found to have improved stiffness, strength and toughness; a unique combination. In addition to impacting the recycling behavior, these improvements also provide the paraffin with greater performance as barrier coatings by minimizing cracks and other defects. A potential application of our work is the use of significantly lower coat weights, which would minimize the waste problem by reducing contaminant loads. Research along these lines also examined the application of textured coatings to produce superhydrophobic surfaces.

Subsections, 3.10 through 3.12, outline research results, which are an offshoot from work towards the primary objectives of this project. It was found quite by accident that highly viscoelastic polymers and polymer solutions such as those that compose PSAs demonstrate interesting interactions with wetting liquids. This behavior was isolated by using a PSA generated through multi-stage thermal stripping of solvent-based acrylic polymers. Initially, this PSA was pursued because it lacked amphiphilic species, which we believed control moisture

uptake and thus their fragmentation behavior when attached to paper substrates during repulping operations. What we observed is that water droplets are unable to move on the surface of these polymers. More specific measurements of wetting showed novel behavior including the formation of a wetting ridge structure substantially larger than those reported elsewhere and the complete halting of the three-phase line, i.e., an extreme example of viscoelastic braking. This allows metastable angles ranging from 0 to greater than 170° to be achieved through changes in sessile drop volume. Greater advancing angles are prevented by the collapse of the drop, producing what we described as stick-and-break propagation. In Wilhelmy plate experiments for metal plates coated with the polymer, this mechanism produces a quasi-periodic pattern of lines composed of ridge structures. We have tied the frequency of these ridges and their magnitudes to properties of both the wetting liquids and the polymers.

The remaining subsections, 3.13 and 3.14, discuss research aimed at understanding how the transport and fate of amphiphilic components impacts the decay, weathering and toxicity of latex films and coatings and adjacent plies in label laminates. Equipment including Raman confocal, environment-controlled AFM and cryo-SEM are used to establish the initial distribution of surfactants in films and adjacent paper plies (e.g., facestocks and liner), monitor their transport under various temperature and humidity conditions and examine the impact of surfactant migration and fate on the latex coalescence process. Our initial studies involved a model polymer produced primarily from the soft monomer *n*-butyl acrylate and lesser amounts of methyl methacrylate (hard monomer) and methacrylic acid (functional monomer). The surfactants used in emulsion polymerization are disodium (nonylphenoxypolyethoxy)ethyl sulfosuccinate (anionic) and nonylphenoxypoly(ethyleneoxy) ethanol (nonionic). The use of species differing in the presence of acid functional groups allowed us to monitor how water solubility and surfactant-polymer interactions effect the distribution of these species during production. Recently, studies were completed and published on how environmental conditions such as temperature and relative humidity impact the surfactant migration over time. This provided a potential mechanism via which surface enriched surfactant can be transferred to the surrounding environment. As discussed in prior subsections, the movement and location of surfactants has a significant impact on the recycling behavior of PSA films and laminates.

### ***3.2 Optimizing the Monomer Composition of Acrylic Water-based Pressure-Sensitive Adhesives to Minimize their Impact on Recycling Operations***

Control of contamination is arguably the most important technical obstacle in expanding the use of recycled fiber.<sup>10-16</sup> An especially challenging category of contaminants to manage are the pressure sensitive adhesives (PSAs). These are soft elastomer-based solutions that are highly viscous and sticky to the touch. They are usually found in recovered waste attached to paper products as part of pressure sensitive (PS) label systems, which consist of facestock coated with a layer of PSA of 20 to 26 μm thick. In the repulping process, which occurs during the initial stages of recycled waste processing, paper products are fiberized in an aqueous environment via heavy mixing. This process also fragments adhesive films which form into small particles. A majority of the removal of generated PSA occurs at the pressure screens and is governed mainly by the size and shape of the particles. Adhesive not removed is introduced into the remaining fiber recovery operations as well as the papermaking process where they can significantly diminish production efficiency and product quality. There is much agreement in the industry

that the most promising approach to eliminate the negative impact of PSA on paper recycling is to design adhesives for enhanced removal early in the process, ideally using existing equipment and process designs. Given the already high efficiency of contaminant removal demonstrated by pressure screens, it is not surprising that this equipment has been the focus of new adhesive products. The most promising are PSAs designed for inhibited fragmentation during repulping to generate larger residual particles.

In this paper, factors governing the degree of fragmentation for emulsion or water-based pressure sensitive adhesives during repulping operations are identified. This work builds on previous studies of thermoplastic or hot-melt PSA. Those efforts demonstrated that the extent of fragmentation is determined by the cohesive strength of the PSA and bulk mechanical properties and surface energy of paper facestocks on which they are coated. Hot-melt systems were investigated prior to water-based formulations because they tend to be less complex. Although the hot-melt designation simply indicates that the PSA can be melt processed, it most commonly refers to formulations composed of a styrene-containing base polymers or polymer blends, tackifying resin and plasticizer. These formulations employ block copolymers that combine styrene segments with those composed of monomers possessing lower glass transition temperatures in their homopolymer form. These so-called rubbery blocks are often composed of ethylene-propylene, ethylene-butene, isoprene or butadiene. The incompatibility of the styrenic and rubbery blocks provides these polymers with separate microphases and phase transitions, which are apparent in dynamic mechanical analysis (DMA) thermoscans. Figure 1a shows a plot of  $\tan \delta$  as a function of temperature for a typical commercial hot-melt PSA. The lower temperature transition is the glass transition for the rubbery blocks; the higher temperature transition is the styrene disruption temperature at which the interactions between styrene functional groups that provide the residual cohesive strength, sometimes described as physical crosslinks, are mostly eliminated.

The performance of a PSA requires a balance between adhesive and cohesive strength. In other words, it must be soft enough to flow into the surface of an adherend at low pressures to wet it, but strong enough to withstand a various loads without failing. For a hot-melt PSA, this balance is achieved within the plateau region of the adhesive<sup>17</sup> (Fig. 5a), which are bracketed by its phase transitions. As is outlined in detail elsewhere, cohesive strength of a hot-melt PSA declines with increasing temperature throughout the plateau region. This loss of strength corresponds to an increase in the degree of fragmentation of PSA films during repulping operations and a decrease in their removal via screening operations. In fact, removal efficiency drops from 100% to nearly 0% over the plateau region. This behavior is fit by an empirical sigmoidal function relating screening removal efficiency to repulping temperature ( $T_R$ ) of the form,

$$\text{Removal Efficiency} = \frac{\exp\left(\frac{\text{SAFT} - T_R}{0.1\Delta T}\right)}{1 + \exp\left(\frac{\text{SAFT} - T_R}{0.1\Delta T}\right)} \times 100\% \quad (1)$$

for which  $\Delta T$  is the width of the plateau region and the adhesive's shear adhesion failure temperature or SAFT is the inflection point of the sigmoid. Figure 5b shows the fit of screening



removal efficiency data for a commercial hot-melt PSA using Eq. 1. This model allows the removal efficiencies of hot-melt PSAs to be predicted based solely on standard adhesive property tests. Thus the engineering of these properties by a competent formulator can reduce the impact hot-melt PSA has on paper recycling operations.

Hot-melt PSA composes a small portion of the PS label market, approximately 20%, while water-based systems accounts for much of the remaining 80% and most of this is acrylic-based. This dominance by acrylic water-based systems of the label market and likely the composition of PSA in recovered waste is strong incentive to investigate the factors controlling their impact on paper recycling. Considerable effort has been invested into the development of environmentally benign water-based PSA. However, few of the published studies attempt to relate removal efficiencies to adhesive properties and composition, and those that do, focus on performance properties (i.e., shear, tack and peel), which should be considered independent of the fragmentation behavior if general solutions are sought. The likely reason for the lack of progress on water-based systems is their complexity. Although styrenic block copolymer based PSAs and water-based films are used for many of the same applications and provide similar performance properties, their chemical composition and processing into label products is quite dissimilar. The terminology water-based derives from the fact that this type of PSA is formulated and processed as an aqueous dispersion. The most common types of water-based PSAs are the acrylics. These are produced via polymerization from primarily alkyl acrylate monomers which require emulsification in an aqueous medium. Their reaction produces a latex dispersion, which can serve as the basis for numerous PSA formulations produced through the addition of tackifying dispersions and crosslinking agents and additives that facilitate coating operations including wetting agents, defoamers and rheology modifiers.

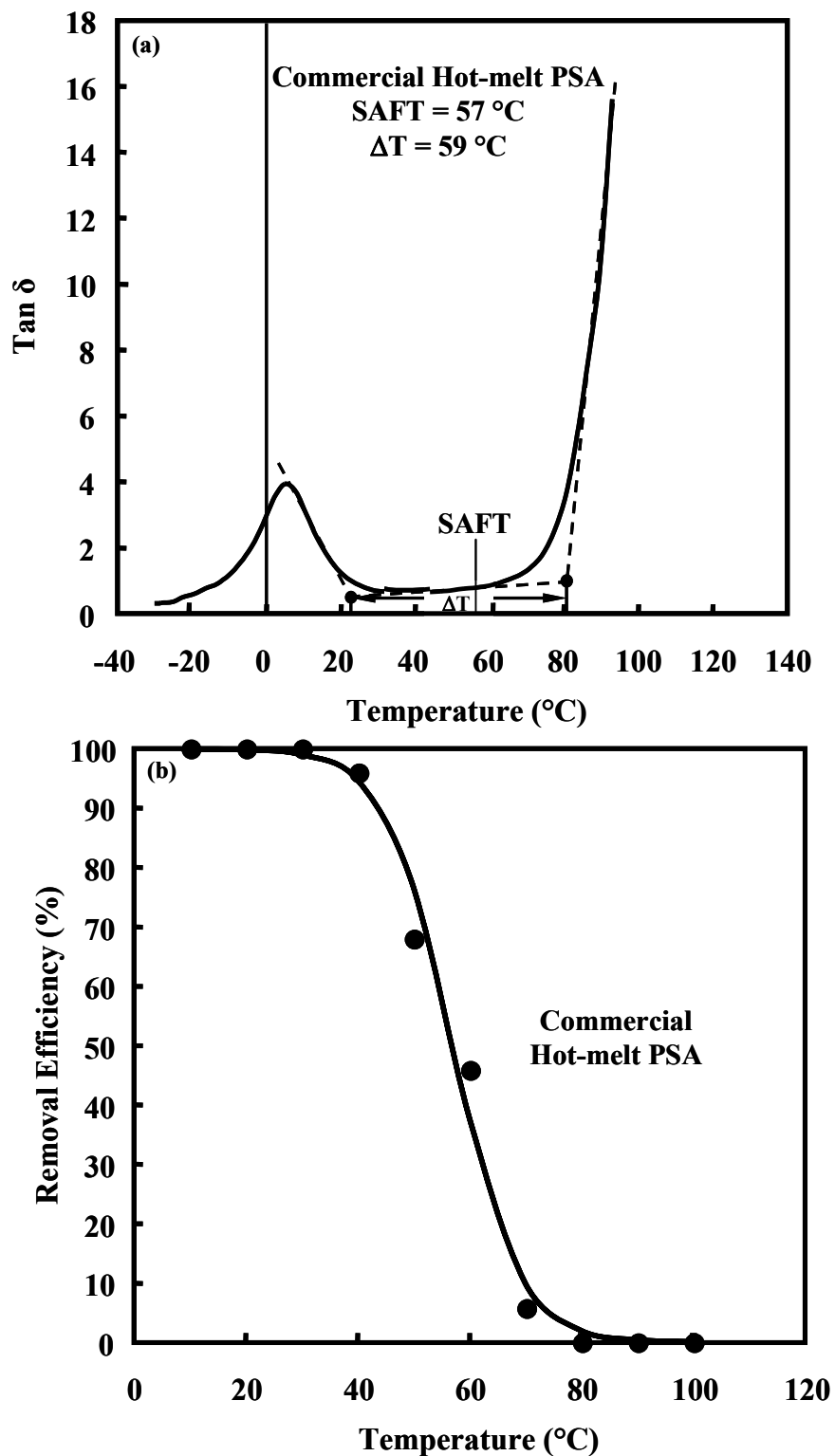


**Figure 5.** (a)  $\text{Tan } \delta$  values measured for a commercial hot-melt PSA as a function of temperature. Also shown are the experimental SAFT and the  $\Delta T$  determination method. (b). Removal efficiencies (points) as a function of temperature for the commercial hot-melt PSA labels produced with untreated paper facestock. The solid curves were predicted using the SAFT and  $\Delta T$  parameters determined for the PSA.

Unlike previous studies involving hot-melt PSA, composition and property parameters are difficult to control independently for water-based systems. For example, changing emulsifiers can also affect molecular weight, latex particle size and the coalescence process to form a film. It can also change the composition and concentration of the additives needed to facilitate coating. Difficulties in carrying out controlled studies of water-based PSA also arise due to the requirement that it be processed as a colloid. While hot-melt PSA can be obtained as a bulk material, water-based PSA must be cast as a thin film. This complicates the characterization of its mechanical properties, which is likely why past studies have relied on performance testing. It is also interesting that previous studies attempt to correlate the properties of dry water-based PSA to behavior of the films in an aqueous environment. Water-based systems are processed with upwards of 8 mass% surfactant based on the dry film and the monomer units of the adhesive polymer are relatively polar. For these systems, it is reasonable to assume that adhesive properties, including cohesive strength, will change in an aqueous environment. Here, a series of commercial water-based PSAs were characterized and their removal efficiencies were tested. These results were used to guide the development of a model acrylic water-based system to better identify controlling variables. Reported data demonstrate that the behavior of PSAs during recycling operations have little connection with their dry properties. The information provided here provides guidelines that will allow manufacturers to design environmentally benign PS label systems.

## **Experimental Section**

**Chemicals and Materials.** Acrylic water-based PSAs were synthesized and formulated at Franklin International (Columbus, OH). Model water-based PSAs were synthesized using commercially available monomers including n-butyl acrylate, 2-ethylhexyl acrylate, styrene, vinyl acetate, methyl methacrylate, acrylic acid and methacrylic acid and commercially available sulfated nonylphenol ethoxylate (ammonium salt) and nonylphenoxypoly(ethyleneoxy) ethanol emulsifiers. Many of the adhesive emulsions utilized sodium persulfate or ammonium persulfate initiators, t-butyl hydroperoxide oxidizer, sodium formaldehyde sulfoxylate reducer, an ammonia buffer and commercial biocides. Emulsions were coated on two-sided release paper using a draw-down coater and dried in an 82 °C oven for 10 minutes. The film thickness target was 1 mil (25.4 μm). Copper (II)-ethylenediamine complex (1 M solution in water) used for the isolation of adhesive rejects was purchased from Acros Organics (Pittsburgh, PA).

**Characterization of Water-based Pressure Sensitive Adhesives.** All performance testing was carried out on 1 mil (25.4 μm) thick films at a controlled temperature and humidity of 22 °C (±1.5°C) and 50% (± 2% RH), respectively. Peel strength of water-based PSAs were measured using an IMASS Inc. (Accord, MA) 180° Slip/Peel Tester Model SP101B at a peel rate of 12"/min. One inch wide polyethylene terephthalate (PET) backed films were peeled from PSTC grade polished stainless steel panels (Ryerson Steel, Chicago, IL). Test laminates were rolled with a 5.0 lb. ASTM quality manual roller. The average peel force from 3 tests was reported for each sample. Shear test strips were prepared with a contact area of 0.5" × 0.5" between PSTC grade polished stainless steel panels and PET-backed films. Samples were rolled with a 4.5 lb. ASTM quality manual roller. Five-hundred gram weights were clipped to the bottom of the test strips. The average time in minutes for the weight to pull the PET-backed films from the plate for 3 tests was reported for each sample. Loop tack strengths of water-based PSA were measured using an Ametek Corporation (Paoli, PA) Chatillon with DFM 10 Digit Force meter.

PSA was direct coated onto PET to form 1" × 5" test strips, which for testing, were looped with the adhesive facing out and used to form a contact area of 1" × 1" on PSTC grade polished stainless steel panels. A dwell time of 1 second and upward travel speed of 12"/min. were used for testing. The average maximum force for 3 tests was reported for each sample.

Glass transition temperatures ( $T_g$ ) were determined using the TA Instruments (New Castle, DE) DMA 2980 Dynamic Mechanical Analyzer. Tested samples were composite structures formed by dipping a glass support cloth (30 mm × 10 mm × 0.3 mm) into the liquid adhesive emulsion. The sample is dried in a desiccator overnight. The thermal locations of the peaks in the loss modulus ( $E''$ ) for scans carried out at 1 Hz. were reported as the  $T_g$ .

Force-displacement curves for PSA films were determined using an Instron (Norwood, MA) 5542 tensile tester equipped with a 10 N load cell. For the dry tests, two pieces of PET films (1" wide by 3" long strips) were used as a sample holder. A 1 mil adhesive film was transferred from release liner over the joint between the 2 PET films and they were placed in the tensile tester grips. All of the dry tests were made at 22 °C and 50% humidity. For water-submerged testing, the tensile tester was equipped with an in-house temperature-controlled bath. For testing, a crosshead speed of 10 mm/min. was used and, unless otherwise indicated, samples were soaked for 1 minute prior to the start of test. At least twenty measurements were made for each sample under both dry and wet conditions, and the average maximum forces were reported for each sample.

Surface energies of water-based adhesives were determined from contact angle measurements for selected liquids. This procedure was described in a previously publication.<sup>6</sup> Also described previously is the removal efficiency determination procedure.<sup>8</sup> This approach was recently shown to correlate well with standard government pilot scale testing for removal efficiencies.<sup>18</sup>

## Results and Discussion

**Importance of Monomer Composition in Determining Removal Efficiency.** The goal of this research is to develop an understanding of which variables control the fragmentation behavior and thus screening removal efficiencies of acrylic water-based pressure sensitive adhesives. Furthermore, the focus is on adhesive components that are actually used in label products that may become part of the recovered paper stream. This requires the cooperation of a major manufacturer given that much of what is known about the synthesis and formulation of commercial PSA is not published in the open literature. During the initial stages of this study, 25 commercial formulations were characterized and their screening removal efficiencies were tested. Unlike hot-melt PSA, which are compounded and coated as a melt, water-based PSA is processed as a colloid with water as the continuous phase and is typically coated onto a silicone release liner for drying. This allows for the coalescence of the latex particles and formation of the adhesive film. The film, backed by the release liner is then transfer coated onto a facestock to produce a laminate or pressure sensitive (PS) label stock.

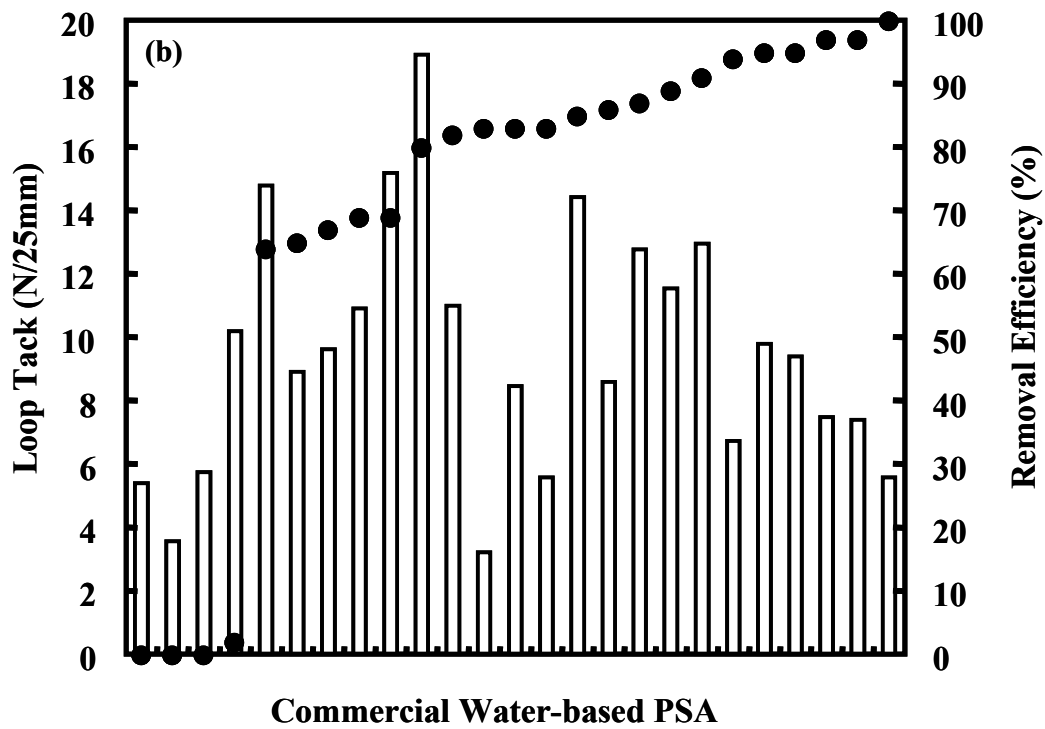
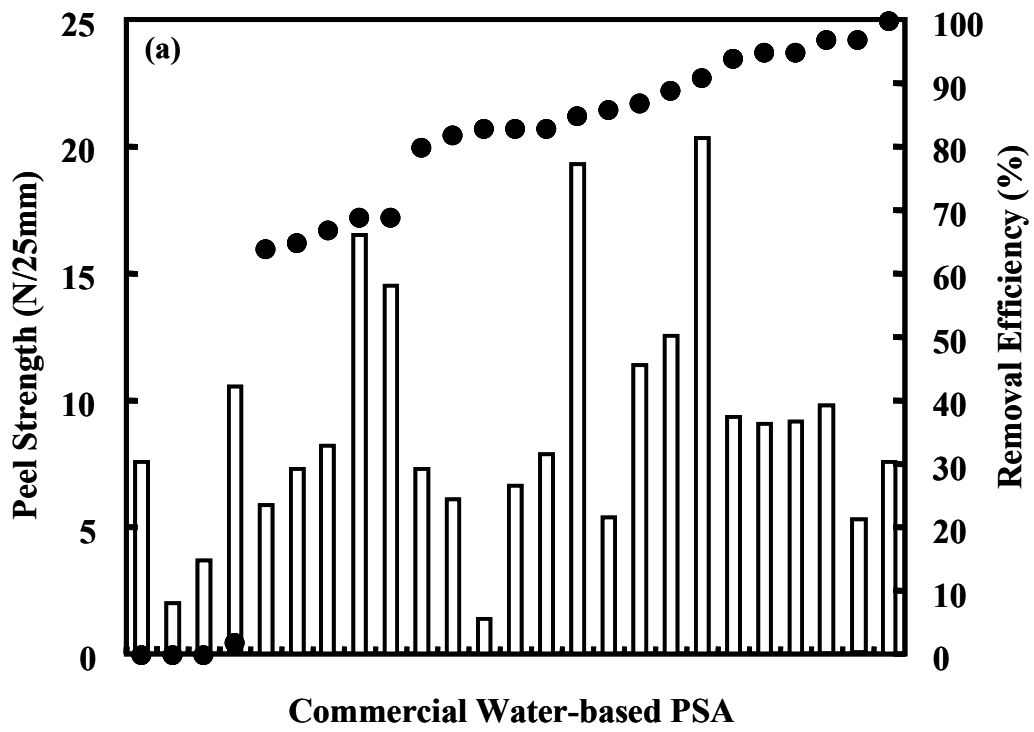
As was discussed in previous publications, choice of paper facestocks can have a significant impact on the fragmentation of the attached PSAs.<sup>19</sup> Here, a commercially produced electronic data processing paper (EDP) is used for all testing. EDP is a broad category of uncoated face papers commonly used in PS labels. Properties of this particular EDP were well characterized

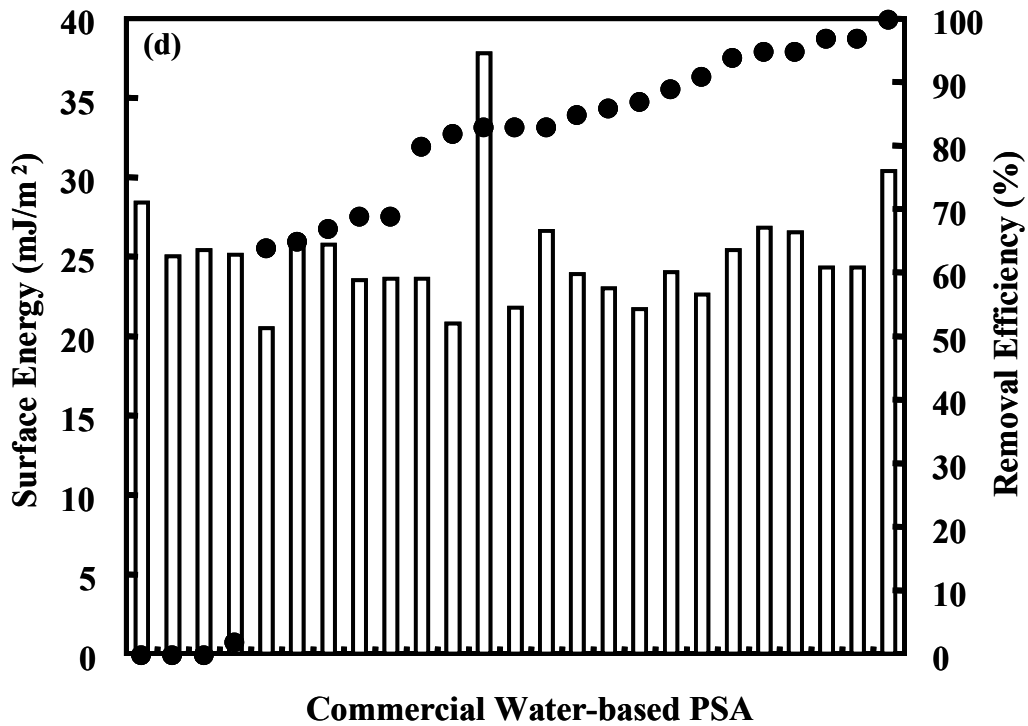
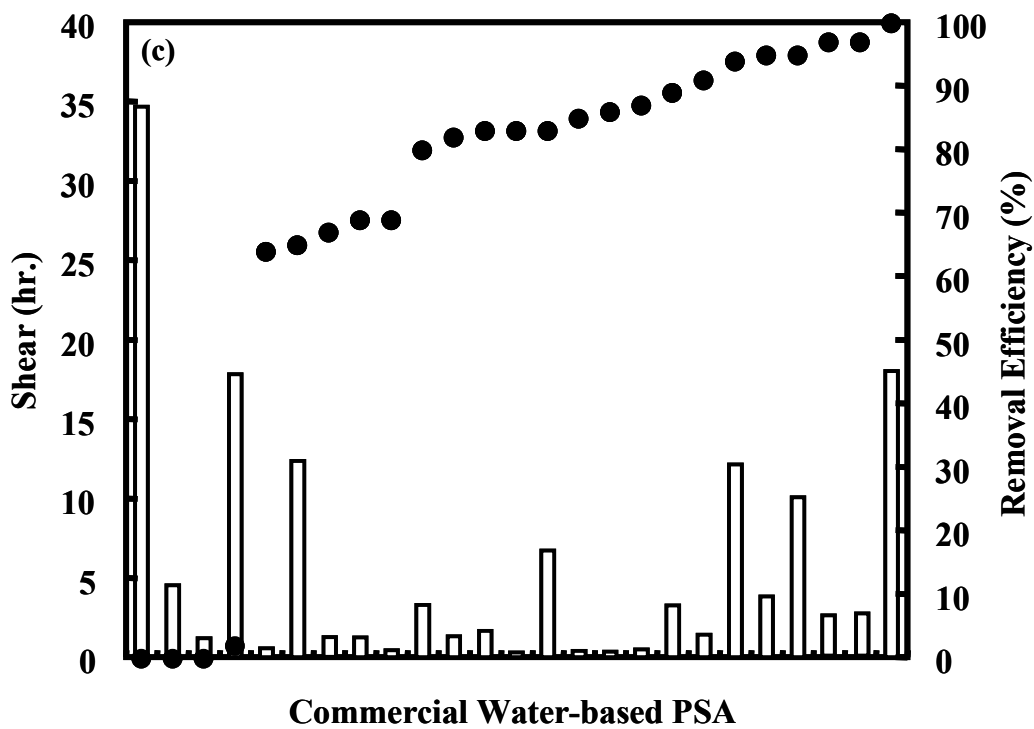
and reported in a previous publication. An issue related to planning controlled experiments for water-based systems is the use of formulation additives. In particular, the use of wetting agents to formulate adhesive emulsions for coating. Given that silicone release liners typically have surface energies in the range of 20-25 mJ/m<sup>2</sup>, a wetting agent is required to produce a uniform coating with a water-based adhesive emulsion. Although it was found that the choice of wetting agent was not the dominant factor in determining whether a PSA is environmentally benign, it does influence the outcome of removal efficiency tests. To avoid this, all adhesive emulsions were formulated for coating using a sodium polyacrylate rheology modifier. This additive allows for the generation of uniform coatings on silicone release liner and does not impact the outcome of removal efficiency testing.

Table 1 lists the physical and performance properties along with measured screening removal efficiencies for 25 commercial, acrylic water-based PSA emulsions formulated for coating using the rheology modifier. No connections are discernable between removal efficiencies and performance properties for the adhesives. This better seen in Fig. 6, for which the measured removal efficiencies are superimposed on the charted values for various performance properties. There also was no connection found between removal efficiencies and the tensile properties for PSA films. (Tensile testing of thin films will be discussed in greater detail in the next section.) These results contradict previous studies that report a correlation between screening removal efficiencies of water-based PSAs and tack, peel and tensile properties for dry films.<sup>20,21</sup>

**Table 1:** Removal efficiencies, performance and surface properties for commercial series of acrylic water-based PSAs.

<b>Commercial Water-based PSA</b>	<b>RE @ 50°C (%)</b>	<b>180° Peel (N/25mm)</b>	<b>Shear (hr.)</b>	<b>Loop Tack (N/25mm)</b>	<b>Surface Energy (mJ/m<sup>2</sup>)</b>
C1	0	7.6	34.7	5.4	28.4
C2	0	2.0	4.5	3.6	25.0
C3	0	3.7	1.2	5.7	25.4
C4	2	10.5	17.8	10.2	25.1
C5	64	5.9	0.6	14.8	20.5
C6	65	7.3	12.4	8.9	25.6
C7	67	7.6	1.3	9.6	25.7
C8	69	16.5	1.3	10.9	23.5
C9	69	14.5	0.5	15.2	23.6
C10	80	7.3	3.3	18.9	23.6
C11	82	6.1	1.3	11.0	20.8
C12	83	1.4	1.7	3.2	37.8
C13	83	6.6	0.3	8.5	21.8
C14	83	7.9	6.7	5.6	26.6
C15	85	19.3	0.4	14.4	23.9
C16	86	5.4	0.4	8.6	23.0
C17	87	11.4	0.5	12.8	21.7
C18	89	12.5	3.3	11.5	24.0
C19	91	20.3	1.4	12.9	22.6
C20	94	9.3	12.2	6.7	25.4
C21	95	9.1	3.8	9.8	26.8
C22	95	9.2	10.1	9.4	26.5
C23	96	11.4	2.6	7.5	24.3
C24	97	11.1	2.6	7.4	24.5
C25	100	7.6	18.0	5.6	30.4





**Figure 6.** (a). 180-degree peel strengths, (b.) loop tacks, (c.) shear values and (d.) surface energies of the commercial water-based PSAs. Superimposed are screening removal efficiencies measured at 50 °C (solid dots).

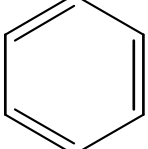


Our results do indicate a connection between removal efficiency and monomer composition. Although the authors were rather vague in their analysis, it was previously reported by Guo *et al.* that the monomer composition of the adhesive polymer is important in determining its removal efficiency.<sup>22</sup> They report that “highly hydrophobic polymers yielded larger adhesive particles that were easily removed during the screening operation”. Here we report more specific findings with regard to composition. The commercial PSAs listed represent 25 different monomer combinations composed of 15 different monomers. The adhesives were developed for a variety of applications, but most are general purpose or are used specifically in label systems. Removal efficiencies for most of the PSAs are relatively high. It is only commercial PSAs 1 through 4 that have little or no removal. These formulations contain both vinyl acetate and acrylic acid monomers. It is also found that the PSAs demonstrating only modest removal efficiencies (e.g.,  $\leq 70\%$ ) contain either vinyl acetate or acrylic acid. From these results, it would appear that the combination of particular monomers produce a critical change in the property controlling the fragmentation of the adhesive. A change that is not apparent from the mechanical, surface or performance properties of the dry films.

**Development and Performance of Model Water-based PSAs.** To better characterize this relationship between monomer composition and removal efficiency, a series of model acrylic water-based adhesive emulsions were synthesized. Acrylic water-based PSAs combine so-called soft, hard and functional monomers to achieve a variety of performance properties. The soft monomers are those that in a homopolymer form have a glass transition temperature ( $T_g$ ) below about  $-40\text{ }^\circ\text{C}$ . These include 2-ethylhexyl acrylate, n-butyl acrylate, n-isobutyl acrylate and iso-octyl acrylate. Hard monomers such as methyl methacrylate, vinyl acetate and styrene produce homopolymers with  $T_g$ s above about  $30\text{ }^\circ\text{C}$ . There are numerous monomers that produce homopolymers with  $T_g$ s between these temperatures including ethyl acrylate, and methyl acrylate that are added to an adhesive to increase cohesive strength. Adhesive polymers in water-based emulsions will usually also contain what are known as functional monomers, which include acrylic acid, methacrylic acid, maleic acid, acrylamide and others. These help stabilize the latex and provide the PSA with functional groups where additional chemical reactions can take place.

The model emulsions synthesized for this study are representative of those used in PS labels. They are composed mostly ( $\approx 81\text{ mass}\%$ ) of soft monomers n-butyl acrylate (BA) and 2-ethylhexyl acrylate (EHA), various combinations of the hard monomers ( $\approx 16\text{-}19\text{ mass}\%$ ) methyl methacrylate (MMA), vinyl acetate (VA) and styrene (STY) and the functional monomers ( $\approx 0\text{-}3\text{ mass}\%$ ) acrylic acid (AA) and methacrylic acid (MAA). The specific monomer structures and formulations are shown in Tables 2 and 3. As described in the Experimental section, all of the PSAs are produced via the same synthesis method and are formulated for coating using only the sodium polyacrylate rheology modifier. Model PSAs 8, 10 and 11 contain the same monomer composition, but were produced with emulsifiers possessing different structures and properties. Comparing the results of removal efficiency testing indicates that emulsifiers are not a dominant factor in determining the fragmentation behavior of the PSAs. In addition to this comparison, several commercial formulations were produced in which the surfactant systems were exchanged, but only relatively minor changes were seen in the removal efficiencies (For example, exchanging the emulsifier for commercial PSAs 4 and 24, with removal efficiencies of 2 and 97%, respectively, resulted in removal efficiencies of 10 and 96%, respectively.)

**Table 2:** Structure of monomers used in the model water-based PSA formulations.

<b>Soft Monomers</b>		
<b>n-Butyl Acrylate (n-BA)</b>	<b>2-Ethylhexyl Acrylate (EHA)</b>	
$\begin{array}{c} \text{CH}_2=\text{CH} \\   \\ \text{C}=\text{O} \\   \\ \text{O}(\text{CH}_2)_3\text{CH}_3 \end{array}$	$\begin{array}{c} \text{CH}_2=\text{CH} \\   \\ \text{C}=\text{O} \\   \\ \text{OCH}_2\text{CH}(\text{CH}_2)_3\text{CH}_3 \\   \\ \text{CH}_2\text{CH}_3 \end{array}$	
<b>Functional Monomers</b>		
<b>Methacrylic Acid (MAA)</b>	<b>Acrylic Acid (AA)</b>	
$\begin{array}{c} \text{CH}_3 \\   \\ \text{CH}_2=\text{C} \\   \\ \text{C}=\text{O} \\   \\ \text{OH} \end{array}$	$\begin{array}{c} \text{CH}_2=\text{CH} \\   \\ \text{C}=\text{O} \\   \\ \text{OH} \end{array}$	
<b>Hard Monomers</b>		
<b>Methyl Methacrylate (MMA)</b>	<b>Styrene (STY)</b>	<b>Vinyl Acetate (VA)</b>
$\begin{array}{c} \text{CH}_3 \\   \\ \text{CH}_2=\text{C} \\   \\ \text{C}=\text{O} \\   \\ \text{OCH}_3 \end{array}$	$\begin{array}{c} \text{CH}_2=\text{CH} \\   \\ \text{C}_6\text{H}_5 \end{array}$ 	$\begin{array}{c} \text{CH}_2=\text{CH} \\   \\ \text{O}-\text{C}=\text{O} \\   \\ \text{CH}_3 \end{array}$

**Table 3:** Monomer compositions of model acrylic water-based PSA formulations.

Model System	Monomer Components						
	Soft Monomer		Hard Monomer			Functional Monomer	
	n-BA	EHA	MMA	VA	Styrene	MAA	AA
M1	70.8	10.0		16.0			3.2
M2	70.8	10.0		16.0		3.2	
M3	70.8	10.0	16.0			3.2	
M4	70.8	10.0	3.2	16.0			
M5	70.8	10.0			16.0	3.2	
M6	70.8	10.0			16.0		3.2
M7	70.8	10.0	16.0				3.2
M8	80.8		16.0			3.2	
M9	80.8		8.0		8.0	3.2	
M10	80.8		16.0			3.2	
M11	80.8		16.0			3.2	

Table 4 lists the performance properties and surface energies for films cast from the model system along with their  $T_g$ s determined via dynamic mechanical analysis (DMA) and average removal efficiencies measured subsequent to 50 °C repulping. As was the case for the commercial formulations, a comparison of removal efficiencies with the monomer compositions indicates that the combination of VA and AA results in films with the lowest removal efficiencies. Keeping everything else in the formulation fixed, replacing VA with MMA or STY increases removal efficiency. Also, replacing AA with MAA increases removal efficiency substantially.

**Table 4:** Removal efficiencies, performance properties, glass transition temperatures and surface energies for model acrylic water-based PSA formulations.

Model System	RE @ 50°C (%)	180° Peel (N/25mm)	Loop Tack (N/25mm)	Shear (min)	$T_g$ (°C)	Surface Energy (mJ/m <sup>2</sup> )
M1	2	10.5	10.2	1069	-5.4	25.1
M2	57	11.2	10.7	449	-3.6	24.5
M3	79	8.1	7.6	4707	-2.0	28.7
M4	10	12.6	21.8	3.5	-2.8	21.0
M5	77	8.1	8.9	1045	-0.1	27.4
M6	70	25.0	10.9	147	-2.6	26.8
M7	75	10.8	12.2	2684	-6.3	27.3
M8	90	13.0	17.8	214	10.5	30.8
M9	84	8.1	7.1	573	0.8	29.3
M10	90	7.6	12.4	248	3.4	36.4
M11	81	4.9	5.8	1890	2.1	29.2

The experimental Log  $K_{ow}$  for the monomers VA, MMA, STY, AA and MAA, where  $K_{ow}$  is the octanol-water distribution coefficient, are 0.73, 1.38, 2.95, 0.35 and 0.98.<sup>23</sup> Log  $K_{ow}$  has been shown to correlate with water solubility for organic liquids,<sup>24</sup> thus it appears that the results are generally consistent with the hypothesis that increasing hydrophobicity enhances the removal efficiency of the adhesive polymer. However, it should be emphasized that only the presence of the most hydrophilic of these monomers results in low removals and both VA and AA are required to produce the extremely poor efficiencies. Thus avoiding these and similar monomers appears to be of key importance in making water-based PSAs more benign. Furthermore, increasing removal efficiencies does not appear to be simply a matter of using the most hydrophobic monomers. For example, removal efficiencies were found to be reduced by replacing the harder BA ( $T_g = -54$  °C, log  $K_{ow} = 2.36$ ) with the significantly more hydrophobic 2-EHA ( $T_g = -80$  °C, log  $K_{ow} = 4.09$ ). Thus it appears that under certain circumstances (e.g., monomers possessing sufficiently high hydrophobicities) the hardness of the monomer is of greater importance.

**Impact of Moisture on Properties of Model PSAs.** In previous publications it was reported that cohesive strength controls the removal efficiency of hot-melt PSA produced with styrenic block copolymers.<sup>17</sup> For these adhesives, it appears that the standard shear adhesion failure temperature or SAFT is an effective means for thermally locating the region where the cohesive strength of PSA films decrease below a threshold value allowing for their fragmentation during repulping operations. Implicit in the removal efficiency model for hot-melt PSA discussed in the Introduction is the assumption that modifications to the strength of these materials when placed in water are minor relative to those induced by temperature changes. That is, placing the hot-melt films in an aqueous environment at temperatures well below their SAFT does not decrease their cohesive to the point that the films readily fragment during repulping. SAFT is not commonly measured for water-based PSA because, unlike hot-melts for which a distinct transition exists, i.e., the styrenic disruption temperature, which results in a dramatic loss in cohesive strength, water-based films lose their strength more gradually over a broad temperature range. Also, from the results discussed in the previous sections, it appears that the interaction between water-based films and water likely plays a significant role in determining their cohesive strengths during repulping.

Acrylic water-based PSA is formulated as an aqueous dispersion of relatively polar monomers, and their films retain a significant concentration of emulsifier and other amphiphilic chemicals. It is likely that these films will swell and lose strength when placed in water. To gauge the extent to which this occurs, an environmental tensile test was devised. For most solids, cohesive strength is gauged through tensile testing. For PSA films, this is difficult, because the films are made to flow for light pressures and yield for small deformations. They are also highly viscoelastic. To complicate matters further, tensile testing here will be carried out in a temperature-controlled, aqueous environment. As described in the Experimental section, tensile samples are produced here by coating the PSA film over 2 separate pieces of 25 mm wide poly(ethylene terephthalate) (PET) films that are placed against each other to form a continuous substrate for the adhesive. All of the films cast for this study are targeted for 1 mil (25.4  $\mu$ m). The ends of the PET are not coated and serve as gripping tabs. The shapes of the curves were repeatable for a particular PSA, but no general trend was discernable (e.g., both brittle and ductile behavior is demonstrated by the PSAs but appears unrelated to removal levels).

What is clear from the tensile tests is the impact water has on strength. Figure 7 shows the maximum force values for the model PSAs that were produced with the same surfactant system. Results are shown for dry films measured at 22 °C and for the wet films (1 minute soaking) measured at 22 and 50 °C. (The maximum force may correspond to failure or yielding depending on the behavior of a particular film.) No correlation between dry film strength and removal efficiency was found and the strength of the films drop significantly when exposed to water. The extent of this drop has no relationship to the strength of the films when dry. Superimposed on the chart is the measured removal efficiency for the PSAs. It would appear that a threshold region exists for the wet strength below which the films demonstrate extremely low removals and above which the films are benign. This threshold value is strongly temperature dependent. Those films that possess wet strengths above about 0.2 N at 22 °C and 0.1 N at 50 °C have removal efficiencies above 75%. (This value is important because it was previously shown that this is sufficient to pass standard government pilot tests for benign adhesives.) The results for both temperatures produce the same demarcation between the benign and problem formulations.

The results above provide for a more general description of what governs the fragmentation of PSAs during paper recycling operations. It appears that a threshold strength exists below which the films readily fragment to a size that is difficult to remove via screening. For hot-melt PSAs produced with styrenic block copolymers, strength drops below this threshold near its SAFT and is therefore primarily temperature-triggered. This is understood as the movement of temperature towards the hot-melt adhesive's styrenic disruption temperature resulting in the loss of physical crosslinking interactions and increased viscous behavior by the rubbery phase. Thus, formulating environmentally benign hot-melt PSA requires that the phase behavior be properly controlled through choice of base polymer, tackifying resin and, to a lesser extent, plasticizer. For acrylic water-based PSAs, strength drops when films are exposed to water. If the strength remains above this value after soaking, the adhesive is environmentally benign.

It appears that the dry strength of the films has no bearing on their strength subsequent to soaking and that PSAs containing combinations of the more hydrophilic monomers VA and AA have lower removal efficiencies. However, it is not clear whether the effect of moisture on acrylic films is a kinetic or thermodynamic. Important insights on the rate dependency of water penetration into PSA film can be obtained by studying the time and temperature dependency of wet tensile results. Figure 8a shows the maximum force as a function of soak time for the model water-based PSAs 1, 5 and 8 at 22 °C. The tensile strength decreases sharply within the first 30 seconds of soaking for all 3 films, but to a much greater extent for PSA 1, which contains both VA and AA. Strength changes little if any with further soaking times indicating that kinetics of water penetration into the film is likely not a controlling factor. Figure 8b indicates the removal efficiency of model water-based PSA 1, 5 and 8 as a function of soaking time in water before starting repulping. No trend in removal efficiency with increasing soaking time is discernable, which is consistent with this conclusion.

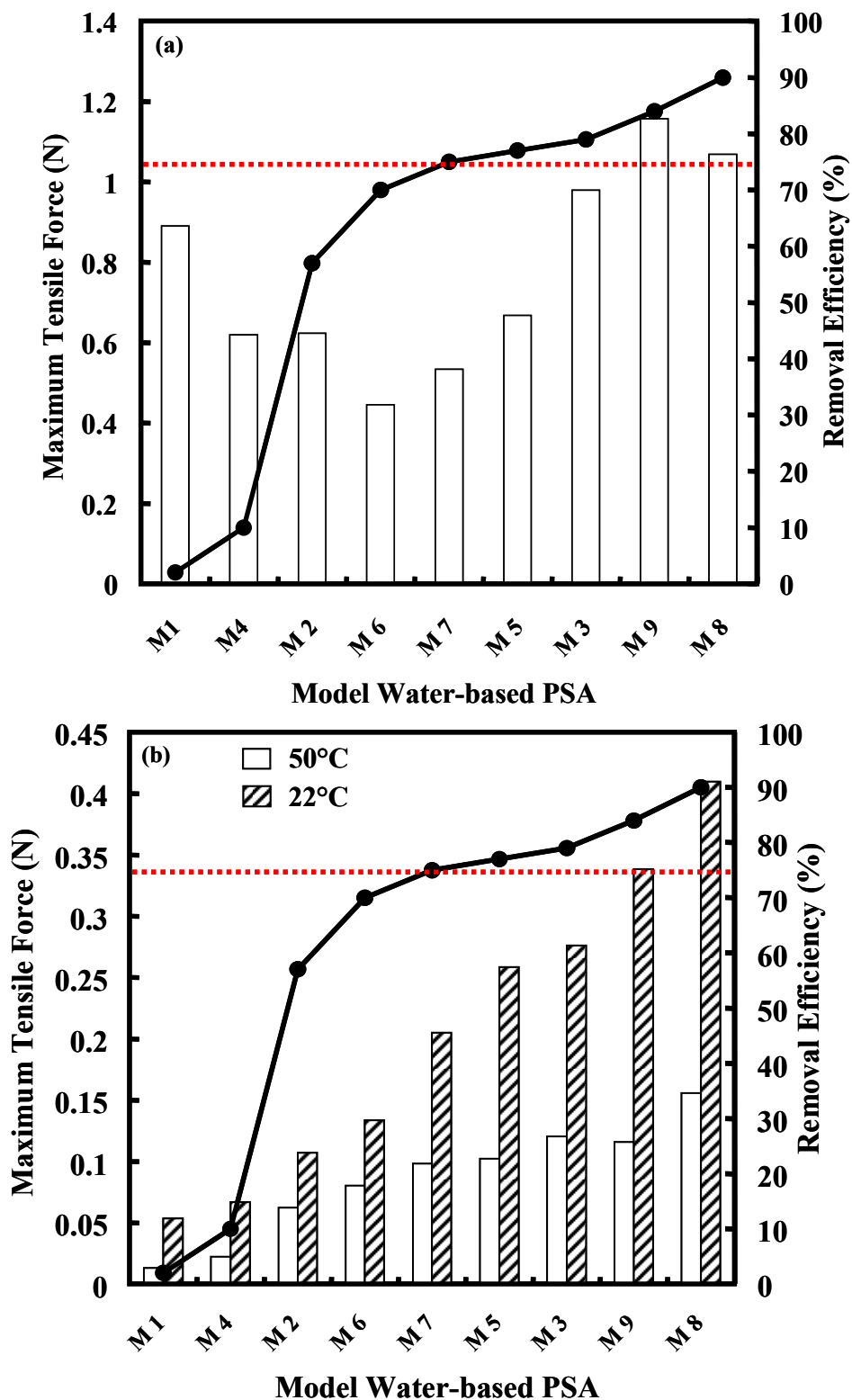


**Figure 7.** (a). Maximum dry tensile force values for the model water-based PSA films (21 °C and 50% RH). Superimposed are their removal efficiencies measured at 50 °C (solid dots). (b). Maximum tensile force values for the model water-based PSAs after soaking in water for 1 minute at 22 °C (solid bars) and 50 °C (striped bars).

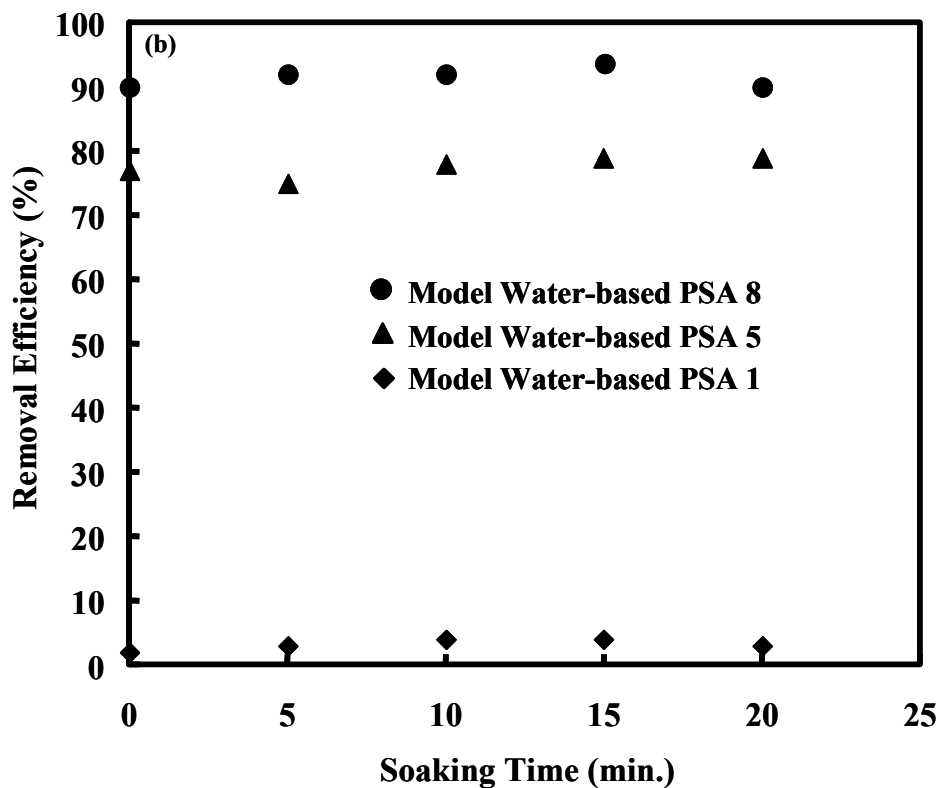
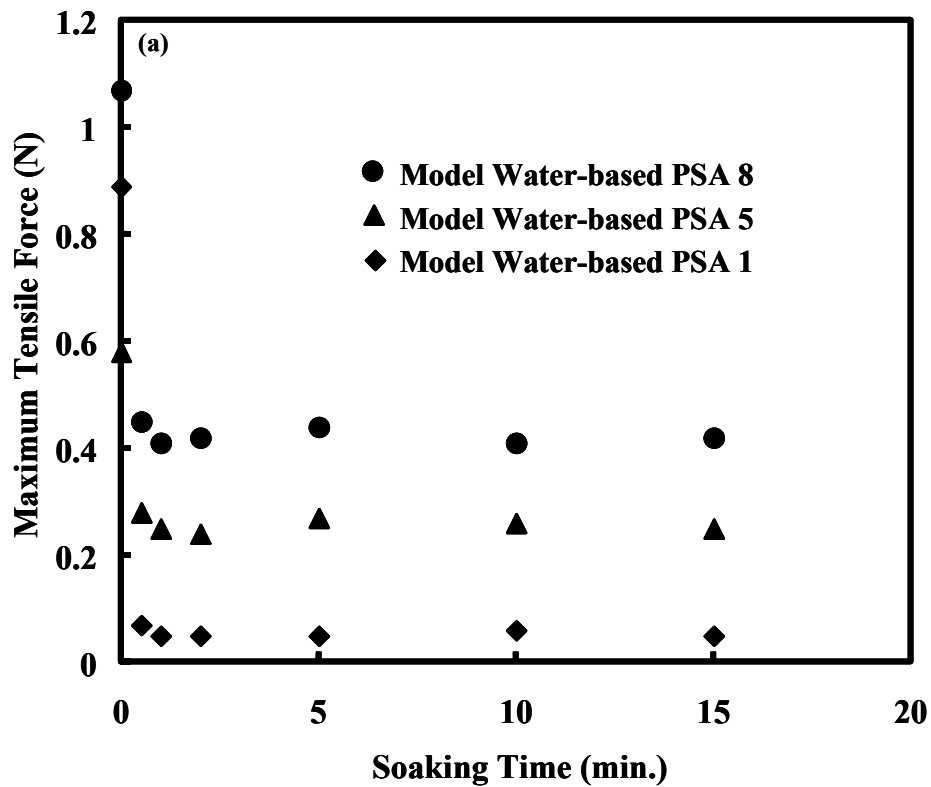


**Figure 8.** (a). Maximum tensile force values for model water-based PSAs 1, 5 and 8 as a function of soaking time at 22 °C. (b). Removal efficiency of model water-based PSA 8 at 50 °C as a function of soaking time prior to repulping.

## **Summary and Conclusions**

From the results presented above, it is apparent that the removal efficiencies of acrylic water-based PSAs can not be predicted from their dry mechanical or surface properties. When placed in water, these adhesives, which compose most of the PS label market, rapidly swell and their strength is significantly degraded. A decrease of more than 60% in the force required to rupture adhesive films after soaking in water for 1 minute at the same temperature was found for all of the commercial and model PSAs examined. It appears that the ability to retain a level of wet strength that is above a threshold value when saturated with water is required for a PSA film to be environmentally benign. This wet strength was found to be governed primarily by the monomer composition of the adhesive polymer. It is clear that the combination of VA and AA monomers produces water-based PSAs that readily fragment during paper recycling operations. It also appears that, in general, VA is one of the more problematic monomers for recyclability used in acrylic formulations. Replacing VA and AA monomers in an adhesive polymer with a more hydrophobic version increases its removal efficiency substantially. Specific demonstrations of this here included replacing the functional monomer AA with MAA and replacing the hard monomer VA with either MMA and/or STY. In each case a dramatic increase in removal efficiency was observed. More generally, it can be concluded that those changes that enhance wet strength, which may include the inclusion of stronger, more water resistant components can be used to limit the fragmentation of a PSA film during repulping and reduce its impact on paper recycling operations.



### ***3.3 Affect of Amphiphilic Additives on the Behavior of Water-based Acrylic Pressure-Sensitive Adhesives during Paper Recycling***

Contamination of post-consumer waste by pressure sensitive adhesive (PSA) presents a significant obstacle to increasing recycling rates.<sup>10,11,13-15</sup> These materials break down during repulping, which involves the use of water and mechanical energy to fiberize paper products. Fragmented pieces of adhesive films are mostly removed with conventional screening and cleaning equipment.<sup>12,16</sup> However, the PSA not removed is passed onto the remaining recycling operations and causes deposits on equipment and defects in the final paper product. The cost of the problems created by the presence of PSA contaminants is substantial and has compelled much research on methods for its control. The most promising and widely accepted of these is the redesign of pressure sensitive (PS) label products to inhibit the fragmentation of PSA films during pulping.

Together, water-based and hot-melt PSA account for 80% of adhesives used on paper labels, with a 3:1 ratio of water-based to hot-melt. Previously, it was reported that the removal efficiency of hot-melt PSA is strongly dependent on the properties of the facestock onto which it is attached.<sup>19</sup> For example, the screening removal efficiency of a commercial label-grade, hot-melt PSA was nearly 50% lower when attached to a commercial facestock containing sizing and wet strength additives versus untreated control. It was hypothesized that increased adhesion between the PSA film and facestock in an aqueous environment resulted in films that possessed a less collapsed, more open structure during repulping, which allowed for greater stress to be induced and resulted in more fragmentation. Relative to hot-melt formulations, water-based acrylic PSAs are more complex. After emulsion polymerization, a single adhesive can be modified with tackifying dispersions, wetting agents, rheology modifiers and other additives to meet a variety of product specifications. Here, the influence of water-based PSA design on adhesive behavior during repulping is examined.

In an earlier publication, the fragmentation of water-based acrylic PSA was shown to be strongly dependent on the monomer composition of the base elastomer.<sup>25</sup> Specifically, it was shown that the presence of both vinyl acetate and acrylic acid monomers produced PSA that readily broke down during repulping operations resulting in a low screening removal efficiency. This conclusion is based on a study of a model system for which the hard and functional monomers of a commercial formulation that readily fragments during repulping were replaced with more hydrophobic components. For example, in one formulation, methacrylic acid replaced acrylic acid, and in another, methyl methacrylate replaced vinyl acetate. Each of these substitutions produced a significant reduction in fragmentation and a substantial increase in screening removal efficiency. It was also shown that the water-based films rapidly swell in water and that the swelling kinetics likely play little role in determining fragmentation behavior. The most salient point from this work is that the strength of water saturated PSA films determines their fragmentation behavior during repulping operations and thus the extent to which they can be controlled with mill screening equipment.

In this work, we focus on amphiphilic additives and their influence on PSA behavior during recycling. This includes emulsifiers used during the synthesis, wetting agents used to aid in the coating of PSA films, and surfactants used in tackifying dispersions. We will present information on how these additives change the molecular structure of the films, the mechanical

properties and the particle morphologies. Furthermore, given that facestock properties affected hot-melt behavior, we will show results for PSAs coated on different facestocks. These findings extend previously published results to provide a more comprehensive understanding of how PSA synthesis, formulation and PS product design impact the behavior adhesives during recycling operations.

## **Experimental Section**

**Chemicals and Materials.** Copper (II)-ethylenediamine complex (1 M solution in water) was purchased from Acros Organics (Pittsburgh, PA). Boise-Cascade Corporation (International Falls, MN) provided papermaking fiber and commercial facestocks. Acrylic water-based PSAs were synthesized and formulated at Franklin International (Columbus, OH). Model water-based PSAs were synthesized using commercially available monomers including *n*-butyl acrylate, 2-ethylhexyl acrylate, vinyl acetate, methyl methacrylate, acrylic acid and methacrylic acid and commercially available sulfated nonylphenol ethoxylate (ammonium salt) and nonylphenoxy poly(ethyleneoxy) ethanol emulsifiers. Many of the adhesive emulsions utilized sodium persulfate or ammonium persulfate initiators, *t*-butyl hydroperoxide oxidizer, sodium formaldehyde sulfoxylate reducer, an ammonia buffer and commercial biocides. The wetting agent utilized in the coating package is 50% FX-1 solution purchased from Eagle Sales (St. Louis, MO). Its composition is described as 21% 2-butoxyethanol and 4% ethanol. The tackifying dispersion was obtained from Arizona Chemical (Jacksonville, FL). It is a commercial product, Aquatac 6085, described by the supplier as an aqueous dispersion of rosin glycerol ester with 2-4% of surfactant content. In order to cast uniform films without wetting agent, a rheological modifier, Alco gum AN-10, was added at about 1%. Alco gum AN-10, manufactured by Alco Chemical (Chattanooga, TN), is a sodium polyacrylate thickener with solid content of 10% and viscosity of 200-400 cps. The effect of a common commercial defoamer was also examined as part of this study. Foam Blast 325 supplied by Emerald Performance Materials (Cuyahoga Falls, OH) was used in studies at levels of 0.15 to 0.6%. Emulsions were coated on two-sided release paper using a draw-down coater and dried in an 82 °C oven for 10 minutes. For most samples, film thickness was targeted at 1 mil or 25.4 μm.

**Characterization of PSAs.** Procedures used in characterizing the PSAs have been described in detail elsewhere.<sup>3,8,9,15</sup> Here these descriptions are repeated some in an abridged form. All performance testing was carried out on 1 mil (25.4 μm) thick films under controlled temperature and humidity conditions, 22 °C and 50 % RH. Peel strength of water-based PSAs were measured using an IMASS Inc. (Accord, MA) 180° Slip/Peel Tester Model SP101B at a peel rate of 12"/min. One inch wide polyethylene terephthalate (PET) backed films were peeled from PSTC grade polished stainless steel panels (Ryerson Steel, Chicago, IL) rolled with a 5.0 lb. ASTM quality manual roller. The average peel force from 3 tests was reported for each sample. Shear test strips were prepared with a contact area of 0.5" × 0.5" between PSTC grade polished stainless steel panels and PET-backed films transferred with a 4.5 lb. ASTM quality manual roller. Five-hundred gram weights were clipped to the bottom of the test strips. The average time in minutes for the weight to pull the PET-backed films from the plate for 3 tests was reported for each sample. Loop tack strengths of water-based PSA were measured using an Ametek Corporation (Paoli, PA) Chatillon with DFM 10 Digit Force meter. PSA was direct coated onto PET to form 1" × 5" test strips, which for testing, were looped with the adhesive facing out and used to form a contact area of 1" × 1" on PSTC grade polished stainless steel

panels. A dwell time of 1 second and upward travel speed of 12"/min. were used for testing. The average maximum force for 3 tests was reported for each sample. Glass transition temperatures ( $T_g$ ) were determined using the TA Instruments (New Castle, DE) DMA 2980 Dynamic Mechanical Analyzer. Tested samples were composite structures formed by dipping a glass support cloth (30 mm  $\times$  10 mm  $\times$  0.3 mm) into the liquid adhesive emulsion. The thermal locations of the peaks in the loss modulus ( $E''$ ) for scans carried out at 1 Hz. were reported as the  $T_g$ . Force-displacement curves for PSA films were determined using an Instron (Norwood, MA) 5542 tensile tester at a crosshead speed of 10 mm/min. For the dry tests, two pieces of PET films (1" wide by 3" long strips) were used as a sample holder. A 1 mil adhesive film was transferred from release liner over the joint between the 2 PET films and they were placed in the tensile tester grips. All of the dry tests were made at 22 °C and 50% humidity. For water-submerged testing, the tensile tester was equipped with an in-house temperature-controlled bath. At least twenty measurements were made for each sample under both dry and wet conditions, and the average maximum forces were reported for each sample. Surface energies of water-based adhesives were determined from contact angle measurements for selected liquids.

**Procedure for Testing the Removal of PSA Labels.** A known amount of pressure sensitive adhesive film ( $\approx 1.5$  g) was transfer coated onto paper face stock ( $\approx 5$  g) using a heavy roller to produce a label system. Subsequent to the lamination process, the release liner was removed and the PSA/substrate system ( $\approx 6.5$  g) was attached by hand to envelope grade paper ( $\approx 8$  g). These laminates were intermixed with copy paper (287 g). All paper samples were conditioned at 23°C and 50% RH prior to use. The mixture of copy paper and laminates was then cut into 0.25" wide strips using a commercial shredder. Tap water (3 L) that had been heated to the selected temperature with an immersion heater was combined with the shredded sample in an Adirondack 450H laboratory pulper (Adirondack, NY) and mixed at 60 Hz for 30 minutes. The repulper was equipped with a heating/cooling jacket connected to a recirculating water bath to maintain temperature during testing. The temperature change of the contaminated fiber slurry for a 30-minute repulping experiment was determined to be  $\pm 2^\circ\text{C}$  over the range of temperatures investigated (10 to near  $100^\circ\text{C}$ ). The resulting fiber slurry was passed through a Valley vibrating flat screen equipped with a 15-cut slotted screen (i.e., slotted openings of 0.38 mm), which is a size that provides strict requirements for separation during recycling operations. Screening rejects containing adhesive particles and fiber were removed from the screen plate. Rejected PSA particles were isolated from fibrous material for mass analysis using copper(II)-ethylenediamine (CED) mixed with a magnetic stir rod for approximately 8 hours to dissolve cellulose fiber. Adhesive particles were isolated via filtration and dried at  $105^\circ\text{C}$  to a constant weight. Rejected PSA mass was reported as a Removal Efficiency, which is the percentage of PSA added to the repulper that is rejected at the screen. The reproducibility of removal efficiency measurements was found to be  $\pm 3\%$ . This procedure was described in previous publications,<sup>8,9,15</sup> and was recently shown to correlate well with standard government pilot scale testing for removal efficiencies.<sup>16</sup>

## Results and Discussion

**Properties of Films Produced from Adhesive Emulsions.** Table 5 shows the monomer composition for the model system of PSAs used in this study, which are denoted PSA1, PSA2 and PSA3. These are based on a common commercial formulation used in the production of PS labels. The adhesive polymers in water-based acrylics combine so-called soft, hard and functional monomers to achieve a variety of performance properties. Soft and hard refer to the glass transition temperatures ( $T_g$ ) of homopolymers produced with these monomers. Soft and hard monomers would produce homopolymers with  $T_g$ s of below about  $-40^\circ\text{C}$  and above  $30^\circ\text{C}$ , respectively. Functional monomers are used to stabilize the latex and provide the PSA polymer chain with functional groups where additional chemical reactions can occur. Table 6 lists the performance properties of the model adhesives, wet tensile strengths and screening removal efficiencies measured at  $50^\circ\text{C}$ . These 3 PSAs were selected for study to provide a range of fragmentation behaviors. As described in detail previously, monomer composition appears to be the dominant factor controlling their fragmentation during repulping operations.<sup>25</sup> In general replacing softer monomers with harder ones or using less hydrophilic monomers increases the removal efficiency. Improvements in screening removal efficiencies appear to be associated with increased wet-strengths, Table 6. These data suggest that additives that change the amount of swelling in water are likely tied to changes in the strength of the films.

**Table 5:** Monomer compositions of model water-based PSA formulations which were synthesized with n-butylacrylate (BA), 2-ethylhexylacrylate (EHA), methyl methacrylate (MMA), vinyl acetate (VA), methacrylic acid (MAA) and acrylic acid (AA).

PSA	Monomer Composition					
	Soft Monomer		Hard Monomer		Functional Monomer	
	BA	EHA	MMA	VA	MAA	AA
PSA1	80.8		16		3.2	
PSA2	70.8	10.0	16			3.2
PSA3	70.8	10.0		16.0		3.2

**Table 6:** Performance properties, wet tensile strengths and removal efficiencies (RE) measured at  $50^\circ\text{C}$  for the model PSAs.

PSA	Loop Tack (N/25mm)	180° Peel (N/25mm)	Shear (min.)	Wet Tensile Strength (N)	RE (%)
PSA1	17.8	13.0	214	0.39	90
PSA2	12.2	10.8	2684	0.21	75
PSA3	10.2	10.5	1069	0.05	2

The results presented above represent the behavior of the base PSA formulation. The additives used to form these films (e.g., sodium polyacrylate rheology modifier, various biocides and defoamers) do not impact the fragmentation behavior of the adhesives.<sup>25</sup> The results reported below are for the additives that do have a significant impact on measured removal efficiencies.

**Coating Package and Removal Efficiencies.** Pressure sensitive labels are commonly manufactured with water-based PSA by a process known as transfer coating, in which, the formulated adhesive latex is first applied to release liner and dried to produce a film. Then this liner-backed adhesive film is pressed onto facestock to produce the label stock. Casting uniform coatings of water-based formulations on release liner requires that the surface tension of the aqueous dispersion be reduced. This can be understood through the spreading coefficient ( $S_{l/s}$ ),

$$S_{l/s} = \gamma_s - \gamma_l - \gamma_{ls} \quad (2)$$

which is negative of this free energy change between final and initial states of a spreading process in which a liquid with a surface tension  $\gamma_l$  is spread on a solid with a surface energy  $\gamma_s$  to form an interface with energy  $\gamma_{ls}$ .<sup>26</sup> A positive spreading coefficient indicates that the liquid spontaneously wets the solid. In the case of water-based PSA formulations, the process of interest involves the wetting of release liner, which has a low surface energy.

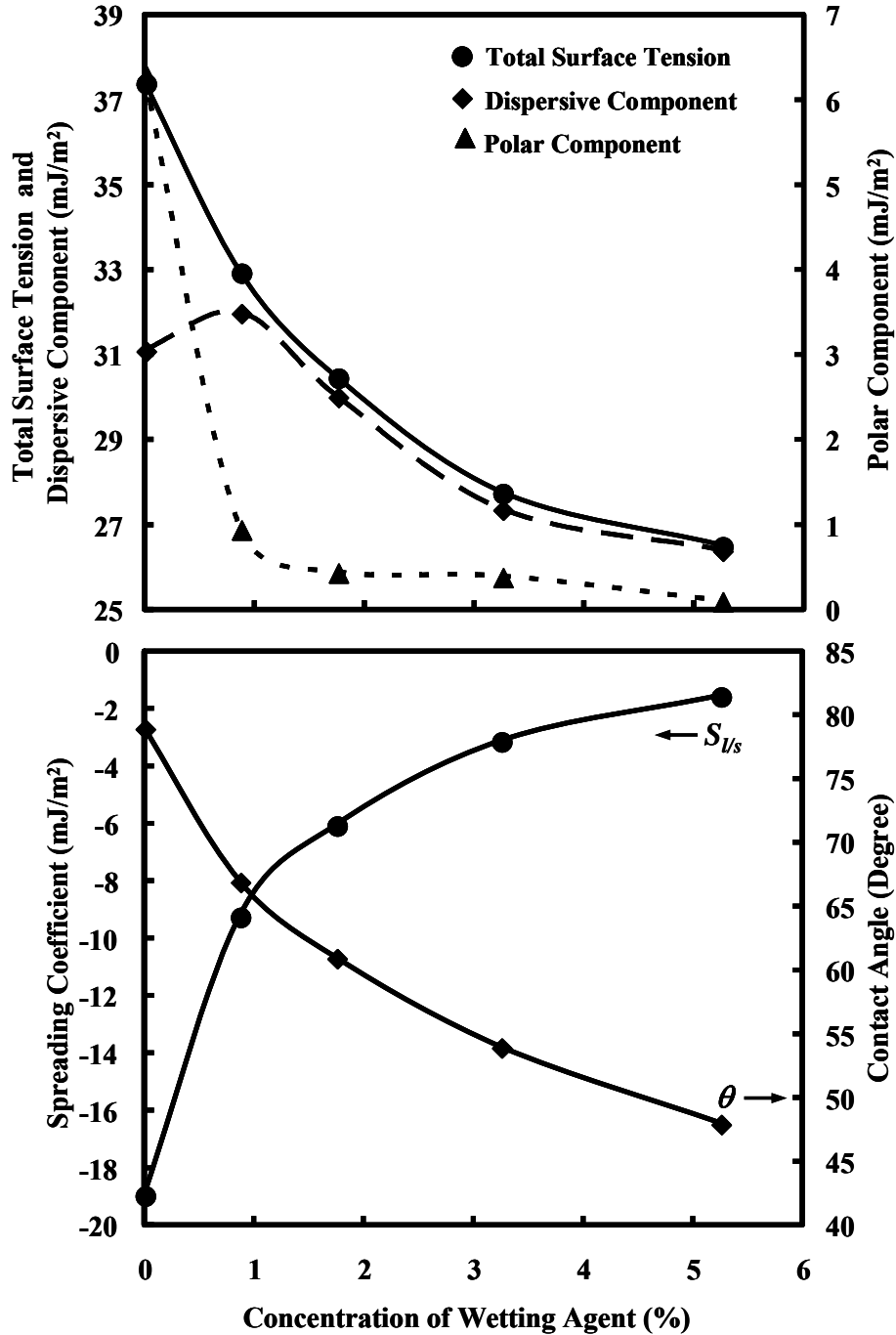
A method for gauging surface energy of a solid is through a series of contact angle measurements using solvents of known surface tensions; a procedure that was described in previous publications.<sup>27-29</sup> This approach assumes that total surface energy for phase  $i$  ( $\gamma_i$ ) can be split into contributions from polar ( $\gamma_i^p$ ) and dispersive ( $\gamma_i^d$ ) interactions, i.e.,  $\gamma_i = \gamma_i^d + \gamma_i^p$ . With these values, interfacial energies between 2 phase  $i$  and  $j$  can be estimated using,<sup>30,17</sup>

$$\gamma_{ij} = \gamma_i + \gamma_j - 2[(\gamma_i^d \gamma_j^d)^{1/2} + (\gamma_i^p \gamma_j^p)^{1/2}] \quad (3)$$

Measurements done on a variety of release liner indicate that it has surface energy values in the range of 18-30 mJ/m<sup>2</sup> consisting almost solely of dispersive contributions, i.e.,  $\gamma_i \approx \gamma_i^d$ . Combining Eqs. 2 and 3 and using this assumption, we have

$$S_{l/s} = 2[(\gamma_l^d \gamma_s^d)^{1/2} - \gamma_l] \quad (4)$$

This indicates that a more positive spreading coefficient is obtained by lowering the surface tension of the liquid phase, while maintaining its dispersive component as high as possible. Figure 9 shows the influence of a commercial wetting agent on the latex for PSA3. Figure 9a shows the affect of the wetting agent on the surface tension and its polar and dispersive components, while Fig. 9b shows how its addition change both the spreading coefficient as well as the contact angle for the latex on a release liner with  $\gamma = \gamma^d = 25.1$  mJ/m<sup>2</sup>. Wetting agents are used in PSA formulations sparingly, usually at levels of 1% or less. This is done to limit the foaming tendency of the formulation, but it also appears to correspond to where the additive has the greatest affect.



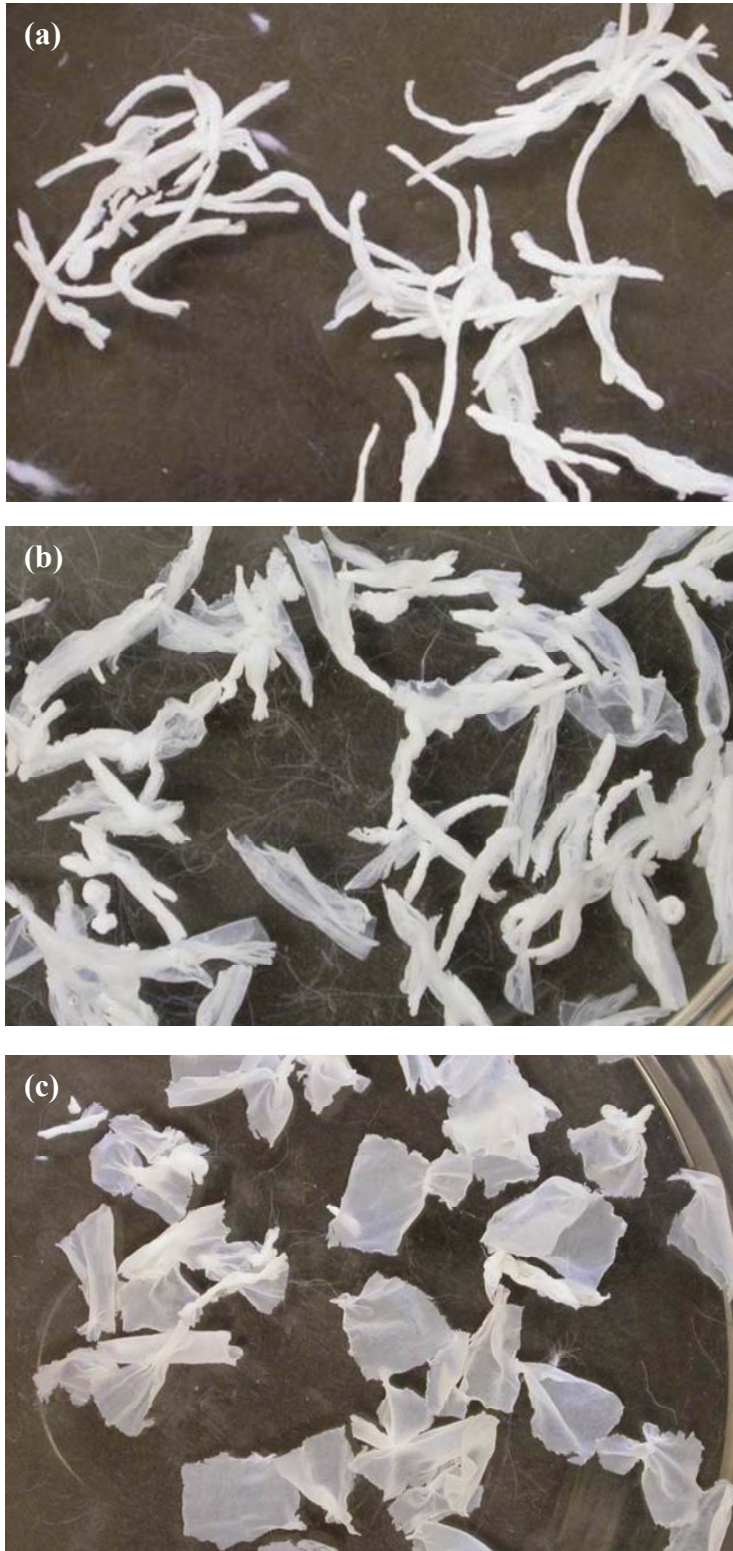
**Figure 9.** a.) Surface tension and polar and dispersive components of PSA3 with variable levels of wetting agent; b.) Spreading coefficient of PSA3 and the contact angle of this emulsion on release liner with variable levels of wetting agent.

Table 7 list the surface energies along with their dispersive and polar components for the model PSA films formulated with various levels of a common wetting agent. Also shown are the cohesion values (maybe better thought of as the work of self adhesion) and measured screening

removal efficiencies. The reversible work,  $W_A$ , to separate PSA surfaces in an aqueous environment is simply  $2\gamma_{sl}$ , where the solid ( $s$ ) is the adhesive film and water is the liquid ( $l$ ). It appears that the surfactant retained in the dried PSA films substantially raises the polar component of their surface energy when placed in water and this reduces the screening removal efficiencies for the model PSAs. Insights on how the wetting agent functions to reduce removal efficiencies can be found in the residual particles screened out of the fiber slurry. Figure 10 shows adhesive particles obtained subsequent to repulping for PSA2 with 3 different wetting agent concentrations. (These are optical images of adhesive particles isolated from an unscreened slurry.) It can be seen that films take on a more open structure and, less obvious, have a smaller size as the wetting agent concentration is increased. This is consistent with the expected lower adhesion between PSA surfaces, and the lower removal efficiencies are consistent with the assertion that the greater the surface area of the adhesive film, the greater the fragmentation during repulping operations.

**Table 7:** Effect of wetting agent on the surface energies, surface energy components and work of self adhesion in water of model PSA films. Also shown are the removal efficiencies (RE) measured at 50 °C.

PSA	Wetting Agent (%)	Surface Energy (mJ/m <sup>2</sup> )	Polar Component (mJ/m <sup>2</sup> )	Dispersive Component (mJ/m <sup>2</sup> )	Work of Adhesion (mJ/m <sup>2</sup> )	RE (%)
PSA1	0	30.4	0.1	30.3	94.6	90
	0.87	30.9	0.0	30.9	103.6	89
	1.75	37.1	7.7	29.4	39.3	83
	3.50	63.3	32.1	31.2	6.0	74
	5.25	64.4	30.7	33.7	7.7	72
PSA2	0	23.2	0.2	23.0	89.7	75
	0.87	26.3	0.1	26.2	93.6	62
	1.75	34.1	7.6	26.5	38.9	47
	3.50	58.6	30.7	27.9	5.9	23
	5.25	59.8	31.7	28.1	5.4	18
PSA3	0	25.1	0.3	24.8	87.1	2
	0.87	24.6	0.1	24.5	93.3	5
	1.75	25.1	0.0	25.1	96.6	10
	3.50	34.2	7.9	26.3	37.9	2
	5.25	57.6	30.5	27.1	5.8	0



**Figure 10.** Morphology of adhesive particles after repulping a.) without any additional wetting agent; b.) with 1.75% wetting agent and c.) with 5.25% wetting agent.



Figure 11 is a plot of the screening removal efficiencies of the 3 model PSAs as a function of their wetting agent concentrations. It appears that the addition of wetting agent has a significant affect on the removal efficiency of PSA2, but little impact on those of PSA1 and PSA3. The impact of the wetting agent on particle structure during repulping appears to be qualitatively similar for all 3 PSAs. It is likely the property most responsible for the observed differences is the wet tensile strength. It can be seen from Table 6 that the wet tensile strength of PSA2 is substantially higher than that of PSA3 and about half of that measured for PSA1. The addition of wetting agent did not decrease these values. This suggests that the observed differences come from the base strength of the PSA films. That is, for strong films such as PSA1, the presence of wetting agent has a small impact on its fragmentation behavior because even in its open configuration, it is strong enough to not break down. The opposite is true for exceedingly weak films such as PSA3, regardless of the additive level, it readily fragments.

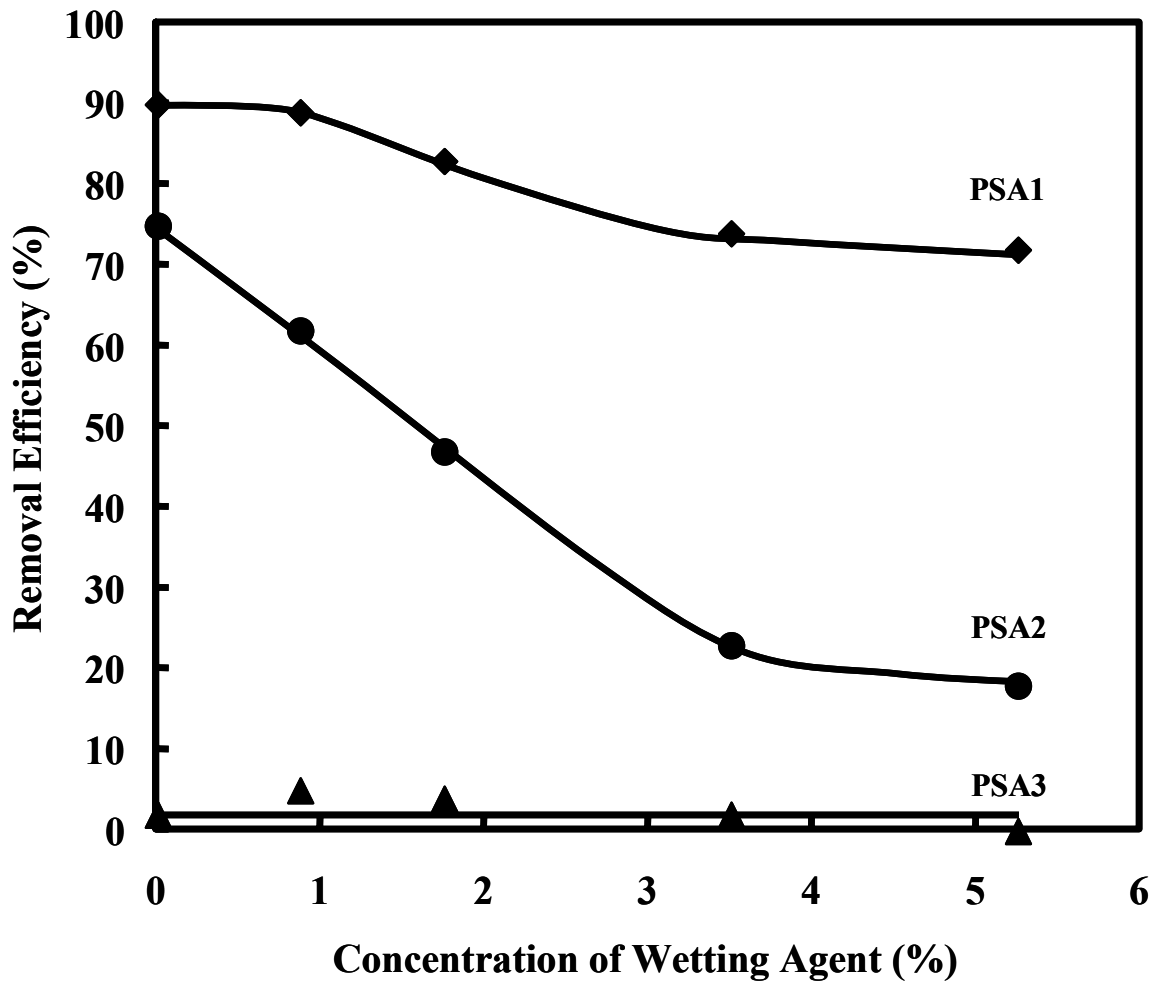


**Figure 11.** Removal efficiency at 50 °C of model PSAs as a function of the wetting agent concentration used in their formulation.

**Tackifying Dispersions and Removal Efficiencies.** Tackifiers are used in a PSA formulation to increase the tack of formed films. Table 8 lists the properties of PSA1 and PSA2 produced with tackifying resin concentrations ranging from 0 to 30% (w/w). (PSA3 was left out because its already low removal efficiency means little or no change is possible.) These are levels that are commonly used in water-based acrylic PSAs. A significant increase in tack is observed with the addition of the dispersion. Accompanying this increase is a decrease in measured removal efficiencies. This would appear to indicate that tackifier is reducing the strength of the films. However, the measured wet tensile strengths are shown to increase with tackifier levels.

**Table 8:** Effect of tackifier dispersion on the loop tack value, glass transition temperature, wet tensile strength, self work of adhesion in water of model PSA1 and PSA2. Also shown are the removal efficiencies (RE) measured at 50 °C.

PSA	Tackifier Dispersion (%)	Tack (lbs)	T <sub>g</sub> (°C)	Wet Tensile Strength (N)	Work of Adhesion (mJ/m <sup>2</sup> )	RE (%)
PSA1	0	2.00	-10.5	0.39	96.8	90
	5	2.46	-9.4	0.40	99.6	91
	10	2.79	-5.9	0.43	100.6	91
	15	2.85	-2.1	0.45	98.8	89
	20	3.11	-1.3	0.46	93.8	88
	30	2.96	-2.1	0.48	45.6	85
PSA2	0	1.70	-22.3	0.21	90.0	75
	5	1.96	-21.1	0.23	95.2	71
	10	2.84	-18.7	0.25	89.2	66
	15	2.75	-16.2	0.28	87.0	60
	20	3.33	-12.1	0.31	84.4	56
	30	3.62	-6.5	0.35	45.4	52

This result, which appears to contradict our previous findings, can be explained upon closer investigation. The strength of the films does increase with the addition of tackifier. This particular tackifying resin is a glycerol ester rosin, which is a relatively hydrophobic species and it has a T<sub>g</sub> of about 40 °C, so when it is combined with PSA1 (T<sub>g</sub> = -10.5 °C) or PSA2 (T<sub>g</sub> = -22.3 °C) it acts to increase the T<sub>g</sub> of the adhesive polymer without increasing its susceptibility to swelling with moisture. However, because the tackifying resin is added to the adhesive polymer in the latex, it is dispersed to form a stable colloid with a surfactant. In this case, the tackifying dispersion contains 2-4% (w/w) surfactant, so the addition of 30% (w/w) tackifier dispersion to the latexes, which have approximately 50% solids levels, introduces as much as 1.2% (w/w) surfactant to the PSA films, which as was described in Table 7 would be expected to decrease the removal efficiencies for the films. Thus, it is reasonable to assume that the benefits to removal efficiencies from the increase in wet-strength are offset by the open morphology of the films induced by the accompanying surfactant. Evidence for this explanation is found in the work of cohesion data calculated from the surface energy data (Table 8). It can be seen that at 30% (w/w) tackifier dispersion levels, this quantity drops for the model PSAs to levels similar to those

found when about 1-2% (w/w) wetting agent is added, but the drops in removal efficiencies are not as large. It was also observed that the model PSAs containing high levels of tackifier dispersion had open adhesive films.

**Influence of Commercial Facestocks on Removal Efficiencies.** Table 9 shows the properties of 3 paper facestocks used in a previous study examining their influence on the fragmentation behavior of attached hot-melt PSAs.<sup>19</sup> In that study, it was demonstrated that both the tensile loss and surface energy of the facestocks determine how much of an influence they have on removal efficiencies of attached hot-melt PSA. (Tensile loss is the percentage drop in tensile strength with the saturation of paper in water, which is controlled primarily by the wet strength of the paper.) It was proposed that both properties impact the extent to which fibrous materials are retained on film surfaces. A higher wet-strength will inhibit the fiberization of the paper and a lower surface energy results in a higher work of adhesion for removing paper fibers from the PSA film in aqueous environments. In the table it can be seen that the CIS (coated-one-side) has the lowest surface energy and tensile loss. This is followed by the EDP (electronic data processing) and the untreated paper handsheets.

**Table 9:** Mechanical and surface properties of 3 paper facestocks used in the study and the removal efficiencies at 50 °C of model PSAs laminated onto these facestocks.

Face Stock	Basis Weight (g/m <sup>2</sup> )	Tensile Loss (%)		Surface Energy (mJ/m <sup>2</sup> )	RE at 50°C (%)		
		Machine Direction	Cross Direction		PSA1	PSA2	PSA3
Untreated Paper	60	98 ± 4		71.1	94	79	10
EDP	77	96 ± 4	96 ± 3	39.7	90	75	2
CIS	77	94 ± 4	94 ± 4	39.7	90	71	4

Listed in Table 9 are the removal efficiencies measured for the model water-based PSAs when attached to the different facestocks. What is interesting is that these changes are not nearly as substantial as those found for the hot-melt PSAs.<sup>19</sup> It is likely that this is due to the composition and structural differences between hot-melt and water-based acrylic PSA. Although the PSAs used in the facestock study were not formulated with wetting agent, water-based PSAs are produced via emulsion polymerization and thus contain a high content of surfactant. The concentration of surfactant in a water-based acrylic PSA film can be as high as 10% (w/w). This surfactant will likely diminish the adhesion between the PSA film and paper facestock to reduce or eliminate its impact. This hypothesis can be tested with some modifications to PSA2. Figure 12 shows the removal efficiency of PSA2 as a function of the emulsifier content in the PSA

formulation. The near 0 sample was produced through the rinsing of films to remove surfactants and their re-drying. The 2x, 3x and 4x samples were produced by simply adding the surfactant to the latex prior to coating. No wetting agent was used in these formulations. It can be seen that removing the emulsifier increases and distinguishes the influences of the C1S and EDP facestocks substantially. The partial removal of the surfactant leads to a decrease in removal efficiencies of more than 20% for the C1S facestock and more than 10% for the EDP. The curves then pass through a maximum, followed by a significant drop in removal efficiencies with increasing emulsifier content in which little or no difference is seen between the influences of the different facestocks. The data again demonstrate a balance between 2 mechanisms. The impact on the film morphology from the commercial facestocks is diminished by the surfactant at low levels, but with increasing surfactant concentrations the films are dispersed open to an even greater extent resulting in a substantial drop in removal.

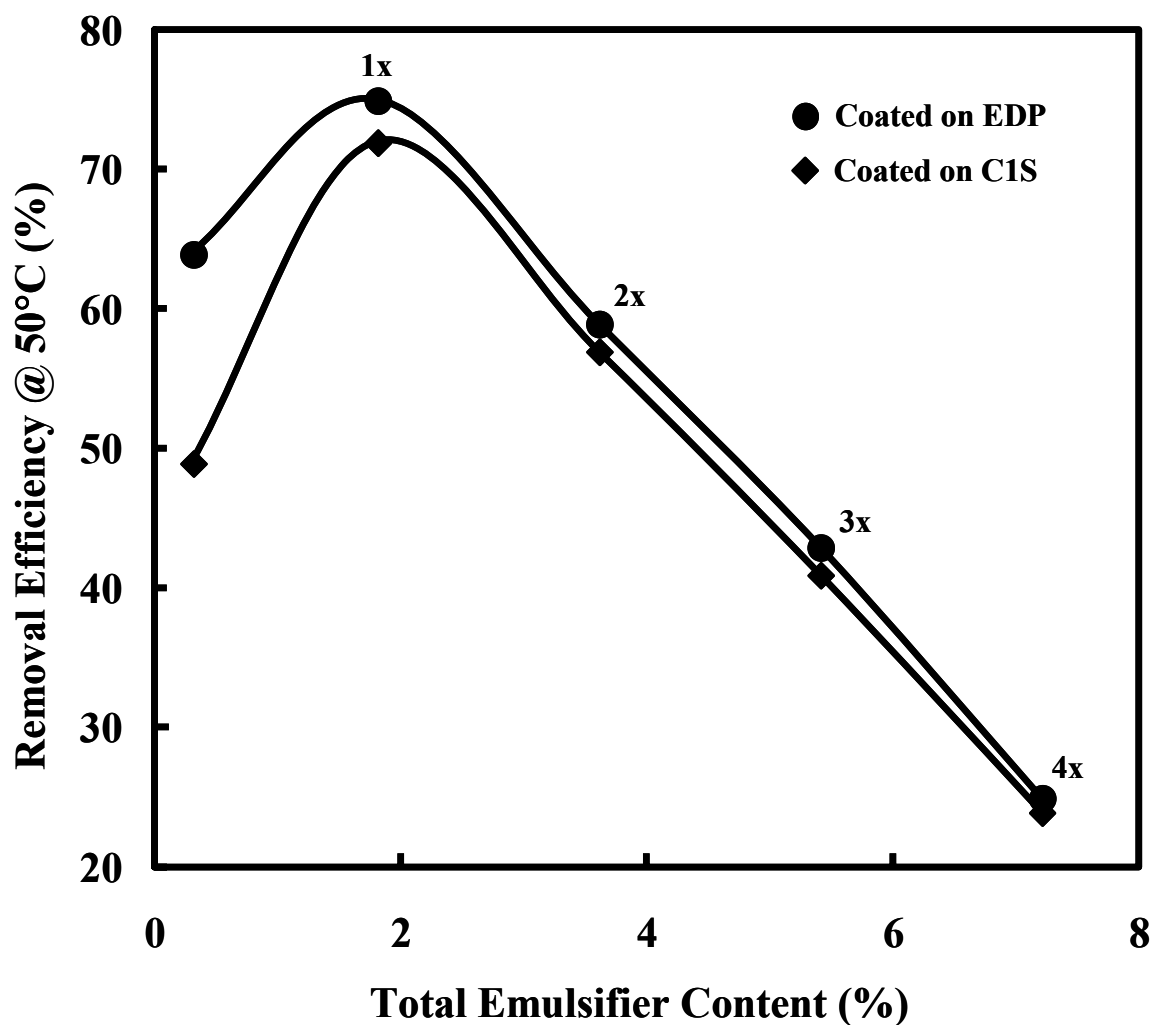


**Figure 12.** Removal efficiencies for PSA2 coated on EDP and C1S as a function of the emulsifier content. The labels on the data indicate the amount of emulsifier that is part of the latex relative to what is typically used in its synthesis, e.g., 1x is the amount of the emulsifier

used in the polymerization and 2x indicates that emulsifier has been added subsequent to synthesis to raise the concentration to twice its typical level in the latex.

### **Summary and Conclusions**

When the results of this study are combined with those reported in previous publications, a general model emerges for the fragmentation of the PSAs commonly used to produce labels. It appears that two major factors govern in large part the extent of the fragmentation and thus screening removal efficiencies. The first is the underlying strength of the film. As discussed, for hot-melt PSAs, reductions in strength sufficient to produce extensive fragmentation are triggered by phase transitions, which are thermally located near common recycling temperatures. The second prevalent factor is the morphology of the film during repulping operations. It appears that the more collapsed the film, the larger the residual particles. This is consistent with a well-established observation that PSAs with the greatest removal efficiencies produce fiber-like residual particles that are tightly wound such as those shown in Fig. 10a.

The surfactants (e.g., emulsifiers and wetting agents) found in water-based formulations, have an impact on morphology of adhesive films during repulping. Increasing the concentrations of these amphiphilic species produces a substantial reduction in measured removal efficiencies for PSA2, which possesses a moderate wet strength. Far less significant reductions were observed for PSA1, which has the greatest wet tensile strength of the model PSAs, and little change was observed for the weakest model PSA, PSA3. It is theorized that these more open or less wound films promote the induction of greater fragmentation forces during repulping, which has the maximum impact on those films possessing strengths near threshold values. Surfactants were also shown to counter the impact of laminate design. It was observed that the use of commercial paper facestocks, which produce a significant decrease in the removal efficiencies of hot-melt PSAs, had only a minor influence on the water-based PSAs. For these systems it would seem that the surfactant counters the influence of the paper by promoting its removal from adhesive film surfaces. Rinsing and drying the adhesive films prior to lamination results in a decrease in the removal with EDP facestock and a large decrease with C1S facestock. With the addition of higher emulsifier concentrations (post synthesis), the removal also drops, but little difference is observed between laminates produced with the different facestocks.

This work provides guidelines for the development of recycling compatible PSAs. The study focused on common commercial additives to demonstrate the reported effects. It is expected that more detailed investigations of any of the additives discussed above will lead to the identification of more effective structures or addition techniques proving greater flexibility in designing recycling compatible PSAs.

### ***3.4 Significant and Concurrent Enhancement of Stiffness, Strength, and Toughness for Paraffin Wax through Organoclay Addition***

Composites composed of polymer matrices that are reinforced by clay have recently attracted great attention from both academic and industrial researchers.<sup>31,32</sup> The separation of the laminate structure of clay in part (intercalated) or whole (exfoliated) produces plates that possess a high specific surface area theoretically providing for efficient load transfer from the matrix. Dispersed plates also act as barriers to diffusion inhibiting the flow of liquids and gasses.

Increases in stiffness, strength and the tortuosity for entering liquids and gasses have been reported for clay-polymer nano-composites. Less studied, has been the dispersion of clay plies in matrices composed of smaller molecule components to produce potentially useful materials. In this communication, results are reported for a composite produced from clay and paraffin wax. Good exfoliation and dispersion were achieved with ultrasonic processing above the melting point of the wax. The formed nanocomposites demonstrate a significant increase in both Young's modulus and tensile strength relative to the matrix, and a dramatic increase in elongation at break. This combination of increased stiffness, strength and ductility has not previously been reported for nanocomposite structures produced with molecular matrices. The unusual mechanical behavior of this material may provide new insight on the nanostructure of clay-based composites.

Paraffin wax is an inexpensive by-product of petroleum refining that is composed predominantly of normal alkanes with carbon numbers ranging from C<sub>18</sub> to C<sub>50</sub>. In its solid form, paraffin wax is soft, weak and undergoes ductile failure at relatively low strain values making it ill-suited for most structural applications. Wax has found wide-spread use as a barrier coating, due in large part to its ease of handling and low cost as opposed to superior performance.<sup>33</sup> Chaiko *et. al.* recently reported improvements as large as 200-fold in oxygen barrier properties for a organoclay-doped wax.<sup>34,35</sup> These authors utilized an alkylammonium salt surfactant modified montmorillonite clay. The cationic surfactants replace sodium cations located between plates of the clay's natural laminate structure resulting in more lyophilic plate surfaces. This type of modification is commonly used to provide nanoscale dispersion of clay in more polar polymeric matrices such as nylon, epoxy resin and polystyrene. However, even in its modified form, dispersion of clay platelets in polyolefinic matrices such as polyethylene and polypropylene remains a challenge usually requiring the use of dispersing agents such as functionalized olefinic polymers.<sup>36</sup> In Chaiko's work, organoclays were surface activated with low-molecular weight polymers (e.g., PEG, PPG) to introduce disorder within the quaternary amine monolayers that coat the basal planes. The edges of the clay plates were then treated with the surfactant 1-hydroxydodecane-1,1-diphosphonate to enhance their compatibility with the paraffin matrix. From this work, it is apparent that a modified organoclay can be exfoliated and dispersed in paraffin wax with the aid of additives resulting in nanocomposites with greatly enhanced barrier properties relative to the matrix.

Here we report on the mechanical properties for clay-paraffin wax nanocomposites generated without the use of additives. Nanocomposites were produced from paraffin wax and an organically modified montmorillonite (OMMT), Cloisite<sup>®</sup>20A, that is available commercially from Southern Clay Inc. (Gonzales, TX). The organoclay is produced through the modification of natural montmorillonite with a dimethyl, dehydrogenated tallow, quaternary ammonium. Its exfoliation and dispersion in the wax matrix is achieved through ultrasonic mixing at temperatures above the melting point of the wax. X-ray and TEM analysis indicate that generated composites possess well-dispersed clay platelets, which are mostly exfoliated at lower concentrations and exfoliated and intercalated for higher concentrations. Figure 13 shows the XRD patterns for the commercial paraffin wax, OMMT, and the wax-clay composites at various clay loading levels. The OMMT clay has a (001) spacing of 2.4 nm ( $2\theta = 3.7^\circ$ ). There is no obvious clay (001) peak in the x-ray scans for composites with clay concentrations up to 2%. This is consistent with fully exfoliated clay. For clay contents of 3% and greater, a broad peak

(indicated by the arrow in Fig. 13) appears to overlap with the (002) wax lamellar peak ( $d=37.7\text{\AA}$ ,  $2\theta=2.34^\circ$ ). This is consistent with an intercalated clay structure in which wax molecules migrate in to pry and separate clay platelets.

TEM micrographs of wax nanocomposites with 2 wt.% and 4 wt.% OMMT are shown in Fig. 14. The clay is well dispersed and highly exfoliated/intercalated. Thin clay tactoids that contain single or only a few clay layers are dispersed throughout the matrix. From these images, exfoliated and intercalated clay coexist. The clay platelets are about 50-150 nm long and a few nanometer thick, thus having an aspect ratio of approximately 15-40. The paraffin wax matrix is white. The dispersion of clay that is not exfoliated or intercalated produces a yellowish green color for the composite. After sonication, this fades to a light yellow or even beige color and the test specimens become more translucent. The excellent dispersion and exfoliation/intercalation are attributed to ultrasonic processing and compatibility between paraffin wax and fatty chains of the OMMT.

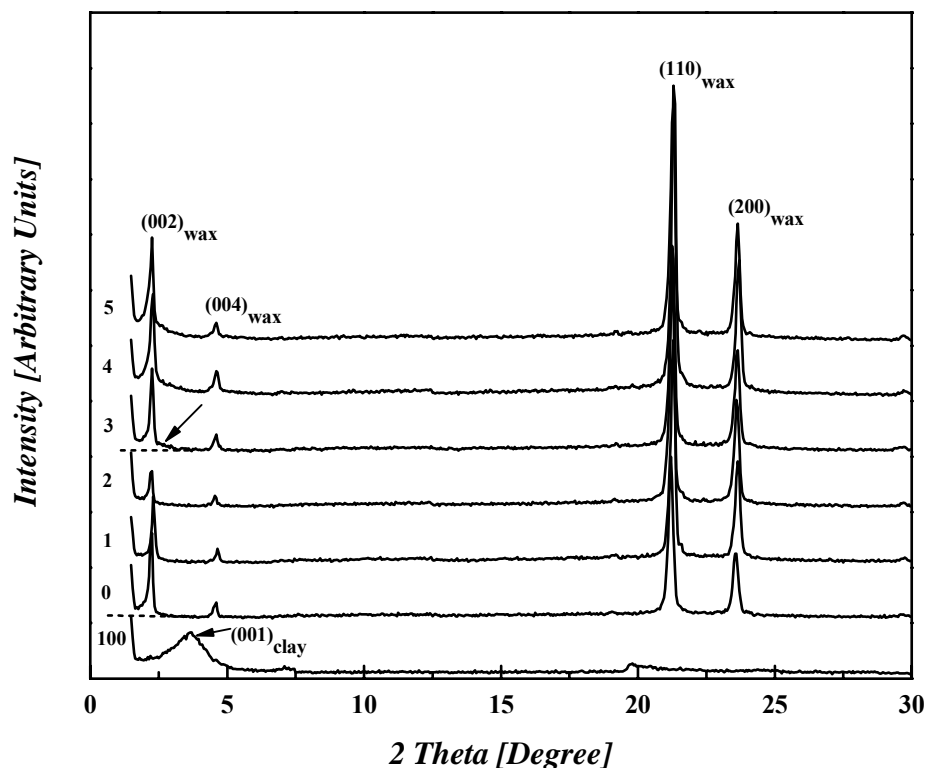


**Figure 13.** Wide angle x-ray scattering (WAXS) scans of OMMT, pure paraffin wax, and wax/clay nanocomposites with 1, 2, 3, 4, and 5 wt.% clay loading (from bottom to top). The clay contents are indicated to the left of the curves. The intensity of the XRD patterns have not been adjusted or modified. Base lines for pure paraffin wax and wax nanocomposite with 3 wt.% OMMT are extrapolated and shown as dashed lines.

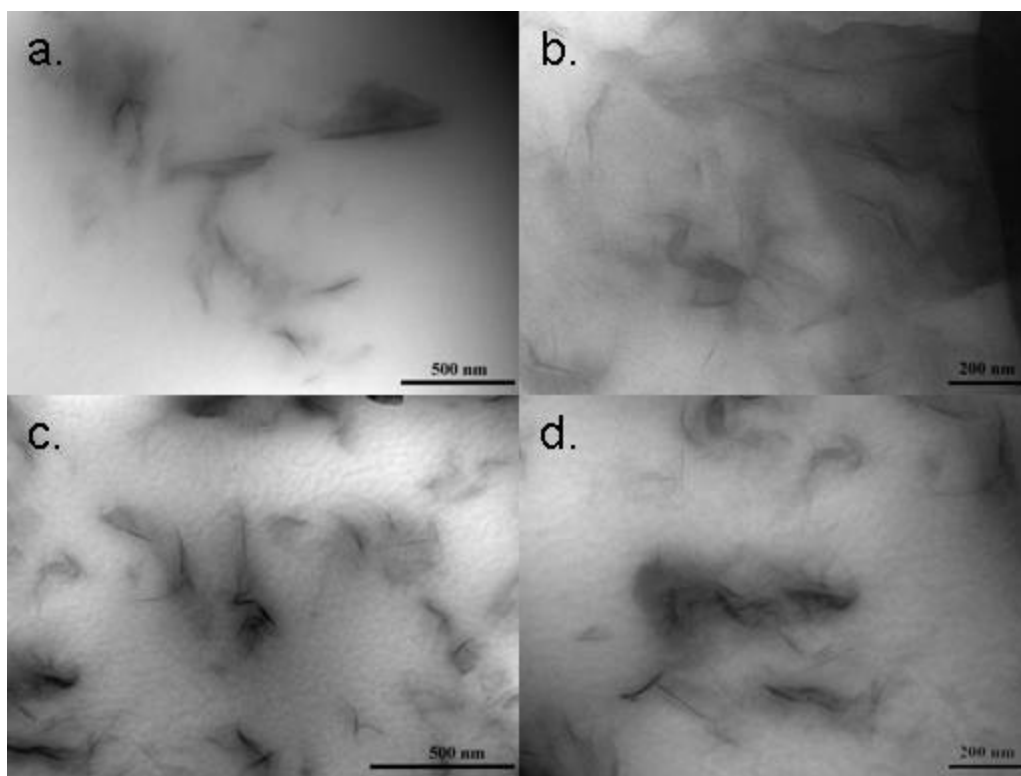


**Figure 14.** Bright field TEM micrographs of wax nanocomposites with 2 wt.% (a, b), and 4 wt.% (c, d) OMMT.

Thermal locations for the phase transitions of organoclay-paraffin wax nanocomposites at various clay concentrations are compared by Differential Scanning Calorimetry (DSC) thermograms in Fig. 15. The scans shown are for the second heating cycle to eliminate thermal history effects and were collected to examine whether incorporating clay shifts the thermal location of phase transitions. Wax possesses a series of pre-melting mesophases, so-called rotator phases, in which molecules retain their long range positional order but gain a degree of rotational freedom along their long axes.<sup>5, 37</sup> The lower temperature transition that is evident in the thermogram for pure wax, i.e., the matrix phase, and in the nanocomposites for all clay concentrations corresponds to a solid-solid polymorphic transition between the crystalline and lowest temperature rotator phase. The higher temperature transition is the melting point for the matrix and nanocomposites of various clay contents. No shift in the locations of these transitions due to the introduction of clay is apparent from DSC analysis. Also, the estimated heats of fusion,  $\Delta H_m$ , obtained through the integration of the area under the endothermic melting transitions are all quite similar indicating that clay induces a negligible change in the crystallinity of the paraffin. The degree of crystallinity of polymers is often estimated by comparing the area under the amorphous halo, which is a broad transition in the XRD pattern, to the area under the crystalline peaks.<sup>38</sup> In Fig. 13, the (110) and (200) peaks of the wax-clay nanocomposites are sharp and an amorphous halo is barely visible, which indicates that the wax matrix retains its high degree of crystallinity with clay addition. The structure of the clay nanocomposites was also probed using Dynamic Mechanical Analysis (DMA), which did not indicate temperature



shifts in phase transitions, and optical imaging, which did show no significant modification to crystal

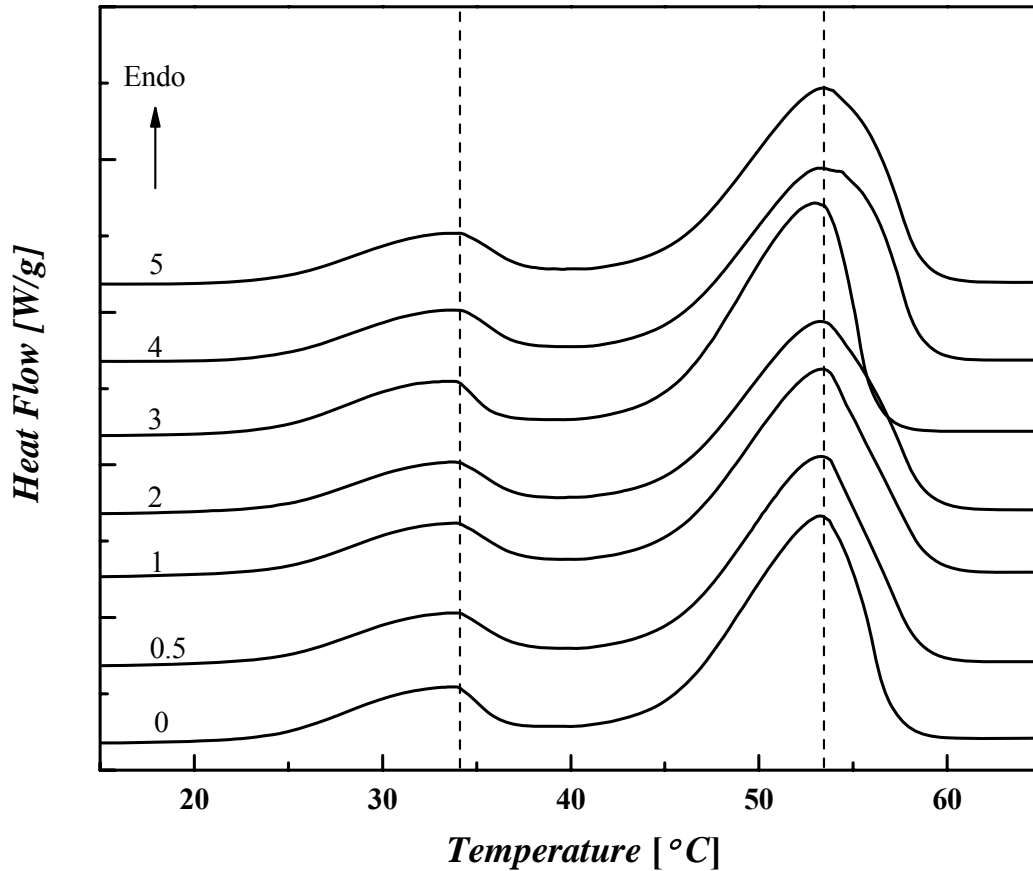


**Figure 15.** DSC thermograms of pure paraffin wax and wax composite; the numbers on the curves are wt. % of OMMT clay.

Fig. 16 shows typical engineering stress-strain curves of wax-clay nanocomposites containing clay levels of 0, 0.5 and 5 wt.%. The curves indicate ductile behavior in that samples yield to failure. No strain hardening was observed. The shapes of engineering stress-strain curves for the nanocomposites are similar to those of the matrix material, but the magnitudes of the various tensile properties have been greatly increased. Tensile properties of pure paraffin and wax-clay nanocomposites are summarized in Table 10.

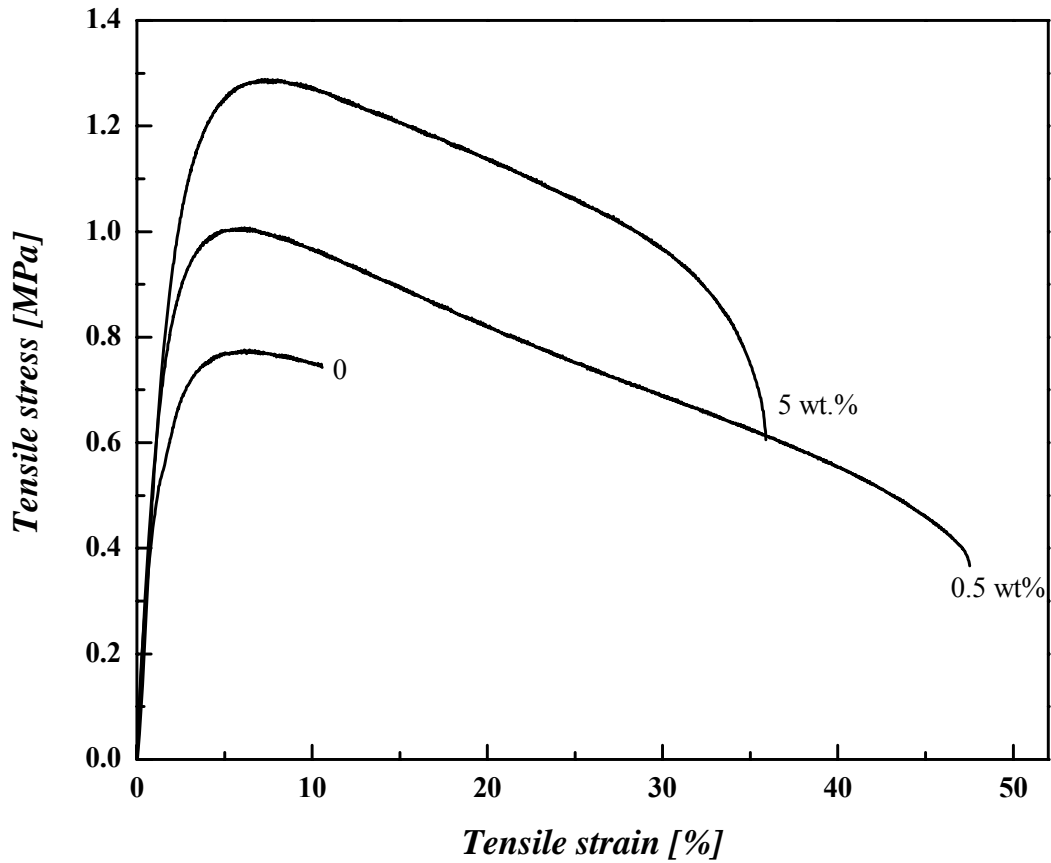


**Figure 16.** Typical engineering stress-strain curves for pure paraffin wax, wax nanocomposite with 0.5 wt.% and 5 wt.% OMMT (from bottom to top). OMMT contents are indicated next to the curves.

**Table 10:** Tensile properties of pure paraffin wax and wax composite with various OMMT loadings.

OMMT content (wt.%)	Tensile strength (MPa)	Young's modulus (MPa)	Elongation at break (%)	Energy at break (J)
0	0.77	61.4	12	0.11
0.5	0.91	71.8	51	0.56
1	1.00	72.8	62	0.54
2	1.06	99.5	65	0.61
3	1.15	94.3	42	0.52
4	1.13	91.6	34	0.46
5	1.22	80.4	32	0.47

With increasing clay concentrations, tensile strengths of nanocomposites increase accordingly. At 5 wt.% clay content, tensile strength was found to increase by 58.4%. Young's modulus was also found to increase. A 40% increase was measured at a 2 wt.% clay loading. However the nanocomposite stiffness declines from this maximum for higher loadings. The most dramatic influence of the clay is on the toughness of the paraffin wax. Pure paraffin wax typically breaks just after yielding; at 25°C an average elongation at break of 12% was measured for the matrix phase. Adding just 0.5 wt.% of OMMT produced an average elongation at break of 51%, 325% higher than that of pure paraffin wax. Further addition of clay initially increased the elongation at break, which reached a maximum at about 2 wt.% clay concentration and then declined with higher clay contents. This trend was also observed for the energy at break, a relative measure of toughness for the tested samples (Table 10), which showed a maximum value of 0.6 J at 2 wt.% loading, a 450% increase over that measured for the unmodified matrix.

Adding clay to polymers commonly increases the brittleness of the composite relative to the virgin polymers.<sup>39-41</sup> Increased elongation at break has been reported for some polymeric matrices and attributed to modifications to the degree of crystallinity and crystal structure.<sup>42-45</sup> To the best of our knowledge, the data reported here shows the first simultaneous increase in stiffness, strength and toughness with the addition of exfoliated clay to a molecular matrix. In addition, no significant modifications were observed to the thermal locations of phase transitions, crystal structure or morphology of formed nanocomposites relative to the pure paraffin wax.

Given the lack of observed structural modifications, the explanation for the observed tensile properties of the nanocomposites appears to be in the interaction between the n-alkanes that compose the matrix and alkyl chains that are bound to clay surfaces via electrostatic interactions. It was demonstrated that sonication of the melt is sufficient for achieving exfoliated and intercalated organoclay. The increases in Young's modulus and tensile strength are thus consistent with strong interactions between the matrix and the clay plates that may possess moduli and tensile strengths as much as 3 orders of magnitude higher than that of the wax, which is quite soft and weak. The more perplexing issue is the dramatic increase in toughness. The low ductility of paraffin wax relative to polymers such as polyethylene originates from its short chain lengths. Paraffin wax is highly crystalline and there is little entanglement between crystallites, thus upon stretching, the crystallites slide relative to each other and break after a short extension. It has been proposed that the increased elongation of polymer-clay nanocomposites may result from the mobility of exfoliated clay platelets, which provides a mode for energy dissipation.<sup>73</sup> It is also possible that clay platelets act as physical cross-links. Both platelet motion and long-range interactions through physical crosslinks are potential candidates for the observed toughening in paraffin matrices.

The results presented in this communication demonstrate the first concurrent enhancement of stiffness, strength and toughness of a molecular (or more precisely, a crystalline oligomer) matrix through the addition of nanodispersed clay. Furthermore, the evidence indicates no significant modification to the structure, morphology or phase behavior resulting from the nanodispersed clay. This narrows possible explanations for the toughening mechanism, which is believed to stem from the anchoring of the short chain n-alkanes that compose the paraffin wax to the alkyl chains that are electrostatically bound to the surfaces of the embedded clay platelets. Explaining this mechanism will likely have general implications for other nanocomposite structures. In addition, the technique by which the composites were produced here does not

involve the use of dispersants and other additives as was reported previously; rather an organoclay was dispersed and exfoliated in the wax matrix using mechanical means (sonication). Utilization of this new technique to generate toughened paraffin coatings will be pursued for moisture barrier applications.

### **Experimental Section**

**Materials and Preparation of Nanocomposites.** Cloisite<sup>®</sup> 20A, a natural montmorillonite modified with a quaternary ammonium salt, was obtained from Southern Clay Products, Inc. (Gonzales, TX). Cloisite<sup>®</sup> 20A has a (001) spacing of 2.4 nm. Paraffin wax (IGI 1230) with a DSC melting point of 53°C was supplied by the International Group, Inc. (Toronto, ON, Canada). Wax-clay nanocomposites were prepared by mixing the clay at concentrations of 0.5, 1, 2, 3, 4 and 5 wt.% with melted paraffin wax. The melt was mixed for 10 min. in a 750 Watt High Intensity Ultrasonic Processor (frequency 20 kHz) purchased from Cole-Parmer (Vernon Hills, IL), set at 100% amplitude and a pulsing setting (2 s/1 s on/off). A temperature controller was used to prevent overheating of the sample by terminating the ultrasonics when the sample reached 90°C.

**Characterization of Nanocomposites.** Test specimens for tensile testing were generated by pouring sonicated molten composite samples into a 1-inch deep pan that was lined with a release liner. The composite samples were cooled and solidified by floating the pan in a tub of water to a film of uniform thickness. Dog-bone shaped specimens (Type I, ASTM standard D638-95) were cut from the composite sheet using an in-house metal cutter template. Tensile testing was carried out using an Instron (Instron Corporate, Norwood, MA) 5543 tensile tester equipped with a Eurotherm 2216e temperature controller. Young's modulus, tensile strength, elongation at break, and tensile energy absorption were extracted from each test, which was run at 25°C using a crosshead speed of 10 mm/min. At least 10 specimens were tested for each clay loading level and results were averaged. X-ray diffraction patterns of the paraffin wax, Cloisite<sup>®</sup> 20A, and composites were obtained at 25°C for 2 theta of 1.5° to 30° using a Scintag (Scintag, Inc. Cupertino, California) XDS 2000 Diffractometer. The morphology of the clay in the sonicated wax matrix was evaluated with a JEOL 1200 transmission electron microscope, operated at an accelerating voltage of 120 kV. Thin sections of wax and wax/clay nanocomposites (~ 90 nm thick) were prepared at – 90°C using a Reichert UltraCut S Ultramicrotomes equipped with a Model FC-S Cryo Attachments. Sections were placed on 200-mesh Formvar/carbon-coated copper grids for TEM observations. Phase transitions of paraffin wax and wax/clay nanocomposites were studied with a TA Instruments Q1000 Differential Scanning Calorimeter. Thermograms were obtained under nitrogen atmosphere over a temperature range of 15°C to 65°C.

### ***3.5 Brittle–Ductile Transitions and the Toughening Mechanism in Paraffin/Organoclay Nanocomposites***

Since the initial publications demonstrating enhanced properties for nylon-6 containing exfoliated montmorillonite (MMT) clay,<sup>46</sup> the topic of clay-polymer nanocomposites has been an active research area. Significant enhancements in mechanical, barrier and degradation properties over the pure polymers have been reported.<sup>31-31</sup> A common observation for thermoplastic materials with nanoclay inclusion is an impressive increase in the Young's modulus and yield stress. However, this increase is usually accompanied by a reduction in elongation at break.<sup>39-41</sup> Some important thermoplastic polymers that could possibly be used in composites are brittle in

their neat form and thus being able to maintain or improve their ductility, while using clay to enhance stiffness and yield stress, is desirable.

Previously, we reported the preparation of organically modified montmorillonite (OMMT)/paraffin wax nanocomposite which demonstrated significantly improved mechanical properties, apparently a novel observation for a oligomeric matrix.<sup>47</sup> The organoclay was compounded with molten paraffin wax via ultrasonic processing and shown to be a mixture of exfoliated and intercalated morphology throughout the matrix based on transmission electron microscopy (TEM) and X-ray diffraction (XRD) results. Paraffin wax containing clay concentrations ranging from 0.5 to 5.0 wt.% was found to have significantly higher Young's moduli and yield stress relative to the wax matrix. More impressive was the observation that these enhancements were accompanied by a significant improvement in the elongation at break: A nearly 400% increase was observed for a clay concentration of 0.5 wt.%. Such significant and concurrent increases in strength, modulus, and ductility have rarely been reported for thermoplastic nanocomposites in the literature.<sup>45</sup> Due to the absence of changes in crystallinity, crystal structure, and phase transitions with the addition of clay, it was suggested that the toughening mechanism may result from physical cross-linking with clay platelets acting as anchoring points.<sup>47</sup>

In this paper, results from a further investigation on the toughening mechanism are reported. For the first time, temperature dependencies of tensile properties for pure wax and wax/clay nanocomposites were conducted at temperatures between 10 °C and 30 °C. The results showed that with addition of clay, the brittle-ductile transition of paraffin wax shifted to lower temperatures. This shift explains the increased ductility at 25 °C for nanocomposite compared to pure wax reported in the previous study.<sup>47</sup> Polarized optical microscopy (POM) was used to evaluate the influence on the morphology of paraffin wax in the presence of exfoliated clay platelets. Small changes were found in crystallite size but cannot be fully responsible for the observed shift in brittle-ductile transition temperature. 2-D XRD and TEM study on strained samples showed that in the nanocomposites the molecular axes of wax crystallites and exfoliated organo-clay platelets were preferentially oriented parallel to the stretching direction. The information presented here greatly augments the previous study that reported tensile test results under ambient conditions and provides a better understanding on the role organo-clay plays in toughening matrices.

## **Experimental**

**Materials and Preparation of Nanocomposites.** Paraffin wax (IGI 1230A) with a DSC melting point of 53°C was supplied by the International Group, Inc. (Toronto, ON, Canada). Cloisite<sup>®</sup> 20A, a natural montmorillonite modified with a quaternary ammonium salt, was obtained from Southern Clay Products, Inc. (Gonzales, TX). Wax-clay nanocomposite with a clay concentration of 2 wt.% were prepared using a procedure described in detail a previous paper.<sup>37</sup> Samples were compounded by mixing the Cloisite 20A with melted paraffin wax for 10 min using a 750 W high intensity ultrasonic processor. The molten nano-composite was poured into a shallow pan lined with release liner for cooling and dog-bone specimens (Type I, ASTM Standard D638-95) were cut using an in-house metal cutter template.

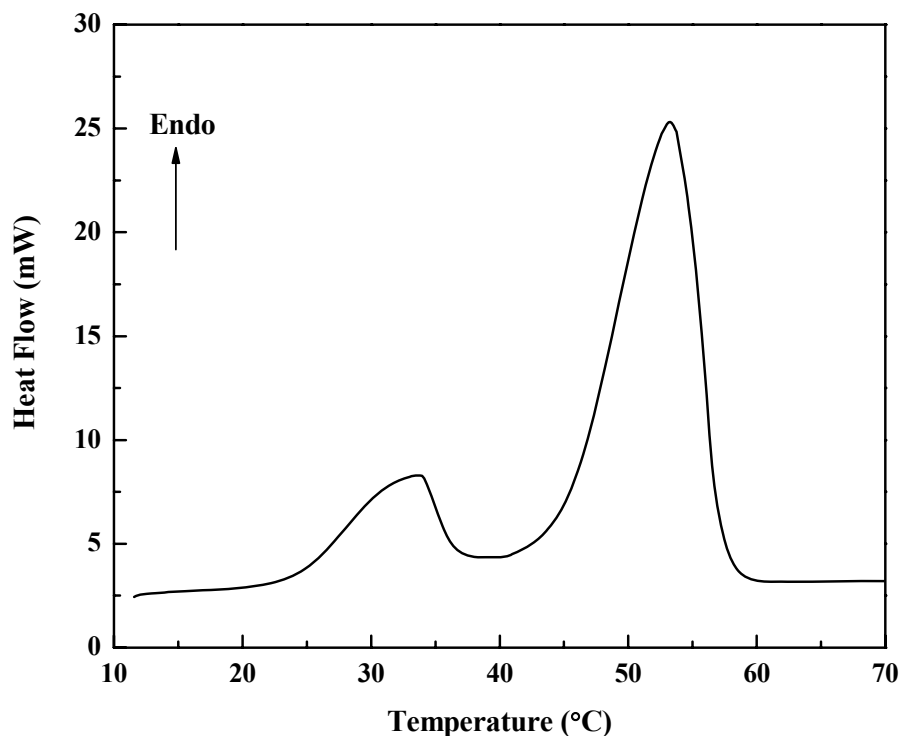
**Characterization of Nanocomposites.** Tensile properties of wax and its nanocomposite were measured every 5 °C from 10 to 30 °C using an Instron (Instron Inc., Norwood, MA) 5543 tensile tester equipped with a Eurotherm 2216e temperature controller according to ASTM standard D638-95. The details were described elsewhere.<sup>47</sup> Elongation at break, modulus, and stress at maximum load were plotted against temperature. Images of the failed specimens were recorded with a Nikon digital camera. Morphologies of fracture surfaces after tensile tests were examined using a JEOL FEG 6500 Scanning Electron Microscope (SEM) at an acceleration voltage of 5 Kv. The fracture ends of the tensile specimens were coated with 50 Å platinum prior to SEM examination.

Phase transitions of paraffin wax were studied with a TA Instruments (New Castle, DE) Q1000 differential scanning calorimeter. Thermograms were obtained under nitrogen atmosphere over a temperature range of 15 to 65 °C with heating/cooling rates of 10°C/min. The second heating cycle was used to eliminate the thermal history of the wax samples.

The morphologies of wax crystallites for pure paraffin and clay nanocomposites were investigated using a Reichert Zetopan Microscope (Austria) with both polarized and steep oblique illumination. Small pieces of the samples were melted on a glass slide on a hot plate, spread with the edge of another slide and then cooled in 3 ways: normally cooled by placing them on a tabletop, slowly cooled on the hotplate with the power turned off, or fast cooled in an ice/water bath.

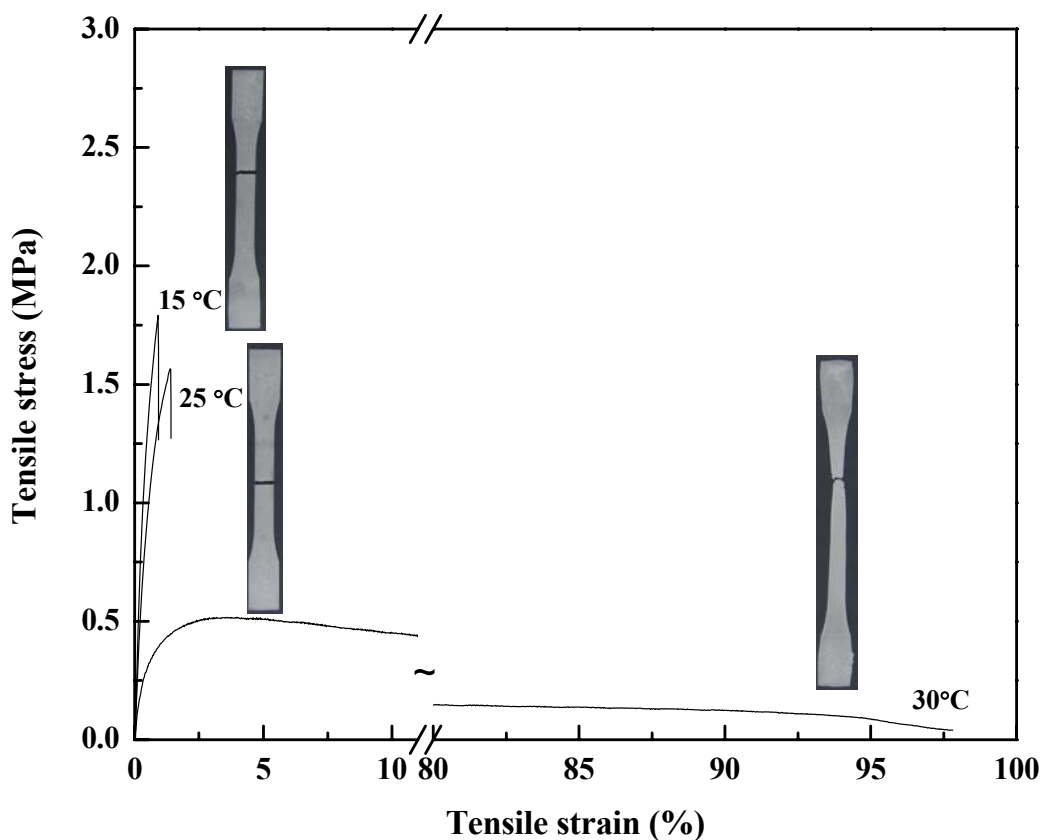
## **Results and Discussion**

**Temperature Dependency of Tensile Properties.** The mechanical properties of paraffin wax are very sensitive to temperature, especially in regions between room temperature and the melting point of wax. This is a result of the presence of a series of pre-melting mesophases, so-called rotator phases, that occur in mixtures of normal alkanes, including paraffin waxes, in which molecules retain their long range positional order but gain a degree of rotational freedom along their long axes.<sup>5,48</sup> Figure 17 shows a differential scanning calorimetry (DSC) thermogram for the pure paraffin wax. Evident are 2 significant thermodynamic events. The higher temperature event is the melting transition. The lower temperature event is the transition from the crystalline phase into the premelting mesophase region of the wax, which begins at approximately 22°C and peaks at about 33°C. The fact that the mesophases for this particular paraffin wax overlap with normal ambient conditions, where it would likely be utilized, is not uncommon. This is the case for most paraffin waxes. As will be demonstrated, the thermal approach into this region has a significant impact on the mechanical properties of paraffin wax and its nanocomposites.



**Figure 17.** DSC scan of the commercial paraffin wax.

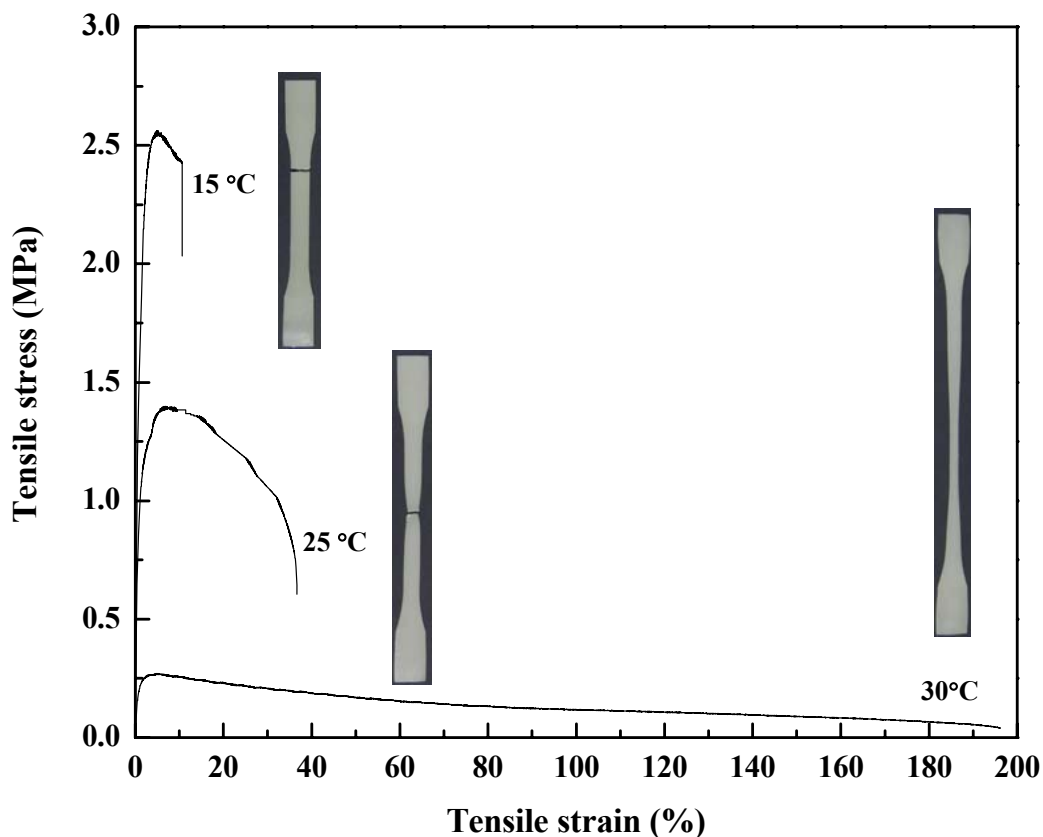
Figure 18 compares the engineering stress-strain curves for pure paraffin wax at three different temperatures, 15, 25 and 30 °C. Also shown on the plots are photographs of the failed tensile test specimens. Qualitatively Young's modulus and tensile strength of wax decrease with increasing temperature. At 15 and 25 °C, the paraffin wax experiences brittle failure. Elongation-at-break values are less than 5%, and there is an absence of a distinct yield point. Brittle behavior is also evident from the 15 and 25 °C failed test specimens, which show no evidence of neck formation. At 30 °C where the wax enters into its mesophase region, it begins to demonstrate ductile behavior, clearly yielding and then failing for an elongation of approximately 100%. The formation of a slight neck can be seen in the photo of the test specimen.



**Figure 18.** Comparison of engineering stress-strain curves of the pure paraffin wax at 20, 25 and 30 °C. Photographs of the failed specimens are also shown.

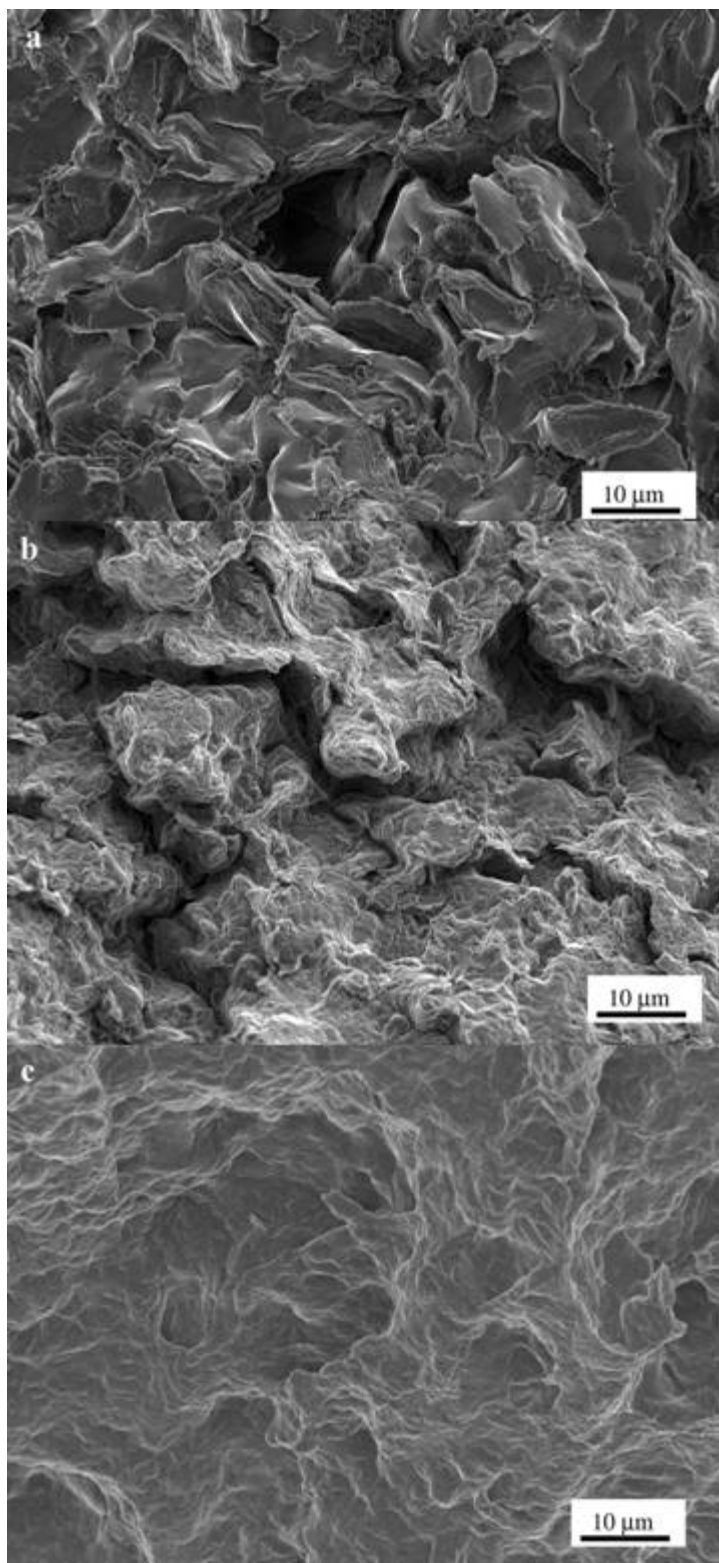
Figure 19 shows the engineering stress-strain curves for 2% organo-clay/wax nanocomposite. As for the pure paraffin wax, results are reported for three temperatures (15, 25 and 30 °C) and photographs of representative failed tensile test specimens are shown. As was previously reported for 25 °C, the dispersion of clay platelets in paraffin wax simultaneously increases stiffness, strength and ductility. This is clear from the engineering stress-strain curves shown. For all 3 temperatures, the nanocomposite demonstrates ductile behavior. As with the pure paraffin wax, the stiffness and strength of the 2% nanocomposite decrease with increasing temperature, while ductility increases. Necking was found in most test specimens for 25 and 30 °C and typical examples of failed specimens are shown for each temperature. At 30 °C, a lack of failure at the maximum crosshead height of the environmental tensile tester occurred for most of the specimens. This corresponds to an elongation at break of just over 200%. Significant necking and a narrowing region can be seen in the 30 °C specimen shown indicating that this is a more stabilized process in the nanocomposite than the pure wax.





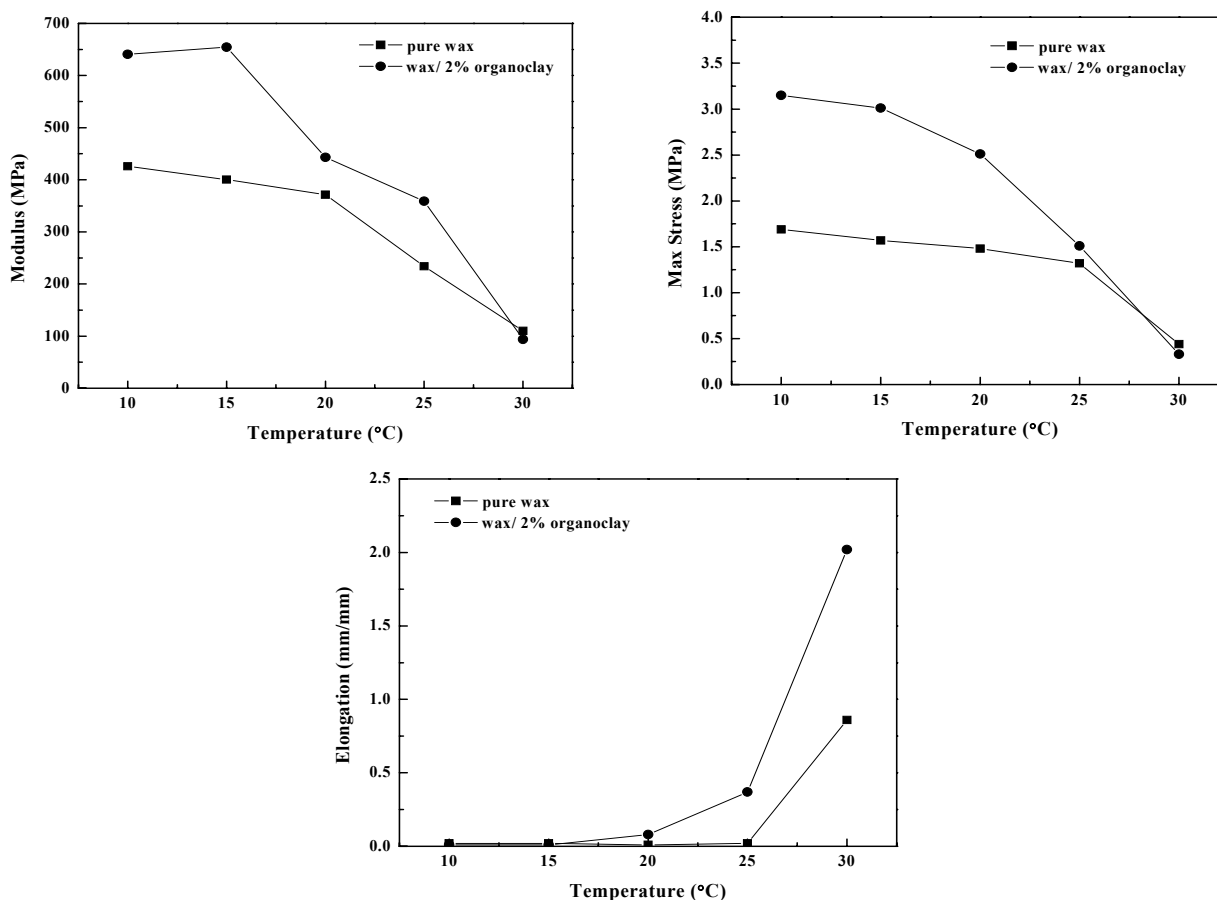
**Figure 19.** Comparison of engineering stress-strain curves of the paraffin wax nanocomposite containing 2 wt.% organo-clay at 20, 25 and 30 °C. Photographs of the failed specimens are also shown.

Figure 20 shows the typical morphologies of fracture surfaces after tensile tests at 25 °C and 30 °C for pure paraffin wax and at 25 °C for the nanocomposite. The fracture surface of pure paraffin wax at 25 °C (Fig. 3a) is relatively smooth, indicating little energy dissipation. The fracture surface for the pure wax at 30 °C (Fig. 3b) shows a substantial increase in surface area versus the 25 °C sample. For the nanocomposite at 2 wt.% clay loading, the fracture surface (Fig. 3c) is more similar to the 30 °C pure wax sample except that it appears to possess a finer crystallite size.



**Figure 20.** SEM images showing the fracture surfaces as a result of tensile loading for (a) pure paraffin wax at 25 °C, (b) wax nanocomposite with 2 wt.% OMMT at 25 °C, and (c) pure paraffin wax at 30 °C.

Figure 21 summarizes and compares tensile properties for pure wax and its 2% organo-clay nanocomposites at temperatures that range from 10 to 30 °C. As discussed above, Young's modulus and maximum stress (maximum stress here indicates tensile strength for brittle specimens and yield stress for ductile specimens) both decrease as the wax and nanocomposites thermally move into their mesophases. Standard tensile tests could not be carried out on samples above 30 °C due to the significant fluid-like behavior of the specimens, but it appears that differences in the stiffness and strength between the wax and the nanocomposite become small as this region is approached. Thus the advantages provided by the clay appear to be diminished as the wax gains greater molecular freedom. It increases sharply with increasing temperature for both the pure wax and its nanocomposites. This distinct change in ductility is often used as a demarcation point between brittle and ductile behavior, the so-called brittle-ductile transition. For the pure paraffin wax, this transition occurs at approximately 25 °C, which is consistent with the behavior indicated by its engineering stress-strain curves and the images of the failed tensile specimens and fracture surfaces. For the nanocomposite, this transition occurs at a lower temperature, between 15 and 20 °C.



**Figure 21.** Temperature dependencies of (a) Young's modulus, (b) maximum stress and (c) elongation at break for pure paraffin wax and wax nanocomposite with 2 wt.% OMMT.

The temperature dependent tensile test data above indicate that for ambient temperatures, the exfoliation and dispersion of the clay provides the nanocomposite with elongations similar to

those observed at higher temperatures for paraffin wax. That is, the addition of organo-clay platelets shifts the brittle-ductile transition to a lower temperature. According to the Ludwig-Davidenkov-Orowan hypothesis,<sup>49</sup> the mechanism, either fracture or yielding, that requires the lowest stress under the test conditions is the observed behavior. Thus, when the stress required for plastic flow drops below that for brittle fracture, the material will demonstrate ductile behavior, i.e., yielding, necking and possibly cold drawing. Given that the yield stress is increased for the nanocomposite compared to pure wax matrix, a possible explanation for this shift in brittle-ductile transition temperature is that the presence of organo-clay has increased the stress required for brittle fracture. It is also likely that the thermal location of the observed enhancement in ductility, i.e., in the thermal proximity of the crystalline-rotator phase transition, is an important factor. The fact that the brittle-ductile transition temperature for pure wax occurs near this transition may mean that a relatively sensitive balance between brittle and ductile behavior exists and small enhancements in either will result in significant changes in ductility.

**Crystallite Size and Ductility.** Previously, DSC and XRD data were presented that indicated that the presence of exfoliated and intercalated organo-clay did not influence the wax phase, thermal locations of phase transitions, crystal form or crystallinity.<sup>47</sup> The presence of crazing and shear banding in wax/clay nanocomposites, two major toughening mechanisms for polymers, were not observed using SEM, TEM and POM. Another possibility, examined here, is contributions from changes in crystallite size induced by the organo-clay platelets. It is well known that for metals the grain size has a strong affect on ductility and toughness.<sup>50</sup> Typically, grain size refinement makes crack propagation more difficult increasing the stress required for brittle fracture, which will often shift the brittle-ductile transition to a lower temperature. However, this effect is not well characterized in polymers<sup>51</sup> and, it appears to the authors, it has been characterized to an even lesser extent for oligomers.

In hopes of demonstrating the influence of crystallite size on ductility, the tensile properties of specimens of pure paraffin wax and the 2% organo-clay nanocomposite prepared using several cooling rates were examined. Fast cooling or quenching was achieved by submerging the molten wax sample pan in an ice bath. The samples were also cooled at room temperature, and in an oven that was initially held at 40 °C and shut off when the wax sample was placed inside providing for a slow cooling process that lasted over several hours. Figure 5 shows POM images of these pure paraffin wax samples. Paraffin wax crystallites have a lamellar structure. Edge-on aggregates of lamellae of paraffin wax can be clearly seen in the images. Differences in crystallite size caused by difference in cooling rate are obvious from these images. The differences in crystallite size were also evident from the appearance of the wax samples. Compared to normally cooled translucent samples, the quenched samples are more opaque and the slow cooled ones are more transparent, indicating the quenched samples have a crystal size comparable to the wavelength of light so that they scatter light strongly and the slow cooled samples have crystals (with no intervening voids) much larger than the wavelength of light so that they almost do not scatter light. The tensile test results carried out at 25 °C showed that for paraffin wax, the fast cooled (quenched in ice/water) sample has the largest elongation at break, 0.355, followed by normally cooled, 0.024, and slowly cooled sample, 0.008. These results demonstrated that the reduction in crystallite size can significantly increase the ductility of wax at a given temperature.

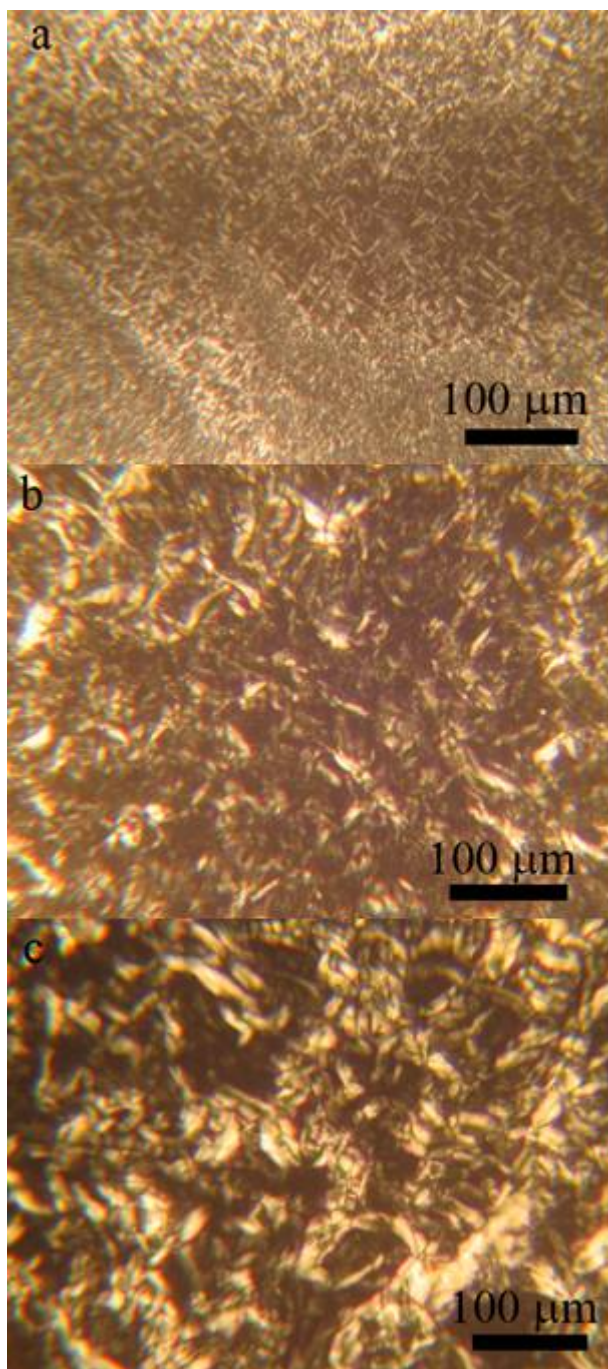


**Figure 22.** Polarized optical images for pure paraffin wax prepared using (a) fast, (b) normal and (c) slow cooling. (See text for details.)

Figure 23 shows optical microscopy images taken with reflected and polarized light for regular wax and wax-clay nanocomposites for 2% and 5% clay loadings. Comparing the images of pure wax (Figs. 23a and 23b) and wax nanocomposites (Fig. 23c-23f) shows that the crystallites of the nanocomposites are slightly smaller and less regular than that of pure wax, which is consistent

with the heterogeneous nucleation of clay. However, the decreases in crystallite size induced by the clay are much smaller than those induced through quench cooling and did not even result in noticeable changes in x-ray diffraction (XRD) peak broadening or a shift in the DSC melting temperature. Thus, the decrease in crystallite size caused by the clay, although consistent with increased ductility, would appear to be too small to account for the magnitude of change in elongation at break observed for the nanocomposite. However, the results indicate that smaller grain size may well contribute to a shift in the brittle-ductile transition temperature.

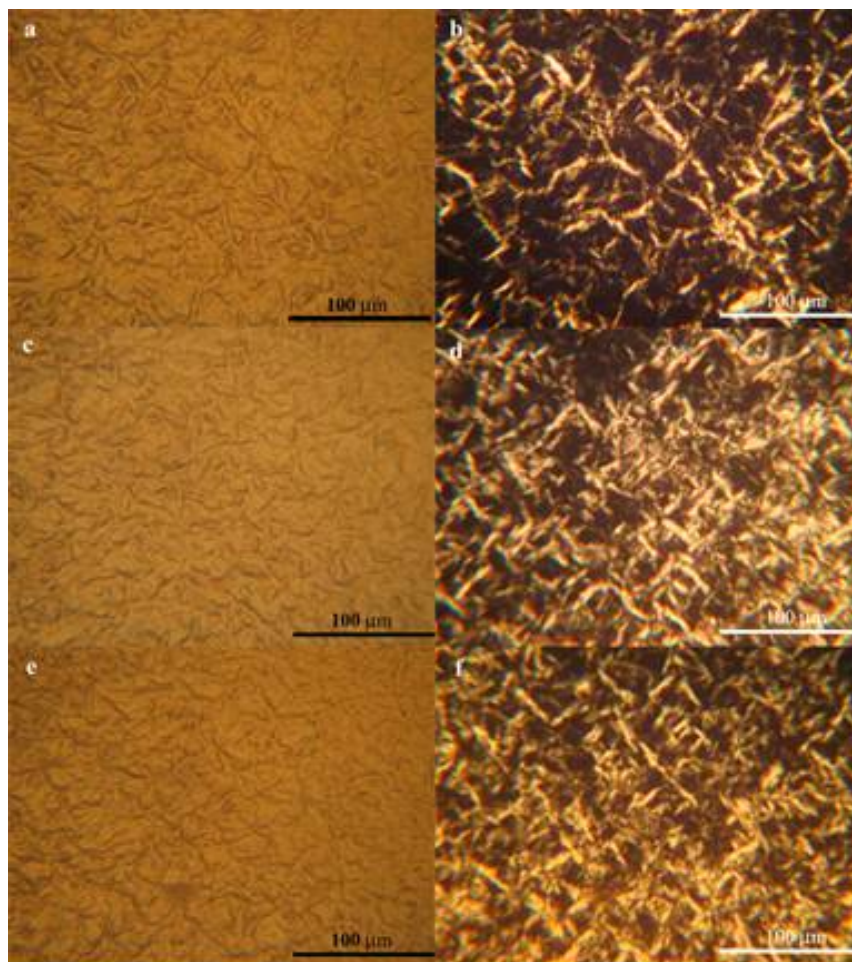


**Figure 23.** Optical micrographs of pure wax and wax-clay nanocomposites: pure wax observed with (a) reflected light and (b) polarized light, 2 wt.% OMMT-wax composite observed with (c) reflected light and (d) polarized light and 5 wt.% OMMT-wax composite observed with (e) reflected light and (f) polarized light.

**Preferred Orientations with Uniaxial Deformation.** The low ductility of pure paraffin wax at low temperature originates from its short chain length, which provides only limited connections between crystalline lamellae and even less between crystals. An applied tensile load likely separates neighboring lamellae, as well as pulling apart lamellae within the crystals, leading to

the formation of cracks between lamellar layers and at the crystallite boundaries, and the resultant failure of the material. The organo-clay used here was treated with surfactants that possess hydrophobes with a structure resembling those of the wax molecular components. In the previous work,<sup>47</sup> it was proposed that the chemical compatibility between the wax molecules and bound modifiers on the clay platelets likely allowed for cross-linking points where individual wax crystallites are connected possibly promoting higher ductility through mechanisms such as bridging.

In an attempt to identify contributions from such mechanisms, the structure of the wax-clay nanocomposite was studied with 2-D XRD and TEM. WAXS patterns of wax nanocomposite with 4 wt.% OMMT before and after stretching were collected and compared. These patterns were obtained with the x-ray beam parallel to the specimen thickness direction (termed “through” direction). In Fig. 24a, the two outer rings are from wax (110) and (200) reflections, and the two inner rings are from wax lamellar structure. The n-alkane chains and the lamellae are randomly oriented in the un-stretched sample. After tensile stretching, the intensities of the two outer rings are no longer azimuthally uniform; the intensity in the equatorial direction is higher than the meridional direction, which indicates that the n-alkane chains have begun to align parallel to the stretching direction (SD). This orientation is not surprising and has been widely observed in both crystalline and amorphous polymeric samples. After stretching, the two inner reflections change from uniform rings to arcs with intensity concentrations on the meridians (see Fig. 24b), which indicates that wax lamellae are preferentially aligned perpendicular to SD, in agreement with the parallel molecular orientation.

The preferred orientation of the wax lamellae can be better seen from the SAXS patterns shown in Fig. 25. Pure wax samples were stretched at 30 °C, to obtain a comparable strain level to wax/clay nanocomposite samples stretched at 25 °C. For both pure paraffin wax and wax-clay nanocomposite, before stretching the wax lamellae are randomly oriented. After stretching, the lamellae are preferentially oriented perpendicular to the stretching direction, with the SAXS patterns resembling those of drawn polyethylene. For polyethylene, they are interpreted as arising from the presence of folded chain lamellae oriented perpendicular to the draw direction,<sup>52</sup> the spacing being on the order of 100 Å. Here the spacing (inner ring or arc in Fig. 25),  $c/2 = 36$  Å, corresponds to the extended chain, lamellar thickness, with the molecular axes being parallel to draw. A diffuse continuous intensity (indicated by an arrow in Fig. 25c) was observed for the composite material but not the pure paraffin wax sample (Fig. 25a). We suggest this diffuse scattering is primarily due to tactoids of intercalated clay with various expanded spacings, which do not produce a SAXS periodicity.

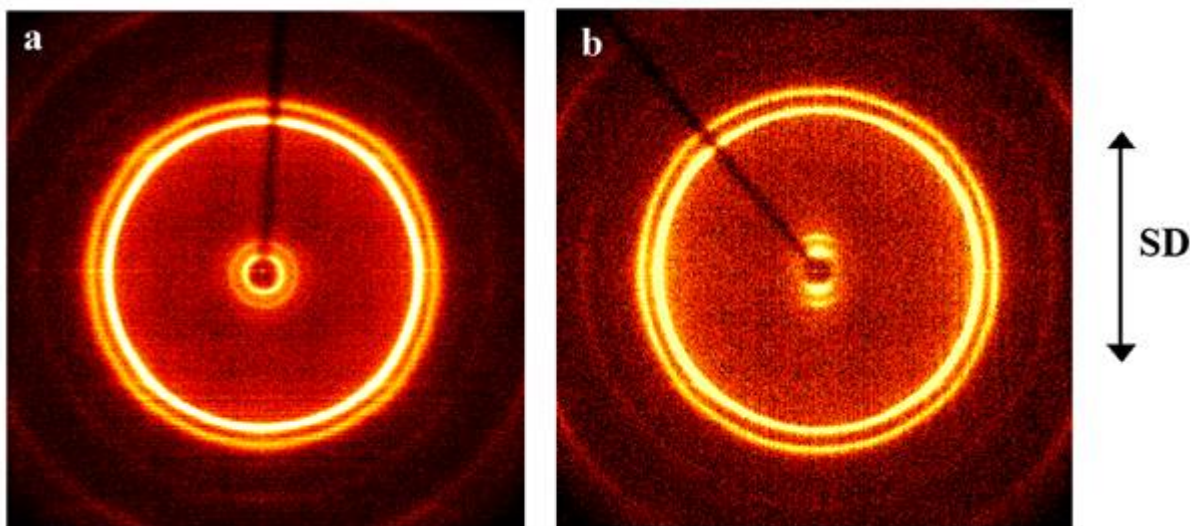


**Figure 24.** WAXS patterns of 4 wt.% OMMT-wax nanocomposites (a) unstretched and (b) with 56% longitudinal strain. The arrow indicates stretching direction (SD).

After stretching, this diffuse clay scattering elongated along SD, which can be interpreted as an indication of perpendicular orientation of the clay tactoids relative to SD (Fig. 25d). (The streak to the right of the beam stop in Fig. 25 is attributed to an artifact – scattering from the edge of the beam stop.) TEM micrographs show that the clay platelets are randomly oriented in the unstretched nanocomposite sample (Fig. 26a). Clay is dispersed either exfoliated or as stacks of a few platelets, i.e., tactoids, with a thickness of a few nanometers. The aspect ratio of the clay ranges from approximately 20 to 50. After stretching, the clay platelets are preferentially oriented parallel to the stretching direction (see Fig. 26b). Similar parallel orientation of clay under uniaxial deformation has been previously reported for Nylon 6-clay nanocomposites.<sup>40</sup> However, the parallel orientation of clay indicated by TEM appears to directly contradict the SAXS analysis (Fig. 25d), which indicates that the clay tactoids are oriented perpendicular to the applied load. A possible explanation for this contradiction is that the larger intercalated clay tactoids tend to align perpendicular to SD as indicated in Fig. 26c (see the arrow), while exfoliated clay prefers to align parallel to SD. It is unclear why the tactoids should align in this fashion; parallel orientations have been observed in drawn LPE/clay composites.<sup>53</sup> The perpendicularly oriented intercalated tactoids would be expected to make a dominant contribution to the diffuse SAXS intensity. Voids could also contribute if elongated perpendicular to the stretch direction; this would be opposite the void orientation often found in drawn polymers which results in a streak on the equator.<sup>52</sup> The parallel orientation of the exfoliated clay platelets relative to the load direction, as seen from TEM images, means that they are oriented perpendicular to the crack propagation direction if brittle failure occurs and may act as bridging to the neighboring lamellae which are preferentially oriented perpendicular to SD and toughen paraffin wax.



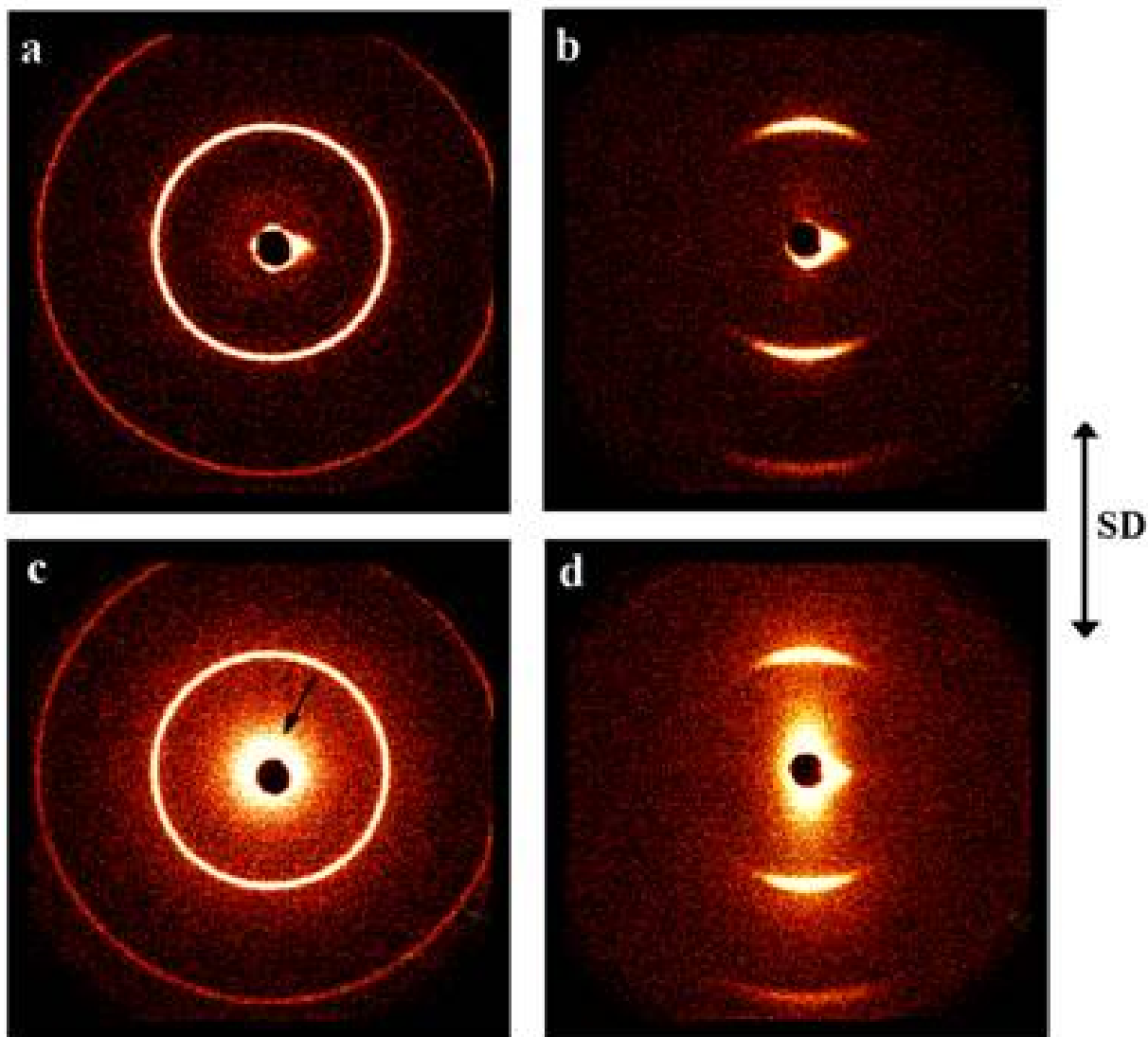


**Figure 25.** SAXS patterns of (a) unstretched pure paraffin wax and (b) pure paraffin wax with 67% longitudinal strain, (c) unstretched 4 wt.% OMMT-wax nanocomposite, and (d) 4% OMMT-wax nanocomposite with 75% longitudinal strain.

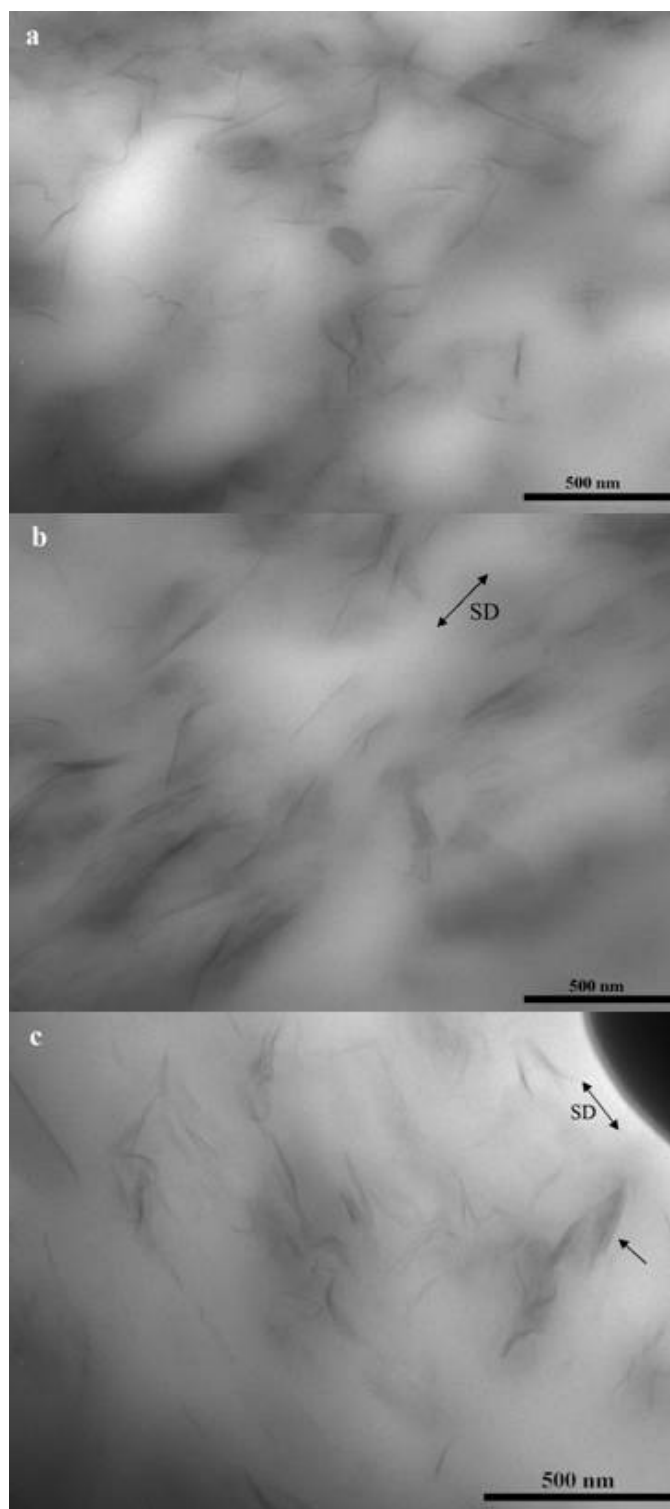


**Figure 26.** TEM micrographs of 4 wt. % OMMT-wax nanocomposites for an (a) unstretched sample, (b) stretched sample showing parallel orientation of clay platelets relative to SD, (c) stretched sample with the arrow indicating the perpendicular orientation of large intercalated clay tactoids relative to SD.

## Conclusions

Tensile tests conducted at temperatures between 10 and 30 °C showed that for both the paraffin wax and its 2% organo-clay nanocomposite, the stiffness and strength decreased gradually with increasing temperature, while ductilities increased dramatically as temperature was increased towards the mesophase region. The clay platelets provided the nanocomposite with a greater stiffness and strength relative to the pure wax, but these enhancements diminished as the low temperature solid-solid transition was approached. The elongation at break value for the nanocomposite was similar to that of the pure wax when the temperature was lower than 15 °C and a significant enhancement was imparted by the organo-clay above this temperature. A shift in the brittle-ductile transition to lower temperatures for the nanocomposite provided it with the anomalously high elongation at break relative to the pure paraffin wax under ambient conditions.

POM images showed that in the nanocomposites clay slightly reduced the crystallite size of paraffin wax, possibly by acting as a nucleating agent. It was also shown that varying the crystallite size in the paraffin wax with variable cooling rates significantly impacted ductility; samples with smaller crystallite sizes demonstrated greater elongation at break values. However, the reduction in wax crystallite size in the nanocomposite by the addition of clay was far less than that observed in pure paraffin wax by increasing the cooling rate even though these two methods achieved similar enhancement in ductility. This result indicates that crystallite size refinement likely is not the sole toughening mechanism for wax nanocomposites, but may contribute. Upon tensile deformation, exfoliated clay platelets were observed to align parallel to the load direction and wax lamellae preferred a perpendicular orientation. These preferred orientations indicate the participation of clay during the straining process and place the platelets in a position, for example, to act as a bridging agent, which would increase the stress required to produce brittle fracture, and thus shift the brittle-ductile transition to a lower temperature.

Results presented here provide a more complete view of the ductility enhancement of nano-dispersed clay on paraffin wax. The clay has a strong influence on the location of the brittle-ductile transition, accounting for the dramatic differences observed in elongation at break between pure paraffin wax and its nanocomposites under ambient conditions. This shift likely results from a significant enhancement in the stress required for brittle fracture, which can be provided by the organo-clay platelets through their interaction with the matrix during loading (e.g., bridging) and by reducing the crystallite size.

### ***3.6 Dynamic Rheological Study of Paraffin Wax and its Organo-Clay Nanocomposites***

Paraffin (macrocrystalline) wax is a mixture of hydrocarbons consisting mainly of normal alkanes with carbon numbers that range from about 18 to 45. As a low-cost petroleum by-product, wax is attractive as a raw material. However, it is quite weak and brittle and thus ill-suited for applications requiring structural stability. In previous work, the tensile properties and structures of nanocomposites produced through the intercalation and exfoliation of organically modified clay in a commercial paraffin wax were reported.<sup>47,54</sup> These nanocomposites were shown to possess significantly greater stiffness and yield strength relative to the pure wax for low organo-clay loadings. More impressive was the observation that their ductility as gauged by elongation at break increased nearly 4-fold at 25 °C. It was also reported that enhancements of tensile properties diminished as the wax-based materials thermally neared the lowest temperature solid-solid phase transition for the paraffin wax at about 30 °C upon which wax enters into its mesophase region. Accurate tensile measurements above these temperatures were not possible due to the increased fluidity of the wax matrix.

In this paper, the viscoelastic properties of the paraffin wax and its organo-clay nanocomposites are investigated over a broad temperature range that includes its low-temperature crystalline state, mesophase region, and melt. Due to its low molecular weight and unusual phase behavior, the rheological properties of paraffin wax are difficult to characterize, and there are few published studies on this topic.<sup>55-58</sup> It is believed that this is the first study on dynamic rheological properties of paraffin wax and its composites over a broad temperature range, and the first such study of an organo-clay nanocomposite generated with an oligomeric matrix.

The information presented provides insights on the interactions that occur between the organo-clay and wax matrices and on the processing and use of the generated composites.

#### **Experimental**

**Materials.** Paraffin wax (IGI 1230A) with a differential scanning calorimeter (DSC) melting point of 53 °C was supplied by the International Group, Inc. (Toronto, ON, Canada). Cloisite<sup>®</sup> 20A, a natural montmorillonite modified with a quaternary ammonium salt, was obtained from Southern Clay Products, Inc. (Gonzales, TX). Wax-clay nanocomposites with a clay concentration of 0.5, 1, 2, 3, 5 wt.% were prepared using an ultrasonic processor. The procedure was described in a previous paper.<sup>47</sup> Wax-clay composite at 3 wt% clay was also prepared by mixing with a magnetic stirrer bar at a temperature above the melting point of wax.

**Materials Characterization.** Phase transitions of paraffin wax were studied with a TA Instruments (New Castle, DE) Q1000 DSC. Thermograms were obtained under helium atmosphere over a temperature range of 15 to 65 °C with heating/cooling rates of 10°C/min. The first heating, first cooling, and second heating cycles were collected. X-ray diffraction was carried out on a Scintag (Cupertino, CA) XDS 2000 theta/theta goniometer with a 2.2 kW sealed copper x-ray source and solid-solid detector. Crushed wax was added to a copper sample holder (25mm × 25mm × 1 mm) to fill the inscribed circle (diameter = 10 mm, depth = 0.5 mm). The sample holder with wax in it was then heated on a hot plate to allow wax to melt. Excess molten wax was removed by absorbing with tissue paper. After cooling to room temperature, wax

samples were scanned with a 2 theta range of 1.5 to 30°. The temperature of samples was raised at a rate of 0.5 °C /min to obtain scans for temperatures of 25, 30, 32, 33, 35, 37 and 39 °C.

Three geometries and two rheometers were used to collect rheological data for paraffin wax and its organo-clay nanocomposites. For solid samples, dynamic shear measurements were conducted on an ARES Rheometer with air bearing motor and 2K force rebalance transducer (TA instruments). Below 36 °C, where wax is in its low-temperature crystalline state, rectangular specimens (approximately 2 ¼ " long, 1/2" wide, and 1/16" thick) were measured using torsion rectangular geometry. Throughout the mesophase region for wax from about 36 to 55 °C, parallel plate (8 mm dia.) geometry was utilized. A strain sweep was performed for each sample at 1 rad/s to obtain the linear viscoelastic region. Temperature ramps were conducted at a ramping rate of 3 °C/min, angular frequency of 1.0 rad/s. Strain frequency sweeps were collected from 100 to 0.1 rad/s at -50 and 40 °C, respectively. Dynamic shear measurements were also conducted on molten wax-clay nanocomposites using a TA Instruments AR-G2 using parallel plates with a diameter of 40 mm. Strain (nanocomposites) sweeps were conducted on each sample to identify the linear viscoelastic region, and dynamic frequency sweeps were conducted at 70 °C from 100 to 0.1 rad/s.

## Results and Discussions

**Phase Behavior of Paraffin Wax and its Nanocomposites.** Paraffin waxes demonstrate complex phase behavior. Between fully ordered crystalline states and isotropic liquid phases, waxes possess several layered plastic crystalline mesophases, in which molecules retain positional order upon gaining a rotational degree of freedom about their long axes. These states are common for normal alkane mixtures including paraffin waxes and are often referred to as rotator phases and pre-melting states given the increased rotational freedom and thermal location just prior to melting points, respectively. The structures of rotator phases in individual and binary mixtures of normal alkanes have been examined extensively using thermal analysis and x-ray scattering, which have identified five distinct rotator phases involving spacing and tilt modifications to the low temperature crystal structure.<sup>11,59-61</sup> In contrast, the rotator phases of real wax systems have been studied little due primarily to their complexity in composition.<sup>62-66</sup>

Figure 27 shows the DSC scan of the commercial paraffin wax used throughout this study. The scans shown are the cooling and second heating cycles. For the heating cycle, the lower temperature transition that begins at about 22.9 °C with a peak at approximately 33.5 °C corresponds to the pre-melting solid-solid transition. The higher temperature transition with a peak at 53.2 °C is the melting transition. The cooling cycle reveals two solid-solid transitions with peak temperatures of 29.5 and 32.7 °C. The phase transitions of paraffin wax were further examined with x-ray diffraction (XRD). Figure 28 shows the overlay of XRD scans for paraffin wax obtained at a series of different temperatures. At 25 °C, the paraffin wax possesses an orthorhombic phase. When the temperature is increased to 30 °C, a high temperature orthorhombic rotator phase ( $R_I$ ) appears, co-existing with the low temperature orthorhombic phase. With increasing temperature, there is greater conversion from the low temperature orthorhombic phase to the high temperature orthorhombic rotator phase. Further heating results in greater distortion in basal plane until, at 37 °C, a hexagonal rotator phase ( $R_{II}$ ) is reached prior to the melting transition. These observations are consistent with those reported by Craig *et al.* in two recent papers which explained the existence of the low and high temperature orthorhombic

phases as due to pre-ordering amongst the crystallizing normal alkanes.<sup>63,64</sup> They propose that similar chain length n-alkanes crystallize as pockets of like-sized molecules clustering within homogenous wax crystallites. As the temperature reaches the first rotator phase transition, molecular heterogeneous regions are induced into the rotator state while the pockets of the like-sized molecules are more stable and will remain in the low temperature orthorhombic state and enter the orthorhombic rotator phase only after higher temperatures are reached.

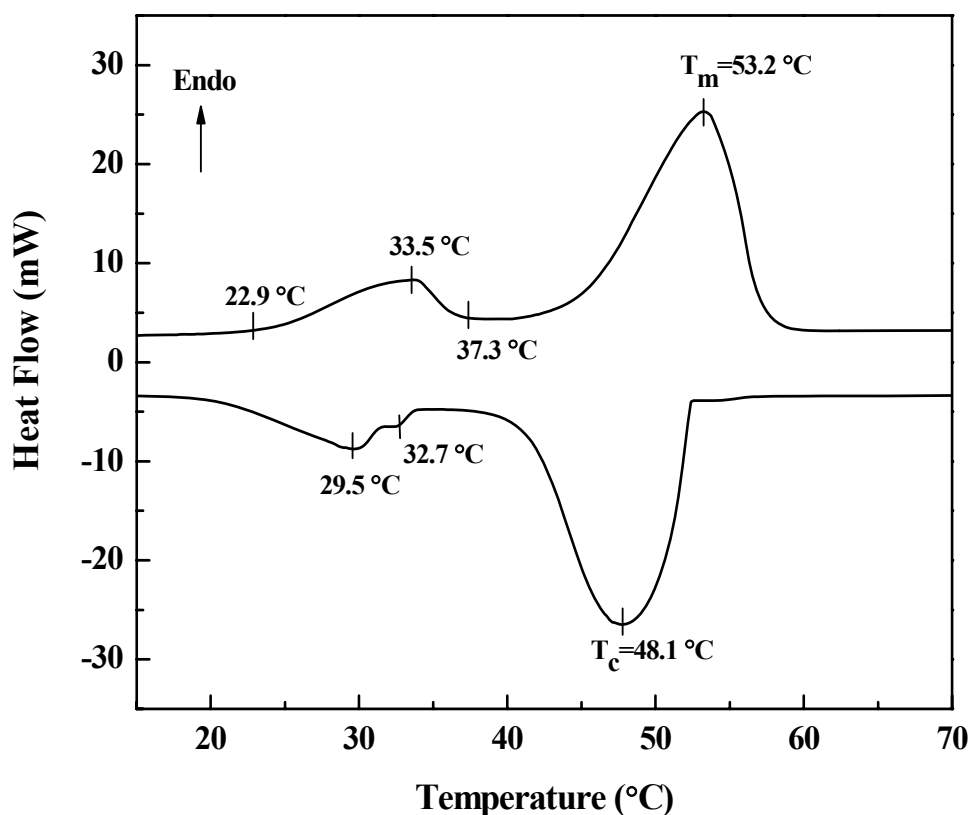


**Figure 27.** DSC scan of a commercial paraffin wax. The lower temperature peaks correspond to the pre-melting solid-solid transitions and the higher temperature transition is the melting transition (top: second heating, bottom: cooling).

As will be demonstrated in the subsequent section of this paper, movement of the paraffin wax into its rotator phases substantially changes its mechanical properties. Changes in dynamic mechanical properties in the crystalline and mesophase region, rheological properties in the melt, and the influence of clay on these properties are examined below.

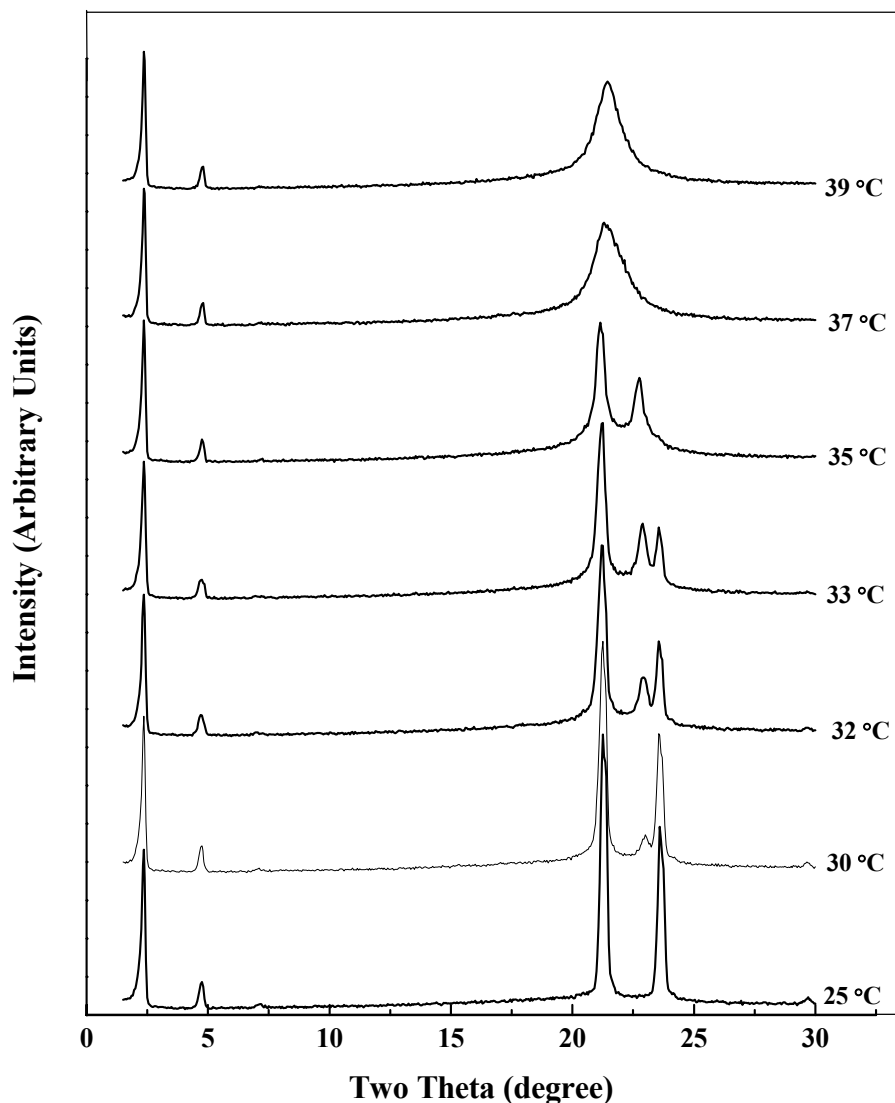


**Figure 28.** X-ray Diffraction plots of paraffin wax at various temperatures.

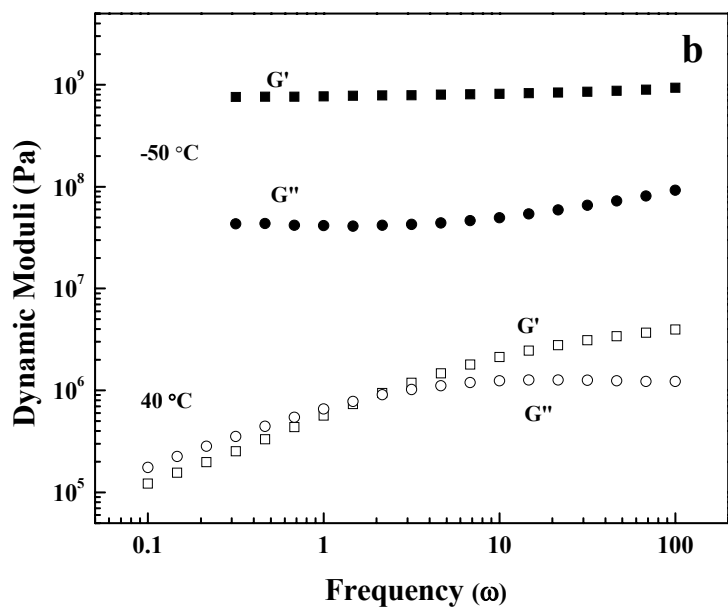
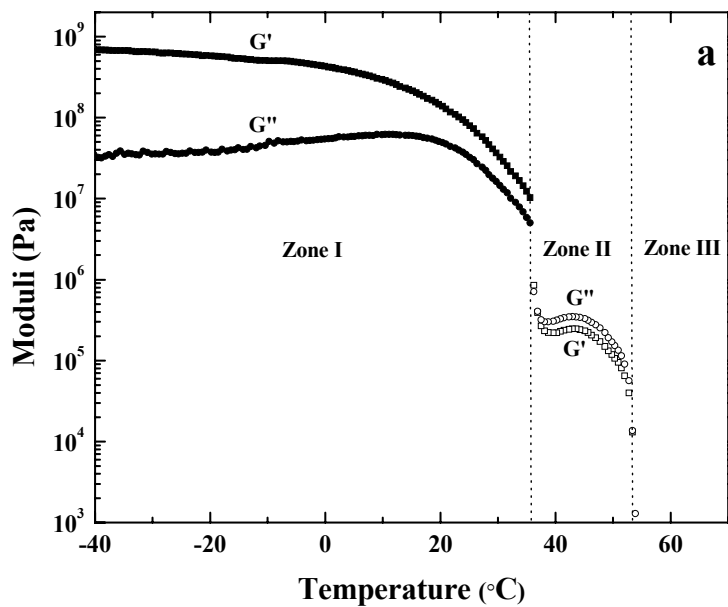
**Dynamic Mechanical Analysis of Paraffin Wax and its Nanocomposites.** Dynamic mechanical analysis was used to study paraffin wax in both the low temperature crystalline state with rectangular torsion bars and the rotator phase region with 8 mm parallel plates. The different geometries were used to optimize the accuracy of the measurements. A superimposed temperature sweep at 1 rad/s from  $-40$  to  $55$  °C for the pure paraffin wax is shown in Fig. 29a. In the plot, three regions are noted: the low temperature crystalline region (zone I), the mesophase region (zone II), which contains the rotator phases, and the isotropic liquid or melt region (zone III). As expected, upon transitioning into the mesophase region, the dynamic moduli drop sharply. The storage modulus ( $G'$ ) decreases from  $7 \times 10^8$  Pa at  $-40$  °C to below  $10^6$

Pa at 40 °C, and the loss modulus ( $G''$ ) decreases from  $3 \times 10^7$  to  $2 \times 10^5$  Pa over the same temperature span. When temperature is further increased to about 50 °C, another sharp drop in both moduli is observed due to the onset of melting.

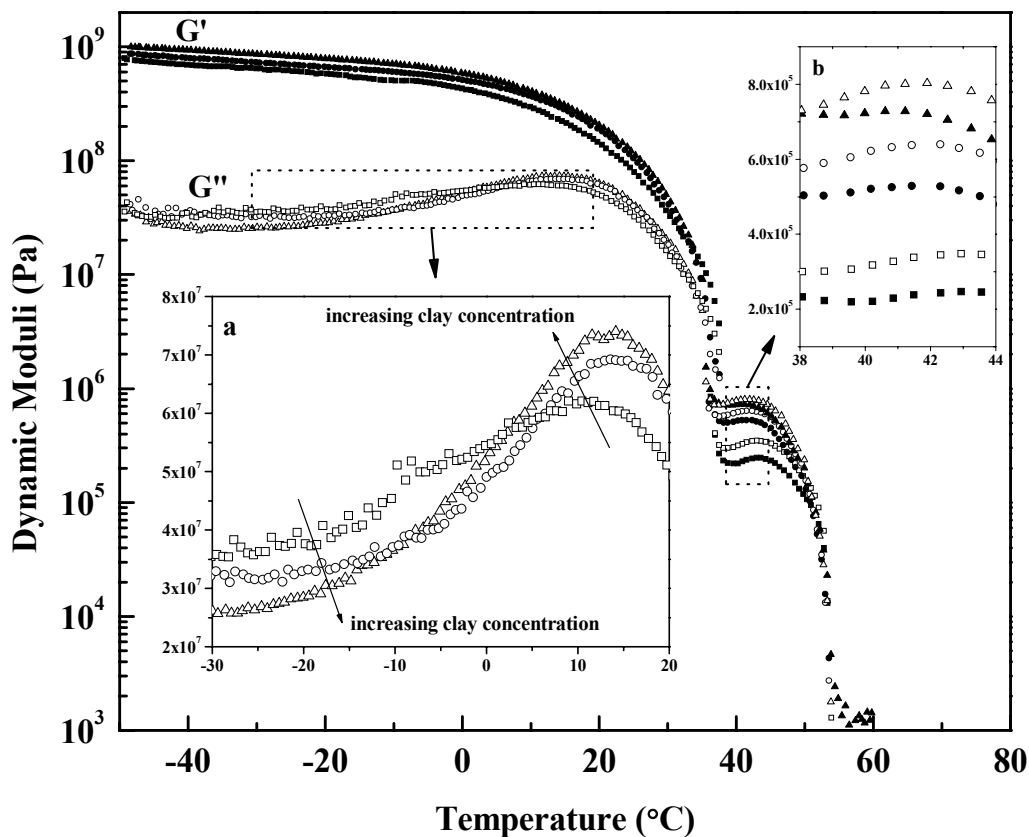
In addition to the sharp decrease in both the loss and storage moduli as paraffin wax enters the rotator phase region, there is a change in the relative magnitude of these quantities indicating an increase in its viscoelastic behavior. In the crystalline region (zone I),  $G'$  is significantly larger than  $G''$ , showing predominantly elastic behavior. When entering the mesophase region (zone II),  $G''$  is similar but slightly larger than  $G'$ , indicating a significant increase in the viscous behavior of wax. The change in viscoelasticity from the crystalline to the rotator phase can also be seen from the frequency sweeps (see Fig. 29b) of paraffin wax obtained at -50 °C (crystalline phase) and 40 °C (rotator phase). At -50 °C,  $G'$  values are predominant over  $G''$  values over the entire frequency range measured. At 40 °C, wax is solid-like ( $G' > G''$ ) at high frequencies and liquid-like ( $G' < G''$ ) at low frequencies, with a crossover occurring ( $G' = G''$ ) at about 2 rad/s.

Figure 30 compares dynamic moduli as a function of temperature collected at 1 rad/s for paraffin wax and its nanocomposites with highly exfoliated organo-clay concentrations of 1 and 3 wt%. It can be seen that the addition of clay increases the storage moduli for all of the temperatures tested. For the loss modulus, the influence of clay is temperature dependent. At sufficiently low temperatures ( $< -10$  °C), increasing clay concentrations reduce the loss moduli, but for temperatures near the mesophase transition and throughout the premelting region, clay raises the loss moduli. Inset a in Fig. 30 enlarges the loss moduli plot for temperatures ranging from -30 to 20 °C. From this isolated region, the change in the dependency of  $G''$  values on clay content with temperature can be clearly seen. A narrowing of the phase transition peak with the addition of clay was also observed. Inset b demonstrates that the exfoliated clay has a significant impact on the storage and loss moduli within the mesophase region.





**Figure 29.** (a) Temperature dependence of  $G'$  and  $G''$  of a commercial paraffin wax. Solid data points were obtained with rectangular torsion bars and open data points were obtained with 8mm parallel plates. The data was collected at 1 rad/s. (b) Frequency dependence of dynamic moduli for pure paraffin wax at  $-50$  and  $40^{\circ}\text{C}$ .



**Figure 30.** Temperature dependency of storage moduli  $G'$  (solid symbols) and  $G''$  (open symbols) for pure wax (squares:  $\blacksquare, \square$ ), wax nanocomposites with clay concentrations of 1 wt% (circles:  $\bullet, \circ$ ) and 3 wt% (triangles:  $\blacktriangle, \triangle$ ). The data was collected at 1 rad/s.

**Melt Rheology of Clay Nanocomposites.** Figure 31 shows the dynamic strain sweeps for the wax nanocomposites at three different clay loadings and a fixed temperature of 70 °C, which is approximately 20 °C above the melting point of the wax. Due to instrument limitation, the data on pure wax can not be reliably obtained. Large linear viscoelastic regions are observed for the nanocomposites in which  $G'$  is independent of the strain. There is a reduction in the linear region for the 5 wt% clay concentration nanocomposite. Strain amplitudes of 1% were used to collect frequency sweeps for all nanocomposite samples. Figure 31 shows logarithmic plots of complex viscosity,  $\eta^*$ , versus angular frequency,  $\omega$ , at 70 °C. The complex viscosities of the nanocomposites increase monotonically with organo-clay loading. All of the samples demonstrate shear-thinning behavior at low frequencies. The nanocomposite with 0.5 wt% clay shows a plateau region at high frequencies where the clay platelets are unable to follow the shear induced disturbance and the dynamics is then controlled by the liquid wax itself.<sup>66</sup>

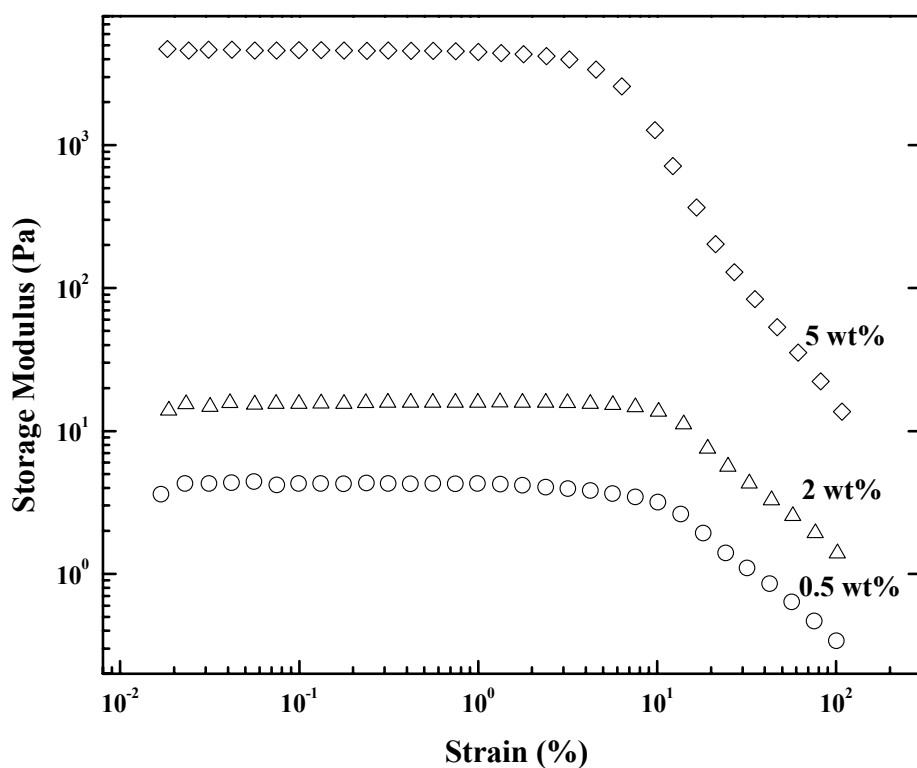


**Figure 31.** Dynamic stress sweep for wax nanocomposites with three different clay concentrations at 70 °C and 1 rad/s frequency. The clay concentrations are indicated next to the curves.

The shear-thinning region is fit well by an empirical power law expression of the form

$$\eta^* = A\omega^n \quad (5)$$

where  $\omega$  is the oscillation frequency and  $A$  and  $n$  are fitting constants. The exponent,  $n$ , extracted from linear fits of the low frequency data are listed next to the curves in Fig. 32. This term is often referred to as the shear thinning exponent. Values for the wax nanocomposites with several different organo-clay concentrations are all close to -1. Wagener *et al.* reported that the shear thinning exponent can be used to compare the degree of exfoliation of clay platelets in a polymer matrix. They concluded that well exfoliated samples display a higher magnitude of  $n$ , while the absence of exfoliation results in  $n$  values closer to zero.<sup>67</sup> The fact that the value of  $n$  is independent of clay concentration indicates the good exfoliation of clay up to 5 wt%, the highest concentration used in this study.

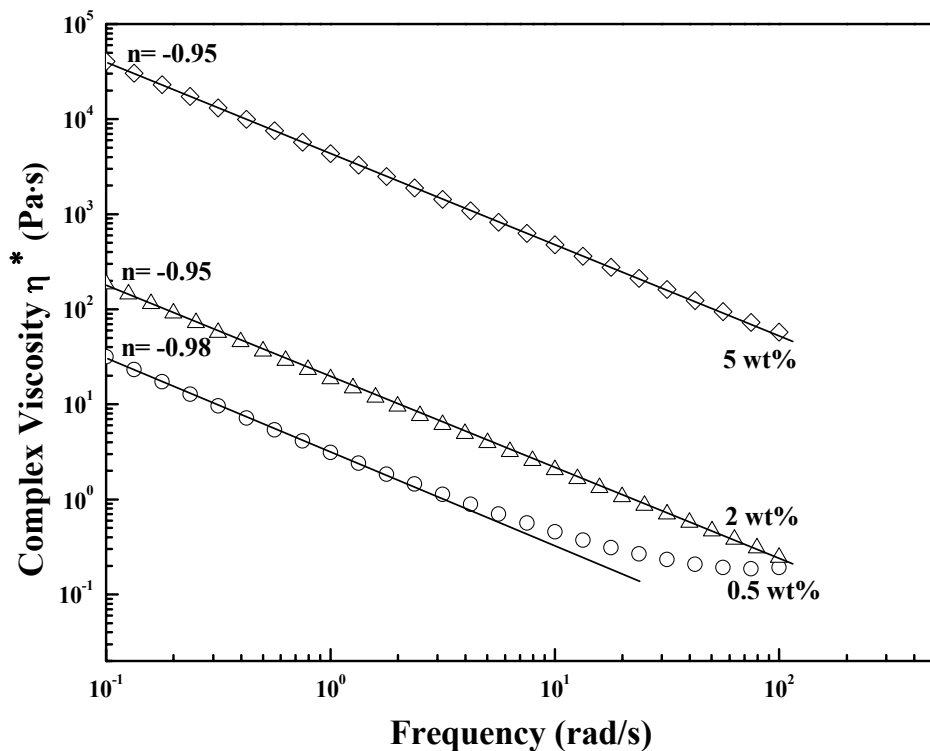


**Figure 32.** Frequency dependency of complex viscosities,  $\eta^*$ , for wax nanocomposites at three different clay concentrations. The clay contents as well as the values for the shear thinning exponent,  $n$ , are listed next to the curves.

To further investigate the relationship between the shear thinning exponent and the degree of exfoliation of organo-clay in the paraffin wax matrix, samples containing 3% organo-clay were melt processed using both sonication with an ultrasonic processor and simple stirring with a magnetic stir bar. Tensile tests for the samples carried out at 25 °C show a modulus, yield strength and % elongation at break values for the sonicated and stirred samples of 95MPa, 0.8MPa and 41%, and 68MPa, 0.9MPa and 26%, respectively. Both samples demonstrate significant improvements over the pure paraffin wax for which values of 61.4 MPa, 0.77 MPa and 12%, respectively, were obtained. The greater stiffness and ductility for the sonicated sample are attributable to the higher degree of exfoliation. Figure 33 compares the complex viscosity of stirred and sonicated composite samples. The differences are substantial. The sonicated mixture exhibits greater shear thinning behavior than the stirred sample and fits of the data with Eq. 5 resulted in an  $n$  value of  $-0.73$  for the stirred sample, while the value for the sonicated sample ( $n = -0.95$ ) is significantly lower and close to  $-1$ . Also shown in the figure are storage and loss moduli values for the two samples. For the sonicated sample,  $G'$  was greater than  $G''$  for the entire frequency range tested, while this was only the case for low frequencies with the stirred sample, which possessed a crossover point. It is interesting that the degree of exfoliation could not be confirmed for these samples using x-ray diffraction (XRD). This is demonstrated in Fig. 34, which shows the XRD scans for a 2-theta range of 1.5 - 30°. The clay signal is absent in the scans for both sonicated and stirred samples even though the rheology data and our previous TEM study indicate significant difference in the degree of exfoliation between the two samples. Thus, melt rheology may provide a useful technique for gauging the extent of exfoliation in the wax matrix as was demonstrated for polymer matrices.<sup>66</sup>

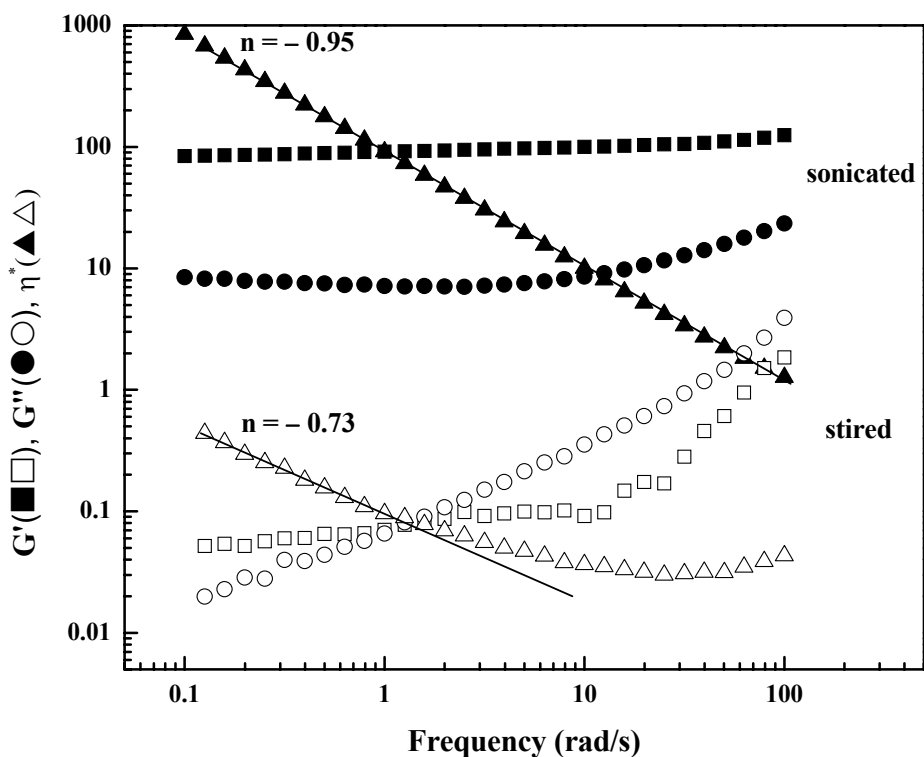


**Figure 33.** Frequency dependency of storage moduli (squares), loss moduli (circles) and complex viscosities (triangles) for wax/clay nanocomposites at 3 wt% clay concentration prepared via sonication (filled symbols) and stirring (open symbols).

A comparison of the frequency dependency of dynamic moduli for the nanocomposites measured at 70 °C is shown in Fig. 35. There is a monotonic increase in dynamic moduli with increasing clay content. The nanocomposites all show solid-like behavior ( $G' > G''$ ) at low frequencies. For polymer nanocomposites, the low frequency solid-like behavior was also observed and attributed to the physical jamming or percolation of the exfoliated/interacted clay network.<sup>68,69</sup> It was suggested that beyond a critical clay loading, percolation threshold, the clay layers or tactoids are unable to rotate freely and thus prevent polymer chains from completely relaxing at low frequencies and result in solid-like behaviors.<sup>70</sup> It has also been reported that exfoliated nanocomposites showed percolation behaviors at lower clay concentrations than the intercalated nanocomposite systems.<sup>71-72</sup> The fact that the wax/clay nanocomposites exhibited a low frequency solid behavior at clay concentration as low as 0.5 wt% indicates a good exfoliation of clay as previously revealed by TEM.<sup>47</sup> With increasing clay content, the onset of frequency dependency is shifted to higher frequency values. The nanocomposites with lower clay loadings, 0.5 and 2 wt%, approach a crossover at high frequencies. When clay concentration increases to 5 wt%, there is a solid-like response with nearly frequency-independent storage and loss moduli over all of the frequencies tested. The parallel  $G'$  and  $G''$  with  $G' > G''$  indicates a gel-like structure due to network formation from the well-dispersed silicate layers.<sup>73,74</sup> Gelling was indeed observed when trying to re-melt wax nanocomposites at clay concentrations greater than 3 wt%.

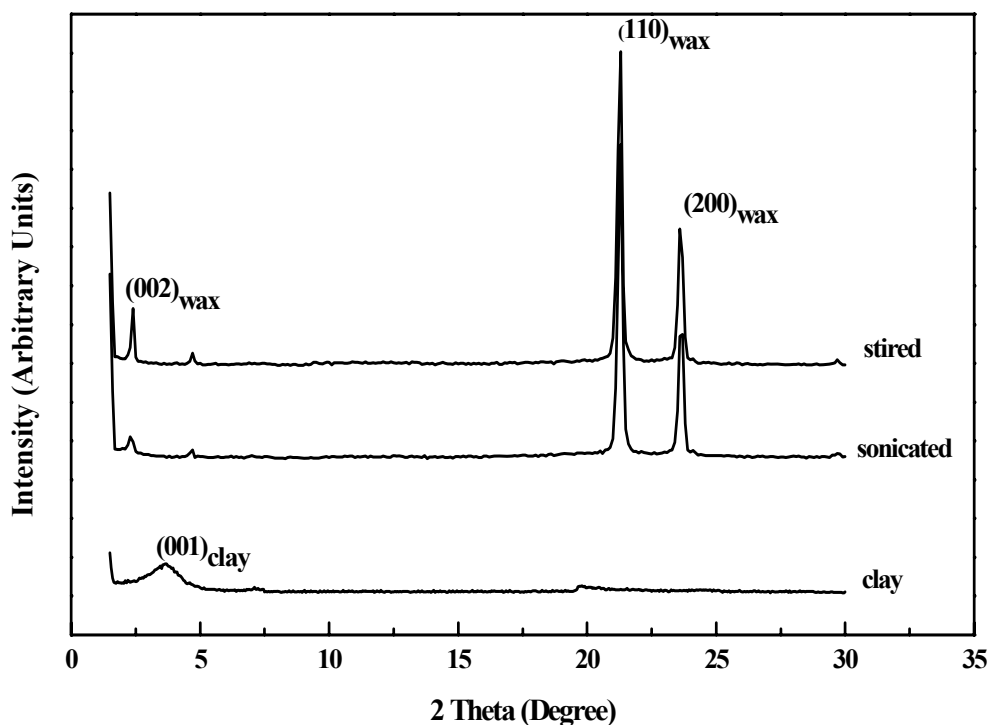


**Figure 34.** XRD scans of wax-clay composites prepared by stirring and sonication. The scan of the organo-clay is also shown.

### Conclusions

Paraffin wax is an inexpensive petroleum by-product that is soft, weak and brittle and thus provides limited performance when exposed to even small loads in service. In addition, wax often possesses rotator phases and softens near room temperature, which further limits its potential applications. It was shown in a previous work that clay addition significantly improved the mechanical properties of wax. In this work, the viscoelastic behavior of wax and its nanocomposites were studied over a broad temperature range, where accurate tensile measurements are not possible, providing insight on the mechanism by which nano-disperse clays interact with an oligomeric matrix to produce uncommon enhancements in properties.

DMA analysis shows the wax softens significantly and is more viscoelastic in its pre-melting region. The exfoliation of organo-clay increases the storage modulus and decreases the loss modulus in the low temperature crystalline phase, while increasing both dynamic moduli in the mesophase region. This result means that the reinforcing effect of clay is retained in the mesophase region. The rheological study of molten nanocomposites shows a large increase in complex viscosity with clay addition. These nanocomposites samples demonstrate shear thinning behavior and the complex viscosity versus angular frequency data are fit well by a power-law function, where the shear thinning constant is strongly related to the degree of exfoliation of clay that is difficult to obtain via XRD. The molten samples demonstrated low frequency solid-like behaviors which is consistent with the good exfoliation obtained using

ultrasonic processing. Melt rheology data for the nanocomposites provide important information on wax-layered silicate interactions and the structure-property relationship in nanocomposites and may also offer a useful gauge of the extent to which an organo-clay has been exfoliated and dispersed in wax matrices.

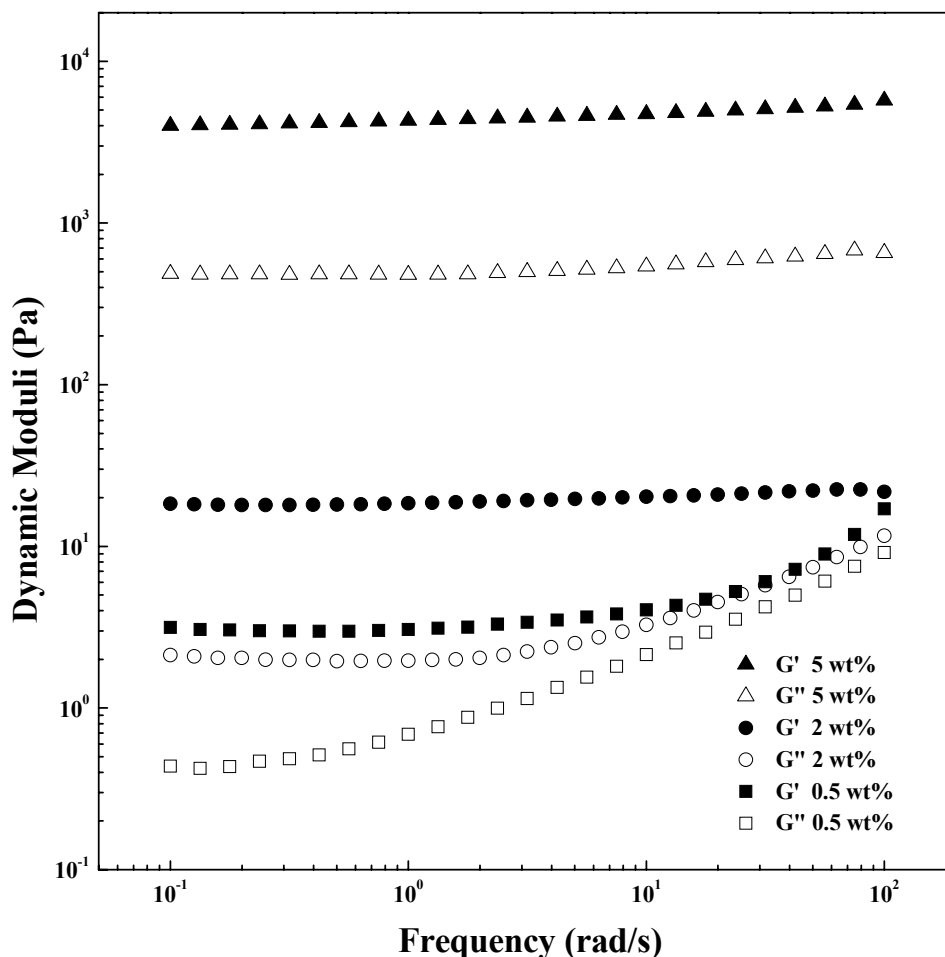


**Figure 35.** Frequency dependence of dynamic moduli (solid symbols for  $G'$  and open symbols for  $G''$ ) for three wax/clay nanocomposites. The clay contents are indicated next to the curves.

### 3.7 Investigation of Wax Removal Mechanism during Mechanical Pulping of Wax Coated Old Corrugated Containers (OCC)

Paraffin wax is commonly used as a barrier coating for corrugated containers. Nearly 1.3 millions tons of wax treated boxes are produced each year, which are used to ship perishable goods such as produce, meats, and seafood.<sup>75</sup> These wax-coated boxes are 100% non-recyclable presently because wax cannot be effectively separated from paper fiber in current paper recycling processes. They must be manually sorted out from uncoated boxes at grocery stores, and landfilled or incinerated. Due to difficulty in identifying these wax-coated boxes, a small

percentage of them enters the recycling stream causing significant contamination of recycled fiber and serious production interruptions. Therefore, various approaches have been taken to reduce the presence wax contamination and production upsets caused by wax-coated boxes including enhanced removal by screening by operating repulping at lower temperatures, use of dispersion chemical that requires high repulping temperatures, and floatation removal, which takes advantage of the low density of wax relative to water. Details about these approaches can be found in a good review article authored by John McEwen in 1992.<sup>33</sup>

Despite these extensive efforts, none of the above approaches appear to be effective or commercially feasible enough to be considered an industry accepted solution. The objective of this paper to investigate how wax breaks down during repulping and the mechanism involved in screening removal of wax particles. It is hoped that the insights provided by this work will help in the development of future approaches for controlling wax-coated boxes during paper recycling operations.

### **Materials and Methods**

**Materials.** Commercial waxes were provided by International Group Inc. (Toronto, Canada) and Chevron Inc. (San Francisco, CA). IGI 1230A and Chevron 128 were used in this study. Hexanes (5 isomers plus methylpentane) used in Soxhlet extractions were obtained from Mallinckrodt Chemicals (Phillipsburg, NJ, USA). Wax dye, Orcosolve Oil Blue B, was obtained from Organic Dyestuffs Corporation (East Providence, RI).

**Repulping.** Uncoated corrugated board was cut into 1 inch by 1 inch squares. The squares were Dip-coated with molten wax so that approximately 3 grams of wax was picked up. The coated squares were mixed with uncoated squares to get a total weight of 100 grams. Repulping was conducted in an Adirodack Formax pulper equipped with a temperature control unit at 3% consistency for 20 minutes. The pulp was screened with a 15-cut screen (0.38 mm screen slots, Valley Flat Screen). The accepts were collected to make handsheets and the rejects were collected, dried and run Soxhlet extraction. Repulping was conducted at various temperatures to study the temperature dependence of wax removal efficiency.

**Quantification of Removal Efficiencies.** For each repulping experiment, 10 1.2g handsheets were made from the screening accepts according to TAPPI Method T-205 om-88. Each handsheet was placed between two clean blotters and dried using an Emerson Speedy Drier (setting one step from max) for 10 minutes to melt and spread the wax contaminants. The dried handsheets were weighed and those with weight close to 1.20 g were used in the image analysis. A handsheet was wet floating on the surface of water (in a filled tub). The sheets were then imaged using a Fujinon digital camera and Pax-it software. Image analysis was conducted using Pax-It image analysis function. Wax percentage coverage of at least seven handsheets is reported along with calculated averages and standard deviation.

Soxhlet extractions of repulping rejects were performed using cellulose thimbles with hexane as the solvent. The dried, pre-weighted repulping rejects were ripped into small pieces to expose the wax and placed into a pre-weighted thimble. For each extraction, about 150 mL of hexane was used and the extraction was allowed to proceed for 8 to 12 hours. After the extractions were complete, the thimbles were removed from the Soxhlet extractors, left in the hood for 4 hours to



evaporate the solvent, and then dried in an oven at 45 °C for at least 6 hours before weighting. The wax rejects can be calculated from the weight loss after extraction.

**Optical Microscopy Imaging.** Specimens were prepared for observation of fiberization of wax-coated board during repulping. Ten to fifteen pieces corrugated board squares (1 in. × 1 in.) were coated with wax and mixed with uncoated board. The pulping was run for a period of time at 35 °C, stopped, and then several pieces of the wax-coated board fragments were taken out. Then the repulping was continued for another period of time and several pieces of wax-coated board fragments were taken out. This procedure was continued for repulping times of 1, 3, 5, 10, 15 and 20 mins. Wax was mixed with 0.5% blue dye to make the searching for wax coated board fragments in the pulp easier. The pulp after 20 mins repulping was screened and the rejects were collected. The wax coated board fragments obtained at different pulping times and the repulping rejects were dried and imaged using a LEICA Z16 APO optical microscope. Pictures were taken with a digital camera (PAXcam) and Pax-It software.

The pulping fragments were coated with 50Å platinum and imaged with a JEOL 6500 Field Emission Gun-Scanning Electron Microscope. A coated plastics recipe and voltage of 5kv was used during the imaging.

## RESULTS AND DISCUSSION

**Image Analysis and Soxhlet Extraction.** Image analysis has been widely used to evaluate the contaminants in paper and pulp. It has been used by Forest Products Laboratory at Madison to test the recyclability of pressure sensitive adhesives<sup>76</sup> and recommended by Fiber and Box association to test the recyclability of wax coated corrugated containers.<sup>77</sup> Image analysis allows a direct visualization of contaminants in the recycled products. However, there are a number of disadvantages to this approach. Table 11 lists the wax coverage results of several handsheets made from the same batch of repulping accepts. It can be seen that the error of wax coverage measurement from image analysis is significant; the standard deviation is about 25% of the average value. Efforts to correlate the amount of wax contaminants with the area coverage calculated from image analysis were not successful. Thus, it appears that an approach that is convenient and provides a quantitative gauge of the actual mass of wax contained in a paper sample would nicely complement if not replace the image analysis approach.

**Table 11:** Image analysis results.

Handsheets #	Handsheets Weight (g)	Wax Coverage (%)
1	1.23	5.13
2	1.19	4.68
3	1.21	4
4	1.21	2.45
5	1.23	5.15
6	1.23	3.72
7	1.24	3.12
Average	1.22	4.04
Standard Deviation	0.02	1.02

Through some trial and error, an approach found to provide such information is a Soxhlet extraction. In this method, a solvent, hexane, is used to selectively dissolve wax and separate wax rejects from the paper rejects. The amount of wax rejects can be determined from the weight loss after running Soxhlet extraction and wax removal efficiency is defined as the ratio of wax rejects to the amount of wax initially present in the pulper. A detailed procedure is described in TAPPI standard T204 om-88. To determine the accuracy of this new approach, wax and board were mixed at several different ratios and Soxhlet extractions were carried out. The results of this study are listed in Table 12. For pure wax, the determination of wax amount is quite accurate. Hexane dissolves almost all the wax as shown by trial #5 in Table 12. When the actual repulping rejects are used, the error comes from the fact that besides wax a small but significant amount of the board material can also be dissolved by hexane. For 3.84g pure board (Trial #1 in Table 12) subjected to Soxhlet extraction, 0.12g weight loss was obtained meaning that the same amount (about 3%) of materials from brown fiber was dissolve by hexane. In general, the use of Soxhlet extractions to determine the amount of wax in a mixture of wax and corrugated board has errors less than 5% compared to about 25% using our image analysis (see Trials 2, 3, 4 in Table 12). This method also saves time and labor. The making of handsheets and imaging of numerous samples is time consuming. For this approach, the dried rejects are simply placed in a pre-weighed thimble, the thimble is weighed, the extraction run, and the thimble and its contents are again weighed subsequent to drying. The amount of rejected wax is the weight loss after the extraction. So compared to image analysis, Soxhlet extraction is a simpler and more quantitative approach. It is used in this paper to determine the wax removal from a slotted pressure screen.

**Table 12:** Soxhlet extraction of wax-coated board.

<b>Trial #</b>	<b>Weight of board (g)</b>	<b>Weight of wax (g)</b>	<b>Weight loss after extraction (g)</b>	<b>Error* (%)</b>
1	3.84	0	0.12	3.1
2	3.02	1.98	2.06	4.0
3	2.99	1.03	1.07	3.9
4	3.0	2.98	2.97	-0.34
5	0	3.01	3.00	-0.33

\* For Trial 1: Error (%) = weight loss after extraction / initial board weight × 100%

For Trial 2-5: Error (%)=(weight loss after extraction –initial wax weight)/ initial wax weight × 100%

**Temperature Dependency of Wax Removal.** Aiming to find the optimum repulping temperature for maximum wax removal, the temperature dependency of wax removal efficiency was studied here. Wax removal efficiency is defined as the ratio of the weight of wax rejects determined from a Soxhlet extraction and weight of initial wax coated onto the corrugated board used in the repulping. Figure 36 shows that maximum wax removal was achieved within a temperature window from about 35 °C to 45 °C. It is believed that this unique temperature dependence is tied to the mechanical properties of wax. At lower temperatures, wax is brittle and tends to break into smaller pieces when being bent by the shear stress in the repulper. These small wax particles will go through the screen and result in lower removal at lower temperatures. As temperature increases to about 30 °C, wax begins to enter its rotator phases in which molecules gain a rotational freedom along their long axes while maintaining the long-range

positional order.<sup>5</sup> In these rotator phases, wax becomes ductile and has a lower tendency to break under pulper shear stress. As a result, larger wax particles and higher wax removal efficiencies are obtained. As temperature further increases and gets close to the melting point (~50 °C), wax loses all its cohesive strength and breaks into very fine particles and results in very low wax removal.

The bulk mechanical properties of wax determine the basic shape of the temperature curve. The presence of fiber in the wax coated board increases wax removal by retaining wax on fiber rejects. The wax-coated board has higher wax removal than the same weight of wax film and uncoated board mixture at temperatures lower than about 45 °C, above which fiberization is much easier and the reinforcing from fiber is not significant (Fig. 36).

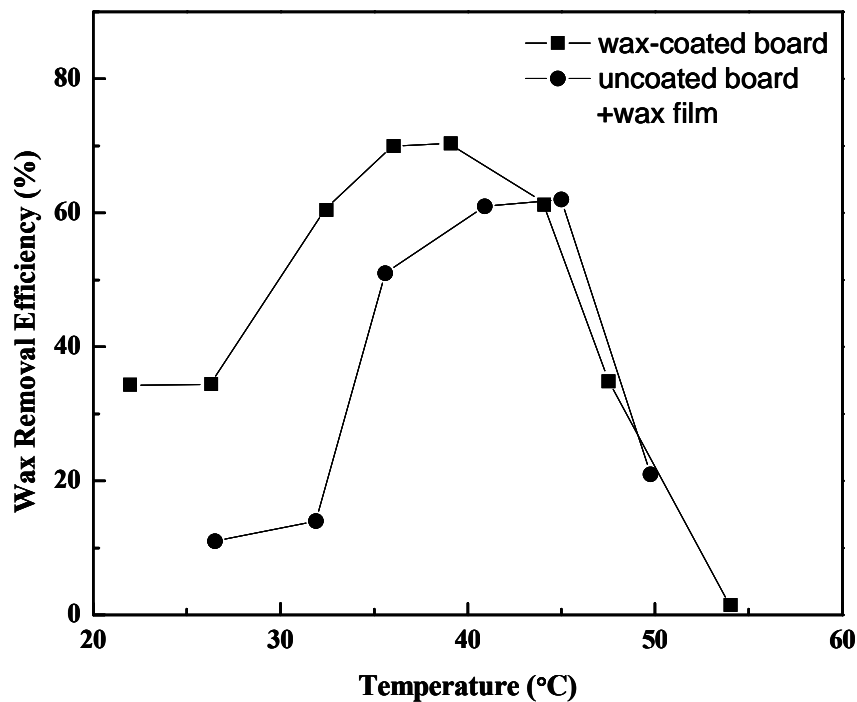


**Figure 36.** Temperature dependence of wax removal efficiency for wax-coated board (■) and a mixture of wax film and uncoated board (●). Wax used was Chevron 128.

Looking at the above results, a wax removal of 60 to 70% from a slotted pressure screen can be obtained by selecting suitable repulping temperatures (10-20 °C lower than wax melting temperature), which is achieved at a loss of fiber yield. At higher repulping temperatures, more fibers can be recovered while wax loses its strength and the reinforcing from fiber, and thus breaks into smaller particles resulting in little of it being removed.

**Observation of the Fiberization of Wax Coated Board during Repulping.** The temperature dependency test shows that at temperatures between 35-45 °C about 60-70 % wax removal can be obtained. Next it is examined why the remaining wax cannot be removed. For this, fiberization of wax coated corrugated board was tracked at 35 °C by stopping the pulper at various times and examining the morphology of the wax-coated board and its fragments. It is

shown that after 1 (Figure 37a) and 3 minutes (Figure 37b) of repulping, the wax coated board bends under the shear stress of pulper. After constant bending, wax flakes from the bending cracks allowing water to soak in and contact with the fiber. Fiber loses its strength upon contact with water and breaks into smaller pieces (Figure 37c). This fiberization process continues and after 10-20 minutes repulping wax-coated board fragments into roughly circular plates with radii about 3-6 mm (Figure 37d, 37e, 37f ). Figure 37g shows the final rejects, which has detached wax (see black arrow), and paper rejects with wax attached on it (see white arrow). These detached wax particles are mostly from bending cracks and the wax trapped between corrugating medium and liner; the latter likely results in larger particles that will be rejected. Figure 38 clearly shows that wax is missing from one of the bending cracks as shown in Fig 37. If after repulping the detached wax particles are small enough, they will pass through screen together with the recovered fiber and become contaminants. It is worth pointing out that most of the wax removed was attached to board fragments. Paraffin wax is used as a moisture barrier in wax coated corrugated containers. It also acts as a reinforcement, especially under moist conditions. One consequence of this increase in mechanical properties is that it is difficult to fiberize the wax-coated boxes compared to uncoated boxes. Table 13 shows that for repulping of 100 g uncoated board at 35 °C, only 3.9 g of rejects was collected. While for repulping of 60 g wax coated board, nearly all was collected as rejects.

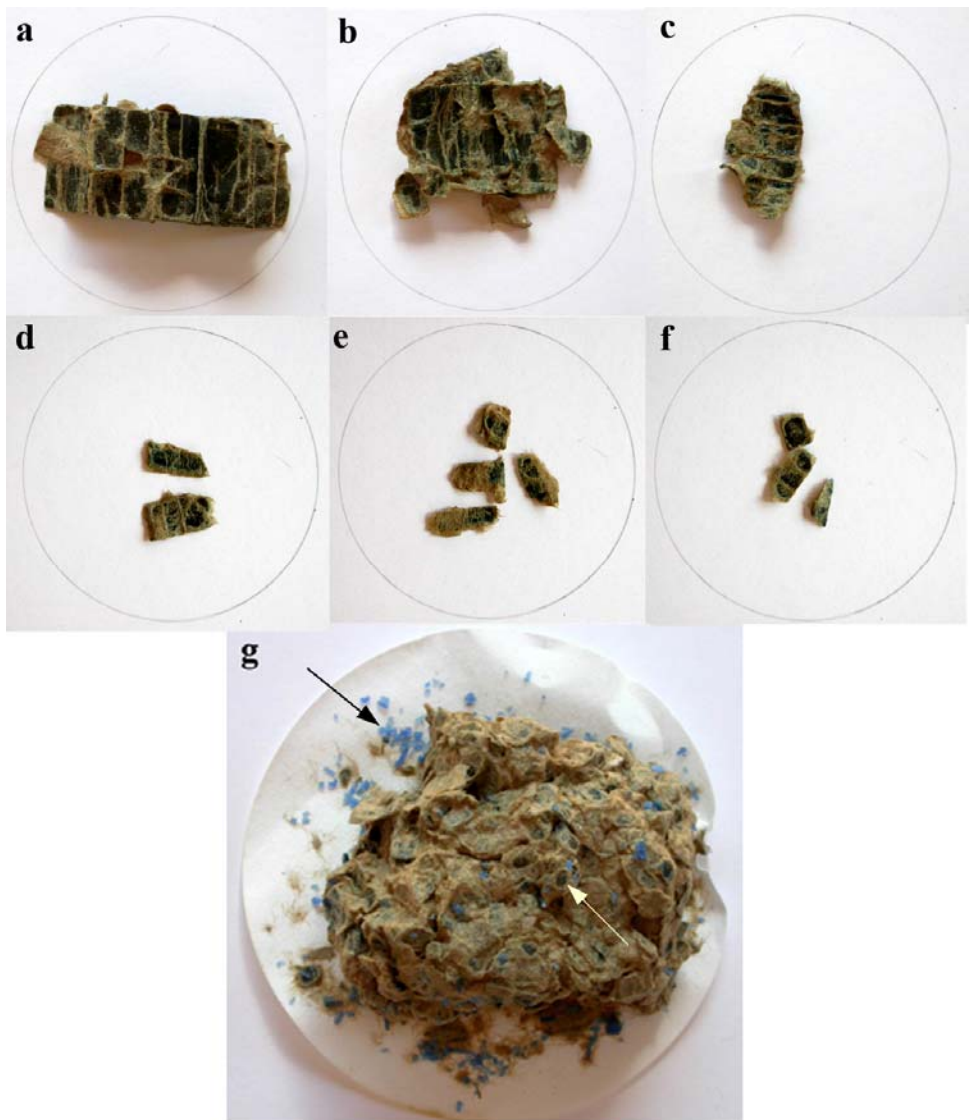


**Figure 37.** The fragments of wax-coated board after running repulping for 1min (a), 3min (b), 5min (c), 10min (d), 15min (e), and 20min (f). The circle in the image has a diameter of 6.7cm. Image (g) is the rejects collected from the screen. The repulping temperature is 35 °C.

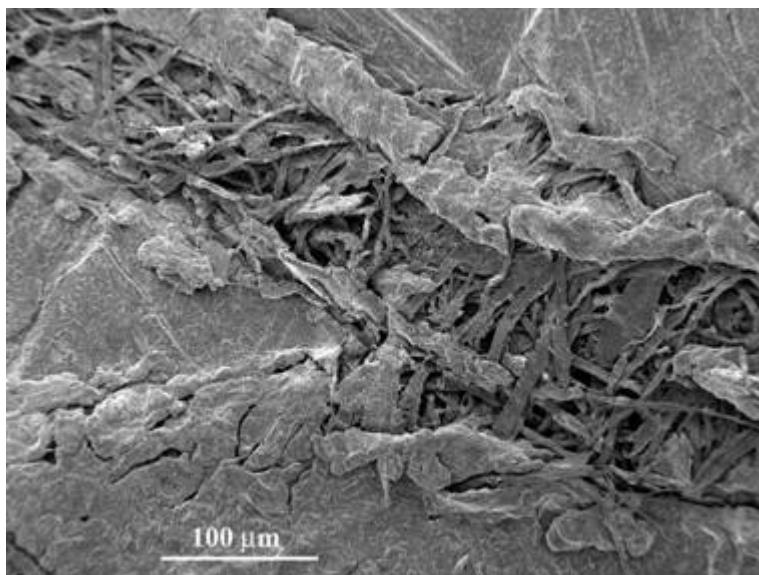


**Figure 38.** SEM image of repulping fragments shown in Fig. 37c.

**Table 13:** Reject weight of wax-coated and uncoated board: Chevron wax 128, repulping 35 °C.

Trial #	Weight of wax-coated board(g)	Weight of uncoated board (g)	Weight of rejects (g)
1	60.0	0	59.0
2	0	100	3.90

The above results showed that it is difficult to separate the wax that penetrates into the fiber by mechanical pulping and most of the wax was removed as wax coated board fragments. Keeping wax at the board surface (eg. curtain coating) or adding a water-soluble primer layer will help wax detach from fiber and increase fiber yield and possibly wax removal. Preliminary results showed that when curtain coating or a water-soluble primer layer was applied, wax removal was actually lowered. When detached from the fiber surface and losing the reinforcing fiber, wax itself was too weak to withstand the shear force in the pulper and thus broke into small particles that could not be rejected by the screen. A combination of a primer layer and stronger waxes (higher molecular weight or blending with polymers) probably will result in higher wax removal and high fiber yield. One concern with water-soluble primer layer is the performance of wax-coated board since its good water barrier properties and higher strength strongly depend on the highly hydrophobic nature of wax and its deep penetration into fiber.

Another possible approach is to use wet-strengthened fiber and more ductile wax so that wax stays attached to fiber that does not break in the pulper and get rejected. One disadvantage is that all the fibers are lost. Dissolving or dispersing wax is the best way to remove the penetrated wax and recover the fiber from wax-coated board. However, lowering the cost is the main challenge.

## Conclusions

Soxhlet extraction was applied to test wax removal using slotted pressure screens. This method proved to be a simpler and more quantitative approach than image analysis, which is currently used in paper industry. Temperature dependency of wax removal efficiency was investigated. The results show that maximum screening removal, about 60-70%, was achieved between 35-45 °C. In this temperature range, wax has good ductility and still enough strength; both are important for improving wax removal. Tracking the fragmentation of wax coated board at optimum removal temperatures provides insight on the origin of wax contamination. Most of the small wax particles that pass through the screens and become contaminants in the recycled products come from bending and shearing of the wax-coated board in the repulping processes.

### *3.8 Properties of Paraffin Wax/Montmorillonite Nanocomposite Coatings*

Paraffin or macrocrystalline wax is an inexpensive thermoplastic composed primarily of normal alkanes with carbon numbers that range from about 18 to 45. In their solid form, paraffin waxes are semicrystalline with low melting points (i.e., ~40 to 60 °C) and heats of fusion on the order of 150 J/g. In the melt, paraffin wax has a low viscosity and a surface tension of approximately 25 mJ/m<sup>2</sup>. Paraffin wax is used in a variety of products and applications. Here the interest is in its use as a moisture barrier.<sup>78,79</sup>

The modest cost, ease of processing, low surface tension and viscosity all combine to make paraffin wax a seemingly excellent sealant against liquid and vaporous water. For example, wax will readily flow into porous structures such as paper or fabric to fill its network of pores providing it with a low energy surface and enhanced structural stability. However, wax is quite brittle with a low stiffness and strength and cracks readily form due to thermal stresses as it cools severely diminishing its barrier properties. In addition, paraffin wax possesses a series of pre-melting or rotator phases at temperatures just prior to its melting transition.<sup>65</sup> In these mesophases, alkane molecules acquire increased rotational freedom while retaining positional order, which is why they are often referred to as rotator phases. These modifications in crystal structure are accompanied by significant changes in strength and wetting behavior.

In this paper, preliminary results of a study on the influence of exfoliated organo-clay on the processing and wetting of paraffin wax are reviewed. In previous publications it was shown that Cloisite<sup>®</sup> 20A, a natural montmorillonite organically modified with a quaternary ammonium salt, could be readily dispersed and exfoliated/intercalated in a paraffin wax matrix up to about 5%. The presence of the clay platelets simultaneously and substantially enhanced the stiffness, strength and ductility of wax at room temperature. Here, results on the performance properties of the wax are reviewed. It would be expected that the presence of the exfoliated organo-clay would influence the performance of the wax as a moisture barrier treatment and impact its dimensional stability. These effects are reported on here. Furthermore, it was found that heating molten wax over a long time period, consistent with its industrial application as a moisture barrier treatment, results in a change in its wetting behavior. As will be discussed, this change could be characterized as a decay, which is arrested by the introduction of organo-clay platelets.

**Mechanical Enhancements of Paraffin Wax with Organo-Clay.** Figure 39 shows thermomechanical data for a commercial paraffin wax. Two transitions are evident in the

differential scanning calorimetry (DSC) thermoscans shown in Fig. 39a. The higher temperature transition is due to the melting of the wax while the lower temperature event is a phase transition between a crystalline state and the lowest temperature rotator phase for the wax. Although they are often difficult to locate via conventional thermomechanical techniques, a wax can possess multiple rotator phases in the region prior to the melting transition. As would be expected, in the rotator phase region the strength and stiffness of the wax decreased considerably. This can be seen from Fig. 39b, which shows the young's moduli, tensile/yield strength and the elongation at break for several temperatures. The data was extracted from stress-strain data collected using an Instron Inc. (Norwood, MA) model 5543 tensile tester equipped with an environmental chamber according to ASTM standard D638-95.

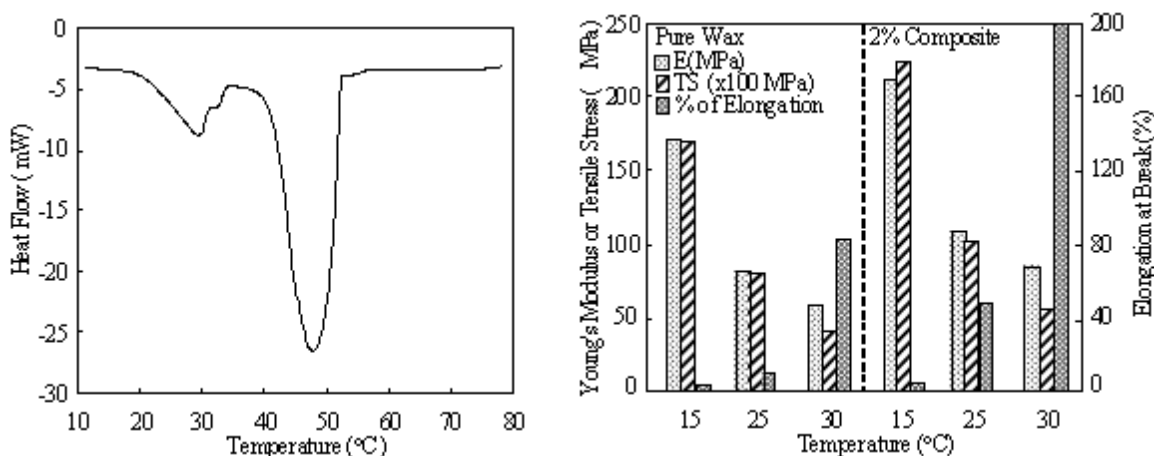


**Figure 39.** a.) Differential scanning calorimetry thermoscan of the commercial paraffin wax. b.) Mechanical properties including the Young's modulus, tensile/yield strength and elongation at break for the pure paraffin wax and its nanocomposites at various temperatures.

At low temperatures, the wax demonstrates brittle fracture, and the maximum stress occurs at breakage. As the temperature nears the low temperature crystalline-rotator phase transition, the modulus and strength of the wax decreases significantly, it begins to yield prior to breaking and demonstrates greater elongations at breaks.

Also shown in Fig. 39 (part b) are tensile test results for paraffin wax in which 2% organo-clay has been dispersed and exfoliated/intercalated. The Cloisite<sup>®</sup> 20A was added to melted wax and mixed with a high intensity sonicator probe. The clay was shown to be a mixture of exfoliated and intercalated morphology throughout the matrix with transmission electron microscopy (TEM). Images indicated that the organo-clay was present as thin tactoids containing a single or only a few clay layers. These particles were about 50-150 nm long and a few nanometers thick with an approximate aspect ratio of 15-40.

As was discussed in previous publications,<sup>47,54</sup> the introduction of nanodispersed organo-clay significantly enhances not only the stiffness and strength of the paraffin wax, but also its ductility. Nanocomposite samples began yielding prior to failure at much lower temperatures and their elongations at break were substantially increased relative to the pure paraffin wax. The



observed enhancements were diminished as the temperature of the nanocomposites were increased and it entered the onset of the crystalline-rotator phase transition.

**Dilatometry and Thermal Stress.** An issue with using wax as a barrier coating is its high thermal expansivity. This combined with its low stiffness and strength result in extensive cracking when wax coatings are solidified on rigid surfaces. The presence of cracks significantly increases its permeability to liquids and gases. The thermal stability of wax/clay nanocomposites were investigated using dilatometry. Figure 40 shows the relative volume expansion of pure paraffin wax and its nanocomposite produced with 2 wt.% organoclay as a function of temperature. When the temperature is below 24 °C, the relative expansivity values for pure wax and the nanocomposite sample are almost same. When temperature increases to above 24 °C, the pure paraffin wax shows a higher increase rate than that of nanocomposite. The maximum expansion temperature for pure paraffin wax and its nanocomposite are 43.7 and 38.2 °C, respectively. The maximum relative expansivity value for pure paraffin wax is about twice that of the nanocomposite.

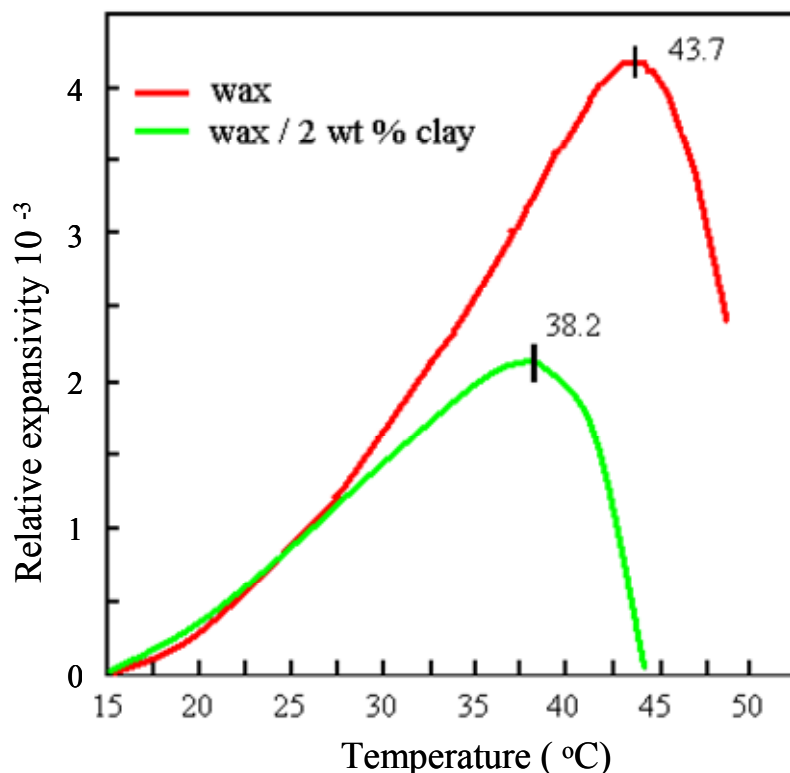


**Figure 40.** Relative thermal expansivity of paraffin wax and its nanocomposite with 2 wt.% organoclay.

Figure 41 shows scanning electronic microscopy (SEM) images of the pure paraffin wax and nanocomposites containing 2 and 5 wt.% organo-clay. Changes in topology due to the clay addition are evident from the images. Small ridges in the size range of about 50 microns cover the composites surface in random patterns while the pure wax surface has a plain flat surface. It was also found that the development of micron-size cracks appeared to be inhibited with increasing organo-clay content. In pure wax, extensive cracking is apparent. The cracks grow

up to several hundred microns in length. There are significantly fewer cracks and they are shorter in the 2 wt.% organo-clay sample. While the 5 wt.% organo-clay content sample appears to possess a crack-free morphology.

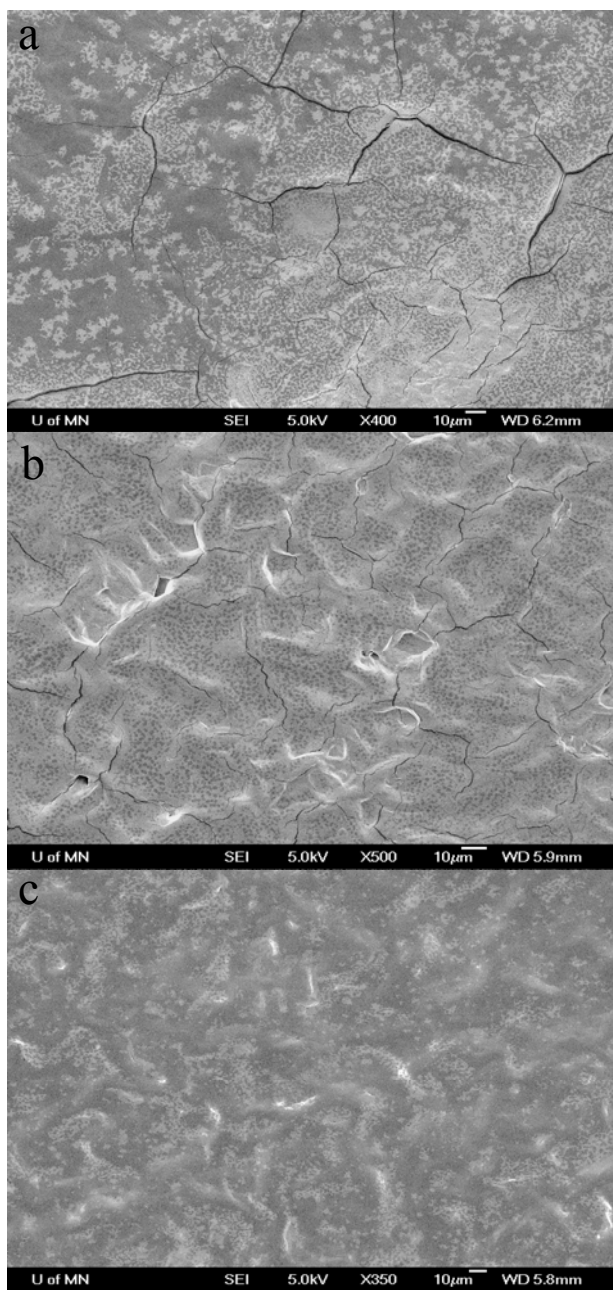


**Figure 41.** SEM image on clay/wax morphology. (a) pure wax; (b) 2 wt.% organo-clay; (c) 5 wt.% organo-clay.

The inhibition of crack formation upon cooling is likely governed in large part by the modification of the thermal expansivity of the wax, but the increased strength and ductility imparted by the organo-clay also plays a role. Although no permeability data are reported here,

preliminary measurements showed that films of the nanocomposite containing 5 wt.% organo-clay demonstrated significantly lower permeability to moisture than those from the pure wax.

**Surface Energy and Wetting.** The wetting of paraffin wax films by water is of interest when its barrier properties are sought after. The introduction of organo-clay does not appear to significantly influence contact angle values. However, an interesting observation is that contact angles are influenced by the length of time molten wax is heated. Figure 42 shows dynamic contact angle results for pure paraffin wax and its 2 wt.% organo-clay nanocomposite measured at 16 °C. The x-axis is the time period the molten wax was heated prior to being solidified to form 2 mm thick films covering a 20x20x0.2 mm steel plate. The dynamic contact angle measurements were performed following the Wilhelm plate method with a Kruss (Hamburg, Germany) Model K100 tensiometer. For the advancing angles, both the pure wax and organo-clay composite have relatively constant contact angle values. However, the receding angle decreases with increased heating time periods, and it can be seen that the decay is significantly tempered by the presence of the clay. For samples being heated for ten hours before solidification, the receding angle for pure wax dropped about 35 degrees, while the receding angle for its organo-clay nanocomposite only decreased slightly.

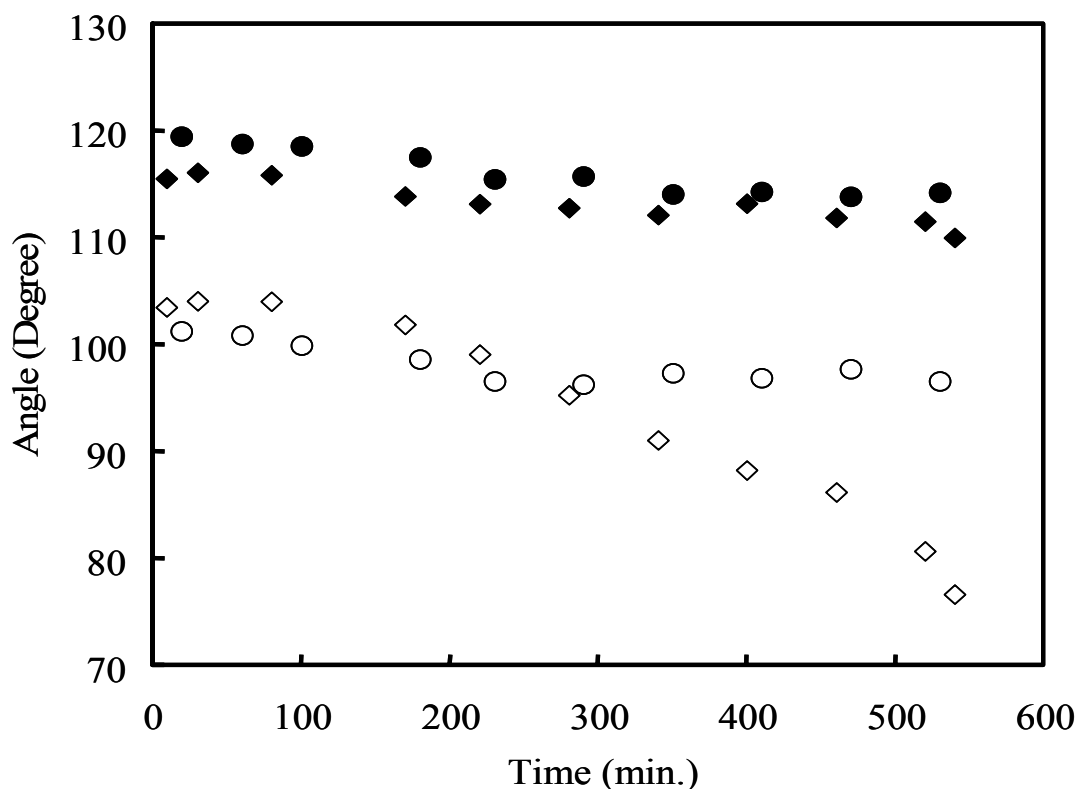


**Figure 42.** Molten heating time dependence of the advancing (solid) and receding (open) contact angle for pure wax (circles) and wax/clay nanocomposite at 2 wt.% clay concentration (diamonds) at 16 °C.

DSC and x-ray diffraction (XRD) results show that the crystallinity of pure paraffin wax decreases by more than 50% with 10 hours of heating of the melted wax prior to solidification, while little change was observed for the nanocomposite for the same heating time. The melt point also

decreased slightly with the drop in crystallinity and the wax was noticeably softer and weaker. Paraffin wax crystals have a well-defined lamella layer structure with a distinctive stepped platelet of monomolecular or bilayer thickness.<sup>62</sup> The hydrocarbon molecular chains are positioned almost perpendicular to the lamella layers in the crystallites. With the decrease in crystallinity, a more disordered structure is exposed to the surface. The greater disorder would be expected to increase surface energy, which would produce relatively more hydrophilic regions. It has been suggested that the contact line may interact preferentially with the heterogeneities; the increasing relative hydrophilic area has more impact on the receding process.<sup>80</sup> A defect of lower contact angle within the contact line perimeter will impede recessing, causing a lower receding contact angle.<sup>81</sup> This may be the reason for the nearly constant advancing angle and the decrease in receding angle observed here.

Other probe liquids, such as formamide and ethylene glycol, also showed the same tendency of the dynamic contact angle change for pure and the organo-clay/wax composites.

### Conclusions

The dispersion and exfoliation of the Cloisite<sup>®</sup> 20A in paraffin wax matrices enhances stiffness, strength and ductility of the formed Nanocomposite. The addition of the clay platelet reinforcements also appears to provide the composites with greater dimensional stability with heating and cooling, which likely accounts for the lack of crack formation in the films. The clay also appears to produce greater stability in the surface properties of the composites, which manifests itself in more stable wetting behavior for films generated from the melt.

### 3.9 Dependency of Contact Angle Hysteresis on Crystallinity for *n*-Alkane Substrates

The equilibrium contact angle,  $\theta_0$ , results from the balancing of surface tension forces along the line of intersection for the contacting phases. This is described by the well known Young's equation, i.e.,

$$\gamma_{lv} \cos \theta_0 + \gamma_{sl} = \gamma_{sv} \quad (6)$$

in which  $\gamma_{ij}$  is the tension for interfaces formed between solid (s), liquid (l) and vapor (v) phases.<sup>82,83</sup> Equation 1 applies to perfectly smooth and ideally clean surfaces, which, in practice, are rare. Measured angles will usually lie between upper and lower limits. The upper limit is the advancing angle,  $\theta_a$ , in which a liquid front is promoting advancement and the lower limit is the receding angle,  $\theta_r$ , in which it is promoting its recession. The difference between these angles is often used as a measure of hysteresis in the measurement,  $\Delta\theta$ , i.e.,  $\Delta\theta = \theta_a - \theta_r$ , which has been the focus of numerous studies over the years, but remains poorly understood especially for random defect distribution surfaces.<sup>84,85</sup> A major cause of contact angle hysteresis are surface defects such as roughness and chemical heterogeneities,<sup>86-94</sup> but surface deformation,<sup>95-97</sup> surface configuration changes<sup>98,99</sup> and adsorption or desorption<sup>100,101</sup> can also contribute and are sometimes the dominant factor determining this value. Hysteresis has even been reported to exist on nanometric or molecular smooth surfaces leading some to suggest that it is an intrinsic property of the spreading liquid.<sup>87-89</sup>

Waxes are synthetic or natural in origin and share the common characteristics of being hydrophobic and malleable. A common use for waxes both in nature and industry is to provide a moisture resistant barrier. A good example of this is the epicuticular wax, which is secreted by the lotus leaf. The so-called lotus effect is characterized by anomalously high wetting resistance to water as well as self-cleaning tendencies, resulting from a combination of the low surface energy of the wax and its nano- to micro-size hierarchical structure on leaf surfaces.<sup>81</sup> Interest in this phenomenon has prompted studies that often recreate the effect using paraffin wax whose low melting point allows its convenient molding into structures used for examining the influence of roughness on contact angle and contact angle hysteresis.<sup>93,102</sup> The use of paraffin wax as a model substrate has become quite common in studies of surface phenomenon due in large part to its perceived inert structure and lack of complexity.<sup>103,104</sup> Paraffin wax is composed primarily of normal alkanes ranging in carbon numbers from about C<sub>18</sub> to C<sub>45</sub>. It is a naturally occurring material that requires an artificial separation process to isolate it from crude oil with its specific composition being dependent on the method used in its extraction and isolation as well as its geographical origin.<sup>105,106</sup>

In this paper, data on the contact angle hysteresis for the wetting of paraffin wax by water will be presented and discussed. It is demonstrated that assuming wax to be a stable, homogeneous material can be rather tenuous. Specifically, it will be shown that changes in crystallinity, which can be modified via the heating of wax in its molten form, impact contact angle hysteresis. The wetting behavior of heat treated samples, characterized with differential scanning calorimetry (DSC) and x-ray diffraction (XRD), were investigated using both the Wilhelmy plate method and sessile drop analysis. It was found that the receding contact angle decreased with crystallinity, while the advancing contact angle remained nearly constant, decreasing only slightly. To determine the role of surface topology, samples were pressed and the roughness gauged using atomic force microscopy (AFM). Our findings indicate that the observed behavior is governed primarily by the greater heterogeneity associated with the increased disorder not the minor modifications in surface roughness, which accompany changes in crystallinity.

### **Materials and Methods**

Paraffin wax (IGI 1230A) was supplied by the International Group, Inc. (Toronto, ON, Canada). The molten samples were obtained by melting about 20 g of the original paraffin in a small open vessel at 140 °C. The unheated sample is denoted as W<sub>0</sub>, while samples kept in a molten state at 140 °C for periods of approximately 6 and 12 hours are denoted as W<sub>1</sub> and W<sub>2</sub>, respectively. The compositions of the paraffin wax samples were determined using a Hewlett Packard (Avondale, PA) 5890A gas chromatograph equipped with a 7673A controller. For injection, wax samples were dissolved in hexane at a concentration of 1 mg/mL. Differential Scanning Calorimetry (DSC) analysis of paraffin wax was performed with a TA Instruments (New Castle, DE) Q1000 differential scanning calorimeter. Thermograms were obtained under nitrogen atmosphere over a temperature range of 15 to 70 °C with heating/cooling rates of 10 °C/min. X-ray Diffraction (XRD) was carried out on a Scintag (Cupertino, CA) XDS 2000 theta/theta goniometer with a 2.2 kW sealed copper x-ray source and solid-solid detector. Crushed wax was added to a copper sample holder (25 mm × 25 mm × 1 mm) to fill the inscribed circle (diameter = 10 mm, depth = 0.5 mm). Wax samples were scanned with a 2 theta range of 1.5 to 30°. Using a PicoPlus PicoSPM (Agilent Technology, Foster City, CA) system, the surface topology of wax was characterized at ambient conditions. A pulse-force mode was utilized with integrated silicon

cantilevers possessing a tip curvature radii of 5-10 nm. The spring constant of the cantilever is manufacturer-specified in the range of 30-60 N/m and the measured resonant frequency was within 10% of 300 KHz. An alpha 300R confocal Raman microscope equipped with a UHTS200 spectrometer and a DV401 CCD detector from WITec (Ulm, Germany) was employed to collect Raman spectra from wax sample surfaces. A Nikon 100x objective was used for all measurements. An Ar-ion laser with the wavelength of 514.5 nm and maximum power of 50 mW was used for excitation. The lateral resolution of the confocal Raman microscope according to the theory of light diffraction is about 250 nm and the vertical resolution is about 500 nm. The scan area of the sample was about 20  $\mu\text{m}$  x 20  $\mu\text{m}$  with a resolution of 100 x 100 points. The integration time was 0.1 s for each point. Measurements were made on wax films cast on glass slides.

Dynamic contact angle measurements were performed following the Wilhelmy plate method using a Kruss Model K100 tensiometer at room temperature (Hamburg, Germany). The liquid phase wax was solidified to form about 1 mm thick film covering a 20 mm x 20 mm x 0.2 mm steel plate on both sides. In order to diminish the roughness effect, the coated plates were placed between 2 sheets of silicone release liner and pressed by a 5 kg weight until the wax solidified. Coated plates were immersed in deionized water purified to 18 M $\Omega$  cm with Type II Laboratory SpectraPure Water System (Tempe, AZ) at a velocity of 6 mm/minute. Two advancing-receding cycles were recorded for each plate with an interval time between cycles of 1 s. Force data were collected for every 0.01 mm of plate displacement. For each wax sample, at least seven coated plates were tested. The surface tension of water was measured after each test to confirm that the liquid had not been contaminated. Static contact angle was measured under ambient conditions by sessile drop method with Kruss Drop Shape Analysis System DSA10 (Hamburg, Germany). A 5  $\mu\text{l}$  drop was placed to the wax surface by gently lowering and attaching it and then removing the needle. Static contact angle was obtained from a fit of the drop profile using a horizontal baseline. The analysis was carried out within seconds of the drop being deposited. At least 20 deionized water drops with volume of about 5  $\mu\text{l}$  were measured and averaged for each wax sample.

## Results

Figure 43 shows the GC-MS results for the wax samples. All of the samples have similar carbon number distributions. The average carbon number for the untreated paraffin wax (sample  $W_0$ ) is 24.5. The heated samples ( $W_1$ ,  $W_2$ ) show a slight increase in this value (24.9 and 25.5, respectively). Figure 44 is an overlay of XRD patterns for the paraffin wax samples at room temperature. All samples possess an orthorhombic phase, which is common for paraffin wax. In the short spacing region ( $\theta > 20^\circ$ ), two intensive peaks are apparent at 21.3 and 23.7 degrees corresponding to (110) and (200) of the orthorhombic structure. The two small peaks seen in the long spacing region correspond to (002) and (004) indicating a regular periodic layer structure. All three samples have almost identical patterns except for the intensity, which decreases with increased heating time. Thus there does not appear to be a modification to the structure of the crystalline portions of the sample due to heating. Figure 45 shows DSC thermograms for the samples. Two peaks are apparent for all 3 waxes with both heating and cooling. The low temperature peaks correspond to a solid-solid phase transition between the crystalline phase and lowest temperature rotator phase. Rotator phases are plastic crystalline states in which molecules retain their long range positional order but gain rotational freedom normal to their long axes.

The high temperature peaks are a result of the melting transitions. The melting points appear to decrease slightly and the transitions become less distinctive with increased heating. In general the peaks associated with the identified phase transitions shift to the lower temperatures and broaden as the wax is heated for longer time periods. This is consistent with decreasing crystallinity.

Both DSC and XRD data were used to estimate crystallinity of wax samples using approaches that are commonly used for crystalline polymers for estimates of relative changes in structural order. The degree of crystallinity is calculated from DSC thermograms using the ratio between the melting enthalpy of the sample (i.e., the area under the melting transition peak) and that for a completely crystalline reference standard containing the same average carbon number. The theoretical value of melting enthalpy for a 100% crystalline *n*-alkane solid with a carbon number of 24 is about 245 J/g, which is calculated using the expression  $\Delta H_m = 303.8 - 1429/n_{\text{carbon}}$ .<sup>107</sup> In practice, it has been observed that the  $\Delta H_m$  value for highly ordered paraffin waxes is approximately  $226.2 \pm 8.4$  J/g and this value is nearly independent of chain length.<sup>108</sup> Here,  $\Delta H_m$  values for our samples determined via integration were compared against this 226 J/g value. Calculations from XRD data use ratios of peaks in the angle range from 10° and 28°. The 2 sharp peaks at 21.5° and about 23.7° are attributed to the crystalline paraffin phase. The degree of crystallinity was calculated from the ratio of the intensity area under the peaks and entire peak area. Crystallinities calculated using both methods are shown in Table 14. It can be seen that similar values are obtained using both techniques.

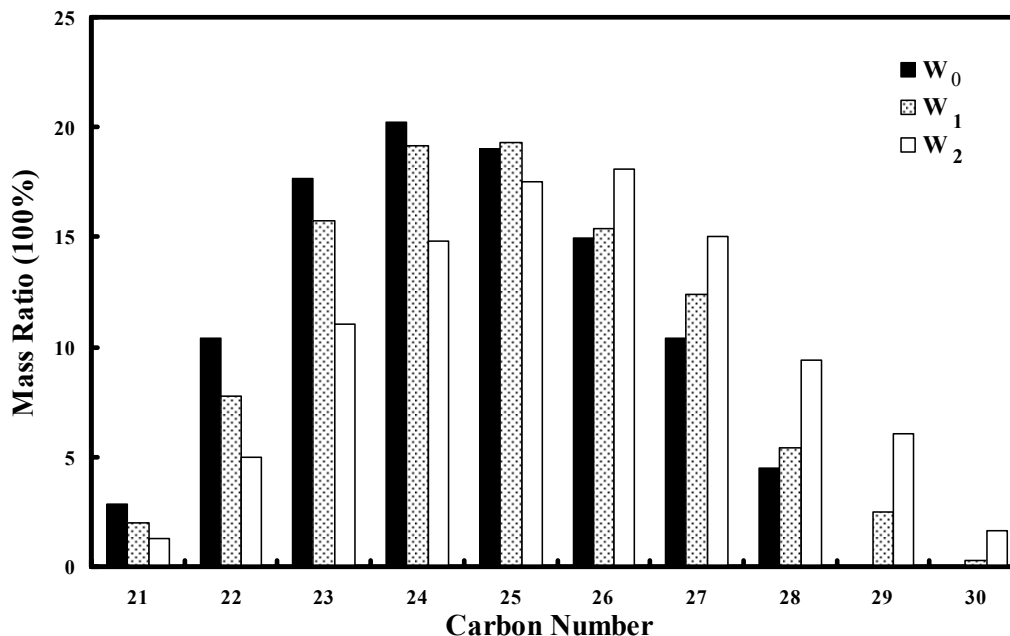


**Figure 43.** GC-MS analysis of the paraffin samples. Average carbon numbers for samples W<sub>0</sub>, W<sub>1</sub>, and W<sub>2</sub> were 24.5, 24.9, 25.5, respectively.

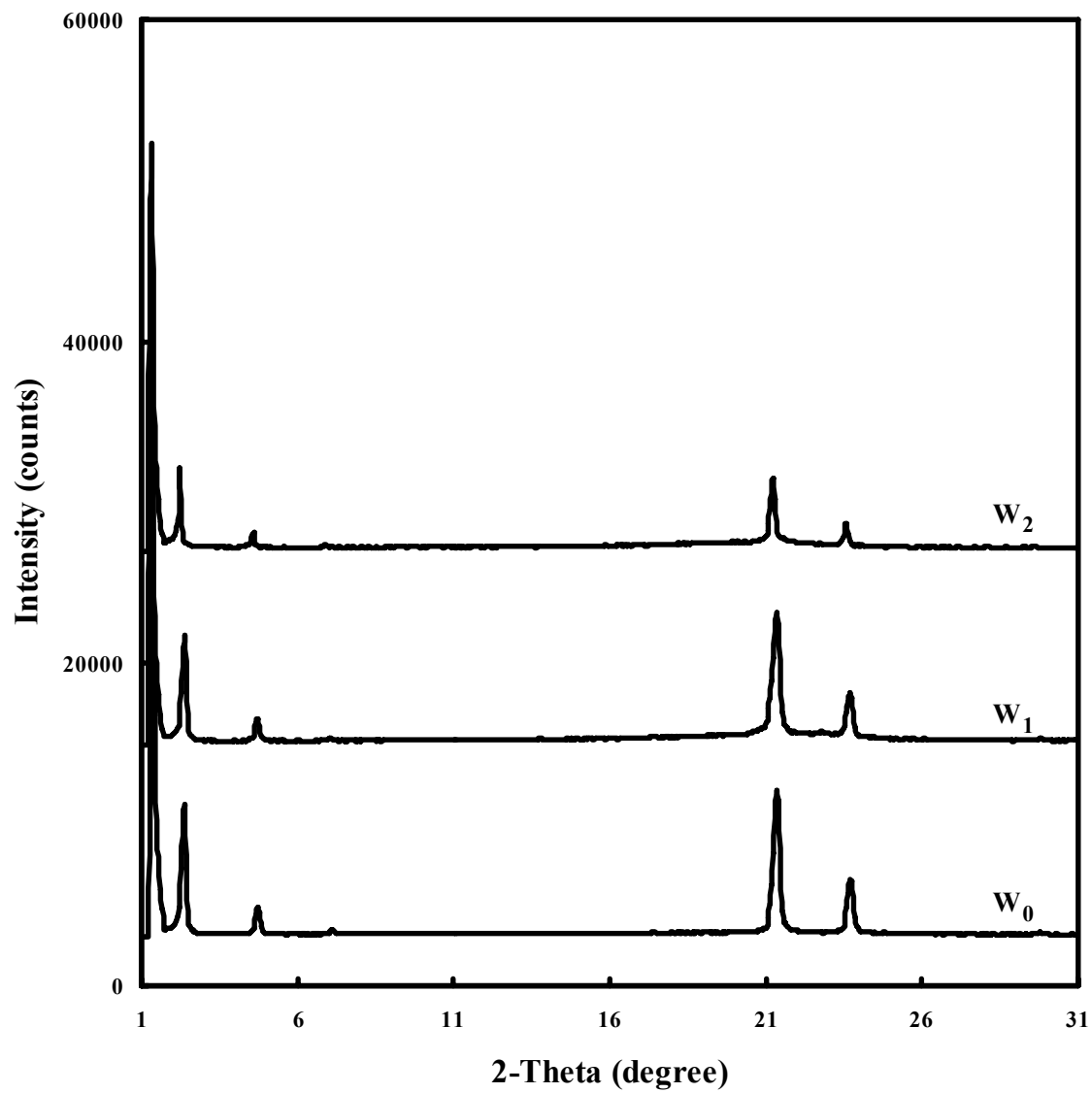


**Figure 44.** X-ray diffraction analysis of the paraffin samples carried out at room temperature.



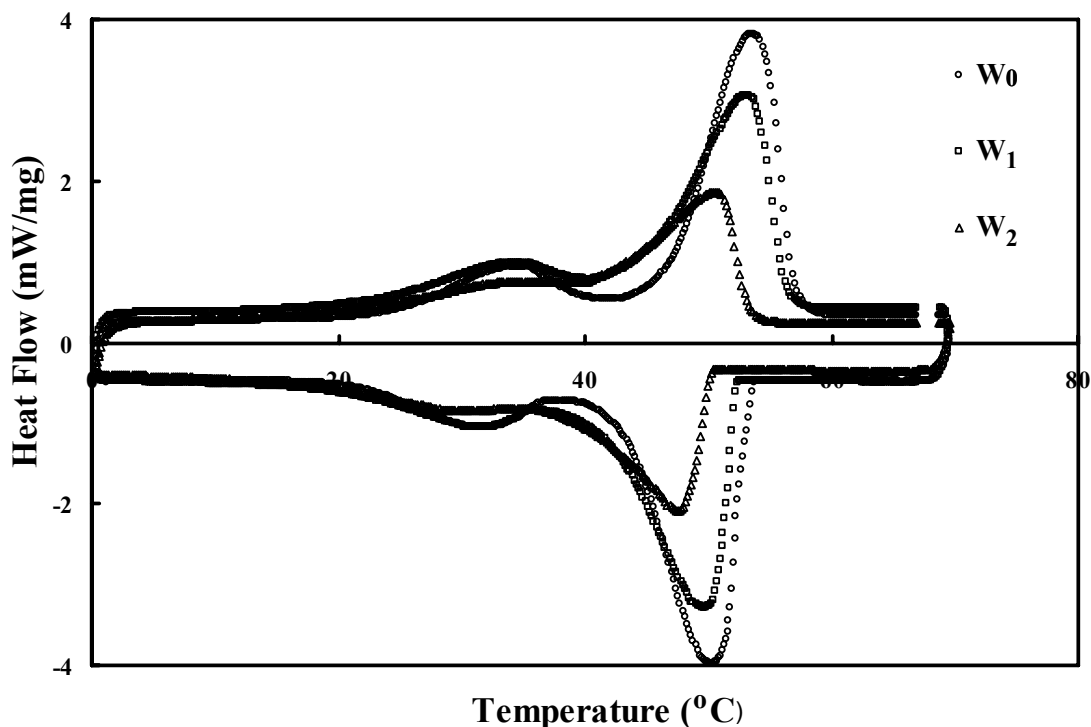


**Figure 45.** DSC thermograms of the paraffin samples.

**Table 14:** Calculated crystallinity for paraffin waxes using XRD and DSC data.

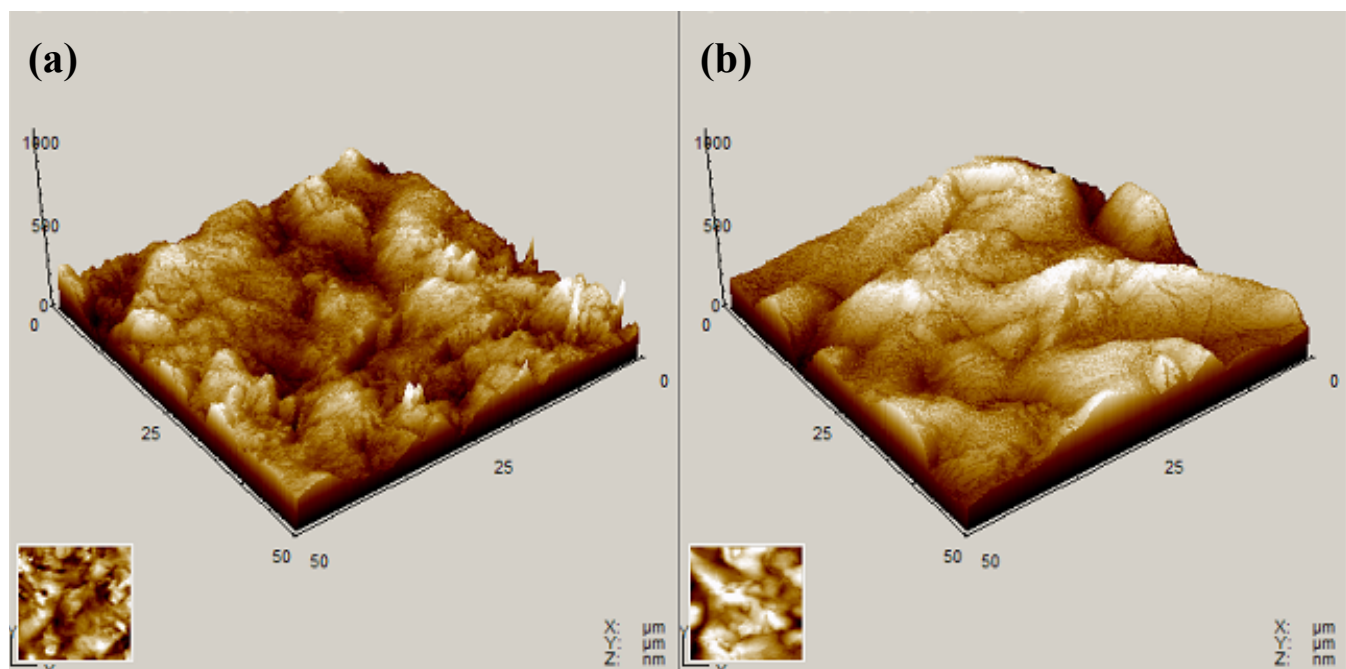
Paraffin Wax Sample	XRD Crystallinity (%)	DSC Crystallinity (%)
W <sub>0</sub>	67	60
W <sub>1</sub>	54	48
W <sub>2</sub>	29	27

Table 15 lists dynamic contact angles measured for paraffin wax coated plates when immersed in water. The original paraffin wax sample, W<sub>0</sub>, was found to have the greatest advancing and receding angles for the first run,  $113.8 \pm 2.6^\circ$  and  $96.4 \pm 1.7^\circ$ , respectively. The second run showed a slight decrease in both advancing and receding angles. When the plates used in measurements were stored under ambient conditions for 1 week, no changes in dynamic angles were observed when the measurements were repeated. The treated samples had similar advancing angles to that found for W<sub>0</sub>, but their receding angles were significantly decreased depending on the time they were heated with sample W<sub>2</sub> having the lowest value.

**Table 15:** Dynamic contact angles for paraffin waxes.

Paraffin Wax Sample	Advancing contact angle (first run)	Advancing contact angle (second run)	Receding contact angle (first run)	Receding contact angle (second run)
W <sub>0</sub>	113.8 ± 2.6	111.1 ± 2.8	96.4 ± 1.7	95.6 ± 2.0
W <sub>1</sub>	110.6 ± 4.0	110.4 ± 3.3	86.5 ± 3.9	87.4 ± 4.1
W <sub>2</sub>	111.8 ± 2.6	111.7 ± 2.9	72.0 ± 3.1	70.3 ± 1.3

Figure 46 shows topographs of W<sub>0</sub> and W<sub>2</sub> measured using AFM. As described, the samples were pressed between 2 sheets of release liner, which smooths the surface. The measured average roughness (R<sub>a</sub>) for W<sub>0</sub> is 65.3 nm, while its root mean-square roughness (R<sub>q</sub>) is 81.8 nm. The W<sub>2</sub> sample is slightly smoother with R<sub>a</sub> and R<sub>q</sub> values of 49.7 nm and 62.9 nm, respectively. Figures 47a-b show the Raman spectrum results for W<sub>0</sub> and W<sub>2</sub>. Presented plots are for average Raman spectra in the  $\nu$  (C-C) region between 800 and 1600 cm<sup>-1</sup> and the  $\nu$  (C-H) region between 2800 and 3100 cm<sup>-1</sup>. A scan area of 20  $\mu$ m x 20  $\mu$ m was used for both samples. Assignments of the Raman spectra of these systems are based on those previously reported for similar alkyl chain systems.<sup>109,110</sup> Figures 47c-d show area mapping by the intensity ratio of two C-H stretching bonds (I<sub>2884</sub>/I<sub>2852</sub>). The color scale from the dark to bright represents an intensity ratio increase from about 0.9 to 1.8. The images indicate that both samples are chemically heterogeneous. The W<sub>2</sub> sample has fewer bright regions compared with W<sub>0</sub>, and the sizes of these regions are significantly smaller and more dispersed. Some very dark regions (I<sub>2884</sub>/I<sub>2852</sub> ~ 1) are apparent for the heat treated samples.



**Figure 46.** AFM surface analysis of the smoothed (a) original, W<sub>0</sub>, and (b) 12 hour heat-treated, W<sub>2</sub>, paraffin wax samples.

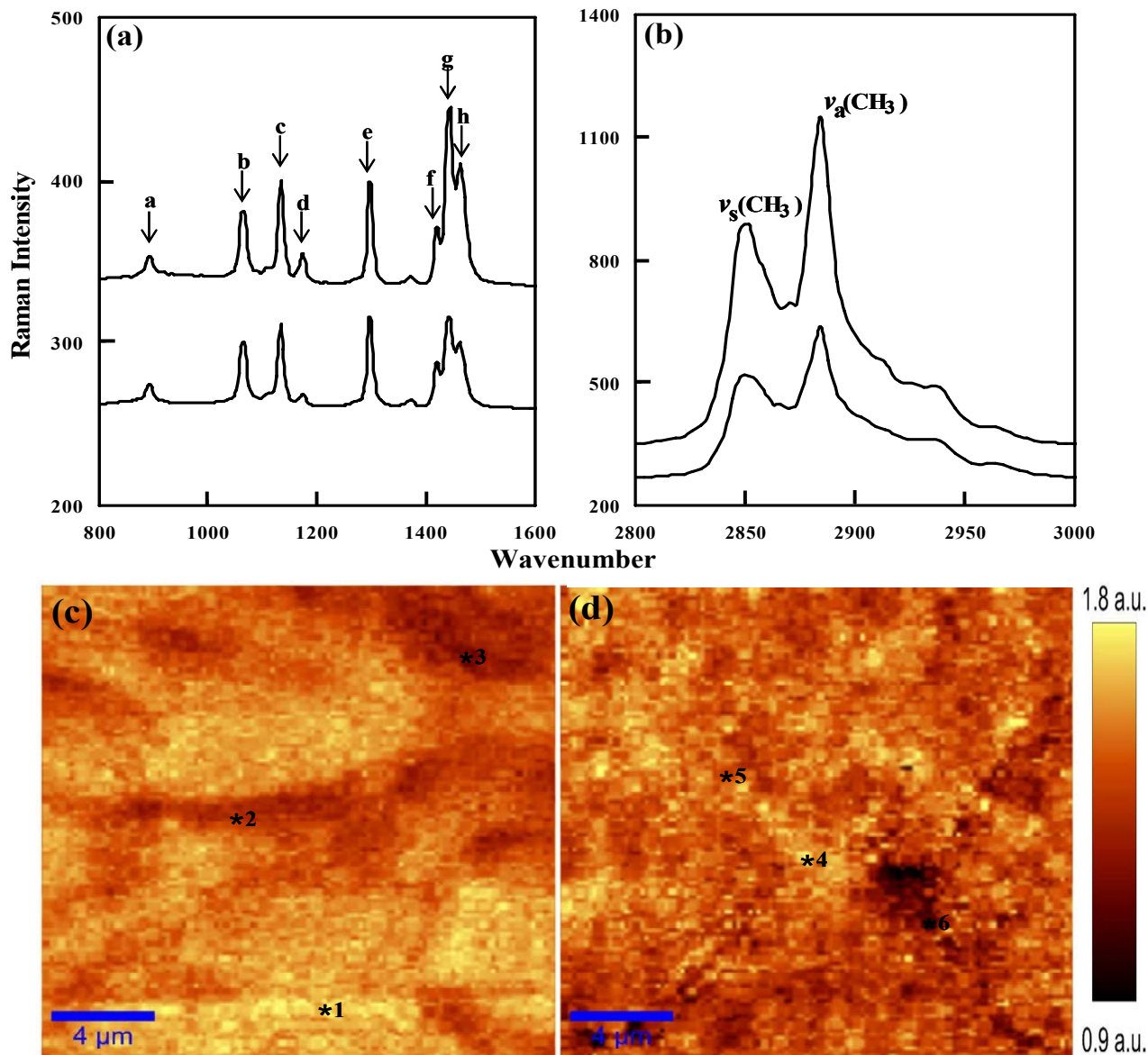


**Figure 47.** Raman confocal microscopy analysis of the paraffin wax before and after heat treatment in the (a)  $\nu(\text{C-C})$  and (b) the  $\nu(\text{C-H})$  regions (top - unheated, bottom - heated), and the mapping of the intensity ratios of  $I_{2884}/I_{2852}$  on wax sample surfaces for the (c) unheated and (d) heated samples. These ratios range between 1.8 and 0.9, e.g., values for the \* marked regions are 1 = 1.8, 2 = 1.4, 3 = 1.2, 4 = 1.8, 5 = 1.4, and 6 = 0.9. Peak identification: (a)  $890\text{ cm}^{-1}$   $\text{CH}_3$  Trans-rock; (b)  $1065\text{ cm}^{-1}$  CC skeletal stretch; (c)  $1133\text{ cm}^{-1}$  CC stretch; (d)  $1174\text{ cm}^{-1}$  CC stretch; (e)  $1300\text{ cm}^{-1}$   $\text{CH}_2$  deformation; (f)  $1422\text{ cm}^{-1}$   $\text{CH}_3$  deformation; (g)  $1461\text{ cm}^{-1}$   $\text{CH}_2$  deformation; (h)  $1461\text{ cm}^{-1}$   $\text{CH}_2$  bending and rocking.<sup>29,30</sup>

## Discussion

Paraffin wax is commonly used in wetting studies with the implicit assumption that it is a simple material that provides a smooth, homogeneous and hydrophobic surface. As shown, the thermal histories of a paraffin wax influence its crystallinity, as well as the surface distribution of its hydrophilic/hydrophobic regions. Furthermore, these changes are associated with a marked reduction in receding contact angles with water. This observation is consistent with that reported previously by Roger *et al.*<sup>111</sup> Their study showed that with purification to enhance the crystallinity of a wax, the receding angle with water significantly increased while the advancing

angle increased only slightly. In this section, data presented above are used to discuss potential causes in contact angle hysteresis.

With the recent interest in superhydrophobicity, self-cleaning surfaces and lotus effect, there is a tendency to associate anomalous wetting behavior with surface roughness. Roughness of wax surfaces, to a great extent, is determined by its crystallinity, and more precisely, by the prevalence of planes, edges, and corners of crystallites at sample surfaces. Accordingly, it is expected that modifications to crystallinity will change the roughness of our sample surfaces. However, the extent of this dependency is expected to be tempered by the fact that paraffin wax is semicrystalline. Figure 48 shows the AFM-determined roughness values for the  $W_0$  and  $W_2$  samples prior to their pressing with the release liner. Surface topologies of the 2 samples are similar, possessing micron-scale bumps. Values for roughness measures are substantially smaller for these samples compared to that for so-called “textured surfaces”, but are about 4 times greater than that of the smoothed wax surfaces. For  $W_0$ , the  $R_a$  and  $R_q$  values were  $0.24\ \mu\text{m}$  and  $0.33\ \mu\text{m}$ , respectively, while those for  $W_2$  were  $0.22\ \mu\text{m}$  and  $0.29\ \mu\text{m}$ , respectively. The reduction in crystallinity did not significantly influence roughness. The advancing and receding contact angles for the  $W_0$  samples prior to pressing were  $116.1 \pm 0.9^\circ$  and  $102.6 \pm 1.2^\circ$ , respectively, while those for  $W_2$  were  $114.1 \pm 1.3^\circ$  and  $84.2 \pm 1.2^\circ$ , respectively. Again, the changes in wetting behavior that accompanies the heat treatment of samples, specifically a stable advancing angle and sharp decline in receding angle, are apparent, implying that roughness is not a major factor in this phenomenon.

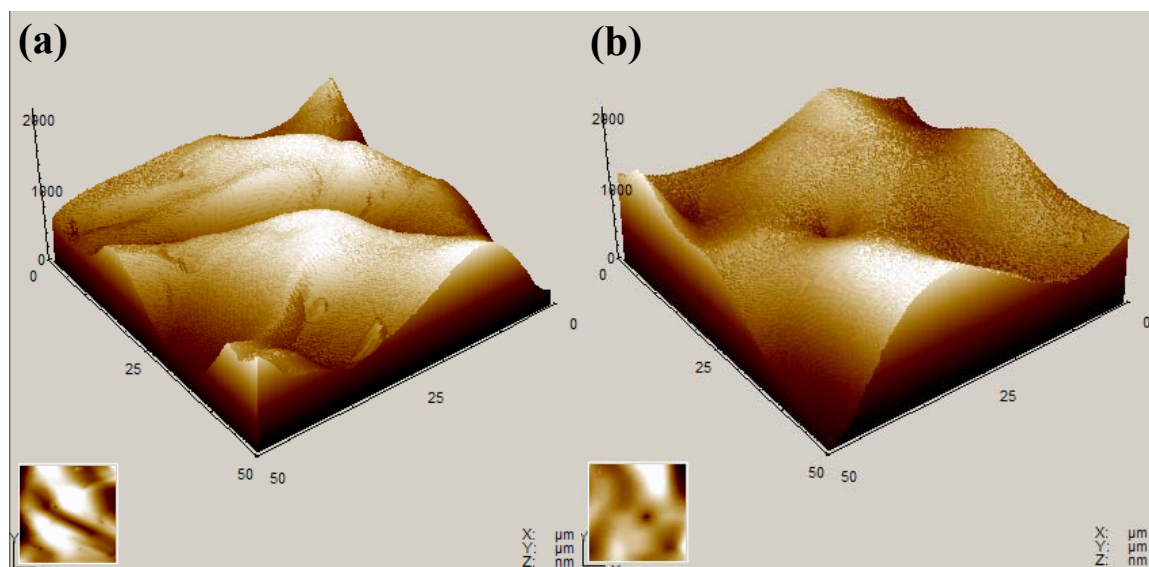


**Figure 48.** AFM surface analysis of the unsmoothed (a) original,  $W_0$ , and (b) 12 hour heat-treated,  $W_2$ , paraffin wax samples.

Having demonstrated that reducing crystallinity has little effect on its surface topology of paraffin waxes and that the wetting behavior of focus here persists even after surface roughness is changed significantly, e.g., 4-fold, the issue remains as to what is producing the observed hysteresis behavior. Raman confocal microscopy was utilized to show changes in surface heterogeneities with a decrease in bulky crystallinity of the paraffin wax. Figures 47a-b show that the Raman spectra for both the treated and untreated samples are identical except for

intensity of the peaks, i.e., there were no chemical composition changes, only changes in alkyl chain conformation during the heat treatment. The ratio of the antisymmetric peak located at  $\sim 2884 \text{ cm}^{-1}$  to the symmetric peak located at  $\sim 2852 \text{ cm}^{-1}$  is associated with the lateral packing order of methylene linkages.<sup>109,112</sup> In the crystalline state, this ratio is in the range of  $\sim 1.6$ - $2.0$ , while in the liquid state, the ratio decreases to  $\sim 0.6$ - $0.9$ . Globally, this ratio was found to decrease subsequent to heat treatment, consistent the XRD and DSC results. More valuable information is found by examining the distribution of this ratio. Figures 47c-d indicate that the paraffin wax has a heterogeneous surface with a distribution of crystallinities. For the original paraffin wax, highly crystalline regions (e.g.,  $I_{2884}/I_{2852} \sim 1.8$ ) of various shapes are found with sizes on the order of several microns. Crystalline areas can still be found on the surface of the heat treated samples, but their size is greatly decreased to sub-micron levels. In addition, the treated samples also possesses areas of low crystallinity ( $I_{2884}/I_{2852} < 1$ ) that near the liquid state value for hydrocarbon chains, corresponding to a liquid-like state.

Crystalline polymers have been shown to be more wettable at lower crystallinities achieved via quench solidification or heating past their crystalline melting temperature.<sup>113</sup> In fact, contact angle was shown to be an effective method for estimating the crystallinity of oxygen plasma treated polymer surfaces.<sup>114</sup> Paraffin wax exists as large crystalline plates which are embedded in an amorphous matrix.<sup>115</sup> The crystalline plates have a well defined lamella layer structure with a distinctive stepped platelet possessing a monomolecular or bilayer thickness. Hydrocarbon molecular chains are positioned almost perpendicular to the lamella layer surface with methyl groups ( $-\text{CH}_3$ ). The amorphous phases include chain-end and branch defect zones and mobile amorphous zones. The amorphous regions are filled by small amounts of oil, which has the same average chain length of the bulk but branched to a greater extent. The surface of a perfect hydrocarbon crystal exposes only methyl groups to the surface and has a low surface energy of about  $21 \text{ mJ/m}^2$ .<sup>116</sup> With decreasing crystallinity, paraffin wax develops a more disordered surface structure involving a greater concentration of methylene linkages ( $-\text{CH}_2-$ ). Fox and Zisman demonstrated that an increased density of methyl groups at the air/solid interface decreases its wettability by water,<sup>117</sup> while the same increase for methylene linkages had the opposite effect.<sup>118</sup> In other words, more crystalline wax has a lower surface energy. Our findings were consistent with these observations.

The preferential influence on either the advancing or receding contact angle is a well established phenomenon. Bartell *et al.* showed that, for a hydrophilic surface, the advancing contact angle was highly sensitive to the treatment history, while the receding contact angle was largely independent.<sup>119</sup> De Jonghe *et al.* investigated the hysteresis of a binary matrix containing Si-SiO<sub>2</sub>.<sup>120</sup> The receding angle for water on the Si-rich hydrophilic matrix equaled that found on the pure Si surface while the advancing angle increased. It was suggested that this was a result of surface friction caused by the presence of the less wettable SiO<sub>2</sub> defects. It was also found that once the SiO<sub>2</sub> surface content was beyond 50% and the surface became SiO<sub>2</sub>-rich, the advancing angle became equal to the angle on pure SiO<sub>2</sub> while the receding angle decreased with the increasing surface friction from the more wettable Si defects. Similar findings have been reported for other surfaces including titanium surface, solution treated glass, cellulose derivatives, polymer thin films and partially depleted monolayer.<sup>121-124</sup> Iwamatsu showed, for a two different surface energy surfaces as alternating strips, the advancing angle was equal to the high equilibrium contact angle surface and the receding angle was equal to the low equilibrium

contact angle surface.<sup>125</sup> Theoretical analysis based on the energy barriers between allowable metastable states found that for surfaces that are primarily hydrophobic, i.e., with coverage by hydrophobic surface of >50%, the advancing angle is slightly lower than the high equilibrium contact angle surface and remained relatively constant over a wide range of coverage while receding angle was extremely sensitive to small variations.<sup>126</sup> The opposite behavior is found for surfaces that are primarily hydrophilic. The critical value for fractional coverage was found to be about 0.5 to determine the energy barriers controlling hysteresis.<sup>124-126</sup>

It has been proposed that the behavior described above is a result of the preferential interaction of the wetting line with heterogeneities.<sup>80,81,127,128</sup> The contact line is strongly distorted by local defects and the shape and length could significantly change during the motion.<sup>129</sup> For the propagation of a wetting line it must overcome the maximum energy barrier inhibiting its motion. Thus, the defects of a higher contact angle outside the contact line perimeter will impede advancement while the defects of a lower contact angle inside the contact line perimeter will impede recession. These defects may also modify the motion of the wetting line, which may be understood by examining the wetting of post structures, which also results in an asymmetric change in the dynamic contact angle, e.g., up to 20 degrees in receding contact angle in one study.<sup>127</sup> The Raman spectra mapping results showed that the wax surface is chemically heterogenous with a complex crystallinity mixture of sub-micron size patches. The increased area of the less hydrophobic patches could cause a great impact on the receding contact angle and the receding line movement.

Wax samples for which the surface roughness had been reduced still clearly show the significant decrease in dynamic receding contact angles accompanied by a minor (insignificant) reduction in the advancing angles. Thus, the case has been made that surface texture is not the primary contributor to the wetting behavior, the focus of this paper, but differences are observed in hysteresis between the smoothed and non-smoothed surfaces, which indicate that roughness is playing a general role in the wetting. For both the  $W_0$  and  $W_2$  samples, hysteresis for the rougher surfaces is about 25% less than that found on the smoother surfaces. Two basic models to understand the influence of heterogeneities on contact angle is Wenzel and Cassie-Baxter model. In Wenzel's model, the contact angle was modified by the roughness of the surface and in Cassie-Baxter model, the contact angle was depended on the ratio of two different surface energy species. The change is consistent with the movement of wetting away from the Cassie-Baxter type and towards that of the Wenzel type. It is also observed that the decrease in receding contact angles between the  $W_0$  and  $W_2$  samples for the smoothed and non-smoothed surfaces show that this change is larger for the smoother surface, 24° versus 18°. These observations can be explained in the context of the mixed wetting state to provide a more general description of the movement of the three-phase line on the surface of paraffin wax. The rougher the surface, the more Cassie-Baxter character the wetting demonstrates and the less contact there is with the actual wax surface. This also reduces the concentration of hydrophilic defects at the actual wetting line. By pressing the surface, schematically demonstrated in Fig. 49, a smoother surface is generated promoting a greater contribution of Wenzel-type wetting, and possibly greater access to more hydrophilic (amorphous) regions. This would provide a greater concentration of hydrophilic defects in contact with the wetting line enhancing the reduction in receding angle, as is observed.

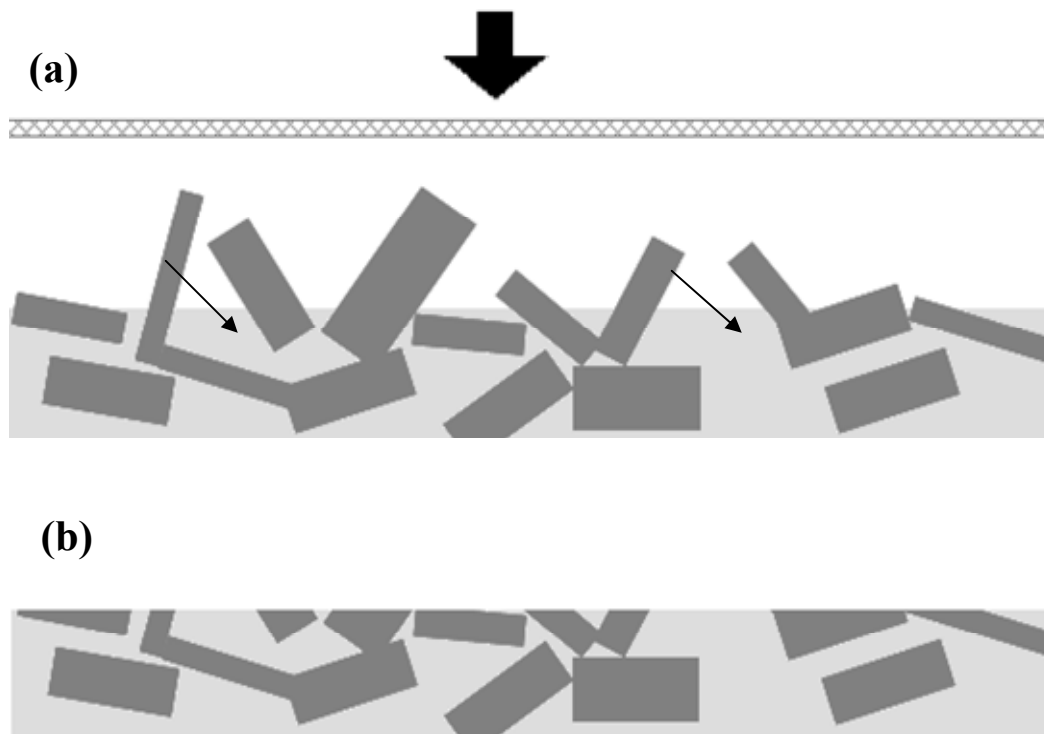


**Figure 49.** Schematic showing the multiple effects of smoothing wax surfaces via pressing with (a) representing the surface prior to pressing and (b) subsequent to pressing. Dark regions represent wax crystallites while the light areas are the more amorphous portions of the surface. The arrows indicate regions of low crystallinity area, which are possibly shadowed by the crystallites prior to pressing.

It is interesting to examine what impact the reported phenomenon would have on static contact angle measurements, which are commonly used in characterizing wetting behavior. Most typical are sessile drop measurements made using the goniometer method. Static contact angle measurements were performed on both rough and compressed wax surfaces. The static contact angles for the rough (uncompressed)  $W_0$  and  $W_2$  samples were  $110.0 \pm 1.9^\circ$  and  $106.4 \pm 2.1^\circ$ , respectively, and for compressed surfaces samples,  $W_0$  and  $W_2$ , were  $108.0 \pm 0.9^\circ$  and  $105.7 \pm 1.1^\circ$ , respectively. Compared with the dynamic values listed in Table 15, static angles are approximate  $5^\circ$  lower. This is consistent with, and in most cases substantially better than, reported comparisons using these techniques.<sup>130-132</sup>

Kwok *et al.* have reported on an examination of published static contact angle data.<sup>133</sup> They propose a method for making static measurements involving the addition of the tested liquid to sessile drops to achieve a constant advancing angle, which they claim is appropriate for gauging surface energies. The fact that our surfaces possess inherent roughness greater than the 1 nm limit they propose as a cutoff required for thermodynamic measures of contact angle, we do not make such claims. Our focus is on the propagation of the wetting line on modified surfaces, which impacts fields such as superhydrophobicity. However, by adopting their approach, static (advancing) contact angle measurements were approximately  $2^\circ$  higher for all samples. Still no

major changes in the wetting behavior were evident. From this analysis, it appears that dynamic measurements using a coated Wilhelmy plate are more sensitive to the impact of topology and chemical changes on wetting.

In summary, it was shown that the dynamic contact angle of water changes for paraffin wax surfaces as crystallinity changes. Local changes in roughness and crystallinity were characterized using AFM and Raman confocal microscopy. It appears that the anomalous wetting behavior characterized by a stable advancing contact angle and sharply decreasing receding angle are due primarily to the chemical modifications occurring for sample surfaces. Specifically, our results indicate a greater and more disperse concentration of hydrophilic area (defects) accompanies its decrease in crystallinity. These regions preferentially pin the receding movement of the contact line while its advancement is relatively uninhibited, producing an asymmetric change in the contact angle hysteresis. It can be argued based on the data presented that the mechanism proposed is mutually exclusive from the influence of surface roughness and their coupling tempers the observed effect.

### ***3.10 Mechanical Pinning of Liquids through Inelastic Wetting Ridge Formation on Thermally Stripped Acrylic Polymers***

Wetting and spreading phenomena are ubiquitous in nature and are of key importance for many applications including oil recovery, pesticide deposition, microfluidics and nanoprinting.<sup>84,85,134-136</sup> Viscous dissipation within a liquid tends to be the primary impedance to wetting, inhibiting attainment of an equilibrium contact angle at the three-phase line.<sup>137</sup> However for soft materials, inelastic deformation of the substrate induced by the vertical component of the liquid's surface tension force can contribute by lifting a ridge that must be propagated for wetting to proceed.<sup>139,139</sup> In this paper we demonstrate through the use of a novel soft polymeric solid that sufficient energy can be dissipated in the formation of this wetting ridge to arrest the progression of the liquid front. This pinning of the three-phase line is primarily a mechanical phenomenon, and it produces rather anomalous behavior including the arbitrary selection of a contact angle in sessile drops and the imparting of regularly-spaced ridge structures on the polymer surface in force wetting. Formed ridges are clearly visible and reveal a hierarchical apex structure where a cutoff area is used in theoretical treatment to avoid a singularity. Recently, there is considerable interest in the control of wetting through alterations in surface micro-/nanostructure or chemical composition.<sup>140-144</sup> Results reported here emphasize that in addition to these modifications, the surface deformation plays a critical role in determining wetting behavior for soft materials, providing new insight into controlled wetting. It also indicates novel applications such as nanofabrication for soft polymers and a greater understanding of wetting and adhesion involving ultra-soft solids such as biological tissues.

### **Experimental Section**

The acrylic thermoplastic was synthesized and processed at Franklin International Company (Columbus, OH). The dynamic contact angle measurements were performed following the Wilhelmy plate method using a Kruss Model K100 tensiometer (Hamburg, Germany). A film of approximately 0.2-0.5 mm thick was formed by dipping a heated steel plate (20mm x 20mm x 0.2 mm) into a bulk sample of the polymer. The film was then smoothed with a heat gun.



Coated plates were immersed in deionized water purified to 18 M $\Omega$  cm with Type II Laboratory SpectraPure Water System (Tempe, AZ) at a velocity of 0.2 mm/minute. Force data were collected for every 0.04 mm of plate displacement. Surface tension measurements were made on the water prior and subsequent to the measurement to insure no contamination. Images of the wetting ridge were obtained by repeating the previously described procedure with a plate that was coated with 50Å of platinum prior to testing. Upon completion of the experiments, the plates were stored in a dry ice box and optical profilometry was then performed within three hours using a Veeco Wyko NT1100 Optical Profiler (Edina, MN).

## Results and Discussion

The material of focus is an acrylic pressure sensitive adhesive developed for wound binding applications. It is generated via solvent polymerization primarily from the monomer 2-ethylhexyl acrylate with much lesser amounts of amide and vinyl aromatic comonomers. The synthesis product is subjected to additional unit operations to strip the solvent, residual monomers and other additives. The polymer has a glass transition temperature of less than -50 °C and at room temperature possesses a Young's modulus in the range of 10 to 100 kPa, similar to that of hydrogels and biological tissues. The observation that water placed on its surface could not easily be removed, even with vigorous shaking, initiated the interest in wetting behavior of this material. This unusual ability halt the motion of water is demonstrated in Figure 50. The images Figs. 50a – 50d follow the evaporation of 5  $\mu$ L sessile drop placed on a thin film of the polymer. The drop forms a circular interface on the polymer surface with a diameter of approximately 2 mm. As the water evaporates under ambient conditions, drop volume is reduced but the diameter of the circular interface remains fixed allowing the contact angle to decrease to 0°. Upon complete evaporation, the drop leaves behind a clearly visible circular pattern with a diameter equal to that of the initial drop (Fig. 50e). By reversing this process by adding water to the drop through a syringe (Figs. 51a through 51c), an apparent contact angle in excess of 150° can be achieved. The use of smaller starting drop sizes (e.g., < 5  $\mu$ L) was necessary to obtain an apparent angle of greater than 160°. Attainment of higher angles is prevented by the collapse of the meniscus under the weight of the supported liquid, which establishes a new wetting line.

A finite contact angle results from the balancing of surface tension forces along the lines of intersection for the contacted phases. This horizontal force balance is described by Young's equation, i.e.,  $\gamma_{sv} = \gamma_{sl} + \gamma_{lv} \cos\theta_0$ , for which  $\gamma_{ij}$  is the interfacial tension for solid (s), liquid (l) and vapor (v) interfaces and  $\theta_0$  is the equilibrium contact angle. Balancing of the vertical force components indicates a load on the substrate about the three-phase line.<sup>83</sup> S. Herminghaus's work showed that the lateral distribution of normal forces exerted onto a flat surface in a range of 50  $\mu$ m.<sup>145</sup> It is a well-established phenomenon that when a liquid is placed on a soft solid, such as those composed of polymeric materials, a ridge forms and propagates with the wetting front inducing a strain cycle in the substrate.<sup>138,139</sup> This ridge is usually quite small and if the material demonstrates predominantly elastic behavior, it has little influence on the motion of the three-phase line, but for materials which are viscoelastic, dissipation of a portion of the strain energy produces a frictional force that resists wetting. This force is the dominant impedance at low velocities and must be compensated for by the spreading force generated from the capillary imbalance to allow the wetting line to advance or recede.

The capillary free energy release rate that drives the three-phase line under nonequilibrium conditions (i.e.,  $\theta_t \neq \theta_0$ ) is  $\gamma_{lv}U[\cos \theta_0 - \cos \theta_t]$ , where  $U$  is the velocity of the three-phase line. Several publications have demonstrated a friction effect of the wetting ridge on soft surfaces.<sup>139,140,146-149</sup> Resistance provided by the moving of the wetting ridge with the three phase line, has been theoretically estimated to be  $(\Delta\gamma_{lv}^2/2\pi G\varepsilon)U$  where  $\Delta$  is the fraction of the energy dissipated due to irreversible processes (i.e., molecular chain motion),  $G$  is the shear modulus of the substrate and  $\varepsilon$  is a parameter introduced in the theoretical treatment to avoid a singularity and considered an estimate for the thickness of the three-phase line<sup>16</sup>. Wetting requires that the capillary free energy should be sufficient to overcome the energy dissipated by ridge propagation. Otherwise, the ridge motion will be arrested, pinning the three-phase line. The system studied here uses a pressure sensitive adhesive substrate, which designed to readily dissipate energy. Estimate  $\Delta=0.1$ ,  $\theta_0=90^\circ$ ,  $\theta_t=180^\circ$  and  $\varepsilon=5$  nm, the requirement for moving the ridge is that  $G \geq 230$  kPa. It appears that the capillary free-energy is insufficient to induce motion of the wetting ridge. Spreading is observed to occur only as a result of the collapse of the drop.

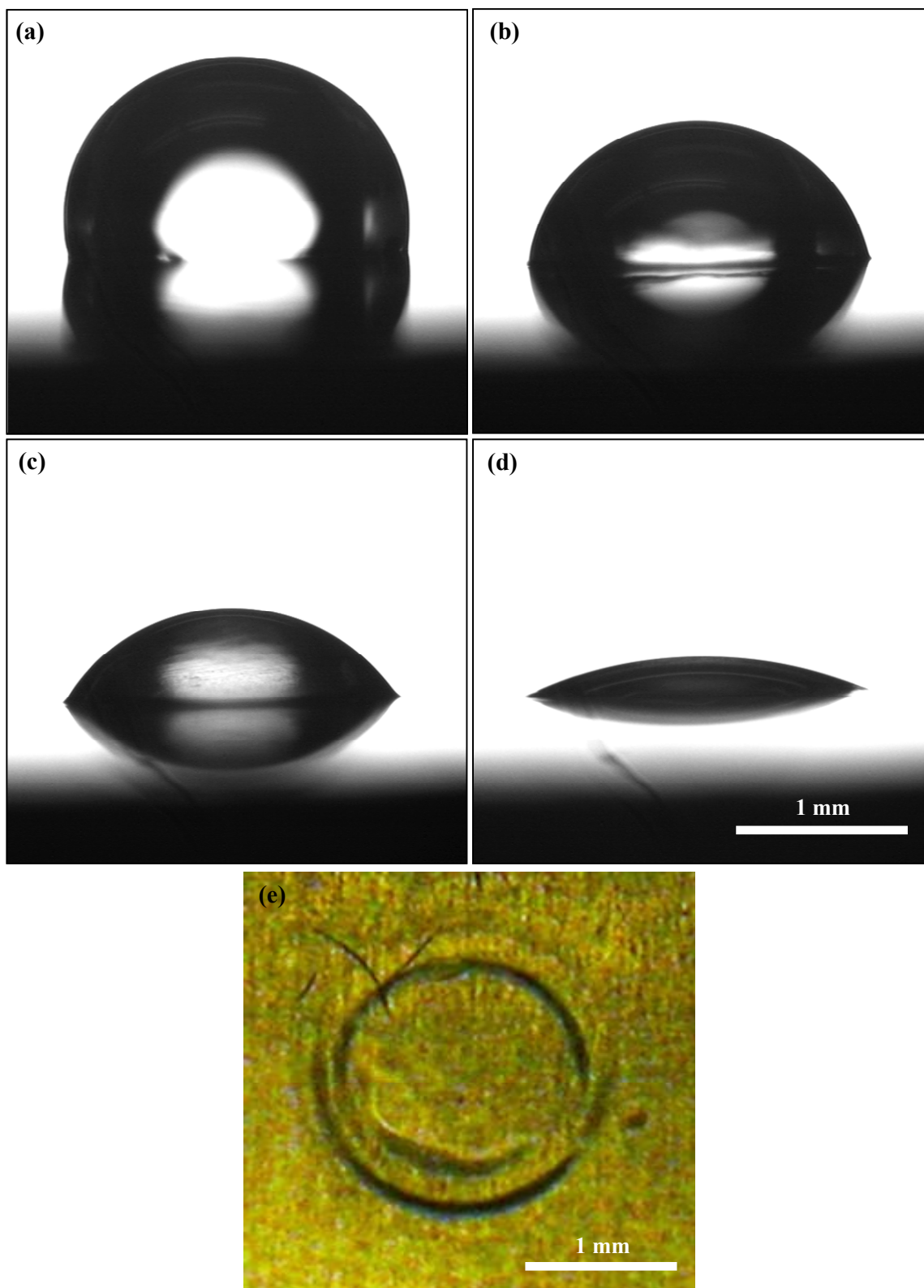


**Figure 50.** The progression of the evaporation for a 5  $\mu\text{L}$  sessile water drop placed on the surface of the polymer film (a through d), and an optical microscopy image showing the residual ring structure on film after the drop has completely evaporated.

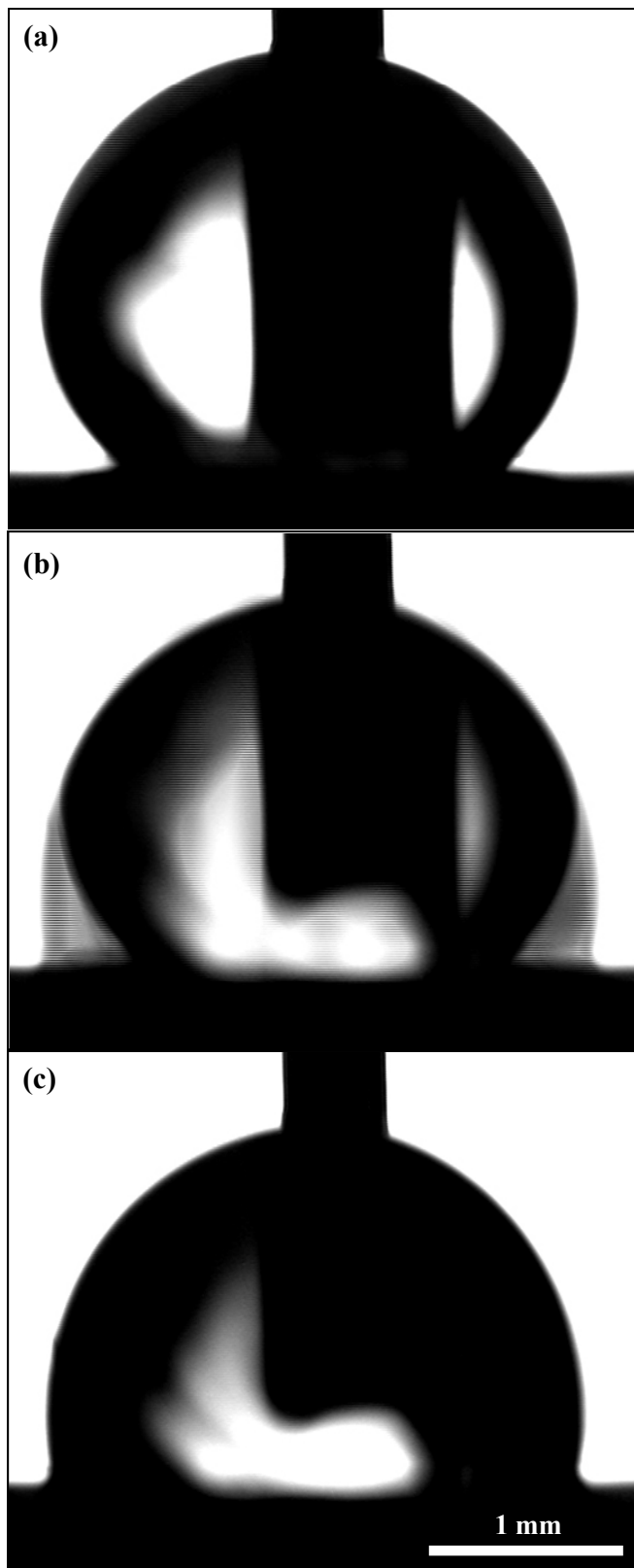


**Figure 51.** The addition of water to the sessile drop (a) eventually resulting in the collapse of the meniscus (b) and establishment of a new wetting line (c).

Greater insight can be gleaned from this system by examining it using the Wilhelmy plate technique. Here a metal plate coated with the polymer is submerged into water at a velocity of 0.2 mm/minute. Figure 52a is an optical image of the wetting ridge pattern formed during an advancing dynamic contact angle measurement. A series of parallel ridges with average width of 0.4 mm at 1 mm intervals can be seen on the lower portion of the polymer coated plate (i.e., the section submerged into the water) while the upper, unsubmerged portion of the plate shows no deformation. These ridges gradually smoothed and disappeared within several days. The ridgelines reproduce the three-phase line profile crossing the plate. Numerous air bubbles with diameters of less than 100  $\mu\text{m}$  are visible along the ridgelines. These are formed minutes after the plate is immersed and cannot be formed by simply soaking the plate in water for the same time period. Figure 52b is the corresponding variation of the force-displacement diagram for the plate shown in figure 52a. The abrupt changes of the force curve display a quasi-periodic variation with a period similar to the separation distance between the wetting ridges in figure 52a and the number of peaks in the force match the number of ridges found on the plate. The adsorption of water effect was also examined by soaking the adhesive plate in water for 8 hours before the advancing experiments. The results showed the force-displacement still exhibited a periodic pattern. The adhesive coated on a cylinder glass surface and sessile drop experiments confirmed such behavior was not caused by the potential defects at the plate edge. The same behavior was also observed after the surface energy of the polymer was modified with 50 $\text{\AA}$  of platinum to enhance their optical properties for imaging. The observed mechanism differs from that responsible for the formation of regular patterns from evaporating polymers solutions<sup>147-151</sup> and colloidal suspensions.<sup>152-156</sup> In these systems, an outward liquid flux forms to compensate the maximum rate of evaporation near the contact line. This transports the dissolved or suspended materials into the border region where it concentrates and then precipitates or aggregates forming an elevated ridge. Here, the polymer is highly insoluble and has been stripped of components they may be leached into the aqueous phase. Coating of the polymer with platinum further inhibits the loss of mass. It is the viscoelastic nature of the polymer rather than its solubility that governs the ridge building mechanism.

The fact that wetting ridges are visible on the surface of the polymer is evidence of significant dissipation of strain energy consistent with the pinning assertion. The resulting deformation allows for the imaging of the wetting ridges via optical profilometry. Figure 53 shows an optical profilometry image of one completely wetting ridge (Fig. 53a) and its topological details (Fig. 53b). The ridge has a height of 6  $\mu\text{m}$  and a width of 400  $\mu\text{m}$ . The height  $h(x)$  of the wetting ridge while in contact with a wetting liquid reportedly decays logarithmically in the direction perpendicular from the three-phase line<sup>138</sup>, i.e.,

$$h(x) \approx \frac{\gamma_{lv} \sin \theta_0}{2\pi G} \ln\left(\frac{d}{x}\right), x > \varepsilon \quad (7)$$

where  $d$  is the maximum deformation distance of the ridge. Equation 7 provides an approximate fit of the ridge shape from Fig. 53. Variation from this model may be attributable to the relaxation of the film, which is clearly apparent after a longer time period (e.g., days). The time

between two peaks for the wetting experiment here is about 6 minutes. Also, the derivation of Eq. 7 assumes elastic behavior. The adhesive polymer discussed here is quite soft, so the final

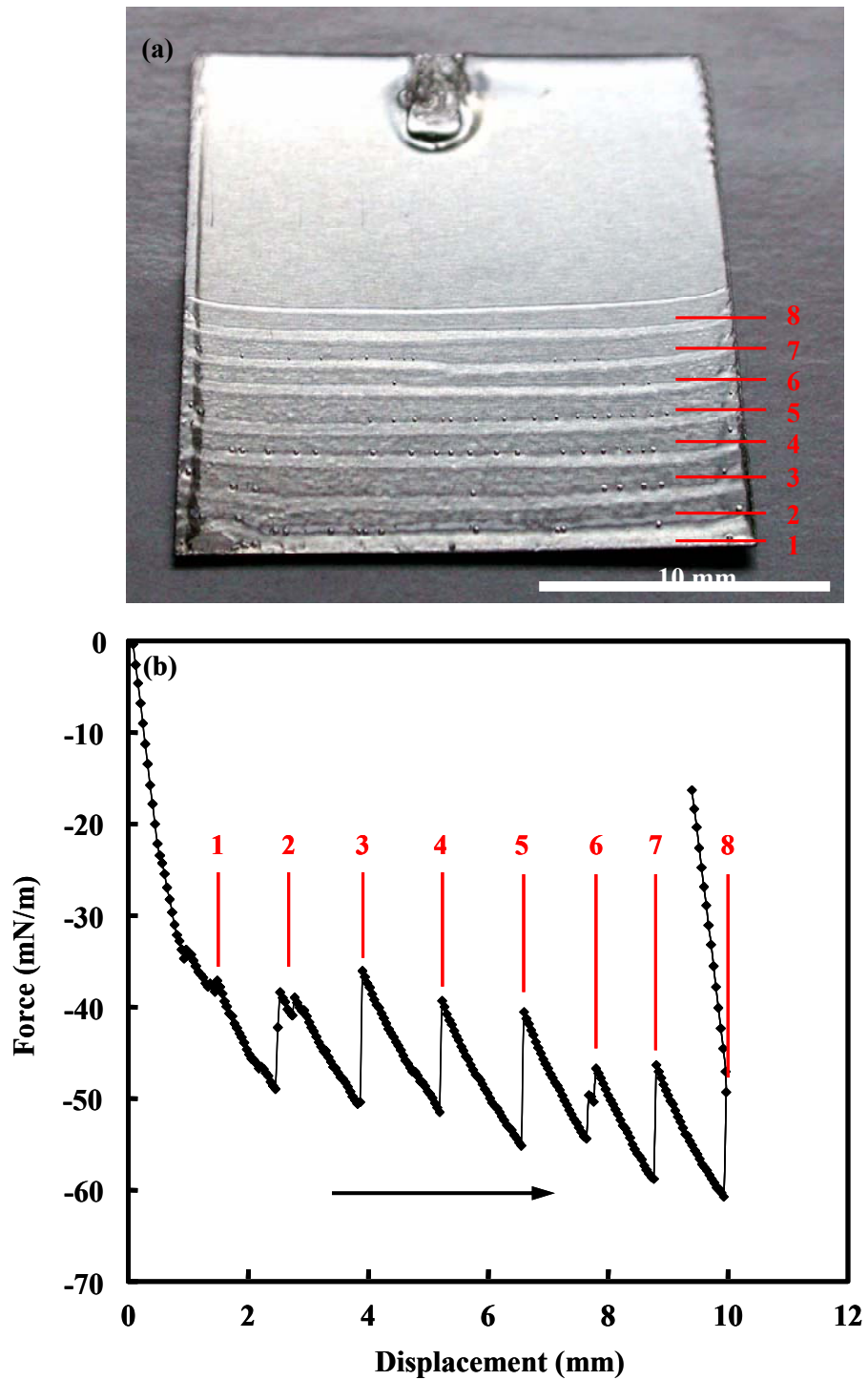


**Figure 52.** The wetting ridge pattern formed on the coated plate during advancing (a). and the corresponding force-displacement curve (b). (The numbers indicate the corresponding wetting ridges and force peaks.)

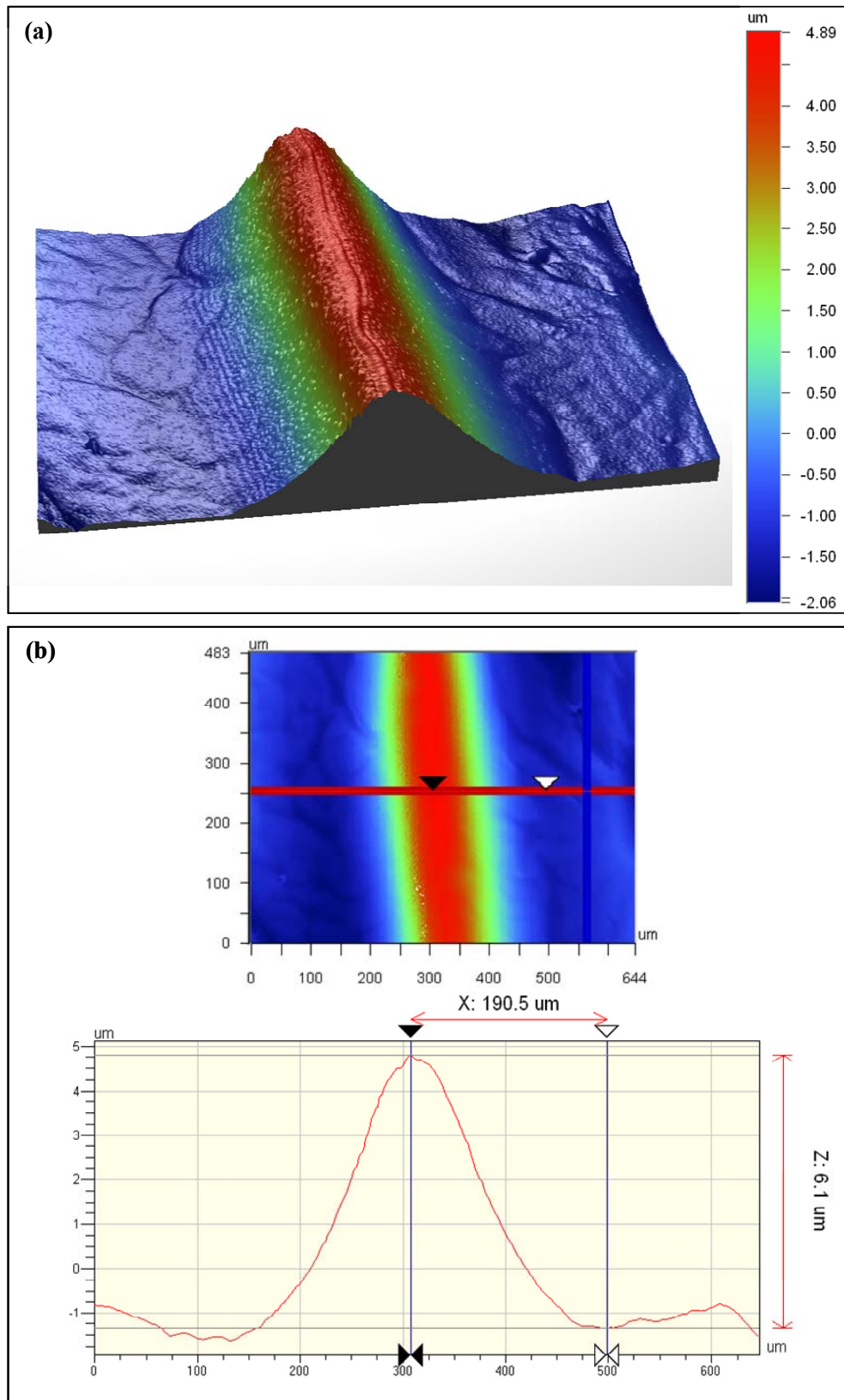


**Figure 53.** Optical profilometry image of a single wetting ridge formed on the plate during dynamic wetting experiments (a) and its topological details (b).

shape of the ridge is likely a result of significant plastic deformation. In addition to wetting speed used here (0.2 mm/min.), a series of advancing speeds ranging from 0.1 mm/min. up to 400 mm/min. were used in experiments. The data (not shown) demonstrate that the amplitude of the deformations and distance between formed ridge structures decrease with increasing wetting speeds, consistent with the proposed mechanism. When the advancing speed exceeds 20 mm/min., the force-displacement curve became smooth, and no regular pattern could be distinguished on the polymer coated plate under optical observation. Of interest from the image is the fine structure centered on the ridge peak. A small rise, 200 nm in height and 20  $\mu\text{m}$  in width, can be clearly distinguished, which was found for all of the wetting ridges imaged. From Eq. 7, this region appears to be of the dimensions consistent with the cutoff distance,  $\epsilon$ . To our knowledge, it is the first directly experimental evidence to show the hierarchical structure of wetting ridge. This region retains evidence of the vertical force placed on a wetting substrate by surface tension forces, information previously only inferred from spreading behavior.

### Summary and Conclusions

In summary, unique wetting behavior not previously reported has been described. The results indicate that the specially processed thermoplastic acrylic polymer possesses the plastic deformation ability to form wetting ridges, which are 2 scales higher than those previously reported.<sup>97</sup> This completely binds the advancement of the three-phase line for water to distinguish its wetting behavior from that of other soft materials such as rubber and elastomers. Ridge structures remain subsequent to the removal of water from the polymer surface and possess apex microstructures. For sessile drops, this deformation manifests itself as changes in the contact angle as the drop volume is reduced or increased. Metastable angles of 0 to 180° are possible, with the higher angles requiring the elimination of the influence of gravitational forces. Advancement requires that the mass of liquid at the wetting front become too large to be supported by the meniscus, and the drop breaks and flows to establish a new three-phase line. This “stick and break” mechanism appears different from the previously reported “stick and slip” motion of a three-phase line, in which the three-phase line is distorted by the presence of topological defects or chemical heterogeneities.<sup>90-95,100,157,158</sup>

Figure 54 presents a cartoon depicting the dynamic wetting behavior for water on the acrylic polymer. The spatial patterns of the wetting ridges and frequency of the force curves correspond in dynamic wetting. It appears that the three-phase line becomes pinned as it forms, and upon advancing the plate into the liquid, the measured surface tension force, which is a negative force resisting this motion, increases steadily until the liquid front breaks and flows. The force-displacement curves in the receding stage are relatively smooth at all speeds, and no deformation to the polymer surface was observed. Furthermore, the ridge structure produced during advancing appears unchanged by the receding process and does not influence the receding measurements. It is reasonable that no deformation is found for the receding liquid. As shown in Fig. 50, the receding angle for the sessile drop is 0°, which provides no vertical force component at the 3-phase line. It is also possible that that recession occurs over a thin liquid film that is acted upon by the vertical forces, rather than the polymer.



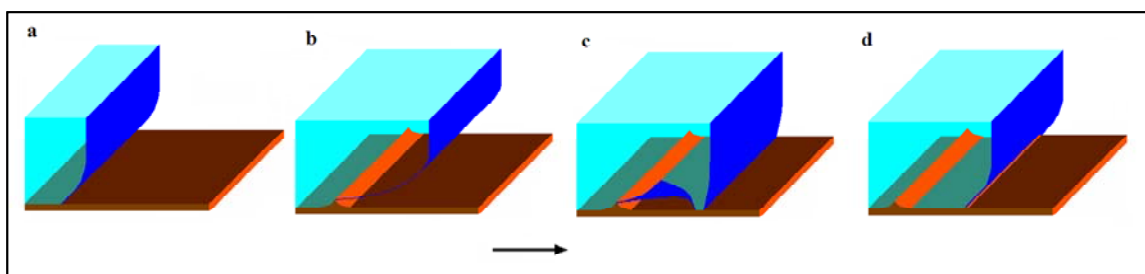
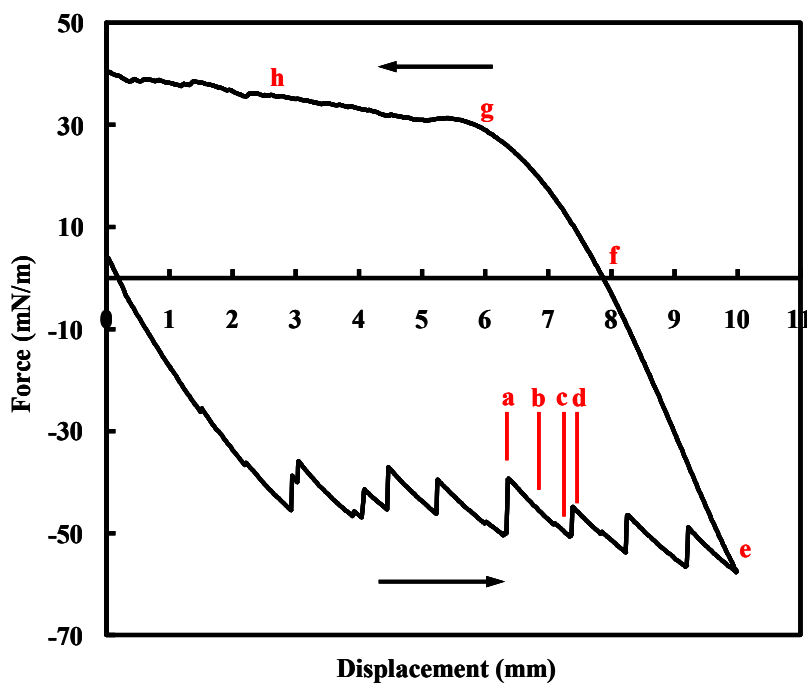


**Figure 54.** (Top) Force-displacement curve for a complete wetting-dewetting cycle obtained at the speed of 0.15 mm/minute. The advancing process has been discussed in the text. The curve for the receding portion of the cycle is found after a long transition in which the contact angle is decreased to  $90^\circ$  (e to f). Unlike the quasi-periodic behavior found during advancing portion of the force-displacement cycle, the receding portion of the curve is relatively smooth demonstrating that this process it is not influenced by the deformation pattern left by the advancing liquid. (Bottom) Schematic cartoons describing the proposed wetting-dewetting behavior of water on the acrylic adhesive substrate. Letters a to d correspond to points marked on the force-displacement curve. The region bracketed by a through d isolate one cycle in the “stick-break” mechanism described in the text. This includes the formation of a new three-phase line following the previous break (a); the formation of a micron-scale ridge, which prevents the advancement of the three-phase-line accounting for the continuous increase in the observed contact angle (b); The eventual collapse of the meniscus region when the weight of the supported liquid becomes too large (i.e., the liquid front breaks) (c); and the establishment of a new three-phase-line about 1 mm in front of the previous line where the process begins again (d).

### 3.11 Characterization of Dynamic Stick-and-Break Wetting Behavior for various Liquids on the Surface of a Highly Viscoelastic Polymer

The dynamic wetting of a solid surface by a liquid is a common phenomenon, which is of great importance for various technological applications. A key issue when wetting a substrate is the energy dissipation of the moving contact line. Theories describing the dissipation of capillary energy have been proposed for both large and small length scales. For example, a treatment by Yarnold, Cherry and Blake, sometimes referred to as the chemical approach, considers molecular scale processes in the immediate vicinity of the wetting line.<sup>159-161</sup> Energy dissipation results from the change in free energy associated with the repositioning of molecules from the liquid to vapor side of the three-phase line. The hydrodynamic model proposed by de Gennes *et al.* associates energy dissipation with the viscous flow in the overall liquid body.<sup>85,137</sup> Both models fit experimental data reasonably well and most likely prevail under different circumstances.<sup>85,137,159-164</sup> When considering soft materials, another source of energy dissipation during wetting is the deformation of the substrate. The ability of the vertical force component acting at the three-phase line to deform a soft surface (see Fig. 55) is a well documented phenomenon.<sup>83,165,166,138</sup> The height of such a ridge,  $h$ , is estimated to be a function of the liquid surface tension,  $\gamma_v$ , the contact angle,  $\theta$ , as well as the substrate's shear modulus,<sup>138</sup>  $G$ , i.e.,

$$h = \gamma_v \sin \theta(t) / G \quad (8)$$

As the wetting line is driven by the capillary force towards an equilibrium contact angle, the ridge must also be propagated. This induces a strain cycle in the substrate as the liquid front moves past. For purely elastic materials, this would not offer any resistance to wetting. However, for viscoelastic substrates, dissipation of energy during this deformation creates friction that can slow the movement of the contact line. This phenomenon, commonly referred to as “viscoelastic braking”, has been described in detail by Shanahan *et al.*<sup>138,139,166</sup> A model, in which all three of the above mentioned energy dissipation mechanisms have been combined has been proposed to explain the different time scale behaviors in dynamics of the wetting process.<sup>167,168</sup>

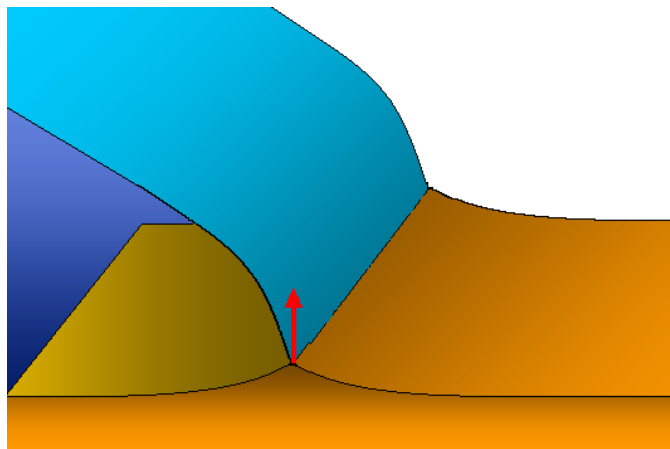


**Figure 55.** Schematic representation of a viscoelastic film being deformed by the vertical force component due to the surface tension of the liquid.

In a previous publication, an acrylic polymeric substrate was introduced for which the energy dissipation due to ridge formation is substantial enough to completely inhibit the progression of water.<sup>97</sup> The formed ridges are 2 orders of magnitude taller than those described previously and remain on the polymer surface for several hours. These structures retain significant detail including the hierarchical apex structure where a cutoff area is used in theoretical treatment to avoid a singularity. It is argued that these observations are consistent with the dominance of the viscoelastic properties of the substrate in determining wetting behavior. The results are not only curious as a wetting phenomenon, but they may provide insight on adhesion and wetting in biological systems. Cellular adhesion is analogous to the wetting of polymer films by complex fluids. The vertical force of the contact line is within the range of typical cell adhesion forces, which governs many cell activities.<sup>145,169</sup> The deformation of the matrix caused by surface tension and the corresponding influence on the liquid movement also has practical importance in microfluidic applications. Much of the microfluidic systems studied involve non-rigid matrices such as poly(dimethylsiloxane), silicone rubber or self-assembled monolayers.<sup>170-173</sup> Yang *et al.* demonstrated that the strong capillary forces can produce a local collapse of the upper walls of the parylene channels to decrease the cross sectional area and the advancing velocity.<sup>174</sup> Also, the formation of nano-scale ridge structures may promote chaotic flow behavior inside the microchannels, which would critically impact microfluidic applications.<sup>175</sup>

In this paper, further characterization results for the dynamic wetting of the viscoelastic acrylic polymer are reported. A comparison is made between the behavior for water and other liquids such as paraffin oil. (The oil consists of low molecular weight, normal alkanes with properties that stand in stark contrast with those of water.) Table 16 lists the properties for water, the paraffin oil and other liquids tested from which it can be seen that they cover the spectrum of properties expected to be of significance to the wetting process. It will be shown that for all of the liquids at low and modest wetting speeds, ridge structures form at the three-phase line, which pin the contact line. Advancement of the line occurs as the mass of liquid at the wetting front becomes too large to be supported by the meniscus as was previously reported for water. It was proposed that this advancement mechanism described as “stick and break” is controlled primarily by the viscoelastic properties of the polymer film rather than the balance of surface tension forces at the three phase line. This argument is supported here using a range of wetting velocities in Wilhelmy plate experiments. The results of these tests are compared with a master curve for the loss and storage moduli of the polymer, which demonstrates the importance of the balance between viscous and elastic behavior in determining the extent to which deformation of the substrate influences wetting.

## **Experimental**

The acrylic thermoplastic was synthesized and processed at Franklin International (Columbus, OH). The dynamic contact angle measurements were performed with the Wilhelmy plate method using a Kruss Model K100 tensiometer (Hamburg, Germany) as described in detail elsewhere.<sup>97</sup> A film was formed by dipping a heated steel plate (20 mm x 20 mm x 0.2 mm) or glass plate (25 mm x 25 mm x 0.2 mm) into a bulk sample of the polymer. The film was then thinned and smoothed with a heat gun and reached a final thickness about 0.2-0.5 mm. Coated plates were immersed into deionized water purified to 18 M $\Omega$  cm with Type II Laboratory SpectraPure Water System (Tempe, AZ) at a various rates ranging from 0.1 to 400 mm/minute. Shape profiles of the wetting ridge were obtained by repeating the previously described

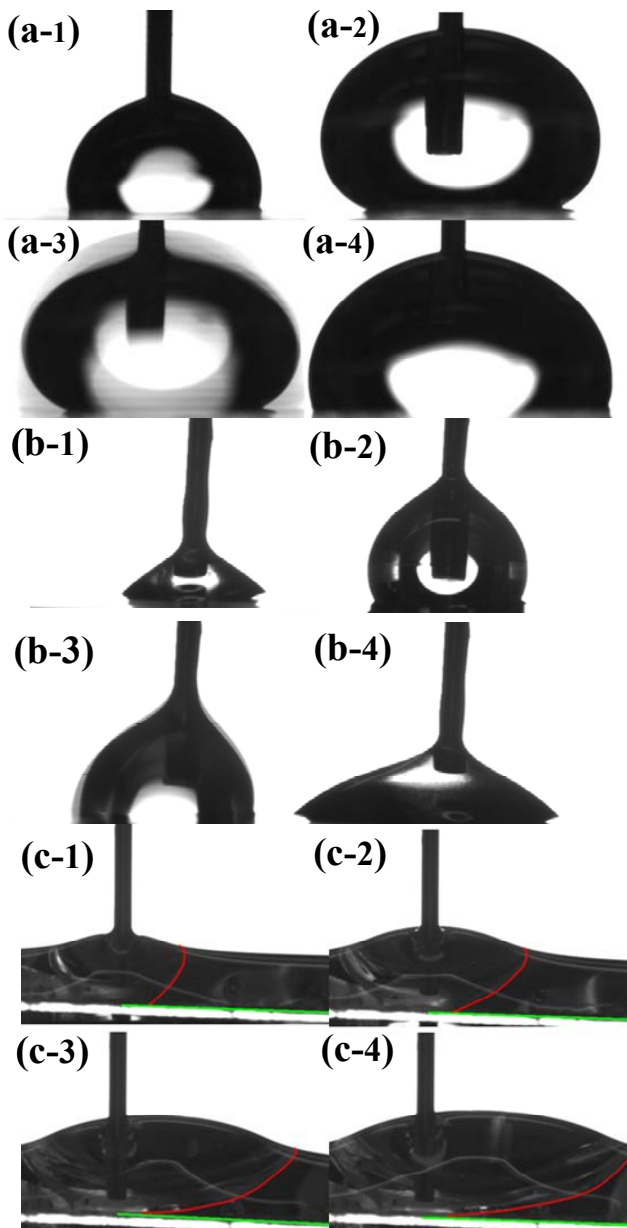
procedure with a plate that was coated with 50Å of platinum prior to testing. Upon completion of the experiments, the plates were stored in a dry ice box and the optical profilometry was then performed within three hours using a Veeco Wyko NT1100 Optical Profiler (Edina, MN). The formamide, ethylene glycol and glycerol were purchased from Mallinckrodt Chemicals (Philipsburg, NJ) with 99% purity. The paraffin oil was purchased from Fisher Scientific (Fair lawn, NJ). Force data were collected for every 0.04 mm of plate displacement. Dynamic mechanical analysis of acrylic Acrylic polymer film was carried out with an AR-2000 ex rheometer (TA instrument Ltd, Fleming Way, UK). Frequency sweeps ranged from 1 to 340 rad/s at a temperature ranging from -20 to 70 °C with a 0.1% strain. Digital pictures of coated plates were taken with a Nikon Coolpix 4500 digital camera immediately following wetting experiments.

## Results

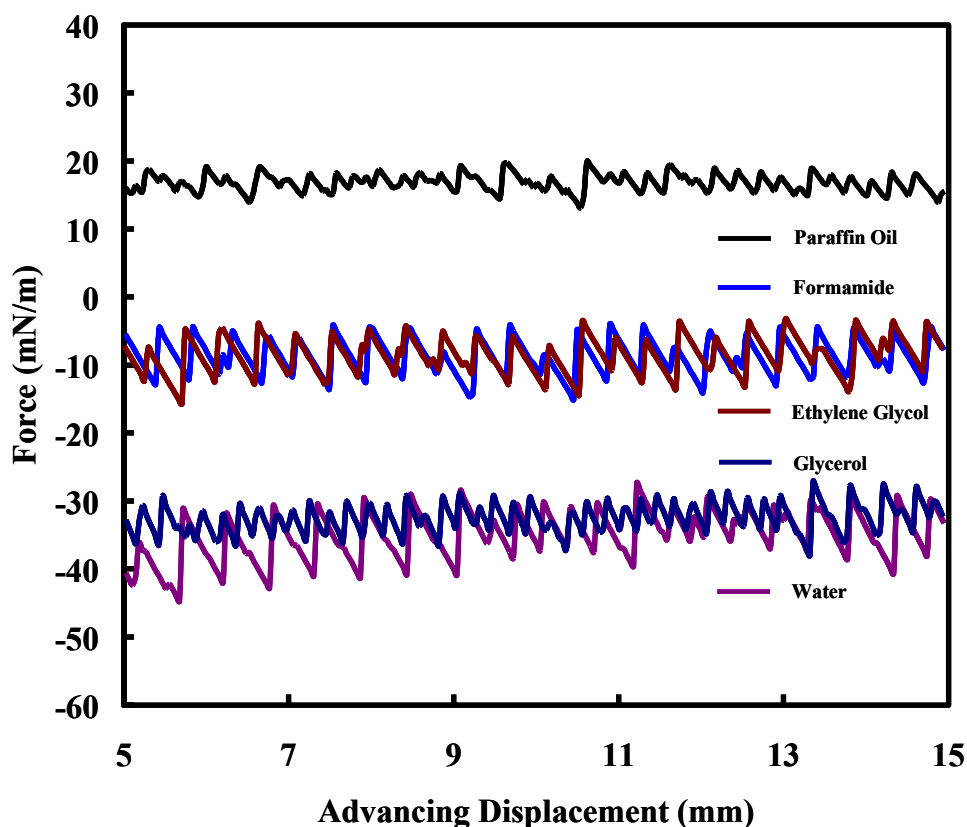
Figure 56a shows a sequence of frames from video recorded during the addition of water to a sessile drop formed on the surface of the acrylic polymer. It can be seen that the original contact line is maintained as the drop volume is slowly increased. Eventually, the drop collapses with the liquid from the top surface spilling around the outside of the contact line perimeter to establish a new wetting line. In other words, as liquid is added to the drop, which increases the contact angle from 100° to greater than 150°, the associated capillary forces are insufficient to propel the wetting line forward. The wetting line is pinned and advances only with the collapse of the meniscus under the weight of the supported liquid involving the establishment of a new wetting line with an angle again near 100°. Figure 56b shows a similar sequence of events for an increasing drop volume composed of paraffin oil. The contact angle increased from about 45° to 120° before the drop collapses and a new wetting line is established with a contact angle near its original value. The maximum angle achieved was found to be dependent on the rate at which the liquid is added, that is, increasing the rate decreased the maximum angle achievable. The idea that the drop collapses under its own weight can be supported by demonstrating that the drop can grown to a greater volume and contact angle by countering gravitational forces. In Fig. 56c the liquids are combined with the purpose of demonstrating the role of gravitational forces on the collapse of the drop. This sequence of frames shows the growth of a water sessile drop immersed in the paraffin oil. With the paraffin oil providing support for the drop via buoyancy, a contact angle in excess of 170° can be achieved.

Figure 57 shows the force-displacement curves for 5 liquids including water, glycerol, formamide, ethylene glycol and paraffin oil. The physical properties for the liquids are listed in Table 16. They range in surface tensions from 31 mN/m (paraffin oil) to 72.6 mN/m (water) and viscosities from 0.81 mPa·s (water) to 714 mPa·s (glycerol). The measurements were made at the same advancing rate (0.5 mm/minute). It can be seen that the force-displacement curves for all 5 liquids demonstrate the quasi-periodic, force-displacement variation pattern, which can be attributed to stick and break behavior. It was found that the pinning force or distance is not dependent on the initial contact angle. The water showed the highest change in force and distance to the re-establishment of a new wetting line while the change in glycerol and paraffin oil is substantially smaller. Formamide and ethylene glycol demonstrate nearly identical patterns. It is observed that during the “stick” stage, the contact line is pinned at the interface while the plate is immersed into water at a constant rate. The depth to which the meniscus is pulled beneath the level surface of the liquid corresponds to a linear increase in the capillary

force, which eventually reaches a maximum value. During the “break” stage, the meniscus collapses and a new contact line is established on the plate a finite distance behind the previous line. This corresponds to the abrupt drop in the force to the minimum value shown as a nearly vertical slope in the force-displacement curve. The collapse occurs on the millisecond time scale compared with the whole pinning process, which can take 10 or more minutes.



**Figure 56.** Sessile drop experiment for water (a), paraffin oil (b) and water surrounded by paraffin oil (c) on the acrylic polymer film. The sequence 1-4 follows the increasing drop volume.



**Figure 57.** The force-displacement curves for the liquids used in the Wilhelmy plate measurements. The advancing rate used for all liquids was 0.5 mm/minute.

**Table 16:** Physical properties of tested liquids

	Surface Tension (mN/m)	Density (g/cm <sup>3</sup> )	Viscosity (mPa•s)	Capillary Length (mm)	Kinetic Viscosity (mm <sup>2</sup> /s)
Water	72.5	1	0.809	2.72	0.809
Formamide	58.2	1.133	3.3	2.29	2.91
Ethylene glycol	48.3	1.109	16	2.11	14.43
Paraffin oil	31.1	0.83	170	1.96	204.82
Glycerol	63.4	1.263	714	2.26	565.32

Figure 58 shows images of the polymer-coated plates subsequent to wetting experiments at rates of 0.1 mm/min and 1 mm/min in water, Figs. 58a and 58b, respectively, and for the same advancing rates in the paraffin oil, Figs. 58c and 58d, respectively. The upper, smooth portions of the plates are the unwetted regions, which have measured RMS roughness ( $R_q$ ) values of about 60 nm. Periodic ridge patterns, enhanced by the added guides can be seen on the lower portions of the plates. Each ridge is associated with a rise and drop in the force displacement curve and thus a stick and break event. It can be seen that increasing the rate at which the plate is lowered into the water decreases the distance between ridges, i.e., stick and break events. This also decreases the size of the induced wetting ridge. The arrows indicate events where the

collapses of the wetting lines were incomplete. The collapse of the meniscus began at the right end of the plate and laterally spread to the left end. The spreading was stopped in the middle and formed a joint point of the three wetting ridge segments, and the curve for the upper ridge connecting with the old one had a logarithmic profile, such events increased with advancing rate. When the rate was greater than 20 mm/min, it became difficult to identify ridge patterns via optical imaging. Optical profilometry images of ridges on coated plates submerged in water show that the average height of the ridges decreased from  $7.6 \pm 1.4 \mu\text{m}$  at 0.5 mm/min to  $2.8 \pm 1.9 \mu\text{m}$  at 1 mm/min. The wetting experiments involving paraffin oil produced similar trends. However, for the same plate speeds, more ridges with smaller spacings were found consistent with more frequent stick and break events. The ridges also appear to be smaller, and at an advancing rate of 1 mm/min, ridges were difficult to distinguish.

To better discern the influence of interface speed on the wetting mechanism, a series of plate advancing rates ranging from 0.1 to 400 mm/min were investigated with water. Figure 59 shows the advancing force-displacement curves for water over 3 orders of magnitude in rate ranging from 0.1–100 mm/min. Three rate regions can be distinguished from the force-displacement curves. At the lowest immersion speed (0.1 mm/min), patterns characteristic of the stick and break motion were evident in the force-displacement curve and it aligned with an ordered ridge deformation pattern on the polymer-coated plate. For the intermediate speed (10 mm/min), the movement of the contact line is more complex. The pattern in the force-displacement curve has the same general shape as those found for the slower rates, but it appears to be composed of partial or disrupted events. This is consistent with the ridge structures found on the plate, which contains primarily partial collapse events involving the interconnection of wetting ridges. At the highest immersion speed (100 mm/min) both a smooth force-displacement curve and plate were obtained. However, it was difficult to determine whether this results from the formation of very tiny ridges that could be carried with the movement of the three-phase line, or the stick and break motion occurring at a high frequency. For the lowest advancing speeds there is some indication of at least a partial displacement of ridge structures. This can be seen in Fig. 60, which shows optical profilometry images for advancing rates of 0.1 mm/min and 0.5 mm/min, respectively. The ridge profile at 0.5 mm/min has height about  $8.5 \mu\text{m}$  and width about  $300 \mu\text{m}$  with a symmetric shape. At 0.1 mm/min, the ridge is significantly larger and has much deformation. It can also be seen that the asymmetry includes a steeper slope in front of the contact line and other signs that the ridge is being pulled in the horizontal as well as the vertical direction.

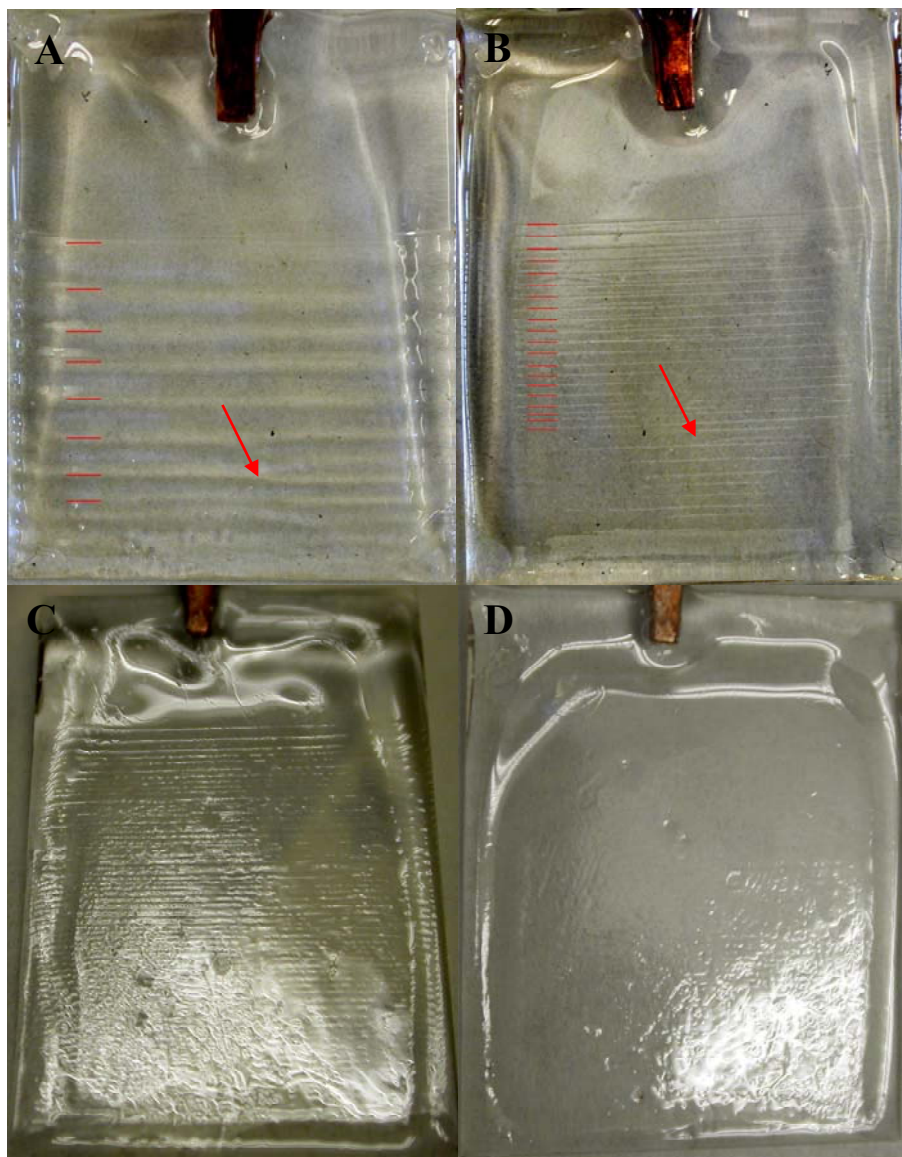


**Figure 58.** The wetting ridge patterns on the surface of the acrylic polymer film surface resulting for advancing rates of 0.1 mm/minute (a) and 1 mm/minute (b) with water and 0.1 mm/minute (c) and 1 mm/minute (d) with paraffin oil. Two incomplete meniscus collapse events (see text) are indicated by the circle and arrows.



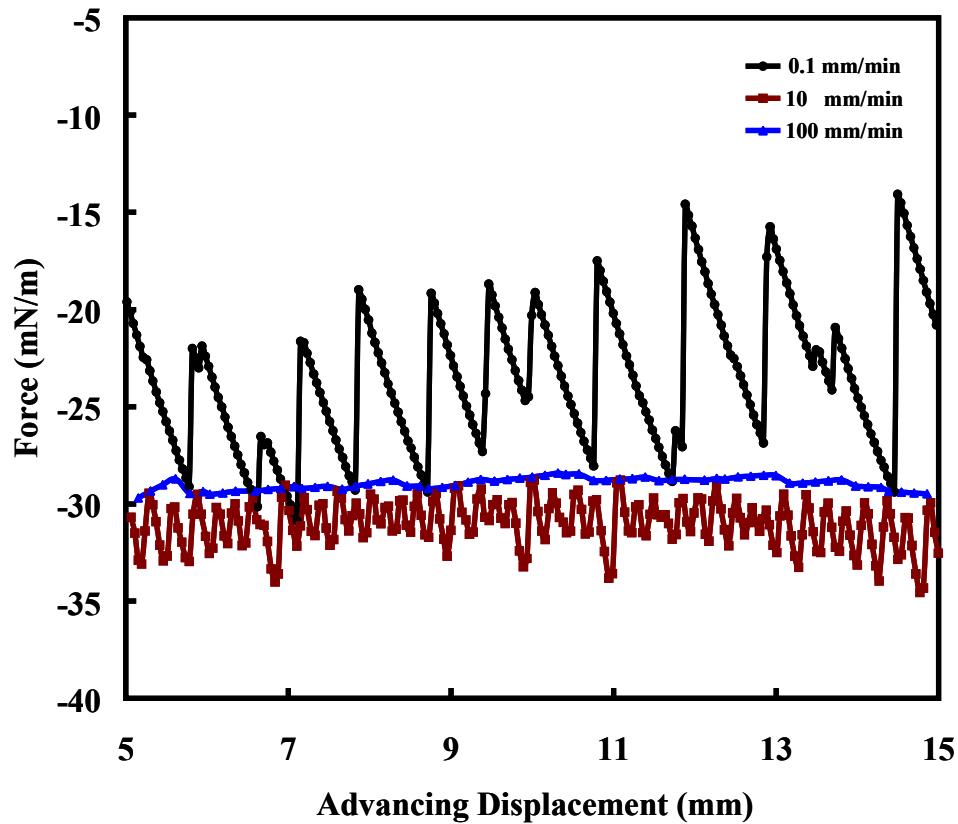


**Figure 59.** Force-displacement curves for the polymer coated plate in water for 3 advancing rates ranging from 0.1 to 100 mm/minute.

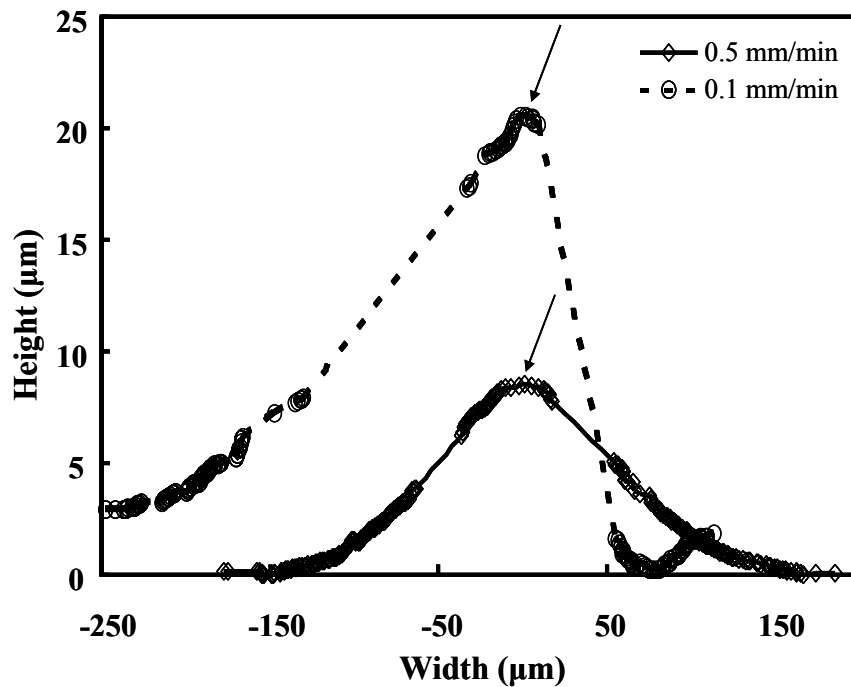


**Figure 60.** Optical profilometry profiles of wetting ridges produced on the polymer coated plate by water with advancing rates of 0.1 mm/minute and 0.5 mm/minute.

Relationships between the separation distance in wetting ridges (i.e., pinning distance), local maximum force resulting from a pinning event (i.e., pinning force), plate advancing rate and kinematic viscosity of liquids are shown in Fig. 61. The pinning force is linearly related to the pinning distance (Fig. 61a) with slopes that increase and plateau at similar values greater advancing rates. At the rate 0.1 mm/min, the slope of the best linear fit for the pinned distance and force was 12 mN/mm, and at rate 10 mm/min, the slope increased to 20 mN/mm. Figures 61b and 61c show the relationships between the average pinning distance and plate advancing rate (Fig. 61b) and pinning force and the advancing rate (Fig. 61c), respectively. Both curves fit a power law shape, dropping sharply in the low rate region and more gradually at higher advancing rates. Extracting these values became more difficult as the plate advancing rate increased through the transition region where the force-displacement curves became more chaotic and eventually vanished as the higher rates were achieved. Figure 61d shows the relationship between the maximum pinning distance and the liquid kinematic viscosity of the five liquids and mixtures of water/glycerol at an advancing rate of 0.5 mm/minute. (A similar correlation is found when viscosity is used.) The pinning distance decreases with increasing kinematic viscosity. It also could be seen from the Fig. 58 when compared the spacing between the water and paraffin oil at the same advancing rate. The glycerol provided the minimum pinning distance in our experiments.

Figure 62 shows the horizontal superposition of the modulus traces along the abscissa to produce the master curve using a reference temperature of 27 °C, both storage modulus  $G'$  and loss modulus  $G''$  are shown. Measurements were made for various temperatures ranging from -20 °C to 70 °C. The inset is the experimentally derived shift factors with the straight line denoting the Williams–Landel–Ferry (WLF) equation fit.<sup>176</sup> For viscoelastic materials under stress, its deformation responds both to the time (frequency here) and temperature. The WLF equation expresses a logarithmic relationship between the time and temperature. The time-temperature superposition principle of the master curve states that with viscoelastic materials, time and temperature are equivalent to the extent that data at one frequency can be superimposed on data at another frequency by shifting the curve along the temperature axis. Both the storage modulus  $G'$  and loss modulus  $G''$  increased with the increasing of frequency. It can be seen that the polymer demonstrates greater viscous behavior for frequencies lower than 0.5 rad/s, which is the approximate crossover point (i.e.,  $G'' = G'$ ), and greater elastic properties for frequencies above this.

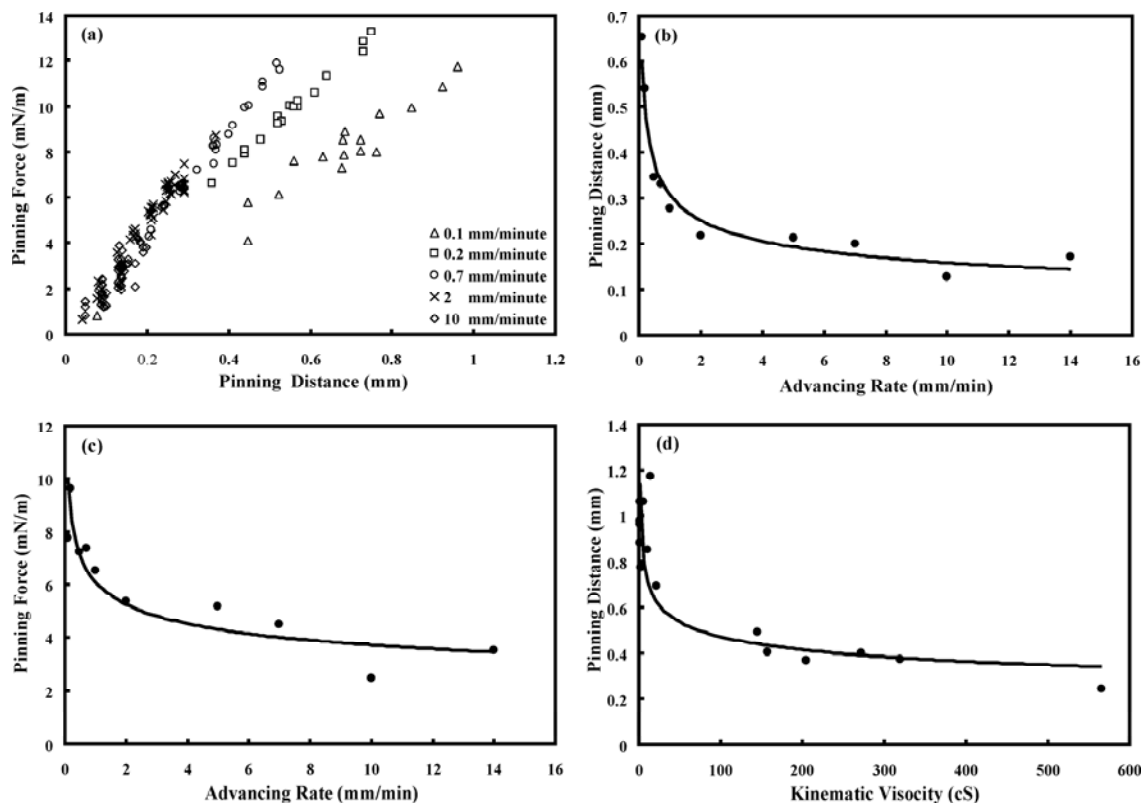


**Figure 61.** Relationships between the pinning force and pinning distance for water at various advancing rates (a), pinning distance and advancing rate for water (b), pinning force and advancing rate for water (c) and maximum pinning distance and kinematic viscosity for the various liquids measured at an advancing rate of 0.5 mm/minute (d).

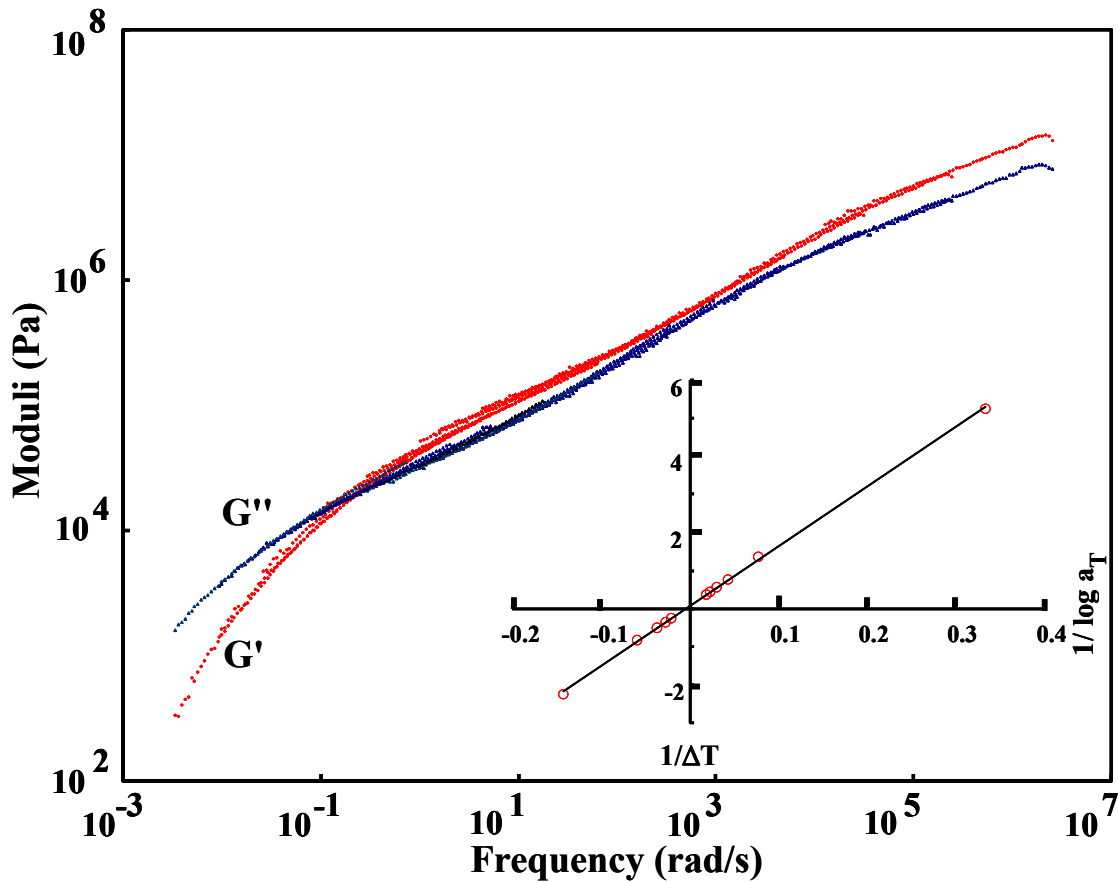


**Figure 62.** Master curve for the acrylic polymer at using a reference temperature of 27 °C. The insert shows the shift factors with the straight line denoting the WLF fit.

### Discussion

It is important at the onset to emphasize that the mechanism described above by which the wetting line progresses is distinctly different from the so called stick and jump motion, which has been studied extensively.<sup>89-92</sup> There, the halting of the contact line is induced via a heterogeneous surface possessing geometric roughness or chemical disorder. When a portion of the contact line meets these defects, it becomes pinned while those regions sufficiently distant continue to propagate. This bends and stretches the contact line accumulating capillary energy. Once a certain local contact angle is surpassed, which is associated with a threshold capillary force, the pinned region accelerates to catch up to the unfettered portions of the advancing wetting line. It has been demonstrated that the force variation between the external force and threshold de-pinning force has an exponent relationship with the average velocity of contact line,<sup>89</sup> i.e.,

$$U \propto (F - F_c)^\beta \quad (9)$$

where  $U$  is the global contact line velocity,  $F$  is the external force,  $F_c$  is the critical or threshold force require to free the pinned contact line regions and  $\beta$  is a universal constant with values that typically range from about 1 to 5. Thus defects on the wetting surface will slow the progression

of the wetting line, which will increase the advancing angle and decrease the receding angle. In addition to surface roughness and chemical heterogeneities, stick and jump behavior has been observed with the adsorption of liquid vapor or surfactant, destabilization of colloidal particles near the wetting line, and molecular rearrangement.<sup>95,100,177</sup>

In the case of the acrylic polymer discussed here, the pinning process does not appear to be caused by a regional defect that distorts part of contact line. It is clear that the pinning mechanism is not a result of a preexisting structure or heterogeneity. It comes about due to the interaction between the liquid and polymer surface. As mentioned above, Shanahan *et al.* have previously described the slowing of the three-phase line in the wetting of polymeric materials as viscoelastic braking.<sup>138,139</sup> In their work, it was assumed that the ridge travels with a continuously moving three-phase line producing a strain cycle as it progresses over a region of the surface. This process manifests itself as a frictional force that resists the spreading of the liquid. For low velocities, it is proposed that plastic deformation of the substrate dominates the energy dissipation; the extent to which is strongly dependent on the ratio between the polymer's loss and storage moduli. We have proposed that our results demonstrate an extreme example of this behavior involving the complete halting of the wetting line giving rise to the observed orderly series of wetting ridges.

For the Wilhelmy plate experiments using protic liquids, nonwetting conditions exist and the meniscus is curved towards the liquid. This results in the formation of a nose in front of the contact line and the advancing fluid undergoes a rolling type motion with the break step of its propagation. Stick and break behavior also occurred for the paraffin oil where wetting conditions exist and the meniscus is curve away from the liquid resulting in a wedge in front of the contact line. It is likely that the nose and wedge meniscus profile in front of the contact line result in different flow fields at the meniscus to dissipate the capillary energy,<sup>179</sup> yet this does not appear to affect wetting behavior. Thus, the observed behavior appears to be characteristic for the soft surface regardless of the interfacial energy, i.e., the surface tension of the liquid is not critical parameter in the stick and break behavior.

The incomplete wetting ridge profiles shown in Fig. 58 suggests that the collapsed might initially happened at one point and then advanced with a fast transverse wave along the contact line.<sup>180,181</sup> This is consistent with the dynamics proposed for the contact line motion at the micro-scale over individual hydrophobic posts, which would involve the wetting of one post of a succeeding dry row followed by a lateral propagation on either side of it to wet the entire row.<sup>182</sup> E. Saiz *et al.* examined the wetting of ceramic surfaces by liquid metals.<sup>183</sup> In this work, four time regimes were identified. When a ridge is quite small, it can be carried by a moving contact line. As the ridge grows rapidly compared with the spreading rate, the contact line will remain attached to the ridge and a sudden perturbation can cause the contact line to breakaway. An observation in the study of various liquids and wetting speeds is that the height of the wetting ridge deformation is related with the pinning distance before the meniscus collapse. This is consistent with the observed wetting of fabricated, hydrophobic surfaces. For example, studies have examined the wetting of hydrophobic surfaces composed of a series of posts of various geometries.<sup>81,129,142,184-186</sup> The controlled rearrangement of the posts allows the surface roughness to be systematically varied. The advancing contact angle on the post structure can be close to 180° consistent with the Cassie model for wetting and the drop will only advance when it is able to feel the

neighboring posts as the body force pulls the meniscus down. When the drop touches the corner of an adjacent post, it will suddenly jump onto the surface of that post and the contact angle relaxes to its minimum.<sup>186</sup> We speculate that in our experiments, the wetting ridges functioned in a fashion similar as the posts of a patterned surface. The difference is that the ridges are created by the vertical surface tension force at the three-phase line, so there is no succeeding ridge for the meniscus.

Variation in the extent to which stick and break motion is found appears most obviously to be related to the viscoelastic response of the acrylic polymer. It is observed that the maximum contact angle obtainable for a sessile drop on the polymer surface is dependent on the rate to which liquid volume is added. This is consistent with the idea that the once the ridge has grown too large to be propagated, the wetting line will not progress until the drop could not be supported by the capillary forces. In the case of the Wilhelmy plate experiments, repetition of this scenario is what produces the periodic ridge structure on the polymer coated plate. It is interesting that a similar type periodic structure is sometimes observed in peel tests involving the removal of a PSA film backed by a flexible substrate from a metal surface. This is most commonly found at low peel rates and/or high temperatures. When observed, the failure surface exhibits a quasi-periodic pattern of polymeric residue stripes, which corresponds to a saw-tooth curve for the peel force versus displacement. The distance between residue stripes and frequency of the saw-tooth force-displacement curves decreases with increasing peeling rate.<sup>187</sup>

Given the similarities between the wetting process and peel testing of adhesive polymers, we adopt a relationship between peel speed,  $v$ , and the dynamic frequency of the deformation experienced in the rupture zone,  $\omega$ ,

$$\omega = 2\pi v/\Delta \quad (10)$$

where  $\Delta$  is the deformation thickness of the polymer film.<sup>188,189</sup> If we assume this relationship holds for wetting,  $v$  is the advancing rate of the contact line. For a supported elastomer film during wetting, viscoelastic deformation is observed for thicknesses greater than about 70  $\mu\text{m}$ .<sup>190</sup> Given that viscoelastic behavior is observed in the acrylic films during wetting, a deformation thickness of 100  $\mu\text{m}$  was assumed. With this value, dynamic frequencies calculated from Eq. 10 for wetting experiments ranged from 0.1 to 400 rad/s. From the master curve (Fig. 61), this range includes the crossover point between viscous and elastic behavior. At the 0.1 rad/s, the values for the storage modulus ( $G'$ ) and loss modulus ( $G''$ ) were about 12 and 14 kPa, respectively, while at 400 rad/s, these values are about 500 and 450 kPa, respectively. The fractional energy dissipation decreases with the increasing ratio of  $G''/G'$  for the polymer.<sup>138,139</sup> It would be expected that the size of the ridge deformation and the fractional energy dissipation will decrease as the advancing rate increases due to the greater stiffness and elasticity of the polymer substrate. This is consistent with the results presented here; increasing the advancing speed diminishes the pinning effect, which is caused by the energy loss during viscoelastic deformation. It is worth mentioning that Extrand and others have observed that as the speed at which a drop moves across a polymer surface increases, there is less impedance to its motion.<sup>191</sup>

In addition to the change in the ridge height and the extent to which the three-phase line is pinned, the viscoelastic nature of the acrylic coating can be seen in the shape of the ridge. Figure

60 shows the ridge formed for 2 different advancing rates with water. It would appear that the wetting line has displaced the pinnacle of the ridge some distance for 0.1 mm/min. For the slower wetting speeds, the ridge is under the force of the wetting line for a longer period of time, in this case about 10 times longer. With the highly viscoelastic acrylic polymer, the higher ridge height is expected, and given that the contact angle is pushed to greater values with the pinning of the three-phase line, the modification to the ridge shape is not surprising. A more quantitative demonstration of this effect can be found in Fig. 61a showing changes in the slope of the force-displacement curve with increasing advancing rates. (The slopes of these lines increase and plateau.) The recorded force change is the parallel force component of the liquid surface tension, which increases in a monotonic fashion with meniscus depth. The height of the capillary is calculated using the equation

$$H = \sqrt{2}\kappa^{-1}(1 - \sin\theta)^{1/2} \quad (11)$$

where  $\kappa^{-1}$  is the capillary length of the liquid and  $\theta$  is the contact angle.<sup>85</sup> The height calculated here for Wilhelmy plate experiments accounts for only a portion of the collapse distance found from the force-displacement curves at low advancing rates, but for higher rates these values are similar. This is consistent with Fig. 61a. Another possible reason for slower increase of the capillary force is the top of the ridge deformation could be bent to a large angle. As previously discussed, the wetting ridge has a complex hierarchical apex structure rather than a simple hedge shape. The nano-ridge on top where the contact line sat on has a steeper angle than the overall slope of the wetting ridge. Thus the actual contact angle is different than that calculated from the measured force based on Young's equation. Either of these possibilities is directly related to the viscoelastic properties of the acrylic polymer film.

A final observation that should be addressed is that different liquids demonstrate the same general behavior in both sessile drop and Wilhelmy plate experiments, but pinning distances vary for the same test speeds in Wilhelmy plate experiments. If the results for water and paraffin oil are compared, it is observed that the oil collapses for a lower contact angle and has smaller spacings between ridge structures on liquid-submerged plates. It also appears that the sizes of ridges formed on the acrylic polymer are smaller for the oil. It would seem reasonable to somehow assign the differences to the higher surface tension of water, but it is important to note that these liquids also differ significantly in density and viscosity. A great insight is provided by examining the wetting behavior for glycerol (Table 16), which has a surface tension slightly lower than that of water and viscosity higher than that of the paraffin oil. Also, its density is greater than that for water. Glycerol showed the smallest pinning distance for the same speeds of all the liquids tested. This would appear to suggest that the viscosity of a liquid is the dominant factor in determining the spacings on the polymer-coated plates used in the Wilhelmy plate experiments. A plot of the pinning distance versus the kinematic viscosity is well fit by a power law function (Fig. 61d).

## Conclusions

The novel wetting behavior reported for the thermally stripped acrylic polymer was further characterized and reported here. Previously it was observed that the three-phase line is pinned to the polymer to the extent that the contact angle for an evaporating drop of water is reduced to 0°. The addition of water moves the contact angle to values in excess of 150° before it propagates

via what is described as stick and break motion involving the collapse of the meniscus due to gravitational forces and the reestablishment of the wetting line. Also observed is a wetting ridge, which is larger than those reported elsewhere, providing significant detail to be extracted on its morphology. It was speculated that highly viscoelastic acrylic polymer, designed for pressure sensitive applications, dissipates the capillary energy regardless of the induced contact angle, halting the movement of the wetting line. Here it is shown that the observed stick and break motion is not restricted to water. Liquids possessing very different properties demonstrate the same general behavior.

The liquids provide different pinning distances (distances between subsequent wetting ridges) and pinning forces (maximum forces change measured during the pinning process) in Wilhelmy plate experiments using metal plates coated with the polymer. A comparison of results for water, formamide, ethylene glycol, paraffin oil, glycerol and water/glycerol mixture indicate that viscosity is the dominant variable governing differences at the same advancing rate. It appears that lower viscosities produce larger wetting ridges and thus greater pinning distances and forces. Both of these quantities decrease with increasing wetting rates and can be fit with a power law function. It was shown that the viscoelastic properties of the acrylic polymer play a dominant role in determining wetting behavior. For higher forced wetting rates, pinning distances and forces are reduced consistent with the master curve for the polymer demonstrating greater elastic behavior for higher deformation frequencies. For the lowest wetting speeds, the separation between wetting ridges is significantly larger than the meniscus height change. This is attributed to the creep deformation of the ridge, which is seen to change its symmetry. For higher wetting speeds the separation of wetting ridge distances converges towards the calculated meniscus height change. Another indication of the ridge deformation leading to increased ridge separation distances is found in the plot of wetting force versus wetting distance, which shows increasing slopes for linear fits with increasing wetting rates. The slope values plateau for moderate and high wetting rates.

### ***3.12 Variety of Wetting Line Propagations Demonstrated on Viscoelastic Substrate***

Mechanisms by which contact lines propagate at a fluid-fluid-solid interface play an important role in processes of interest to both practitioners and researchers across the spectrum of scientific disciplines. Dynamic wetting mechanisms are governed by energy dissipation that occurs through the contact line region.<sup>84,85</sup> While surface chemistry and topology have been the focus of numerous studies on controlled wetting,<sup>192,193</sup> less attention has been paid to the role of the solid surface viscoelastic response at the three-phase line.<sup>95-97,139,146,183,191,194</sup> Viscoelastic materials can impede, even arrest, the motion of a wetting line as a result of capillary energy dissipation through surface deformation. Recently, the authors reported on such behavior in which the wetting line was pinned on the surface of a acrylic polymer and spread only by forcing meniscus collapse.<sup>96,97</sup> This inhibited motion, which is referred to as pinning here, manifests itself as a quasi-periodic series of micron-size ridges formed on the polymer surface as it is submerged into a liquid. Identification of a material that demonstrates such a considerable viscoelastic response under the influence of relatively weak capillary forces provides an opportunity to further examine the wetting behavior of soft surfaces. In this letter, dynamic wetting results are reviewed for fluid combinations that demonstrate complete, partial as well as non-wetting of the acrylic polymer. The liquids induce a range of responses, which are used to



identify the underlying mechanism involved in the stick and break motion. The results contribute to our understanding of how fluids wet soft surfaces including tissues and thus have implications for biological processes such as cell migration and adhesion.

The acrylic thermoplastic was synthesized and processed at Franklin International Co. (Columbus, OH). The material of focus is an acrylic pressure sensitive adhesive developed for wound binding applications. It is generated via solvent polymerization primarily from the monomer 2-ethylhexyl acrylate with much lesser amounts of amide and vinyl aromatic comonomers. The polymer has a glass transition temperature of less than  $-50\text{ }^{\circ}\text{C}$  and at room temperature possesses a Young's modulus in the range of 10-100 kPa, similar to that of hydrogels and biological tissues. The dynamic wettings were performed following the Wilhelmy plate method using a Kruss Model K100 tensiometer (Hamburg, Germany). The advancing and receding rate was chosen as 0.5 mm/minute and the force data were collected for every  $10\text{ }\mu\text{m}$  of displacement. The polymer film was formed by dipping a heated steel rod with diameter as 1.5 mm into a bulk sample of the polymer and quickly pulled out. A 100 ml glass beaker was used to hold the test liquids. The silicone-water mixture was tested with different thickness of the oil layer and the thickness was estimated by its mass over the coverage. Deionized water is purified to  $18\text{ M}\Omega\text{ cm}$  with Type II Laboratory SpectraPure Water System (Tempe, AZ). The silicone oil used in the experiments is from Fisher Scientific #159-500 and has a kinematic viscosity of  $50 \times 10^{-6}\text{ m}^2/\text{s}$ , a surface tension of  $20.8\text{ mN/m}$ , and a density of  $0.963\text{ g/ml}$ . The thickness of the silicone oil layer was estimated by its volume over the cover area. For the thin silicone oil layer, the measurement was performed after more than 2 hours for the oil to completely spread through the container.

Figure 63 shows force-displacement curves, which are representative of the typical wetting behaviors demonstrated when a rigid rod coated with the acrylic polymer is immersed and withdrawn through interfaces composed of (a) water and air, (b) paraffin oil and air, (c) silicone oil and air, and (d) water and silicone oil. Each curve demonstrates a unique combination of advancing and receding contact line propagations. The force-displacement curve for the wetting line at the water-air interface (Fig. 63a) exhibits a quasi-periodic capillary force oscillation in both advancing and receding, with the receding force oscillation having significantly smaller amplitude. The peak force for each period of the oscillation can be directly associated with a micron-size ridge on the polymer surface.<sup>97</sup> These observations are indicative of the so-called stick and break motion. Figure 63b shows the force-displacement curve for the wetting of the polymer-coated rod by the paraffin oil in which it partially wets the polymer surface. Here, the stick and break mechanism is present in advancing but not in receding. Figure 63c shows the force curve for the wetting of the polymer surface by silicone oil, which has a low surface tension and completely wets the polymer. The force-displacement curves for both advancing and receding are smooth and overlap indicating no pinning events and no hysteresis, respectively. Figure 63d shows a typical force-displacement curve for the coated rod through a water-silicon oil interface. Water has the greater density and supports the immiscible oil layer. It can be seen that the curve is smooth during the advancing stage while quasi-periodic force patterns consistent with stick and break motion are apparent during the receding.

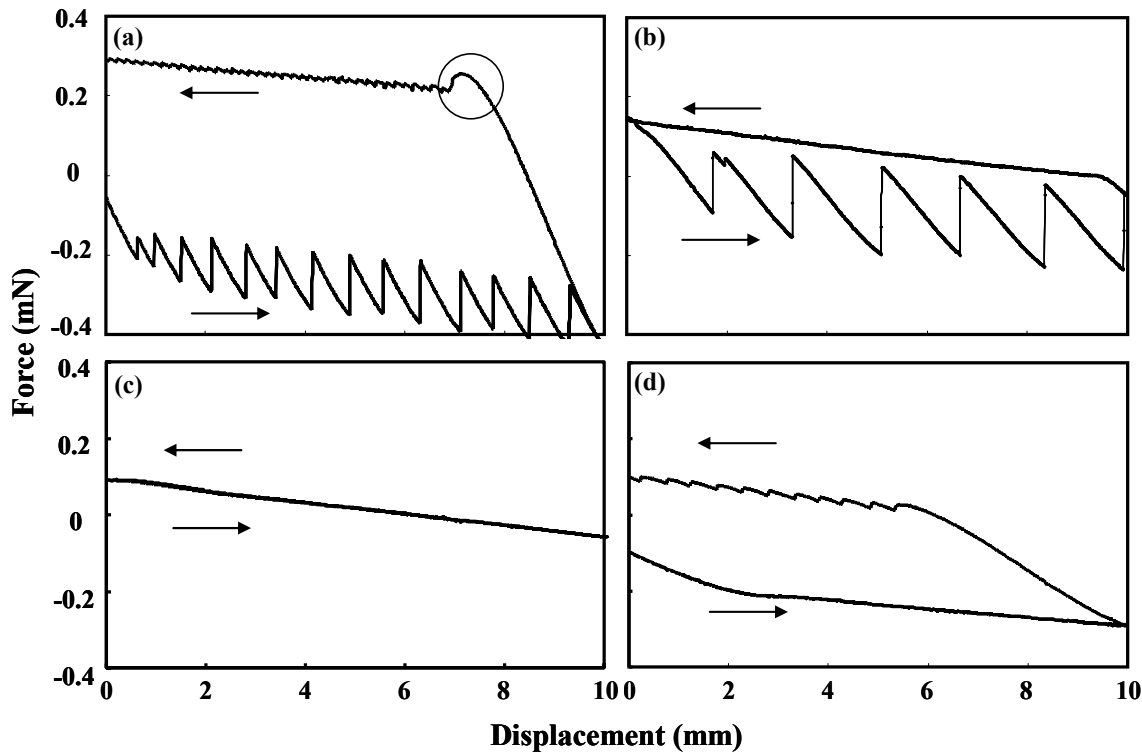


**Figure 63.** Typical force-displacement curves for the different interfaces studied. The arrows indicate the wetting direction (left to right advancing; right to left, receding).

Wetting behaviors for the systems reviewed above are complex as well as diverse, highlighting the question of how the contact line movement is controlled. Previously it was shown that the magnitudes and shapes of formed wetting ridges were dependent on rheological properties of the polymer.<sup>96</sup> These along with the magnitude of the vertical surface tension component determine the extent of deformations induced. Table 17 lists the dynamic contact angles (CAs) for the various interfaces measured in advancing and receding along with the magnitude of the vertical surface tension component. Stick and break motion is absent when the CA is near  $0^\circ$  or  $180^\circ$  due to the small vertical force on the wetting line. Such is the case for the water-silicone oil interface in advancing with a CA of  $175^\circ$ , paraffin oil-air interface in receding with a CA of  $7^\circ$ , and silicone oil, which completely wets the polymer surface in air. The most distinct stick and break motion in Fig. 63 is demonstrated by the paraffin oil-air interface. This results from a range of pinned advancing CAs that begin at  $48^\circ$  and increase to  $141^\circ$ ; a  $100^\circ$  difference in CA centered at nearly  $90^\circ$ , where the vertical component of the surface tension is maximized. A similar effect is observed for the water-air interface at the onset of the receding stage of wetting. The transition process from advancing to receding involves the reduction in angle from about  $150^\circ$  to  $7^\circ$ .

**Table 17:** Dynamic CAs (degree) and vertical surface tension components (mN/m) at the interfaces.

	Advancing		Receding	
	Before collapse	After collapse	Before collapse	After collapse
Water	148° (38)	117° (65)	7° (9)	14° (18)
Paraffin oil	141° (20)	48° (23)	7° (4)	
Silicone oil	0° (0)		0° (0)	
Water – Silicone oil	175° (4)		53° (38)	58° (40)

For a given liquid and wetting rate, a greater vertical surface tension component produces a larger deformation ridge, which for dynamic wetting experiments results in greater pinning forces and distances. For example, the average vertical surface tension component for water measured during pinning in advancing was 52 mN/m, while in receding the value was 14 mN/m (Table 17). This produced average pinning distances at a wetting rate at 0.5 mm/min, for a 1.5 mm rod, of 0.67 mm and 0.13 mm, respectively. In all wetting experiments, the meniscus collapsed more frequency in receding than in advancing. A possible explanation for this is the stability differences of the advancing and receding meniscus. Capillary energy is decreased through the collapse of the meniscus regardless of whether the contact line is advancing or receding. However, the total surface energy decreases if the collapse occurs with recession, which reduces the wetted area. It is also true that gravitational potential energy is reduced for meniscus collapse during the receding process, which lowers the center of mass in the contact line region.

Meniscus height,  $h$ , at the three-phase line formed between 2 fluids with a difference in density of  $\rho$  and interfacial tension  $\gamma$  and a solid cylindrical rod of radius  $R$  can be predicted for a given contact angle,  $\theta$ , as,

$$h = \left[ 2\left(\frac{\gamma}{\rho g}\right)(1 - \sin \theta) \right]^{1/2} \left[ 1 + \left(\frac{\gamma}{\rho g}\right)^{1/2} \frac{1}{R} \right]^{-1/2} \quad (12)$$

where  $g$  is acceleration due to gravity.<sup>195</sup> It is expected that the spacing of ridges formed on the surface of the coated rod should be approximately equal to the difference in the meniscus height between that for the initial contact angle,  $\theta_i$ , and the angle prior to meniscus collapse,  $\theta_c$ , i.e.,  $\Delta h = h(\theta_i) - h(\theta_c)$ . Table 18 shows  $\Delta h$  calculated using Eq. 12, as well as experimentally distances between pinning events (i.e., ridges) on the surfaces of coated glass rods obtained from the force-

displacement curves. Predicted values of meniscus height are well within the uncertainty range ( $\pm 10\%$ ) of our experimental measurements except for the case of receding at water-silicone oil interface. Discrepancy between these values are believed to result primarily from creep behavior given the use of a highly viscoelastic substrate.<sup>96</sup> The cartoon in Fig. 64 attempts to describe this effect. The displacement of the rod is followed by the creeping up of the wetting deformation, thus greater displacement is required to reach the contact angle,  $\theta_c$ , producing a collapse of the meniscus. This is the case, for example, in the wetting at the water-air interface, but this effect can also act to reduce the required displacement. For the wetting at the paraffin oil-air interface in advancing, the pinned contact angle is initially less than  $90^\circ$  but creeps up to reduce the meniscus height, thus less displacement is required to achieve meniscus collapse producing a discrepancy of  $-2.5\%$  between predicted and measured values.

**Table 18:** Experimental pinning values from Fig. 63 and values calculated with Eq. 12.

	<b>Experimental value <math>\Delta h_m</math> (mm)</b>	<b>Calculated value <math>\Delta h_c</math> (mm)</b>
Water – air interface in advancing	$0.671 \pm 0.082$	0.636
Paraffin oil – air interface in advancing	$1.584 \pm 0.086$	1.624
Water – air interface in receding	$0.128 \pm 0.062$	0.119
Water – silicone oil in receding	$0.426 \pm 0.04$	0.237

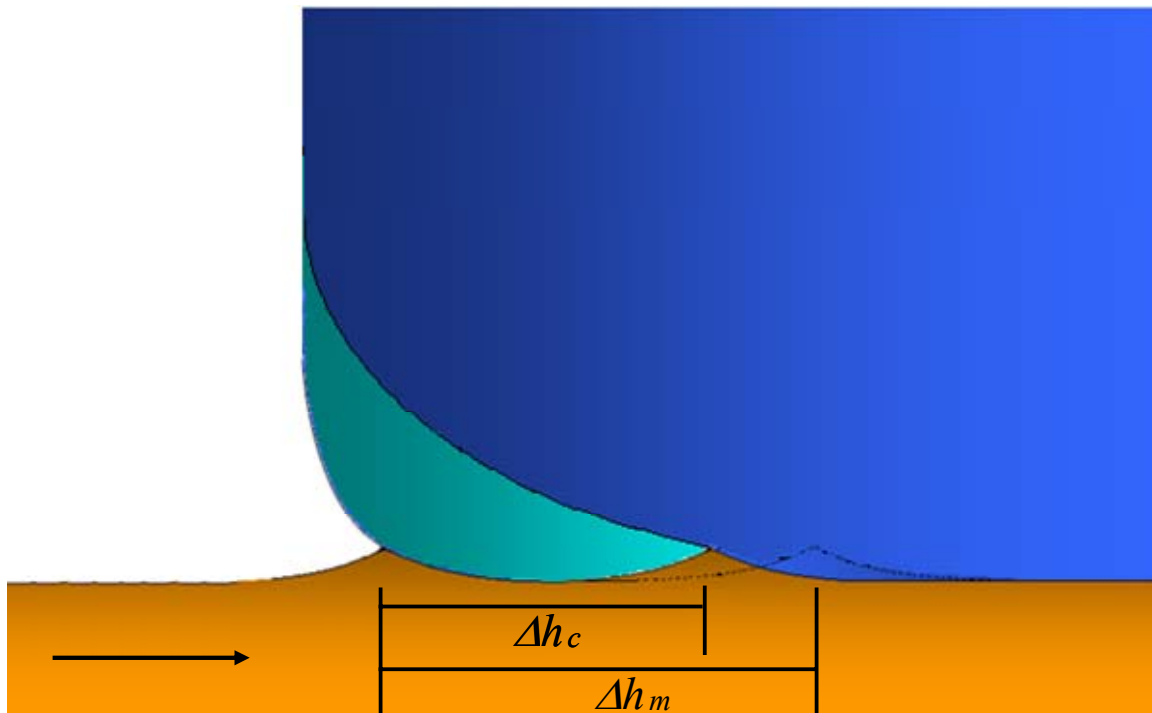
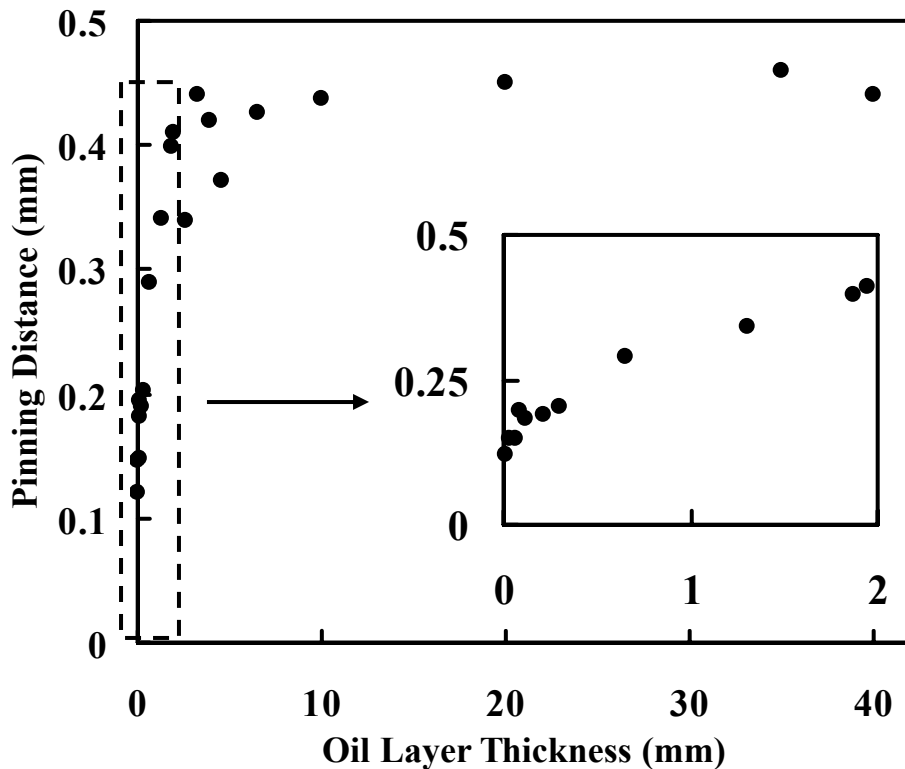


**Figure 64.** Schematic showing the meniscus height difference between the calculated change (indicated as  $\Delta h_c$ ) and the measured change (indicated as  $\Delta h_m$ ) in meniscus height. The distance shown as  $\Delta h_m$  is the measured distance for plate movement and  $\Delta h_c$  is the distance calculated using Eq. 1. The deformation ridge creeps due to the horizontal surface tension component changing the distance required to reach the contact angle for which meniscus collapse occurs by  $\Delta h_m - \Delta h_c$ . The direction of this movement is dependent in the range of contact angles transversed during the pinning process.

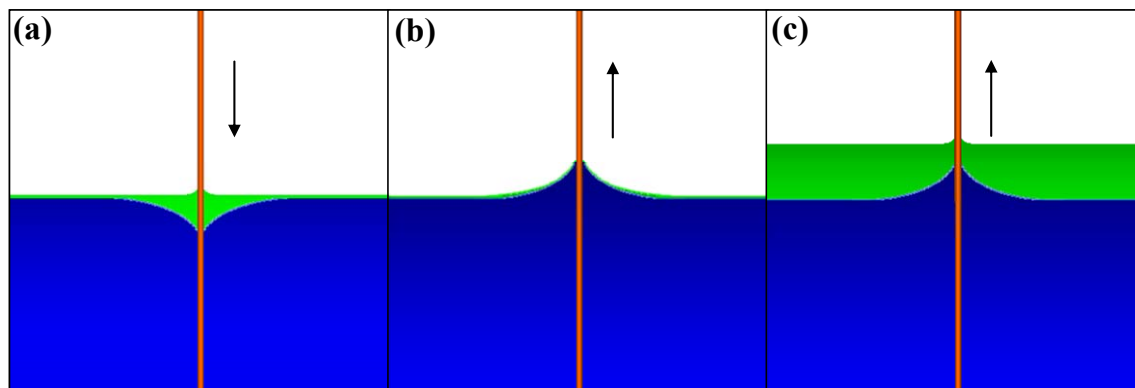
The water-silicone oil interface (Fig. 63d) was the only system the authors have identified that demonstrates a distinguishable stick and break motion solely in receding. The significance as well as the subtleties of this result requires further explanation. Figure 65 shows the relationship between the maximum pinning distance and the thickness of the silicone oil layer in receding. It can be seen that the pinning distance is greatly enhanced by the addition of silicone oil in the thin film region and levels off for higher thicknesses above about 2 mm. For oil layers of 1 mm or less in thickness, the oil was observed to drain off the meniscus and thin consistent with the pinning at the water-oil interface during receding. In many instances, water appeared to be pulled through the oil layer resulting in a region of water immediately surrounding the rod. These effects were not present for the thicker layers and are likely responsible for the relationship shown in Fig. 65.

Figure 66 is a schematic outlining a potential mechanism for the observations made for this interface. During advancing, the upper wetting line (the silicone oil-air interface) forms a CA of  $0^\circ$ , and the lower wetting line (the water-silicone oil interface) forms a CA of approximately  $175^\circ$ . Thus, complete wetting and nearly non-wetting behaviors are demonstrated, respectively,

for this one system. Due to the weak vertical forces at the interfaces, there are no deformations and the oil thickness does not influence on the wetting as the contact line is advanced (Fig 66a). However, when it recedes, the CA at the lower wetting line is reduced to about  $50^\circ$  with a vertical surface tension component of 40 mN/m. This is sufficient to produce deformation on the polymer surface. The pinning results in the lower wetting line being lifted towards the upper the silicone-oil interface. For the thin oil layers, the pinning distance is larger than the thickness of film and the wetting line is pulled through the oil into the air where it likely collapses (Fig. 66b). For the thicker oil layers, meniscus collapse occurs prior to the piercing of the surface of the silicone oil as demonstrated in Fig. 66c, and the pinning distance settles at a constant value.



**Figure 65.** The relationship of the thickness of the silicone oil layer and the maximum pinning distance in receding.



**Figure 66.** Schematic showing the water-silicone oil interface (a) in advancing, (b) in receding for a thin silicone oil layer and (c) in receding for a thick silicone oil layer.

In summary, the wetting systems highlighted here demonstrate that contact line movement on the surfaces of soft materials can propagate through the stick and break mechanism both in advancing and receding. The extent to which this mechanism is demonstrated depends on properties of the substrate, fluids and interfaces formed. (For example, we previously identified viscosity as the dominant variable governing the pinning distance under the same experimental conditions for a water/glycerol mixture.<sup>96</sup>) In general, these data indicate that both adhesion and wetting can be manipulated in complex manners through careful control of the identified variables. Specific applications include microfluids, which involve the flow of small volumes on platforms manufactured using the non-rigid materials such as poly(dimethylsiloxane) (PDMS). Given the observed differences in the wetting mechanism for the advancing and receding contact lines, results presented here indicate that for drops of sizes comparable with the capillarity length of fluid, movements of the front and rear lines can be significantly different creating complex motion on surfaces. Such motions must be understood in the design of microfluidic devices.

### ***3.13 Characterizing the Distribution of Nonylphenol Ethoxylate Surfactants in Water-based Pressure-Sensitive Adhesive Films using Atomic-Force and Confocal Raman Microscopy***

Pressure-sensitive adhesives (PSAs) are those capable of aggressively bonding to most material surfaces simply through the application of light pressure. Water-based PSA films are cast from aqueous colloidal dispersions. Other than the adhesive polymer, the most prevalent chemical in PSA films are emulsifiers, usually composing less than 10 wt.% of adhesive films. While mixtures of anionic and nonionic surfactants are used in commercial products, anionic surfactants are often a dominant component. The surfactant is added to allow for the generation of high-solids lattices ensuring stability of colloidal particles of PSA during the polymerization process. However, they are also believed to cause poor adhesive performance due to their heterogeneous distribution in PSA film.<sup>196-200</sup> Depending on the compatibility between surfactant and latex particles, surfactant may partially dissolve into the adhesive polymer, remain at the interfaces between particles and/or phase-separate from the polymeric solution and migrate to film interfaces.<sup>201</sup>

Due to its significance in determining adhesive product performance, the distribution of surfactants in films cast from acrylic latexes has been a matter of interest for many years. It is believed that the main factors influencing the out-of-plane distribution of surfactants includes the chemical nature of the latex system, aging time, film formation environments (temperature and relative humidity) and the structures of the surfactants.<sup>202</sup> For example, Guigner *et al.* reported very different concentration profiles for a series of surfactants that included sodium dodecyl sulfate, hexadecylpyridinium chloride and hexadecyltrimethylammonium bromide in poly(2-ethylhexyl methacrylate) latex films.<sup>203</sup> Several researchers have reported higher surfactant concentrations at the film interfaces and propose that the enrichment hinders or delays particle coalescence in these regions resulting in weaker films.<sup>204-206</sup> The more pronounced enrichment occurs at the film-air side and results from the aided transportation of free (non-sorbed) surfactant due to the convective movement of water during drying.<sup>207, 208</sup> Kientz and Holl<sup>201</sup> suggested that the distribution of surfactant depends on factors such as the initial surfactant distribution at the interfaces, surfactant desorption during drying and the mobility of surfactant in the drying film. Belaroui<sup>209, 210</sup> and Mallégol *et al.*<sup>211-213</sup> argued that the distribution of water and extent of coalescence during drying also play an important role in determining enrichment/depletion of surfactant at film interfaces.

Given the importance of surfactant distributions to the performance of a water-based PSA, a number of techniques have been applied to characterize concentration profiles. Fourier transform infrared spectroscopy (FTIR),<sup>201</sup> attenuated total reflection (ATR) FTIR,<sup>201-203, 210, 214-218</sup> infrared microscopy,<sup>203</sup> X-ray photoelectron spectroscopy,<sup>207</sup> nuclear magnetic resonance,<sup>203, 211</sup> and Rutherford backscattering spectroscopy (RBS)<sup>212, 219</sup> have been extensively used to collect out-of-plane distribution data of surfactant. However, these techniques either cannot provide layer by layer depth profiling information or only allow for analysis within a few microns of the surface. In fact, most studies published previously examining surfactant-polymer compatibility and mobility of anionic and nonionic surfactants in latex films are based on the results from ATR-FTIR spectra obtained on film-air and film-substrate interfaces.

Confocal Raman microscopy (CRM) is a relatively new technique that has been employed to obtain surfactant distribution information in recent years. It has been shown to be an effective method for the depth profiling of thin films, coatings, membranes and composites.<sup>220, 221</sup> This technique allows one to record a Raman spectrum for a small volume of film without any modification of samples by combining a high resolution confocal microscope with a sensitive Raman spectroscopy system. By applying confocal optics, the sampling volume can be moved along a direction perpendicular to the film surface over several tens of micrometers by tuning the plane of focus of the microscope in a stepwise fashion. Differences in chemical composition of a film can be viewed in Raman spectra at various depths. In this paper, CRM is applied to a series of emulsion-type adhesives, based on a commercial, label-grade, water-based acrylic PSA. The adhesives use both anionic and nonionic nonylphenol ethoxylate emulsifiers. By switching the dominant surfactant from anionic to nonionic, information is obtained on the tendency of these different species to migrate. Atomic force microscopy (AFM) was used for imaging both the film-air and film-substrate interfaces to further characterize the migration process and show the impact of migration on the coalescence of latex particles. This combination of quantitative and qualitative high resolution techniques is shown to be a powerful method for characterizing the movement of surfactants in water-based PSA films and their impact on structure.



## Experimental Methods

**Materials.** Model water-based PSAs were synthesized at Franklin International (Columbus, OH) from the acrylic monomers *n*-butyl acrylate, vinyl acetate and methacrylic acid and a combination an anionic surfactant, disodium (nonylphenoxypolyethoxy)ethyl sulfosuccinate (Aerosol A-103, CAS No. 57706-08-8), and a nonionic surfactant, nonylphenol polyethoxylate (IGEPAL<sup>®</sup> CO-520, CAS No. 9016-45-9). Both surfactants were obtained from CYTEC Industries, Inc. (West Paterson, NJ). Three model systems are reported on here. They are all synthesized using identical synthesis approaches and conditions. The first model PSA system contains 100 wt.% anionic surfactant, second model PSA is produced with an emulsifier combination of 50 wt.% anionic and 50 wt.% nonionic, and the third model PSA contains 90 wt.% nonionic and 10 wt.% anionic. The solids content of produced latexes were 60-63 wt.%. Properties were characterized using techniques described elsewhere.<sup>15,17,23</sup> Solid adhesive was coated onto silicone release liner and dried in oven at 82°C for 10 minutes to produce 1 mil (25.4 μm) thick films. The total surfactant content in films assuming complete retention is 1.8 wt.%. For analysis, films were transferred coated onto glass slides. These are identified throughout the paper as draw-down films. Several PSA film samples were prepared via spin coating on AFM specimen disks. These films are approximately 10 μm thick and were used for the initial surface morphology examination using AFM.

**Determination of Surfactant Molar Mass and Relative Mobility.** A liquid chromatography-mass spectroscopy (LC-MS) system was employed to check the molar mass distribution and formulas of anionic and nonionic surfactants used in PSA emulsions. A reverse phase high performance liquid chromatography (RP HPLC) method was used to separate samples of anionic and nonionic surfactants mixture using a SpectraSYSTEM P4000 LC (Thermo-Electron, Waltham, MA) to determine the retention time of surfactants. Before testing, pH values of anionic surfactant, nonionic surfactant and 50/50 anionic/nonionic surfactants mixture were adjusted to between 4 and 5, which is consistent with pH level of latex emulsion. A Zorbax Eclipse XD8-C8, 25×4.6 mm×5 μm, column (Agilent, Fort Worth, TX) was used and the surfactants were eluted with a mobile phase of solvent A [90% water and 10% Acetonitrile (ACN)] and solvent B [100% ACN] at a flow rate of 1.0 ml/min. Surfactants were separated using a linear gradient from 100% solvent A to 90% solvent B over 19 min. Solvent B was held for 3 min at 90% before returning to initial conditions. The column was equilibrated for 5 min before subsequent injections. Surfactants were detected using a Thermo-Electron LCQ Classic ion trap mass spectrometer (ThermoFisher, Waltham, MA). Spectra were collected in the positive ionization electrospray (ESI) mode.

**Atomic Force Microscopy Imaging of Film Surfaces.** Atomic force microscopy was used to examine surface morphologies of PSA films. Using a PicoPlus PicoSPM (Agilent Technology, Foster City, CA) system, AFM imaging was performed in an environmental chamber with controlled temperature and relative humidity (RH). Intermittent contact or AC mode AFM was utilized. The amplitude of the cantilever is maintained constant during the scanning and the displacement of the piezo scanner through the feedback circuit to maintain this amplitude is recorded as a height image. The phase lag between the cantilever response and the driving oscillation signal is recorded as a phase image. Viscoelastic properties of the surface may also be evaluated from AFM phase images. All tapping mode AFM images presented in this paper

were obtained employing integrated silicon cantilevers with tip radii of curvature 5-10 nm. The spring constant of the cantilever was manufacturer-specified in the range of 30-60 N/m and the measured resonant frequency was within 10% of 300 KHz. Here all PSA films were examined at ambient conditions.

**Confocal Raman Microscopy Characterization of Surfactant Distributions.** An alpha 300R confocal Raman microscope equipped with a UHTS200 spectrometer and a DV401 CCD detector from WITec (Ulm, Germany) was employed to collect single Raman spectra from the pure latex (synthesized by soap free emulsion polymerization method), pure surfactant (supplied by Franklin International), and the model PSA films. A Nikon 100x oil immersion objective was used for all measurements. An Ar-ion laser with the wavelength of 514.5 nm and maximum power of 50 mW was used for excitation. The lateral resolution of the confocal Raman microscope according to the theory of light diffraction is about 250 nm and the vertical resolution is about 500 nm. Since the sampling volume may be smaller than the average particle size of the latex spheres, measurements were conducted on several random locations on the film to minimize the variation. The Raman spectra of all samples, including the pure latex, pure surfactant and the film samples were recorded with an integration time of 240 s and laser power of 20 mW.

A set of latex films with defined concentration of surfactants ranging from 1 to 10% by weight was cast on glass slides. Pure latex with a solid content of 52 wt.% was synthesized by soap free emulsion polymerization. A surfactant mixture containing 50 wt.% anionic and 50 wt.% nonionic surfactant was added in the pure latex at concentrations of 1%, 2%, 4%, 6%, and 10%. These were used to obtain a calibration curve for the calculation of surfactant concentration in the dry PSA draw-down films. Curve fitting software is applied to calculate the ratio of the absorbencies of the surfactant to the polymer peaks. The ratio of the absorbencies of the surfactant to the polymer was then plotted as a function of the ratio of the concentrations and fit with a linear model. The ratio of molar absorption coefficients of surfactant to polymer was calculated from this curve as 0.5733, which is used for the calculation of the concentration of surfactant in the model PSA films from the confocal Raman spectra.

## Results and Discussion

**Properties of Emulsifiers and their Influence on PSA films.** Table 19 lists properties of surfactants used in the synthesis of the PSAs. Industrial surfactants are provided with a range of molar masses differing primarily by the number of ethoxylate linkages present. Both the number average ( $M_n$ ) and weight average ( $M_w$ ) molar masses obtained from LC-MS data are listed in the Table 19. Nonionic surfactants tend to have lower critical micelle concentrations (CMCs) and hydrophilic-lipophilic balance (HLB) values than anionic surfactants possessing similar structures (i.e., similar hydrophobes). This reflects their generally greater hydrophobicity. From the table it can be seen that this general observation is consistent with the properties of the surfactant pair used here. Also listed in the table are estimated Log  $K_{ow}$  values for both surfactants,<sup>22</sup> where  $K_{ow}$  is the octanol-water distribution coefficient. (Log  $K_{ow}$  values have been shown to correlate with water solubility for organic liquids as well as their tendency to distribute into nonpolar phases.<sup>222-225</sup>) The value for the nonionic species is significantly higher than that for the anionic surfactant consistent with its less polar structure.

**Table 19:** Chemical and physical properties of surfactants

Properties	Anionic Surfactant	Nonionic Surfactant
Molecular Formula	$C_{15}H_{23}(OCH_2CH_2)_nC_4H_9O_7Na_2S$ $n \approx 11$	$C_{15}H_{23}(OCH_2CH_2)_nO$ H $n \approx 9$
Molar Mass (g/mol.)	$M_n = 905.26$ $M_w = 935.84$	$M_n = 597.54$ $M_w = 608.32$
Critical Micelle Concentration* (% by weight)	$1.5 \times 10^{-2}$	$2.1 \times 10^{-4}$
Hydrophilic-Lipophilic Balance* (HLB)	15	10
Log $K_{ow}$	- 3.41	3.38

\* values reported by the suppliers

**Table 20:** Properties of model PSAs

Measurement	PSA 1	PSA 2	PSA 3
Anionic: Nonionic wt. %	100:0	50:50	10:90
Latex Viscosity (cps)	88	90	750
Mean Particle Size (nm)	450	690	1250
pH	4.39	4.28	4.32
Molar Mass (g/mol.)	$M_n = 25000$ $M_w = 160000$ PDI = 6.4	$M_n = 29841$ $M_w = 260180$ PDI = 8.7	$M_n = 27500$ $M_w = 209000$ PDI = 7.6
Glass Transition Temperature ( $^{\circ}C$ )	-19.8	-34	-24
Peel Adhesion (lbs.)	2.0	2.0	2.1
Loop Tack (lbs.)	2.6	2.3	2.0
178 $^{\circ}$ Shear Adhesion (min.)	300	200	960
Contact angle with water (degree)	106	110	112

The influence of the different surfactants on performance properties of PSA films cast is shown in Table 20. These properties for PSA 2, with one half surfactant blend being anionic, and PSA 1, produced solely with anionic surfactant, are quite similar. While PSA 3, containing a blend of surfactants composed primarily of the nonionic surfactant, has a larger latex particle size. This PSA has a higher shear, a gauge of cohesive strength, which is likely a result of its high molar mass and/or gel content,<sup>226, 227</sup> which are higher relative to those for PSAs 1 and 2. The differences in molar mass for PSA adhesive polymers may possibly impact surfactant distribution as was suggested by Tzitzinou *et al.*<sup>228</sup> However, by combining results for the adhesive films examined here, underlying trends are distinguishable. Also shown in Table 20 are contact angles for water on the 3 model PSAs. Increasing the concentration of surfactant will

tend to raise the surface energy of a water-based, acrylic film likely due to an increasing concentration of the surfactant at the interface.<sup>229</sup> The interpretation of these values is complicated by the presence of the 2 different surfactants. However, it can be seen that the lowest angle is found for PSA1 and the highest for PSA 3 would appear to indicate higher concentrations of anionic surfactant result in a greater impact on the surface energy. Furthermore, when the films are rinsed with water, the angles are found to increase for all of the PSAs except that for PSA 3, which contains primarily nonionic surfactant, and the soap free PSA has a contact angle with water of 112°, the same as that for PSA 3.

A “water-flux” mechanism has been proposed previously as a mechanism for the transport of surfactant from the aqueous phase to the film-air interface in PSA films.<sup>230</sup> As the film is dried water is drawn to the surface and evaporates leading to the precipitation of surfactant. Thus it would be expected that the surfactant species with the higher concentration in the aqueous phase will become enriched to a greater extent on the surface of the film.

In emulsion polymerization, emulsifiers (surfactants) are added above their CMC and form micelles, which house reacting monomer. Subsequent to polymerization, the emulsifiers stabilize the latex, and in addition to being physically sorbed at the particle-water interface, surfactant molecules may become more intimately tied into the polymer bead. The extent of this interaction determines the extent to which surfactant can be released into the aqueous phase as the interface is consumed by the coalescence process. It has been reported that nonionic surfactants tend to concentrate less than anionic surfactants at latex film surfaces. This has been attributed to inhibited migration for the nonionic species, consistent with a stronger interaction with the polymer phase.<sup>231</sup> Studies examining the sorption behavior of nonylphenol ethoxates at concentrations near and above their CMCs, indicate that species with lower ethoxylate contents have a higher affinity for substrates such as silicates, soils and sediments.<sup>232-234</sup> This is attributed to the increased hydrophobicity associated with these structural changes.

For this study, the anionic species contains a greater number of ethoxylate linkages as well as acid functional groups. It is well known that for aqueous organic acids, the extent of sorption to natural substrates such as soils, sediments and wood correlates with measures of the acid’s hydrophobicity, and it is commonly found that the conjugate base of the acid demonstrates little affinity for the same surfaces.<sup>235, 236</sup> Results from RP HPLC carried out on an equal mass mixture of the 2 surfactants at the same pH as the PSA latexes demonstrate that the nonionic surfactant has a significantly greater affinity for the nonpolar stationary phase in that it elutes several column volumes subsequent to the anionic surfactant and only after significant modifications to the mobile phase consistent, for example, with its significantly higher Log  $K_{ow}$  value. Thus, if the distribution of surfactant species in the films is strongly dependent on their affinity to the polymer phase, significant differences should be apparent in the films cast from the 3 latexes studied here. Given its expected higher concentration in the aqueous phase, the anionic surfactant should deposit at the interfaces at substantially higher levels relative to the nonionic surfactant. Given the different concentrations of anionic and nonionic surfactant used, the model films should provide a decent gauge of the ability of AFM imaging and CRM depth profiling analysis to measure surfactant distribution behavior.

**Imaging of Surfactant at Film Surfaces.** In tapping mode AFM, the cantilever can be driven to interact with the surface in two distinct regimes, namely the attractive regime (or non-contact regime) in which the net interaction between AFM tip and the sample is attractive, and the repulsive regime (or intermittent-contact regime) in which a solid-solid mechanical contact is made and the net interaction is repulsive. When operating in repulsive regime, the viscous or more energy dissipative material often results in less phase lag, which produces a dark contrast on the phase image, while stiff or less energy dissipative materials provides bright contrast. When operating in attractive regime, the phase contrast is usually reversed. The tapping strength or the tip-sample interaction force varies with the free oscillation amplitude ( $A_0$ ) of the cantilever and the amplitude ratio of set-point oscillation  $A$  and  $A_0$ . For the AFM phase images presented here, the cantilever was operated in the repulsive regime with free oscillation amplitude of 300 nm and  $A/A_0 \sim 0.9$ - $0.95$ .

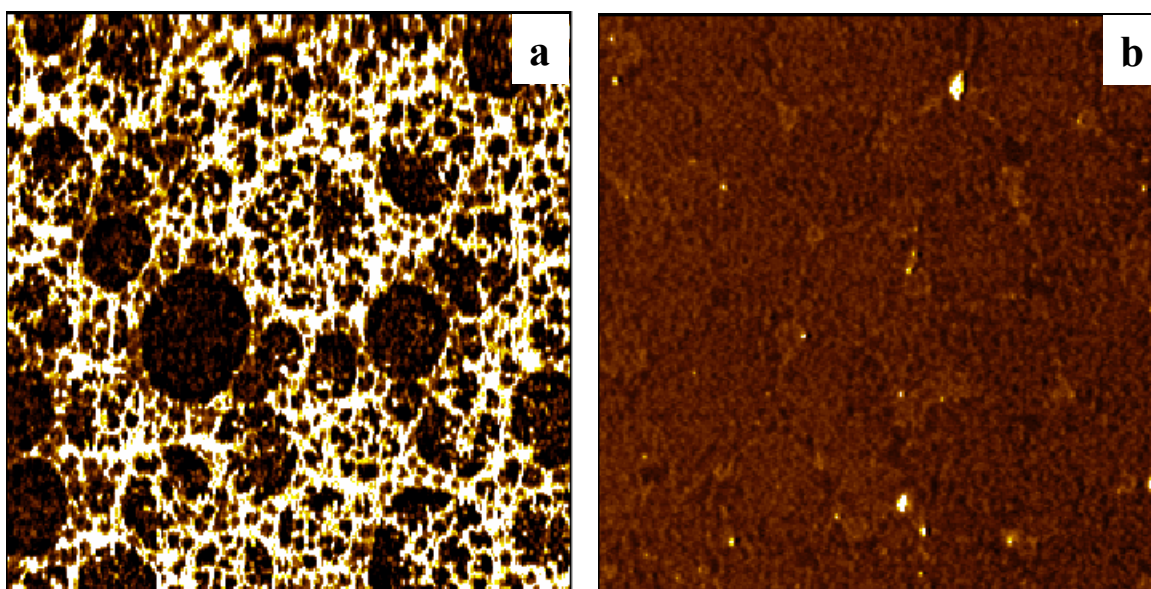


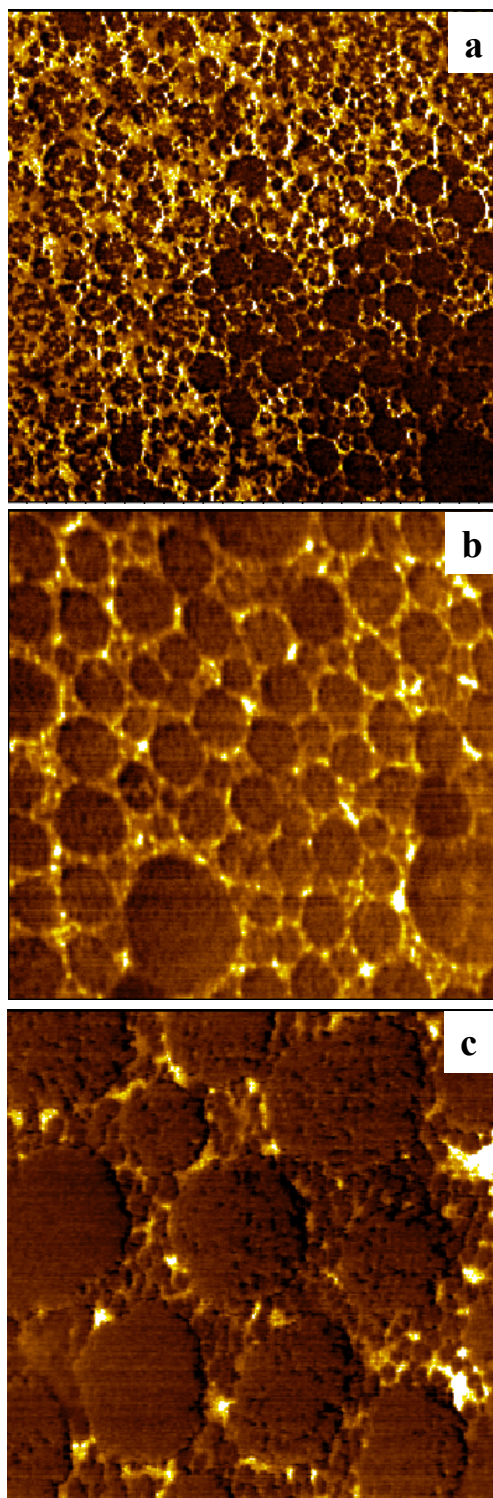
**Figure 67.** (a) AFM phase image of film-air interface of model PSA 2, and (b) film-air interface after soaking in solvent for 5 minutes. (Scan size  $2.5 \mu\text{m} \times 2.5 \mu\text{m}$ )

An AFM phase image of a spin coated, 50:50 wt.% anionic:nonionic PSA film, PSA 2, obtained under ambient conditions (45% relative humidity) is shown in Fig. 67a. The image was recorded at the film-air interface. Dark regions with spherical geometry can clearly be seen. These circular regions have diameters of 200-600 nm, which matches the particle size distribution obtained using dynamic light-scattering carried out on the latex emulsion (Table 20). Near spherical geometry and a well-spaced distribution indicate that the coalescence of latex beads has not occurred, nor has particle compaction. The second phase (bright contrast corresponding to less energy dissipative regions) appears to be the surfactant domain. The combination of an abundant presence of surfactants between and on the surface of latex beads and lack of particle coalescence indicates a likely connection. In order to verify this assumption, a small amount of ethyl alcohol (3 mL) was applied to the surface of the spin-coat model PSA 2 film for short time periods (5 minutes) and removed by further spin-coating. Here ethanol is used instead of water to rinse the top surface of PSA film because it more efficiently removed the surfactant. The phase image of the rinsed surface is shown in Fig. 67b. With 5 minutes of solvent soaking and

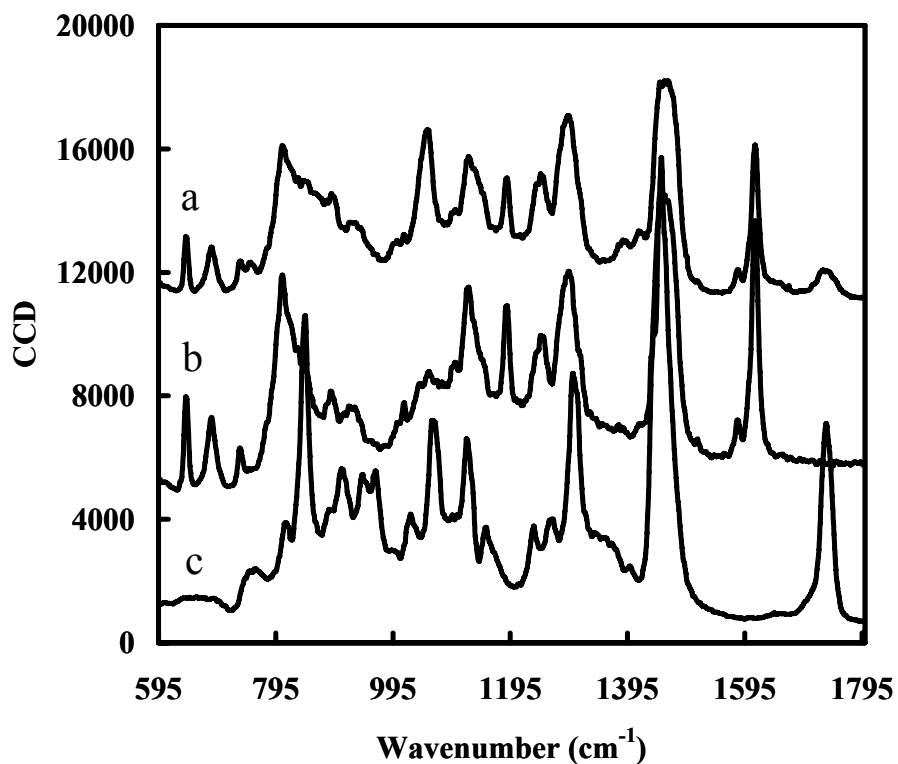
then rinsed by spin coating, the boundaries of latex particles are nearly absent, consistent with coalescence of the latex particles. These observations are a direct indication of the coalescence inhibition mechanism induced by the presence of surfactant. It is consistent with the conclusions from the study conducted by Mallégol *et al.* on the film formation and surface morphology of water-based PSA film.<sup>211-213</sup> It is interesting that the surfactant forms a compact, more elastic structure relative to the latex spheres. Varying tapping strength ( $A/A_0$ ) during the imaging also showed significantly greater compressibility of particle domains.

Figure 68 shows AFM phase images of film-air interfaces of all model PSA draw-down films. It can be seen that the latex beads in nonionic dominant PSA film, PSA 3, are much larger than those that contain more anionic surfactant. As was expected, the amount of surfactant aggregated at this interface is significantly larger for PSA 1 (Fig. 68a), followed by PSA 2 (Fig. 68b), and little surfactant is apparent at the interface of PSA 3 (Fig. 68c). This would indicate a greater tendency of the anionic surfactant to locate at the film surface, which is consistent with the contact angle data reviewed previously.

**Characterizing Surfactant Distribution with Confocal Raman Microscopy.** Figure 69 is a collection of basic Raman spectra for the pure latex and surfactants. The peaks at 1612 and 1735  $\text{cm}^{-1}$  are assigned to an aromatic C-C, on-ring stretch mode for the surfactant and carbonyl stretch mode of the polymer, respectively. The ratio of the absorbencies of the 1612 and 1735  $\text{cm}^{-1}$  peaks are used to quantify the surfactant concentration across the film thickness. It was found that the ratio of any two polymer peaks across the film remains constant. The concentration profile of surfactants in PSA 1 and PSA 2 drawn-down films are shown in Figs. 70 and 72, respectively. It should be noted that the draw-down PSA films are analyzed from the film-air interface, i.e., 0% corresponds to the film-air interface and 100% to the film-substrate interface. At least five locations were randomly selected on each film and Raman measurements were done with 0.5-5  $\mu\text{m}$  increments across the film thickness. The data shown in the figures are the average values obtained from at least five Raman measurements and the error bar is estimated variation of the data. All of the profiles show an enrichment of the surfactant at the interfaces, and evenly distribution in the bulk film. However, the data variation at the interfaces is much higher than that in the bulk film. The concentrations of surfactants drop significantly over a short distance from film-air interface and level at about the 10-20% thickness point. A similar profile is found, but the shape of the concentration curve is distinctly, rising more gradually at the film-substrate interface. In these two PSA films, surfactant enrichment is almost on the same level at film-air and film-substrate interfaces. However, it is evident that surfactant aggregation at the interfaces of PSA 1 is higher than that of PSA 2. This is consistent with the AFM observations, in which the aggregation of the surfactant at the film-air interface of PSA 1 was more significant than that of PSA 2 (Figs. 68a and 68b). Similar findings were also reported by Tzitzinou and Blaroui,<sup>237, 238</sup> who studied the fate of anionic surfactants during film formation of acrylic latexes.



**Figure 68.** Atomic force microscopy phase images of film-air interfaces for drawdown coatings of (a) PSA 1, (b) PSA 2 and (c) PSA 3. (Scan size  $2.5\ \mu\text{m} \times 2.5\ \mu\text{m}$ )



**Figure 69.** Basic Raman spectra of (a) anionic surfactant, (b) nonionic surfactant, and (c) soap-free latex.

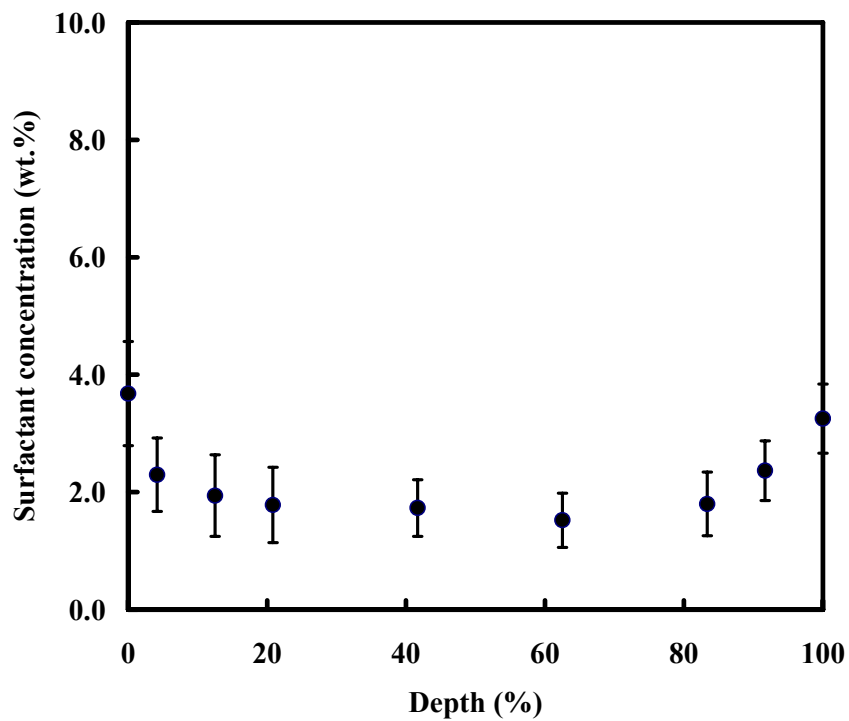


**Figure 70.** Surfactant distribution profile over the entire thickness of a film cast from PSA 1.



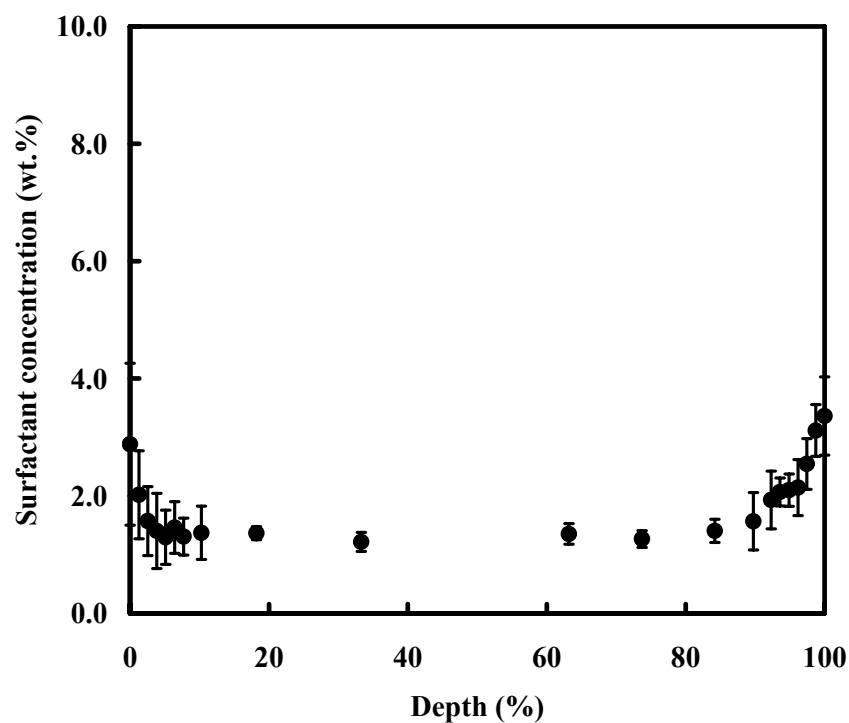


**Figure 71.** Surfactant distribution profile over the entire thickness of a film cast from PSA 2.

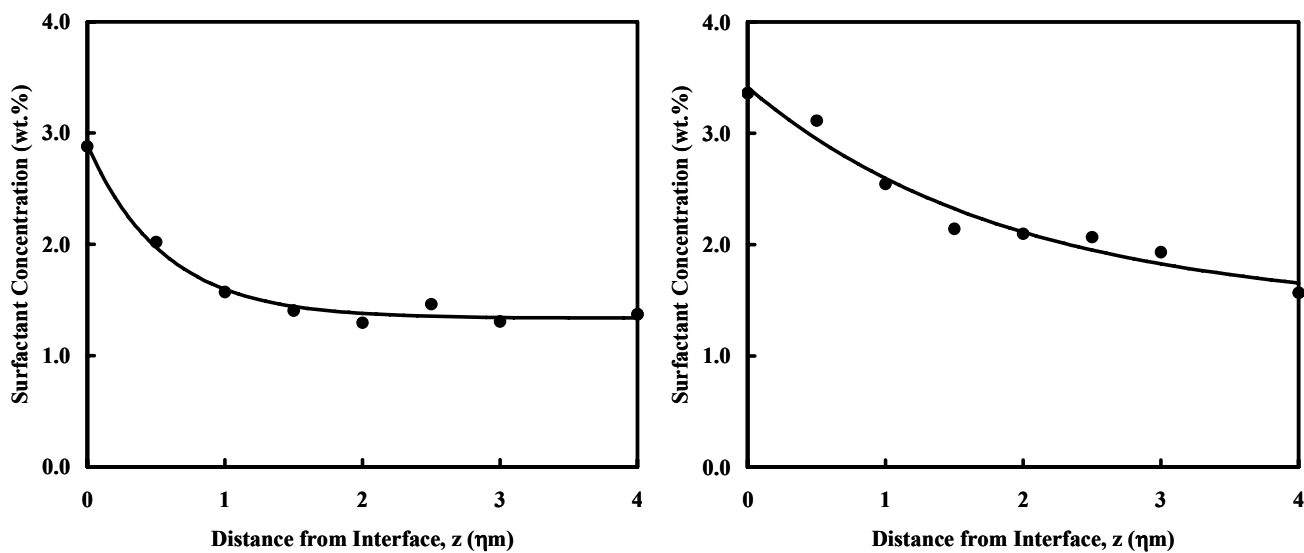


**Figure 72.** Fit of surfactant distribution for PSA 2 at (a) the film-air and (b) film-substrate interfaces using exponential decay model.

In order to better understand surfactant migration mechanism, more detailed analyses were carried out at the surfactant enrichment layers for both interfaces. It is found that the surfactant distribution curves are well fit by an exponential decay model shown in Fig. 72 for model PSA 2. At both interfaces, the surfactant distribution follows this exponential decay model, i.e.,

$$C(z) = C_0 + A \exp(-\alpha z) \quad (13)$$

where  $C(z)$  is surfactant concentration at a depth  $z$  from the interface,  $C_0$  is the bulk phase surfactant concentration, and  $A$  and  $\alpha$  are fitting constants indicating the maximum enrichment of surfactant and rate of decay, respectively. For film-air interface of PSA 2,  $C_0 = 1.34$ ,  $A = 1.56$ ,  $\alpha = 1.79$ , while for film-substrate interface of PSA 2,  $C_0 = 1.41$ ,  $A = 2.00$ ,  $\alpha = 0.52$ . The fitting parameters for model PSA 1 and 3 were also listed in Table 21. (For all 3 PSAs,  $r^2$  values for the model fits were  $> 0.97$ .) The differences in the shape of the surfactant distributions between the film-air and film-substrate are more quantitatively demonstrated by the model.

**Table 21:** Parameters from fit with exponential decay model

Fitting parameters		PSA 1	PSA 2	PSA 3
Film-air interface	$C_0$	1.84	1.34	1.41
	$A$	1.84	1.56	0.88
	$\alpha$	1.37	1.79	0.61
Film-substrate interface	$C_0$	1.43	1.41	-
	$A$	1.83	2.00	-
	$\alpha$	0.36	0.52	-

Films cast with PSA 3 where the nonionic surfactant dominates the binary mixture, only a small surfactant enrichment is found at the film-air interface, as shown in Fig. 73. The surfactant is distributed nearly evenly over the bulk film. These results are consistent with those reported by Evanson *et al.*,<sup>218</sup> who systematically investigated mobility of anionic and nonionic surfactants in ethyl acrylate/methyl acrylic acid latex films using FTIR-ATR. Since they did not have information about the depth profile, they concluded nonionic surfactant distributed evenly in the bulk film because surfactant enrichment was not found at film-air and film-substrate interfaces. A study on emulsion polymerization of styrene and methacrylic acid carried out with polyoxyethylene nonyl phenyl ether nonionic emulsifier found that nonionic surfactant is incorporated inside latex particles.<sup>231</sup> The amount of nonionic emulsifier that partitioned into the latex particle reached as high as 75 wt.% of total surfactant utilized. The lower HLB number of the nonionic surfactant, the greater the amount incorporated inside latex particles,<sup>239</sup> and it is difficult for these species to elute unless facilitated by higher temperatures. The smaller standard deviation of the data shown in the Fig.73 is consistent with a more even lateral distribution of the nonionic surfactant, which would be achieved by its incorporation into latex beads. It can be concluded that the small surfactant enrichment at the film-air interface observed for PSA 3 is likely caused by the migration of the 10 wt.% anionic surfactant in the blend. AFM observation is consistent with this assessment and strongly supports the results from Raman depth profiling of PSA films (Fig. 68c and Fig. 74c).

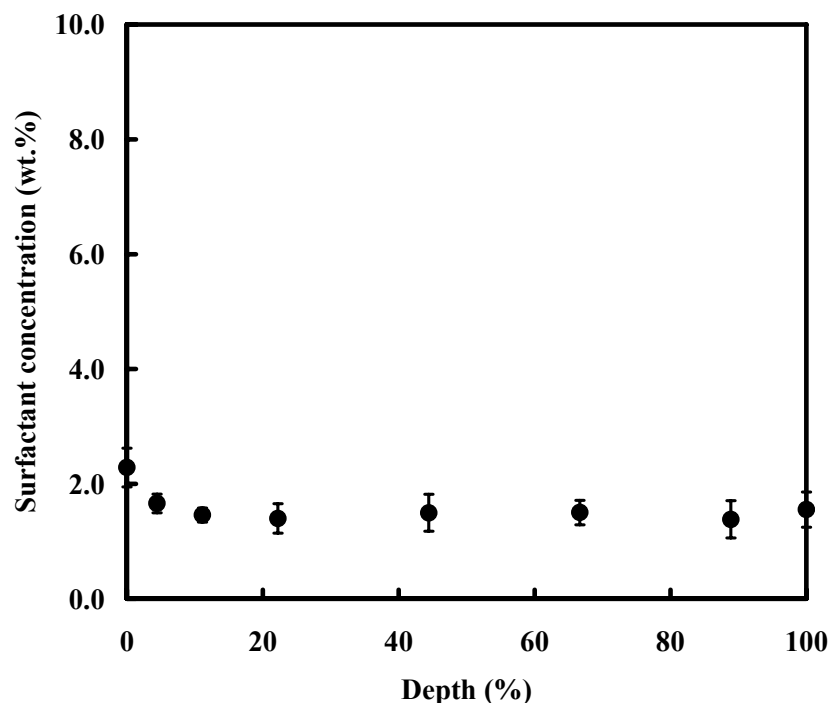


**Figure 73.** Surfactant distribution profile over the entire thickness of a film cast from PSA 3.

The results presented above indicate that nonylphenol ethoxylate surfactants tend to concentrate at film interfaces. The Raman depth profiling of surfactants also demonstrates that surfactant enrichment at the interfaces of PSA film depends primarily on the relative percent of anionic surfactant in the total surfactant content; the more anionic surfactant in the blend, the more significant the surfactant segregation. This is consistent with the water-flux mechanism. As mention above, anionic surfactant is more water soluble and hydrophilic (e.g. higher CMC and HLB number and much lower  $\text{Log } K_{ow}$  value), and thus these molecules are more apt to be found in the aqueous phase available to be carried to the film-air interfaces during water evaporation. However, it still remains to be determined whether the surfactant fate is a matter of kinetics with drying conditions and film structure pushing the distribution towards a metastable state. The films analyzed with CRM were all cast on release liner possessing a surface energy of about  $20 \text{ mJ/m}^2$ . It is interesting that the anionic surfactant migrates to both interfaces to almost the same extent. Figure 74 shows the AFM imaging of film-substrate interfaces of all model PSA drawdown films. The images are consistent with CRM depth profiling of surfactants in the model PSA films with PSA 1 demonstrating that highest surfactant content at the film-substrate interface followed by PSA 2. Little surfactant is found at the film-substrate interface for PSA 3.

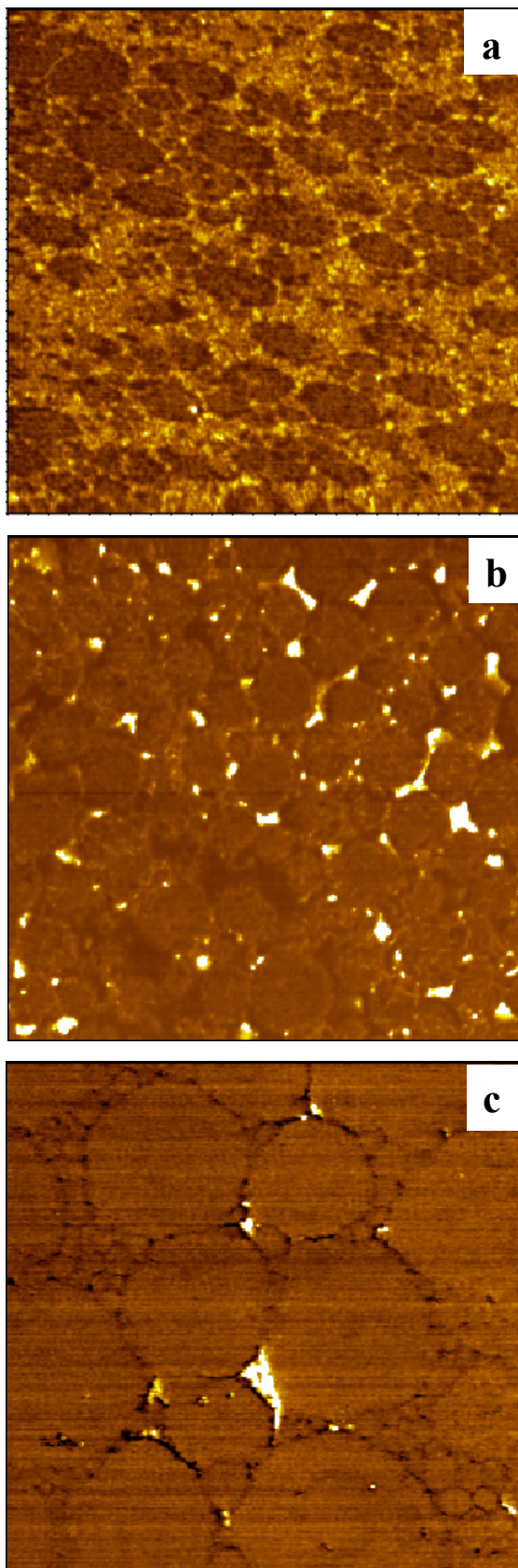


**Figure 74.** (a) AFM phase images of film-substrate interface of drawdown coatings of (a) PSA 1, (b) PSA 2 and (c) PSA 3. (Scan size  $2.5\ \mu\text{m} \times 2.5\ \mu\text{m}$ )

### 3.14 Modifications of Surfactant Distributions and Surface Morphologies in Latex Films due to Moisture Exposure

Surfactants are introduced to water-borne pressure-sensitive adhesive colloidal dispersions during emulsion polymerization in order to control both latex particle size and stability of formed dispersions. However, inclusion of surfactants, which are generally low molecular weight compounds (<1000 g/mol.) can have adverse affects on water resistance and performance properties of adhesives.<sup>196-200, 240</sup> These are caused by the fact that surfactant often concentrates in aggregates at film surfaces during water evaporation and formation.<sup>204, 206, 241-243</sup> Surfactant exudation upon latex film formation has been reported to occur toward film-air and/or film-substrate interfaces to produce a distribution of local surfactant concentrations.<sup>215, 202, 203</sup> It is also possible that surfactant species can migrate beyond adhesive surfaces to contaminate an adjacent ply in an adhesive laminant, for example facestock in printed label constructions. Although it is now well accepted that surfactants can concentrate at adhesive surfaces during coating processes, the mechanism involved is not well understood and thus neither is the subsequent movement and eventual fate of these species in adhesive films.

It has been reported that the main factors influencing migration of surfactants to interfaces during film formation includes chemical composition and structural characteristics of both surfactants and adhesive polymers and temperature.<sup>202, 246</sup> During coating processes, water is drawn to the surface and evaporates carrying with it and concentrating amphiphilic solutes. Thus it is likely that the tendency of surfactant species to collect at film surfaces is governed to large extent by their partitioning between aqueous (continuous) and polymer phases, behavior that is indicated by measures of their hydrophobicity, such as critical micelle concentration, hydrophilic-lipophilic balance, octanol-water distribution coefficient and pK<sub>a</sub> values for acidic functional groups.<sup>246-248</sup> In a previous publication, the authors demonstrated the significantly greater tendency of the anionic form of a nonylphenol ethoxylate surfactant to concentrate at the surface of an acrylic water-based PSA versus that of its nonionic form.<sup>246</sup> The difference was attributed to the greater hydrophilicity of the anionic species due to its ionized acid functional group(s). The importance of temperature in this process has been discussed by several authors. For example, Aramendia *et al.* reported an unexpectedly large amount of conventional surfactant was exuded to film surfaces when annealed at a temperature above the glass transition temperature of the polymer, compared to reactive surfactants (surfmers).<sup>249</sup> Scalarone *et al.* reported similar results demonstrating that aging at temperatures much higher than the polymer glass transition temperature promoted diffusion of surfactants to film surfaces.<sup>250</sup> In both of these examples, it was proven that an elevated temperature induced excess surfactant exudation at film interface by accompanying particle coalescence/water loss or promoted surfactant diffusion rate.

Here, results from an examination of the role of humidity on surfactant migration are discussed. Surfactant distributions in PSA films will likely govern to a great extent their interactions with moisture, thus characterizing this relationship is important to understanding how environmental conditions used for storage impacts performance of pressure sensitive (PS) products. As part of this study, films were cast and aged under various environmental conditions and movements of the surfactant species were monitored via atomic force microscopy (AFM) and confocal Raman microscopy (CRM). The combination of these techniques for this purpose was introduced in a recent article.<sup>246</sup> Past characterization of this mechanism relied almost exclusively on attenuated total reflectance–Fourier-Transform Infrared or ATR-FTIR spectroscopy.<sup>15, 19, 21, 39, 202, 203, 215, 218,</sup>

<sup>245, 247</sup> While this is effective at identifying the presence of the surfactant at the interface, it does not provide information on the overall distribution. Confocal Raman microscopy (CRM) measures the Raman spectra for a small volume of film without any modification of samples by combining a high resolution confocal microscope with a sensitive Raman spectroscopy system providing a powerful method for the depth profiling of thin films, coatings, membranes and composites.<sup>246, 210, 211</sup> Application of CRM, especially near interfaces, and fitting of data with an exponential decay model, provide for quantitative analysis of surfactant distributions at both film-air and film-substrate interfaces. Introduction of AFM phase images further elucidates the redistribution mechanism by providing a picture of how surfactants interact with moisture and the impact this has on surfactant migration.

## Experimental Section

**Materials.** A water-based PSA based on commercial formulations was synthesized at Franklin International (Columbus, OH) from the monomers *n*-butyl acrylate, vinyl acetate and methacrylic acid and a combination of an anionic surfactant, disodium ethoxylated nonylphenol half ester of sulfosuccinic acid (50 mass%), and a nonionic surfactant, nonylphenoxy poly(ethyleneoxy) ethanol (50 mass%). The solids content of produced latex was 60-63 mass% with a mean particle size of 690 nm diameter obtained via dynamic light scattering technique. The total surfactant content in films assuming complete retention is 0.025 mmol/g (1.8 mass%), and the glass transition temperature determined via dynamic mechanical analysis was -34 °C. Adhesive films of 1 mil (25.4 μm) thicknesses were generated by coating latex onto 60 lb. (60 lbs. of mass per 3000 ft<sup>2</sup> or 97.7 g/m<sup>2</sup>) silicone coated release liner using a wire wound rod and drying it in an 82 °C oven for 10 minutes. These so-called “draw-down” films were covered with an 80 lb. (130 g/m<sup>2</sup>) silicone coated release liner for migration experiments. PSA draw-down films were kept at 50% RH and 22 °C prior to being cut into 1 inch strips and introduced into environmental jars containing desiccant (0% relative humidity or RH) and water (100% RH) for long-term storage and humidity cycling tests. Spin-coated films were cast by spin coating PSA latex on 15 mm AFM specimen disks under ambient conditions. These films had a thickness of approximately 10 μm and were used for AFM imaging in an environmental chamber.

**Confocal Raman Microscopy.** An alpha 300R confocal Raman microscope equipped with a UHTS200 spectrometer and a DV401 CCD detector from WITec (Ulm, Germany) was employed to collect single Raman spectra from PSA films. A Nikon 100× oil immersion objective was used for all measurements. An Ar-ion laser with the wavelength of 514.5 nm and maximum power of 50 mW was used for excitation. Lateral resolution of the confocal Raman microscope according to the theory of light diffraction is about 250 nm and vertical resolution is about 500 nm. Since the sampling volume may be smaller than the average particle size of the latex spheres, measurements were conducted at several random locations on the film to minimize the variation. Raman spectra of film samples were recorded with the integration time of 240 s and laser power of 30 mW. Peaks at 1612 and 1735 cm<sup>-1</sup> are assigned to an aromatic C-C, on-ring stretch mode for the surfactant and carbonyl stretch mode of the polymer, respectively.<sup>248</sup> Calibration was carried out with standards produced from the adhesive polymer and pure surfactant. Pure polymer was isolated through dialysis of the latex and dissolution in tetrahydrofuran.

**Atomic Force Microscopy (AFM).** Atomic force microscopy (AFM) was used to examine the variation of surface morphologies of PSA films with relative humidity. Using a Molecular Imaging PicoPlus PicoSPM 3000 (Agilent Technology, Santa Clara, CA) system, AFM imaging was performed in an environmental chamber with controlled temperature and relative humidity (RH). Intermittent contact or tapping mode AFM was utilized. The principles and detailed information concerning this application of AFM are provided elsewhere.<sup>248</sup> For the AFM phase images presented here, the cantilever was operated in the repulsive regime with free oscillation amplitude of 300 nm and  $A/A_0 \sim 0.9-0.95$ , in which the viscous or more energy dissipative material produces a dark contrast on the phase image, while stiff or less energy dissipative materials provides bright contrast. Integrated silicon cantilevers with tip radii of curvature 5-10 nm were employed in AFM imaging. The spring constant of the cantilever was manufacturer-specified in the range of 30-60 N/m and the measured resonant frequency was within 10% of 300 KHz. AFM imaging of the spin-coat PSA films were conducted in ambient temperature but various relative humidity levels from 3% RH to 90% RH. To guarantee that an AFM image is representative, the measurements were conducted at least two times, imaging different regions of the same film sample.

## Results and Discussion

**Surfactant Migration under Constant Humidity Conditions.** Figure 75 shows surfactant concentration distributions or depth profiles for the original PSA films, which were coated, dried and stored at 50% RH and 22 °C. Analysis using CRM was carried out on 4 randomly selected coatings. The samples all have thicknesses of about 1 mil (24.5  $\mu\text{m}$ ) and show similar surfactant concentration profiles, in which surfactant enrichments at the film-substrate interface are higher than that at the film-air interface and bulk phase concentrations of the surfactant blend are close to the added concentration of 0.025 mmol/g. (Draw-down PSA films were analyzed from the film-air interface with 0% corresponds to the film-air interface and 100% to the film-substrate interface.) In Fig. 76, plots of averaged depth profile data are shown for film samples stored for 60 days at 0% RH (Fig. 76a) and 100% RH (Fig. 76b) and 22 °C. Each point is an average calculated for 5 or more measurements. Error bars are provided to indicate the estimated variation of these values. It can be seen that depth profile for the sample stored under dry conditions appears to show a slightly greater enrichment at the interfaces, especially at the film-substrate interface. In contrast, samples stored at 100% RH show a more even distribution of surfactant. It was noted that the thicknesses of PSA films after being aged at 100% RH for two months were found to be greater than that of films aged at 0% RH for the same period.

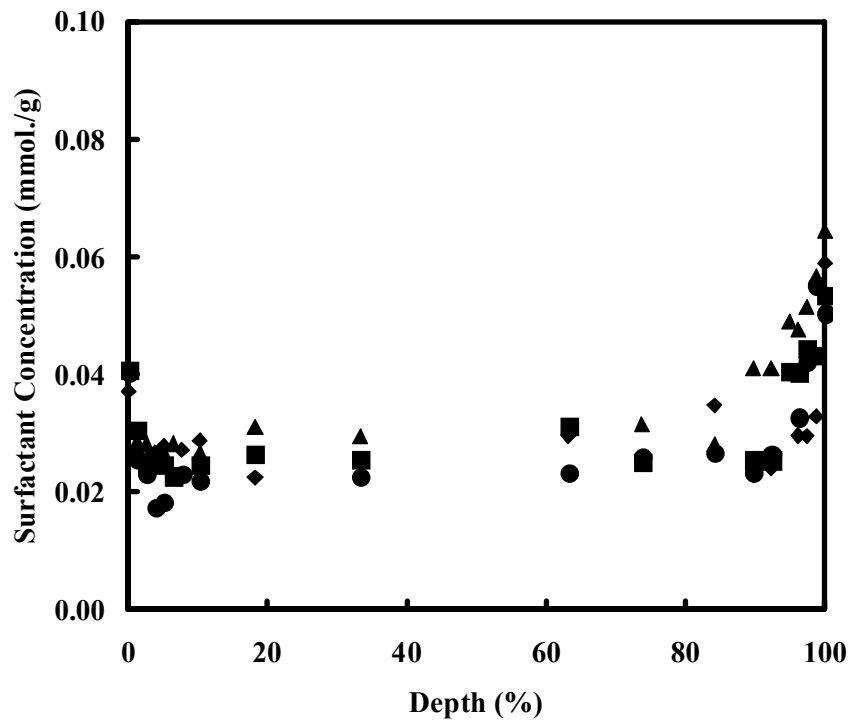


**Figure 75.** Surfactants distribution profile of original model PSA film, which was stored at 22 °C and 50% RH.



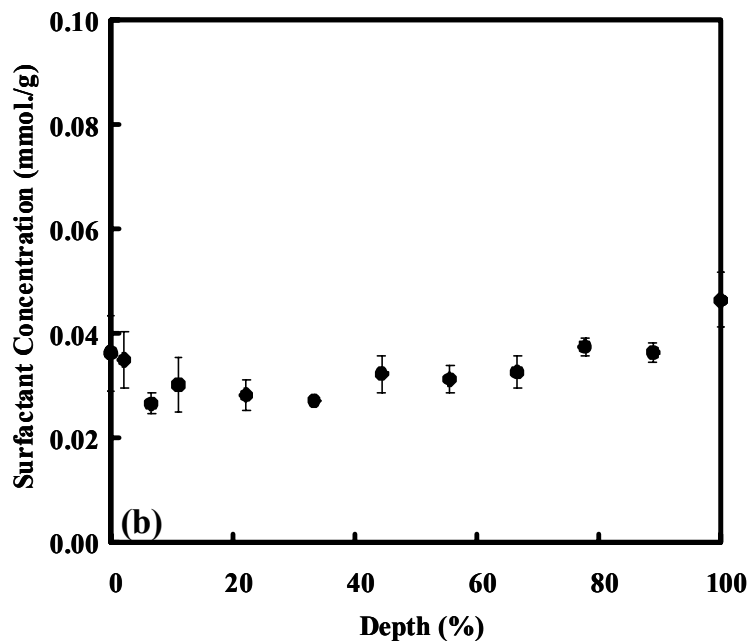
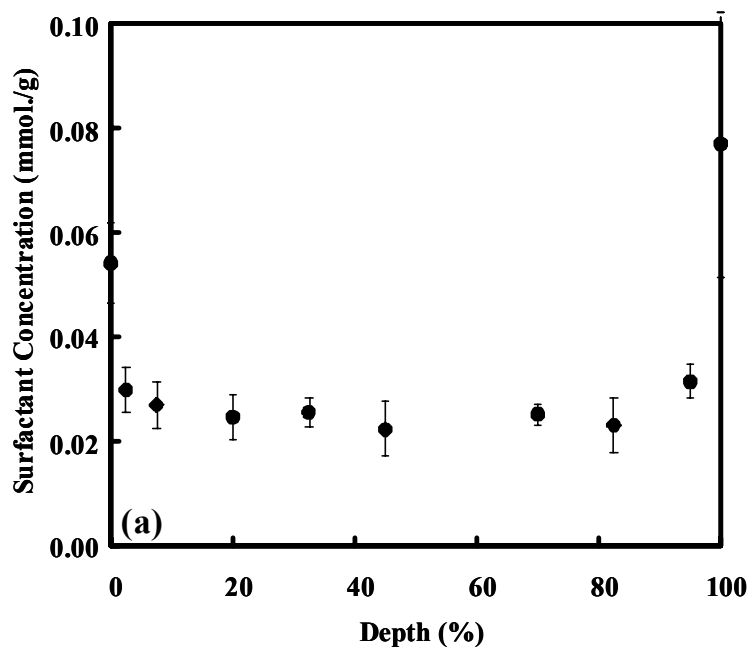


**Figure 76.** Surfactants distribution profiles of PSA film after being aged for 2 months at 22 °C and a.) 0% RH and b.) 100% RH.

**Table 22:** Parameters from fit with exponential decay model for surfactant distributions of model PSA films at 22 °C and relative humidity of 0 and 100%.

Interface	Parameters	50% RH*	0% RH	100% RH
Film-Air	$C_0$ (mmol/g)	0.0248	0.0257	0.0278
	$A$ (mmol/g)	0.0151	0.0284	0.0089
	$\alpha$ ( $\mu\text{m}^{-1}$ )	2.87	1.89	0.61
Film-Substrate	$C_0$ (mmol/g)	0.0257	0.0240	0.0338
	$A$ (mmol/g)	0.0308	0.0495	0.0123
	$\alpha$ ( $\mu\text{m}^{-1}$ )	0.528	0.99	0.14

\*original sample stored at 50% RH

A more direct Raman analyses at interfaces was carried out on the adhesive films. These involved multiple measurements within about the first 5  $\mu\text{m}$  of film surfaces where differences in surfactant concentrations are observed. It was shown previously that these surface distribution curves are well fit by the exponential decay model,<sup>246</sup> i.e.,

$$C(z) = C_0 + A \exp(-\alpha z) \quad (13)$$

where  $C(z)$  is surfactant concentration at a depth  $z$  from the interface,  $C_0$  is the bulk phase surfactant concentration, and  $A$  and  $\alpha$  are fitting constants indicating the maximum enrichment of surfactant and rate of decay, respectively. The fitting parameters are listed in Table 22 along with those for the samples aged at 0 and 100% RH for 60 days. (For all PSA films,  $r^2$  values for the model fits were  $> 0.92$ .) For the purpose of monitoring the impact of humidity on surfactant distributions, Eq. 13 is modified to the form,

$$C(z)/C_0 = 1 + \kappa \exp(-\alpha z) \quad (14)$$

where  $\kappa$  is equal to  $A/C_0$  and defined as the enrichment factor. This dimensionless parameter indicates the surface concentration of a surfactant relative to the bulk. Enrichment factors for the original samples and those aged for 2 months are listed in Table 23. It can be seen that, in general, storage at 100% RH significantly decreases the enrichment factor at both interfaces, while storage at 0% RH increases it. This would indicate that the presence of moisture or the direction the moisture flows determines whether the surfactant enrichment is enhanced or diminished. It also appears that there is a greater change in the enrichment factor at the film-substrate interface than that at film-air interface. It is possible that this difference may result from the design of the storage laminate. As discussed above, PSA films are produced by coating the latex onto a 60 lb. release liner (defined as the substrate), drying the coating in an oven to form the adhesive film, and then covering it with an 80 lb. liner. The 60 lb. and 80 lb. liner have measured water vapor transmission rates of 710  $\text{g}/\text{m}^2$  day versus 488  $\text{g}/\text{m}^2$ , respectively. Thus, we would expect a greater movement of moisture through the film-substrate interface.

**Table 23:** Enrichment factors for PSA films.

<b>Interface</b>	<b>50% RH*</b>	<b>0% RH</b>	<b>100% RH</b>
Film-Air	0.609	1.10	0.320
Film-Substrate	1.198	2.06	0.364

**Surfactant Migration with Humidity Cycling.** From the results presented above, it appears that surfactant enrichment at interfaces is dependent on moisture. What is not clear from the static humidity tests is the mechanism involved. In this section results for the movement of surfactants in PSA films exposed to humidity cycling is reviewed. Each 48-hour cycle involves aging of a PSA film at 22 °C in 0% RH for 24 hours and then at 22°C and 100% RH for an additional 24 hours. The purpose of this study is to help determine if surfactants simply migrate with the moisture flux or if there are changes in the form the surfactant aggregates, latex film or some combination that is being observed.

**Table 24:** Enrichment factors for PSA films aged at 22 °C and cycled between 0% and 100% RH. Also shown are the enrichment factors for a sample stored for 5 days at 22 °C and 0% RH and films that were dissolved in THF prior to coating to eliminate the residual latex structure.

<b>Interface</b>	<b>2 cycles, conditioned at 0% RH for 1 day</b>	<b>Conditioned at 0% RH for 5 days</b>	<b>Dissolved in THF, conditioned for 1 day</b>	
			<b>0% RH</b>	<b>100% RH</b>
Film-Air	0.494	0.626	0.575	0.564
Film-Substrate	0.663	1.955	0.602	0.546

Table 24 lists enrichment factors from surfactant distributions for both adhesive interfaces exposed to 2 full humidity cycles and then dried. The table also shows  $\kappa$  values for interfaces of films stored solely at 0% RH and 22 °C over the same time period. There are increases in the surface enrichment for films stored under static conditions for 5 days at 0% RH, but they are smaller than those found for films stored under the same conditions for 60 days. In contrast samples exposed to humidity cycling demonstrate a reduction in the enrichment factor at both interfaces. Another interesting phenomenon associated with this study is the reduction in variation of concentration measurements. For example, standard deviations associated with first cycles were about 1.0%, by the end of the second cycle they were 0.30%.

It appears that humidity cycles produce a more even distribution of surfactant species, as well as changes in the structure of PSA films. It was previously reported that surfactant aggregates tend to locate in interstitial regions at PSA film surfaces.<sup>246</sup> In order to gauge the impact of residual latex structure on surfactant distribution, a film was cast in which the structure was eliminated. This was accomplished by dissolving the PSA in tetrahydrofuran and coating the solution on 60

lb. release liner, which was then dried and covered with 80 lb. liner. Figure 77 shows AFM height images for the top surfaces of PSA and solvent cast films. It is clear that the latex structure, which is retained at the interface in PSA films (Fig. 77a), is absent at the surface of solvent cast film (Fig. 77b). Surfactant enrichment values from fits of CRM data with Eq. 14 after solvent cast films were aged in 0% RH and 100% RH and 22 °C for one day are also listed in Table 24. It can be seen that surfactant enrichment at interfaces of solvent cast films are lower than what would be expected for latex aged under the same conditions. Surfactant enrichments at both interfaces of aged samples are summarized in Figure 78. There clearly exists a move towards a more even distribution of surfactant.

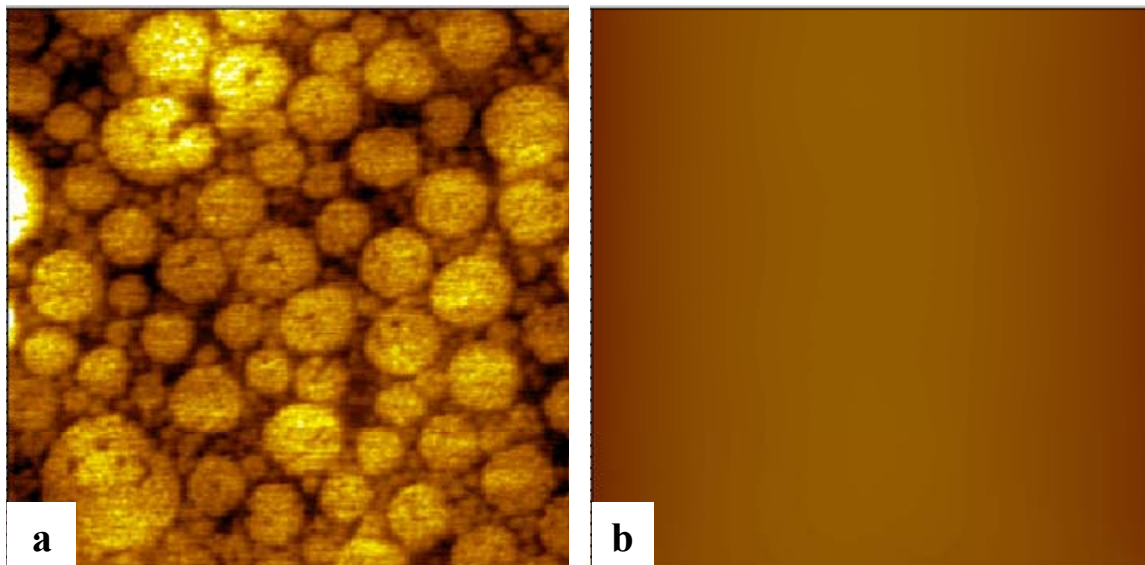


**Figure 77.** AFM height images of the surface of a.) a PSA film showing its residual latex structure and b.) a film produced by first dissolving the latex in THF (scanning size  $5\mu\text{m}\times 5\mu\text{m}$ ).

Figure 79 shows AFM height and phase images of film-air interfaces from a PSA film obtained in a humidity chamber at ambient temperatures. The film is exposed to a cycle that begins with equilibration at 25% RH (Fig. 79a). The RH is then raised to 90% for equilibration (Fig. 79b) and then reduced back to 25% RH (Fig. 79c). For PSA at low RH, the bright regions around the latex particles are thought to be surfactant and salt aggregates. The brightness of these regions relative to the dark background, which is composed of latex polymer, indicates a more elastic substance. These aggregates are spread over the entire film but reside primarily in the interstitial regions between latex particles. Average roughness,  $R_a$ , obtained from the AFM topographs (shown in Fig. 79 middle) is 58 nm and this appears to be due to the aggregated materials. Raising the relative humidity to 90% RH, appears to switch the relative level of viscoelasticity between the surfactant and latex polymer and likely the spreading of the surfactant to form a thin layer, which coats the film. This is consistent with the lower measured  $R_a$ , which is 32 nm. The

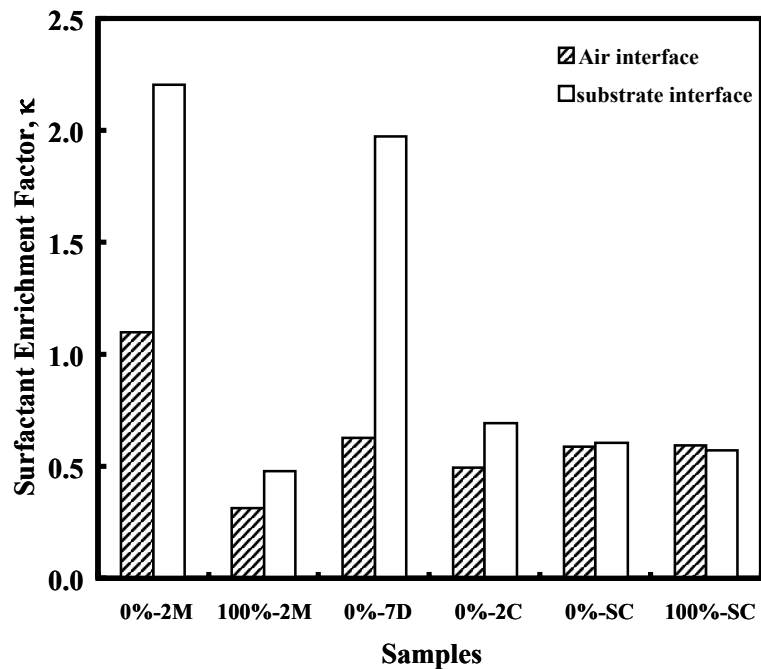


**Figure 78.** Enrichment factors at both interfaces for PSA films aged at 22 °C under various humidity conditions, including 0% and 100% RH for 60 days (0%-2M and 100%-2M, respectively), 0% RH for 7 days (0%-7D), 2 humidity cycles and 0% RH for 1 day prior to testing (0%-2C), solvent cast films stored at 0% and 100% RH for 1 day (0%-SC and 100%-SC, respectively).

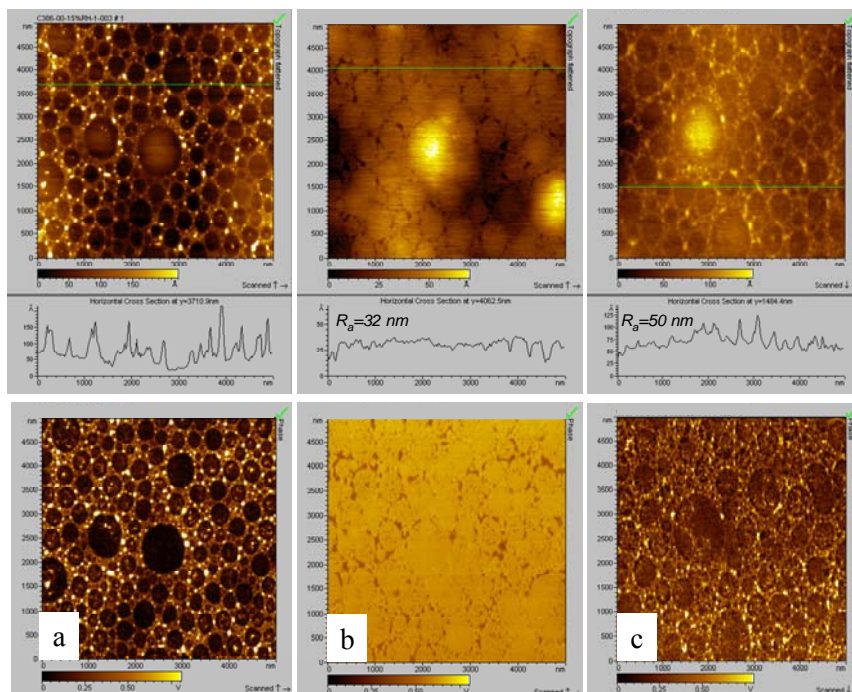


**Figure 79.** AFM images of model PSA film surface obtained at (a.) 22 °C and 25% RH, (b.) 22 °C and 90% RH, and (c.) dry back from 90% RH to 25% RH at 22 °C (upper: height image, bottom: phase image).

phase contrast image for the film after the humidity chamber was brought back to 25% RH over a short time frame is shown in Fig. 79c. Once again shows a distribution of bright specks, but these appear to be more evenly distributed and  $R_a$  again increases to 50 nm, slightly lower than the initial value. More telling are the phase images of the solvent rinsed PSA film obtained at RH levels of 3% and 90%, respectively (as shown in Figure 80). It can be seen that for the PSA film-air interface, the phase contrasts did not change with the variation of moisture, and the roughness is low,  $R_a=34$  nm.

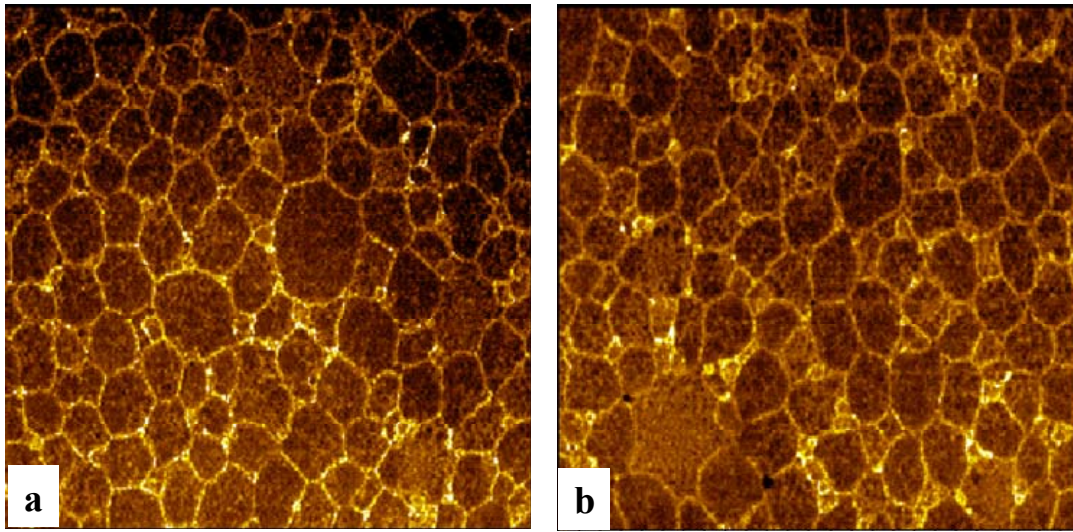


**Figure 80.** AFM phase images acquired for the model film subsequent to rinsing with solvent at 22 °C and (a.) 3% RH and (b.) 90% RH (scanning size  $5\mu\text{m}\times 5\mu\text{m}$ ).

***Surfactant and Polymer Phase Intermixing.*** From the results above, it appears that exposure of the PSA films to high humidity results in the lateral migration of surfactant from aggregates formed during the coating and drying process. This is evident from the AFM images and it also appears to influence the CRM data. The apparent reduction in the enrichment factor at high humidity could indicate that vertical migration of surfactant is occurring. To test for this possibility, experiments were carried out in which pure surfactant was placed on the surface of PSA films and films were aged under extreme humidity conditions. For these experiments, dialysis was carried out on the commercial PSA to remove a majority of the existing surfactant in the formulation. The latexes were then used to cast films to which anionic and nonionic surfactant were added and samples were stored in 0% and 100% RH containers at 22 °C for 1 day.

Figure 81a shows the concentration profiles of the nonionic surfactant in adhesive films aged at both 0 and 100% RH. No difference was observed between samples aged at the different humidity, so values were averaged. Surfactant was added at levels up to 54 mass% in the latex following dialysis. The dotted line indicates the concentrations of surfactant added. It can be seen that amount added becomes evenly distributed throughout the film, even at these high concentrations. It was also found that the nonionic surfactant has the ability to solubilize the

polymer. Thus it appears to be highly compatible with the latex polymer, and this compatibility is not affected by different humidity levels. Although re-addition of surfactant subsequent to dialysis could conceivably produce differences in contact between surfactants and latex particles, these differences would be expected to lessen the degree of interactions and are a stricter test for compatibility. This result indicates that changes in the surfactant distributions are due primarily to the behavior of the anionic species.

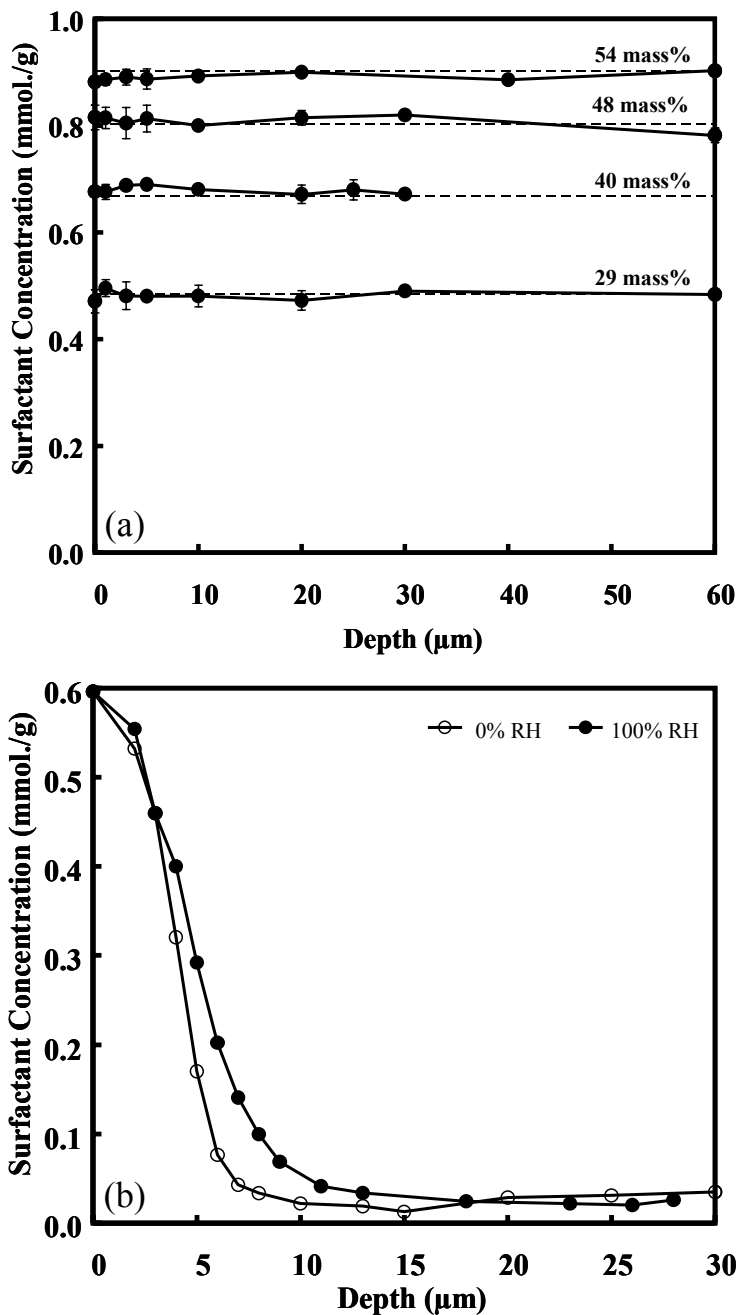


Figure 81. Compatibility of nonionic surfactant (a) and anionic surfactant (b) with polymer phase in the dialyzed model PSA film.

Attempts to generate a curve similar to Fig. 81a by adding anionic surfactant to dialyzed PSA latex produced significant variations in surfactant concentration and increasing interfacial enrichment with greater surfactant addition. This led to an alternative approach in which dried anionic surfactant was applied to the film-air interface of films cast from the dialyzed sample. Figure 81b shows a plot of surfactant concentration versus film depth for anionic surfactant on PSA, which was stored at both 0 and 100% RH. The interface between the nearly pure surfactant layer and film can be clearly identified for 0% RH but is more diffuse under the high humidity conditions. However, the concentration plateaus at what appears to be a similar concentration of  $0.022 \pm 0.004$  mmol./g. It is evident that the anionic surfactant is much less compatible and also appears to be unaffected by changes in humidity. Its level in the polymer phase is slightly lower than the concentrations added to the PSA during its synthesis. From this it might be concluded that enrichment is simply a matter of solubility. However, given the complexity of these systems, further study is necessary, but it appears fair to conclude that the compatibility is a key factor governing distribution behavior. With regard to the vertical movement of the surfactant, the diffuse interface is consistent with the greater mobility of the surfactant. In other words, it is possible that the surfactants migration under high humidity conditions may include its movement to occupy surface area throughout the interfacial region, including that which may exist several microns into the film.

### **Summary and Conclusions**

Measurements using CRM indicate significant enrichments of nonylphenol ethoxylate, anionic surfactant at interfaces water-based acrylic PSAs when stored at 0% RH for an extended time period, and a more even distribution when stored at 100% RH. However, concentration measurements recorded for confocal planes at the surface of films are highly variable for samples stored under the high humidity conditions. Cycling the films between 0% RH (24 hr.) and 100% RH (24 hr.) produced a more even distribution of surfactant at interfaces and a substantially reduced variability in measurements, comparable to that found for the sample stored for 60 days at 100% RH. Similar results were also obtained when films were dissolved in THF and cast. AFM topographs show that surfactant aggregates protrude from the surface of films cast from latex emulsions, which is primarily responsible for the measured surface roughness. With exposure to high humidity, aggregates are no longer distinguishable and the phase contrast of the film surface is reversed. Also, surface roughness is diminished to levels measured when the surfactant is removed. Upon returning to low humidity conditions, aggregates are again apparent, but as a greater number of smaller domains, which are more evenly distributed. It is speculated that the greatly enhanced mobility of the surfactant at high humidity and formation of smaller, more evenly distributed aggregates are responsible for the observed reduction in the enrichment factor at 100% RH and subsequent to humidity cycling, respectively. Although film compatibility is a major factor determining interfacial enrichment, it does not appear affected by changes in humidity. Future work will examine structure in which surfactant materials are held in the latex polymer and well as the spreading behavior observed on polymer surfaces for high humidity.



## 4. Accomplishments

### 4.1 Publications

1. Xu, G. H., Dong, J., Zhang, J., Severtson, S. J., Houtman, C. J. and Gwin, L. E. Modifications of Surfactant Distributions and Surface Morphologies in Latex Films due to Moisture Exposure, *Journal of Physical Chemistry B*, 113(30), 10189-10195, 2009.
2. Pu, G. and Severtson, S. J. Dependency of Contact Angle Hysteresis on Crystallinity for n-Alkane Substrates, *Journal of Physical Chemistry C*, 113(16), 6673-6680, 2009.
3. Pu, G. and Severtson, S. J. Variety of Wetting Line Propagations demonstrated on a Viscoelastic Substrate, *Applied Physics Letters*, 94, 134101-134103, 2009.
4. Xu, G. H., Dong, J., Zhang, J., Severtson, S. J., Houtman, C. J. and Gwin, L. E. Characterizing the Distribution of Nonylphenol Ethoxylate Surfactants in Water-based Pressure-Sensitive Adhesive Films using Atomic-Force and Confocal Raman Microscopy, *Journal of Physical Chemistry B*, 112(38), 11707-11914, 2008.
5. Pu, G. and Severtson, S. J. Dynamic Stick-and-Break Wetting Behavior on the Surface of a Highly Viscoelastic Polymer, *Langmuir*, 24(9), 4685-4692, 2008.
6. Guo, J., Severtson, S. J., Gwin, L. E. and Houtman, C. J. Role of Adhesive Formulation and Laminate Design in Determining Removal Efficiencies of Emulsion-type Pressure Sensitive Adhesive Films from Recycling Operations, *Industrial & Engineering Chemistry Research*, 47(8), 2612-2617, 2008.
7. Wang, J., Calhoun, M. D. and Severtson, S. J. Dynamic Rheological Study of Paraffin Wax and its Organo-Clay Nanocomposites, *Journal of Applied Polymer Science*, 108(4), 2564-2570, 2008.
8. Pu, G., Guo, J., Gwin, L. E. and Severtson, S. J. Mechanical Pinning of Liquids through Inelastic Wetting Ridge Formation on Thermally Stripped Acrylic Polymers, *Langmuir*, 23(24), 12142-12146, 2007.
9. Wang J., Severtson, S. J., and Geil, P. H. Brittle–Ductile Transitions and the Toughening Mechanism in Paraffin/Organoclay Nanocomposites, *Materials Science and Engineering A*, 467(1-2), 172-180, 2007.
10. Guo, J., Severtson, S. J. and Gwin, L. E. Optimizing the Monomer Composition of Acrylic Water-based Pressure Sensitive Adhesives to Minimize their Impact on Recycling Operations, *Industrial & Engineering Chemistry Research* 46(9), 2753-2759, 2007.
11. Wang, J., Severtson, S. J. and Stein, A. Significant and Concurrent Enhancement of Stiffness, Strength, and Toughness for Paraffin Wax through Organoclay Addition, *Advanced Materials*, 18(12), 1585-1588, 2006.

## 4.2 Presentations

1. Severtson, S. J., Xu, G. H., Zhang, J., Houtman, C. J., Gwin, L. E., Migration of Surfactants in Pressure Sensitive Adhesive Films and the Impact on Performance Properties. Proceedings of the Pressure Sensitive Tape Council's TECH XXXII, held in Orlando, FL, May 13<sup>th</sup> - 15<sup>th</sup>, 2009.
2. Pu, G., Guo, J., Gwin, L. E. and Severtson, S. J., Mechanical Pinning of Liquids through Inelastic Wetting Ridge Formation on Thermally Stripped Acrylic Polymers, presented at the 236<sup>th</sup> ACS National Meeting held in Philadelphia, PA August 17<sup>th</sup> – 21<sup>th</sup>, 2008.
3. Xu, G. H., Dong, J., Severtson, S. J., Houtman, C. J., Gwin, L. E., Monitoring Surfactant Migration in Water-based Pressure-Sensitive Adhesive Films using Atomic-Force and Confocal Raman Microscopy, presented at the 236<sup>th</sup> ACS National Meeting held in Philadelphia, PA August 17<sup>th</sup> – 21<sup>th</sup>, 2008.
4. Severtson, S. J., Larry E. Gwin, L. E., and Houtman, C. J., Future Designs of Pressure Sensitive Adhesives, presented at the 12<sup>th</sup> Annual Green Chemistry and Engineering Conference held in Washington, DC, June 24<sup>th</sup> -26<sup>th</sup>, 2008.
5. Severtson, S. J. (Invited), Recycling Compatible Hot-Melt and Water-Based Pressure Sensitive Adhesives. Proceedings of the Pressure Sensitive Tape Council's TECH XXXI, held in Baltimore, MD, May 7<sup>th</sup> - 9<sup>th</sup>, 2008.
6. Severtson, S. J. (Invited), Wetting, Adhesion and Recycling of Polymers used in Pressure-Sensitive Adhesives, Invited Speaker at North Carolina State University, College of Textiles, May 6<sup>th</sup>, 2008.
7. Severtson, S. J. (Invited), Design of Recyclable Materials, presented at the 2008 World Adhesive Conference held in Miami, FL, April 20<sup>th</sup> – 23<sup>rd</sup>, 2008.
8. Houtman, C., Guo, J., Severtson, S., Xu, H., Gwin, L., Properties of Water-Based Acrylic Pressure Sensitive Adhesive Film in Aqueous Environments, 8<sup>th</sup> TAPPI Research Forum on Recycling held in Niagara Falls, Ontario, Canada, September 23<sup>rd</sup> - 26<sup>th</sup>, 2007.
9. Severtson, S. J., Guo, J., Gwin, L. E., and Kroll, M. S., The synthesis and Formulation of Environmentally Benign Pressure Sensitive Adhesives, presented at the 234<sup>th</sup> ACS National Meeting and Exposition held in Boston, MA August 19<sup>th</sup> – 24<sup>th</sup>, 2007.
10. Pu, G., Wang, J., Severtson, S. J. Properties of Paraffin Wax/Montmorillonite Nanocomposite Coatings. NSTI Nanotech, held in Santa Clara, CA, May 20<sup>th</sup> - 24<sup>th</sup>, 2007.
11. Severtson, S. J. (Invited), Making Pressure Sensitive Adhesives Recycling Compatible, Invited Speaker for the 2007 AF&PA Industrial Liaison Meeting, April 25<sup>th</sup>, 2007, held at the Forest Products Laboratory in Madison, WI.

12. Li, H., Severtson, S. J., Houtman, C. J. and Gwin, L. E., Interaction of Pressure Sensitive Adhesive Thin films with Moisture, 2007 Spring AIChE meeting held in Houston, TX, April 21<sup>st</sup> – 24<sup>th</sup>, 2007.
13. Verhulst, R. P., Severtson, S. J., Guo, J. and Houtman, C. J. Properties of Pressure Sensitive Adhesives Found in Paper Recycling Operations. 2006 TAPPI Engineering, Pulping and Environmental Conference held in Atlanta, GA, November 8<sup>th</sup> – 11<sup>th</sup>, 2006.
14. Wang, J., and Severtson, S. J., Development of Recyclable Paraffin-Based Composite Coating for Moisture Barrier Applications, 2005 AIChE Annual Meeting held Cincinnati, OH, October 30<sup>th</sup> – November 4<sup>th</sup>, 2005.
15. Guo, J., Severtson, S. J., Lien, J. A. Controlling Adhesive Behavior during Recycling. Pressure Sensitive Tape Council TECH XXVIII, held in Baltimore, MD, May 4<sup>th</sup> – 6<sup>th</sup>, 2005.
16. Guo, J., Verhulst, R. P., Severtson, S. J., Kroll, M. S., and Houtman, C. J. Limiting the Impact of Pressure Sensitive Adhesives on Paper Recycling by Controlling their Fragmentation during Repulping. 2004 AIChE Annual Meeting held Austin, TX, November 7<sup>th</sup> – 12<sup>th</sup>, 2004.
17. Houtman, C. J., Scallon, K. L., Guo, J., Wang X. –P., Severtson, S. J. and Kroll, M. S., Nowak, M. J., Controlling Adhesive Behavior during Recycling. 7<sup>th</sup> Research Forum on Recycling, held in Quebec City, Canada, September 27<sup>th</sup> – 29<sup>th</sup>, 2004.
18. Verhulst, R. P., Guo, J., Severtson, S. J., Kroll, M. S. and Nowak, M. J., Commercially Feasible Environmentally Benign Pressure Sensitive Adhesive Products, 2004 ASC Fall Convention and Exposition held in Pittsburgh, PA, September 19<sup>th</sup> – 22<sup>nd</sup>, 2004.

### ***4.3 Commercialized Technology***

As discussed in previous sections, publication of approaches for designing adhesives and laminates that inhibit the fragmentation of PSAs during repulping operations allows interested companies to take advantage of our research results. Our industrial partner, Franklin International (Columbus, OH), used the findings to identify 3 existing formulations as recycling compatible (Covinax 418-01, Covinax 379-05 and Covinax 324-39). Also, 3 new recycling compatible formulations were developed (Covinax 2000-EP110, LT0602-062 and LT0602-044). The limited impact of these 6 formulations on paper recycling operations was confirmed at the USDA Forest Service, Forest Products Laboratory (Madison, WI) using the Laboratory Testing Protocol for Paper Labels Coated with Environmentally Benign Pressure-Sensitive Adhesives. (This is currently the most widely accepted protocol for certifying PSAs as recycling compatible.) For more information on Franklin International's recycling compatible product line and their partnership in this project see their website ([www.franklinadhesives.com](http://www.franklinadhesives.com)).

During this project, which focused primarily on water-based acrylics, product development also continued from U.S. Department of Energy Project DE-FC07-00ID13881, which focused on styrenic block copolymer based hot-melt technology. Five hot-melt products were certified as recycling compatible using the Laboratory Testing Protocol for Paper Labels Coated with

Environmentally Benign Pressure-Sensitive Adhesives. These products are marketed by H. B. Fuller Company (St. Paul, MN). Fuller has formed partnerships with several converters and their adhesives can be found in green PS label products.

## 5. Conclusions

### **Development of Recycling Compatible Pressure-Sensitive Adhesive**

- Removal efficiencies of water-based acrylic PSAs are governed by their strength when saturated with water (i.e., their wet strength).
- Wet-strength of PSA films is governed primarily by their monomer composition, relatively minor changes in this content produce significant changes in the wet-strength and fragmentation during repulping operations.
- Amphiphilic chemicals tend to collect at the film-air interface of water-based PSAs influencing their surface properties.
- The presence of wetting agents and emulsifiers increase fragmentation, but the extent of this effect depends on the wet-strength of adhesive films.
- The effect of paper facestocks on water-based acrylic PSAs appears to be tempered by the presence of surfactant species.
- These findings demonstrate the need for a comprehensive approach that considers PSA properties, impact of formulation additives and properties of laminate components when designing recycling compatible PS label products.

### **Design of Nanocomposite Barrier Coatings for Corrugated Boxes**

- Laboratory studies indicate that wax contamination results from the release of wax flakes near failure regions while treated boxes are being broken down and that most of the wax rejects are still attached to the circular board rejects subsequent to repulping.
- There exists a temperature window for maximum wax removal, which is believed to be tied to the plastic crystalline states of wax: removal efficiencies are maximized in the mesophase region of macrocrystalline paraffin waxes.
- Organo-clay can be exfoliated and dispersed in melted paraffin wax via ultrasonic processing and without the use of additives and initial (unpublished) studies indicate this can also be achieved through the use of a twin-screw extruder.
- Nanocomposite wax coatings demonstrate a concurrent enhancement of stiffness, strength and ductility with no evidence of modifications to the crystal structure, degree of crystallinity or phase behavior resulting from the clay addition.

- Wax-clay composite coatings do not show higher removal efficiencies than regular wax, probably because the composite is more brittle and the flaking under shear stress is more serious. This result was found in both laboratory experiments and pilot-trials.
- Nanocomposite coatings do however demonstrate a reduction in surface cracking and a less significant loss in crystallinity with processing. Both of these impact the interaction of coatings with moisture. Crystallinity was found to govern the wetting of coated surfaces with a reduction in crystallinity producing a greater concentration of hydrophilic regions or defects, which tend to pin the receding movement of the contact line.

### **Wetting and Adhesion involving Polymeric Thin Films**

- It was observed that water droplets are unable to propagate on the surface of purified PSA polymers.
- Wetting experiments showed novel behavior including formation of a wetting ridge structure substantially larger than those reported elsewhere, complete halting of the three-phase line, and metastable angles ranging from 0 to greater than  $170^\circ$  achieved through changes in sessile drop volume.
- Greater angles were prevented by the collapse of the meniscus. This required step led to the naming of the observed wetting mechanism as “stick and break” propagation.
- In Wilhelmy plate experiments for metal plates coated with the polymer, this mechanism produces a quasi-periodic pattern of lines composed of ridge structures. We have tied the frequency of these ridges and their magnitudes to properties of both the wetting liquids and the polymers.
- These findings clearly have applications outside of the adhesives market such as microfluidics, which we are currently investigating.

### **Diffusion and Solubility of Surfactants in Polymeric Thin Films**

- An approach was developed, which combines confocal Raman and atomic force microscopy techniques, for probing the distribution of surfactants in latex-cast PSA films.
- A method was devised for measuring surfactant solubility in latex polymers and demonstrated that nonionic surfactants likely do not contribute to interfacial enrichment. Results indicate that surfactant-polymer compatibility may be important factor in determining migration behavior.
- Movement of anionic surfactant species and changes in aggregation regions at film surfaces during exposure of PSA films to changing relative humidity conditions was characterized. Results indicate that storage of PSA products can impact their performance including their recycling behavior.
- Current research is investigating refinement of confocal Raman microscopy for detecting the migration of surfactant species over concerns with the approaches practiced in the

identification of interfacial regions. Results of this work will provide a clearer insight into changes that occur in surfactant distributions and results of long-term storage and exposure to various environmental conditions.

## 6. Recommendations

This project produced an understanding of the properties controlling the fragmentation behavior of PSAs. (The fragmentation of these materials inhibits their removal from paper recycling operations using cleaning and screening processes.) It also provided guidelines for producers on how to design recycling compatible PSA without raising costs or sacrificing performance. These involve the proper selection of monomers and additives and label laminate designs that promote films that are removed from recycling operations with high efficiencies. This work has led to the development of a number of commercial products and initiated efforts to mandate use of recycling compatible structures.

Combined with those from U.S. Department of Energy Project DE-FC07-00ID13881, our findings cover both thermoplastic or hot-melt and emulsion or water-based PSA formulations. These 2 types of PSAs compose nearly all of the PS label market. The next step in this research is the development of guidelines for making these adhesives compostable. As we found in the case of recycling compatible PSAs, reducing or eliminating the major challenges associated with designing of these products should make their pursuit more appealing for producers. This is especially true in the current business climate in which interest in environmental friendly products is high. If similarly successful research can be completed in this area, the means for producing both recycling compatible and compostable, commercially-feasible PS products will be available. In other words, the tools necessary to both isolate and compost the label adhesive.

## 7. Literature Cited

1. [http://www.afandpa.org/Content/NavigationMenu/Environment\\_and\\_Recycling/Recycling/Recycling\\_Facts/Recycling\\_Facts.htm](http://www.afandpa.org/Content/NavigationMenu/Environment_and_Recycling/Recycling/Recycling_Facts/Recycling_Facts.htm).
2. Friberg, T., Progress Paper Recycling, 1996, 6, 70. 2004 AF&PA Recycling Task Group Report, AF&PA/FBA Symposium, October 10, 1996, Chicago.
3. Petrie, Edward. "Tapes and Labels Market Survey." Adhesives and Sealants Dec. 6, 2005 and Dec. 12, 2007 <<http://www.specialchem4adhesives.com/resources/articles/printarticle.aspx?id=1311>>.
4. Severtson, S. J., Coffey, M. J. and Nowak, M. J. Dispersion of Waxes During the Recycling of Old Corrugated Containers, *TAPPI Journal*, 1999, 82(12), 67-74.
5. Sirota, E.; King, H.; Shao, H. Rotator Phases of the Normal Alkanes: An X-ray Scattering Study. *J. Chem. Phys.* 1993, 98, 5809-5824.
6. Putz, H. In *Recycled Fiber and Deinking*; Götsching, L., Pakarinen, H., Eds.; Fapet Oy: Finland, 2000, Chapter 11.
7. Severtson, S. J. and Coffey, M. J., Contaminant dispersants useful in recycling of treated containers, United States Patent 6,548,558 issued April, 15, 2003.
8. Nguyen, D. Prevention of Pitch and Stickies Deposition on Paper-Forming Wires via Adsorption of a Cationic Polymer Associated with Anionic Species. *Tappi J.* 1998, 81, 143-151.
9. Weigl, J.; Wilken, R. In *Pulp, Paper and Board*; Hendry, I.; Hanssens, W., Eds.;

- Elsevier Applied Science: London, **1987**, p 60.
10. Li, C.; Hipolit, K.; Longhini, D. A. Removal of Stickies and electrostatic Inks using Flotation Process, *1996 TAPPI Recycling Symposium*, New Orleans, March 1996; TAPPI Press: Atlanta, **2000**, Vol. 1, p 21.
  11. Guo, J. S.; Ojunga, M.; Trembley, S. D.; Webster, D.E.; Chen, A. T. A Novel Approach in the Design of an Environmentally Benign Emulsion Adhesive. *2000 TAPPI Recycling Symposium*, Washington, D.C., March 2000; TAPPI Press: Atlanta, **2000**, Vol. 1, p 95.
  12. Houtman, C.; Seiter, D.; Sutherland, N. R.; Donermeyer, D. Can Laboratory and Polit Recycling Trials Predict Adhesive Removal in Commercial Recycling System? Results from the USPS Environmentally Benign Stamp Project. *2002 TAPPI Fall Conference and Trade Fair*, San Diego, September 2002; TAPPI Press: Atlanta, **2002**, p 28.
  13. McCaslin, P.C. Developing Pressure-Sensitive Adhesives that can be Removed during Paper Recycling Operations. *2000 TAPPI Recycling Symposium*, Washington, D.C., March 2000; TAPPI Press: Atlanta, **2000**, Vol. 1, p 103.
  14. Bloembergen, S.; McLennan, I.; Cassar, S.; Narayan, R. Polymer Resins Designed for Environmental Sustainability. *Adhes. Age* **1998**, *41*(2), 20-24.
  15. Severtson, S. J.; Wang, X. P.; Kroll, M. S. Development of Environmentally Benign Pressure-Sensitive Adhesive Systems via Modification of Substrate Properties. *Ind. Eng. Chem. Res.* **2002**, *41*(23), 5668-5675.
  16. Stratton, R. A. The Flotation of Sticky Contaminants from Recycled Fiber Streams. *Prog. Pap. Recycl.* **1992**, *1* (4), 31-37.
  17. Nowak, M. J.; Severtson, S. J.; Wang, X.; Kroll, M. S. Properties Controlling the Impact of Styrenic Block Copolymer Based Pressure-Sensitive Adhesives on Paper Recycling. *Ind. Eng. Chem. Res.* **2003**, *42*(8), 1681-1687.
  18. Houtman, C. J.; Scallon, K. L.; Guo, J.; Wang, X.; Severtson, S. J.; Kroll, M. S.; Nowak, M. J. Controlling Adhesive Behavior during Recycling. Presented at 7<sup>th</sup> *Research Forum on Recycling*, Quebec City, Canada, September 27-29, **2004**.
  19. Guo, J.; Severtson, S. J.; Kroll, M. S. Role of Paper Face Stock Properties in Determining Removal Efficiencies of Pressure-Sensitive Adhesive Films from Recycling Operations. *Ind. Eng. Chem. Res.* **2004**, *43*(6), 1443-1450.
  20. Zhao Y.; Yan, Z.; Deng Y. PSA Properties and Screenability in Paper Recycling. *Tappi J.* **2005**, *4*(8), 12-16.
  21. Lucas, B. E.; Venditti, R. A.; Jameel, H. The Effect of Adhesive Properties on Adhesive Particle Breakage and Passage During Paper Recycling Operations. *Progress in Paper Recycling* **2004**, *13*(2), 20-28.
  22. Guo, J. S.; Ojunga, M.; Chen, A. T.; Trembley, S.D. Development of Environmentally Benign Pressure Sensitive Adhesive. <http://www.specialchem4adhesives.com/resources/articles/article.aspx?id=213>.
  23. Hansch, C.; Leo, A.; Hoekman, D. H. Exploring QSAR: Hydrophobic, Electronic, and Steric Constants, American Chemical Society: Washington DC **1995**.
  24. Schwarzenbach, R. P.; Gschwend, P. M.; Imboden, D. M. *Environmental Organic Chemistry*. Chapter 7. John Wiley & Sons, Inc.: New York, NY **1992**.
  25. Guo, J.; Severtson, S. J., Gwin, L. E. Optimizing the Monomer Composition of Acrylic Water-based Pressure Sensitive Adhesives to Minimize their Impact on Recycling Operations. *Ind. Eng. Chem. Res.* **2007**, *46*(9), 2753-2759.
  26. Shaw, D. J. *Colloid and Surface Chemistry*, 4th Ed.; Butterworth-Heinemann, Woburn, MA **1992**.

27. Reynolds, W. F. *The Sizing Paper*, 2nd ed; TAPPI Press: Atlanta, GA **1989**.
28. Krueger, J. J.; Hodgson, K. T. The Relationship between Single Fiber Contact Angle and Sizing Performance. *Tappi J.* **1995**, 78(2), 154-161.
29. Owens, D. K. Estimation of the Surface Free Energy of Polymers. *J. Appl. Polym. Sci.* **1969**, 13, 1741-1747.
30. Owens, D. K. Some Thermodynamic Aspects of Polymer Adhesion. *J. Appl. Polym. Sci.* **1970**, 14, 1725-1730.
31. Ray, S. S.; Okamoto, M. Polymer/layered Silicate Nanocomposites: a Review from Preparation to Processing. *Prog. Polym. Sci.* **2003**, 28, 1539-1641.
32. Usuki, A.; Hasegawa, N.; Kato, M. Polymrt-Clay Nanocomposites, *Adv. Polym. Sci.* **2005**, 179,135-195.
33. McEwen, J. G. E. Wax Contamination in Paper Recycling: Understanding Wax Chemistry and Recycling Waxed Papers. *Prog. In Paper Recycl.* **1992**, 1(2), 11-20.
34. Chaiko, D. J.; Levva, A. A. Thermal Transitions and Barrier Properties of Olefinic Nanocomposites. *Chem. Mater.* **2005**, 17, 13-19.
35. Chaiko, D. J.; Levva, A. A. *US Patent application* 0030187120.
36. Kato, M.; Usuki, A.; Okada, A. Synthesis of Polypropylene Oligomer – Clay Intercalation Compounds. *J. Appl. Polym. Sci.* **1997**, 66(9), 1781-1785.
37. Jeon, H. S.; Rameshwaram, J. K.; Kim, G. Structure-Property Relationships in Exfoliated Polyisoprene/Clay Nanocomposites. *J. Polym. Sci. Pol. Phys.* **2004**, 42 (6): 1000-1009.
38. Alexander, L. E. *X-ray Diffraction Methods in Polymer Science*, John Wiley & Sons Inc, **1969**.
39. Antipov, E. M.; Guseva, M. A.; Gerasin, V. A.; Korolev, Y. M.; Rebrov, A. V.; Fisher, H. R.; Razumovskaya, I. V. *Polym. Sci. Ser. A* **2003**, 45 (11), 1130-1139.
40. Medellin-Rodríguez, F. J.; Hsiao, B. S.; Chu, B.; Fu, B. X. Uniaxial Deformation of Nylon 6–Clay Nanocomposites by In-Situ Synchrotron X-Ray Measurements *J. Macromol. Sci. Phys.* **2003**, 42 (1), 201-214.
41. Fornes, T. D.; Yoon, P. J.; Hunter, D. L.; Keskkula, H.; Paul, D. R. Effect of organoclay structure on nylon 6 nanocomposite morphology and properties. *Polymer* **2002**, 43 (22), 5915-5933.
42. Chen, C. H.; Teng, C. C.; Yang, C. H. Preparation and Characterization of Rigid Poly (vinyl chloride)/MMT Nanocomposites. *J. Polym. Sci. Pol. Phys.* **2005**, 43 (12), 1465-1474.
43. Xu, H. D.; Li, Y.; Yu, D. S. Studies on the Poly(styrene-b-butadiene-b-styrene)/clay Nanocomposites Prepared by Melt Intercalation. *J. Appl. Polym. Sci.* **2005**, 98 (1), 146-152.
44. Zhou, N. L.; Xia, X. X.; Wang, Y. R. Study on Mechanical Property of Exeoliated Silicone Rubber/Clay Nanocomposites. *Acta Polym. Sin.* **2002**, 2, 253-256.
45. Shah, D.; Maiti, P., Gunn, E.; Schmidt, D. F.; Jiang, D. D.; Batt, C. A.; Giannelis, E. P. Dramatic Enhancements in Toughness of Polyvinylidene Fluoride Nanocomposites via Nanoclay-Directed Crystal Structure and Morphology. *Adv. Mater.* **2004**, 16(14), 1173-1177.
46. Okada, A.; Kawasumi, M.; Usuki, A.; Kojima, Y.; Kurauchi, T.; Kamigaito, O. in: D.W. Schaefer, J.E. Mark (Eds.), *Polymer Based Molecular Composites*. MRS Symposium Proceedings, vol. 171, Pittsburgh, **1990**, pp. 45-50.
47. Wang, J.; Severtson, S. J.; Stein, A. Significant and Concurrent Enhancement of Stiffness, Strength, and Toughness for Paraffin Wax Through Organoclay Addition. *Adv. Mater.* **2006**, 18(12), 1585-1588.
48. Sirota, E.B.; King, H.E.; Shao, H.H.; Singer, D.M. Rotator Phases in Mixtures of n-Alkanes. *J. Phys. Chem.* **1995**, 99, 798-804.



49. Ward, I. M.; Sweeney, J. An Introduction to the Mechanical Properties of Solid Polymers, 2nd ed., John Wiley & Sons, **2004**.
50. Jin, S.; Hwang, S. K.; Morris, J.W. The effect of Grain Size and Retained Austenite on the Ductile-Brittle Transition of a Titanium-Gettered Iron Alloy, *Metall. Mater. Trans. A* **1975**, 6, 1721-1726.
51. Gao, X.; Qu, C.; Zhang, Q.; Peng, Y.; Fu, Q. Brittle-Ductile Transition and Toughening Mechanism in POM/TPU/CaCO<sub>3</sub> Ternary Composites. *Macromol. Mater. Eng.* **2004**, 289, 41-48.
52. Geil, P. H. Polymer Single Crystals, Chapter VII, Interscience Publishers, New York, **1963**.
53. Bafna, A.; Beaucage, G.; Mirabella, F.; Mehta, S. 3D Hierarchical orientation in polymer-clay nanocomposite films. *Polymer* **2003**, 44, 1103-1115.
54. Wang, J.; Severtson, S. J.; Geil, P. H. Brittle-Ductile Transitions and the Toughening Mechanism in Paraffin/Organo-Clay Nanocomposites. *Mater. Sci. Eng., A* **2007**, 467(1-2), 172-180.
55. Rossetti, F.; Ranalli, G.; Faccenna, C. Rheological Properties of Paraffin as an Analogue Material for Viscous Crustal Deformation. *J. Struct. Geol.* **1999**, 21, 413-417.
56. Al-Fariss, T. F.; Jang, L. K.; Ozbelge, H. O.; Ghasem, N. M. A New Correlation for the Viscosity of Waxy Oils. *J. Pet. Sci. Eng.* **1993**, 9, 139-144.
57. Tan, S. P.; Adidharma, H.; Towler, B. F.; Radosz, M. Friction Theory Coupled with Statistical Associating Fluid Theory for Estimating the Viscosity of n-Alkane Mixtures. *Ind. Eng. Chem. Res.* **2006**, 45, 2116-2122.
58. McMillan, L. C.; Darvell, B. W.; Rheology of Dental Waxes. *Dent. Mater.* **2000**, 16, 337-350.
59. Ungar, G. Structure of Rotator Phases in n-Alkanes. *J. Phys. Chem.* **1983**, 87, 689-695.
60. Ungar, G.; Masic, N. Order in the Rotator Phase of n-Alkanes. *J. Phys. Chem.* **1985**, 89, 1036-1042.
61. Sirota, E. B.; Singer, D. M. Phase Transition among the Rotatar Phases of the Normal Alkanes. *J. Chem. Phys.* **1994**, 101(12), 10873-10882.
62. Dorset, D. L. The Crystal Structure of Waxes. *Acta. Cryst. B.* 1995, 51, 1021-1028.
63. Craig, S. R.; Hastie, G. P.; Roberts, K. J.; Gerson, A. R.; Sherwood, J. N.; Tack, R. D. Investigation into the Structures of Binary-, Tertiary- and Quaternary-Mixtures of n-Alkanes and Real Diesel Waxes Using High-Resolution Synchrotron X-ray Powder Diffraction. *J. Mater. Chem.* **1998**, 8, 859-869.
64. Craig, S. R.; Hastie, G. P.; Roberts, K. J.; Sherwood, J. N.; Tack, R. D.; Cernik, R.J. In-situ Study of the Solid-Solid Phase Transitions Occurring in Real Diesel Wax Crystalline Systems Using Differential Scanning Calorimetry and High-Resolution Synchrotron X-ray Powder Diffraction. *J. Mater. Chem.* **1999**, 9, 2385-2392.
65. Nowak, M. J.; Severtson, S. J. Dynamic Mechanical Spectroscopy of Plastic Crystalline States in n-Alkane Systems. *J. Mater. Sci.* **2001**, 36, 4159.
66. Petitjean, D.; Schmitt, J. F.; Fiorani, J. M.; Laine, V.; Bouroukba, M.; Dirand, M.; Cunat, C. Some Temperature-Sensitive Properties of Pure Linear Alkanes and n-Ary Mixtures. *Fuel* **2006**, 85, 1323-1328.
67. Wagener, R.; Reisinger, T. J. G. A. Rheological Method to Compare the Degree of Exfoliation of Nanocomposites. *Polymer* **2003**, 44, 7513-7518.
68. Ren, J.; Silva, A. S.; Krishnamoorti, R. Linear Viscoelasticity of Disordered Polystyrene-Polyisoprene Block Copolymer Based Layered-Silicate Nanocomposites. *Macromolecules* **2000**, 33, 3739-3746.
69. Krishnamoorti, R.; Yurekli, K. Rheology of Polymer Layered Silicate Nanocomposites *Curr. Opin. Colloid Interface Sci.* **2001**, 6, 464-470.

70. Gupta, R. K.; Pasanovic-Zujo, V.; Bhattacharya, S. N. Shear and Extensional Rheology of EVA/Layered Silicate-Nanocomposites. *J. Non-Newtonian Fluid Mech.* **2005**, 128, 116-125.
71. Krishnamoorti, R.; Giannelis, E. P.; Rheology of End-Tethered Layered Silicate Nanocomposites. *Macromolecules* **1997**, 30, 4097-4102.
72. Hyun, Y. H.; Lim, S. T.; Choi, H. J.; Jhon, M. S. Rheology of Poly(ethylene oxide)/Organoclay Nanocomposites. *Macromolecules* **2001**, 34, 8084-8093.
73. Zhong, Y.; Zhu, Z.; Wang, S. Q. Synthesis and Rheological Properties of Polystyrene/Layered Silicate Nanocomposite. *Polymer* **2005**, 46, 3006-3013.
74. Gisler, T.; Ball, R. C.; Weitz, D. A. Strain Hardening of Fractal Colloidal Gels. *Phys. Rev. Lett.* **1999**, 82, 1064-1067.
75. AF&PA/FBA Symposium: Repulpable/Recyclable Treatments for Corrugated Boxes, AF&PA, Washington, DC; FBA, Rolling Meadows, IL, **1996**.
76. Rosenberger, R. R.; Houtman, C. J. TAPPI Recycling Symposium, **2000**, Volume 2, USPS, Washington, D.C; USDA-FPS, Madison, Wisconsin; ASC, Bethesda, Maryland; AF&PA, Washington, DC; March 5-8, **2000** Hyatt Crystal City, Washington, D.C. p.713.
77. Voluntary standard for repulping and recycling corrugated fiberboard treated to improve its performance in the presence of water and water vapor. Fiber Box Association, Rolling Meadows, IL.
78. Oscar, H.; Howard, B. Water Repellent Efficacy of Wax Used in Hardboard. *Ind. Eng. Chem. Res.* **1988**, 27, 1296-1300.
79. Martin-Polo, M.; Mauguin, C.; Voilley, A. Hydrophobic Films and Their Efficiency against Moisture Transfer. 1. Influence of the Film Preparation Technique. *Journal of Agricultural and Food Chemistry* **1992**, 40,407-412.
80. Extrand, C. Contact Angles and Hysteresis on Surface with Chemically Heterogeneous Islands. *Langmuir* **2003**, 19, 3793-3796.
81. Gao, L.; McCarthy, T. Contact Angle Hysteresis Explained. *Langmuir* **2006**, 22, 6234-6237.
82. Young, T. *Philos. Trans. R. Soc.* **1805**, London, 95, 65.
83. Israelachvili, J. *Intermolecular & Surface Force*, Academic: London, **1991**.
84. Bonn, D.; Eggers, J.; Indekeu, J.; Meunier, J.; Rolley, E. Wetting and Spreading, *Rev. Mod. Phys.* **2009**, 81, 739-805
85. de Gennes, P. G.; Brochard, W. F.; Quere, D., *Capillarity and Wetting Phenomena Drops, Bubbles, Pearls, Waves*, Springer, New York, **2003**.
86. Muller, B.; Riedel, M.; Michel, R.; Paul, D. S.; Hofer, R.; Heger, D.; Grutzmacher, D., Impact of Nanometer-Scale Roughness on Contact-Angle Hysteresis and Globulin Adsorption. *Journal of Vacuum Science & Technology B* **2001**, 19(5), 1715-1720.
87. Ramos, M. M. S.; Charlaix, E.; Benyagoub, A. Contact Angle Hysteresis on Nano-Structured Surfaces. *Surface Science* **2003**, 540, 355-362.
88. Jin, W.; Koplik, J. Wetting Hysteresis at the Molecular Scale. *Physical Review Letters* **1997**, 78(8), 1520-1523.
89. Schaffer, E.; Wong, P. Contact Line Dynamics near the Pinning Threshold: A Capillary Rise and Fall Experiment. *Physical Review E.* **2000**, 61 (5), 5257-5277.
90. Moulinet, S.; Guthmann, C.; Rolley, E., Dissipation in the Dynamics of a Moving Contact Line: Effect of the Substrate Disorder. *J. of Eur. Phys. B.* **2004**, 37, 127.-136

91. Nikolayev, V. S., Dynamics and Depinning of the Triple Contact Line in the Presence of Periodic Surface Defects. *J. Phys.: Condens. Matter.* **2005**, 17, 2111-2120.
92. Ramos, S.; Tanguy, A. Pinning-depinning of the Contact Line on Nanorough Surface. *J. of Eur. Phys. E.* **2006**, 19, 433-440.
93. Bartell, F. E.; Shepard, J. W. The Effect of Surface Roughness on Apparent Contact Angles and on Contact Angle Hysteresis. I. The System Paraffin-Water-Air. *J. Phys. Chem.* **1953**, 57, 211.-215.
94. Fang, C.; Drelich, J. Theoretical Contact Angles on a Nano-Heterogeneous Surface Composed of Parallel Apolar and Polar Strips. *Langmuir* **2004**, 20(16), 6679-6684.
95. Gilcreest, V. P.; Carroll, W. M.; Rochev, Y. A.; Blute, I.; Dawson, K. A.; Gorelov, A. V. Thermoresponsive Poly(N-isopropylacrylamide) Copolymers: Contact Angles and Surface Energies of Polymer Films. *Langmuir* **2004**, 20, 10138-10145.
96. Pu, G.; Steven, J. S., Characterization of Dynamic Stick-and-Break Wetting Behavior for various Liquids on the Surface of a Highly Viscoelastic Polymer. *Langmuir* **2008**, 24 (9), 4685-4692.
97. Pu, G.; Guo, J. H.; Larry, E. G.; Steven, S. J., Mechanical Pinning of Liquids through Inelastic Wetting Ridge Formation on Thermally Stripped Acrylic Polymers. *Langmuir* **2007**, 23(24), 12142-12146.
98. Yasuda, T.; Okuno, T.; Yasuda, H. Contact Angle of Water on Polymer Surfaces. *Langmuir* **1994**, 10, 2435-2439.
99. Faibish, R. S.; Yoshida, W.; Cohen, Y., Contact Angle Study on Polymer-Grafted Silicon Wafers. *Journal of Colloid and Interface Science* **2002**, 256, 341-350.
100. Tavana, H.; Yang, G.; Yip, C. M.; Appelhans, D.; Zschoche, S.; Grundke, K.; Hair, M. L.; Neumann, A. W. Stick-Slip of the Three-Phase Line in Measurements of Dynamic Contact Angles. *Langmuir* **2006**, 22, 628-636.
101. Tavana, H.; Simon, F.; Grundke, K.; Kwok, D. Y.; Hair, M. L.; Neumann, A. W., Interpretation of Contact Angle Measurements on Two Different Fluoropolymers for the Determination of Solid Surface Tension. *J. of Colloid and Interface Science* **2005**, 291(2), 497-506.
102. Johnson, R. E.; Dettre, R. H. *Contact Angle, Wettability, and Adhesion, Advances in Chemistry Series* **1964**, 43, 112.
103. Dann, J. R., Forces Involved in the Adhesive Process: I. Critical Surface Tensions of Polymeric Solids as Determined with Polar Liquids. *J. of Colloid and Interface Science* **1970**, 32(2) 302-320.
104. Dann, J. R., Forces Involved in the Adhesive Process: II. Nondispersion Forces at Solid-Liquid Interfaces. *J. of Colloid and Interface Science* **1970**, 32(2) 321-331.
105. Dirand, M.; Chevallier, V.; Provost, E.; Bourouka, M.; Petitjean, D. Multicomponent Paraffin Waxes and Petroleum Solid Deposits : Structural and Thermodynamic State. *Fuel* **1998**, 77(12), 1253-1260.
106. Zheng, M. J.; Du, W. M. Phase Behavior, Conformations, Thermodynamic Properties, and Molecular Motion of Multicomponent Paraffin Waxes: A Raman Spectroscopy Study. *Vibrational Spectroscopy* **2006**, 40, 219-224.
107. Matthai, M.; Laux, H.; Hildebrand, G. An Investigation of the Dependence of Penetration on the Temperature and Composition of Paraffin Waxes. *Eur. J. Lipid Sci. Technol.* **2001**, 103, 292-298.

108. Dorset, L. Chain Length and the Cosolubility of n-Paraffins in the Solid State. *Macromolecules* **1990**, 23, 623-633.
109. Ho, M.; Pemberton, J. E. Alkyl Chain Conformation of Octadecylsilane Stationary Phases by Raman Spectroscopy. 1. Temperature Dependence. *Anal. Chem.* **1998**, 70, 4915-4920.
110. Faolain, O.; Hunter, M. B.; Byrne, J. M.; Kelehan, P.; Lambkin, H. A.; Byrne, H. J.; Lyne, F. M. Raman Spectroscopic Evaluation of Efficacy of Current Paraffin Wax Section Dewaxing Agents. *Journal of Histochemistry & Cytochemistry* **2005**, 53(1), 121-129.
111. Roger, R. D.; Bartell, F. E. Hysteresis of Contact Angle of Water on Paraffin. Effect of Surface Roughness and of Purity of Paraffin. *Journal of Colloid Science* **1953**, 8(2), 214-223.
112. Dierker, S. B.; Murray, C.A. Characterization of Order in Langmuir-Blodgett Monolayers by Unenhanced Raman Spectroscopy. *Chemical Physics Letters* **1987**, 137(5), 453-457
113. Allen, G. P.; Ludwig, B. A. Effect of Polymer Crystallinity on the Wetting Properties of Certain Fluoroalkyl Acrylates. *Journal of Polymer Science:Part A* **1969** 7, 3053-3066.
114. Hyun, J. A New Approach to Characterize Crystallinity by Observing the Mobility of Plasma Treated Polymer Surfaces. *Polymer* **2001**, 42(15), 6473-6477.
115. Reynhardt, E. C., NMR Investigation of Fischer-Tropsch Waxes. II. Hard Wax. *J. Phys. D: Appl. Phys.* **1985**, 18, 1185-1197.
116. Strom, G.; Ferderiksson, M.; Stenius, P. Contact Angles, Work of Adhesion, and Interfacial Tensions at a Dissolving Hydrocarbon Surface. *Journal of Colloid and Interface Science* **1987**, 119(2), 352-361.
117. Fox, H. W.; Zisman, W. A. The Spreading of Liquids on Low-Energy Surfaces. III. Hydrocarbon Surfaces. *J. of Colloid Sci.* **1952**, 7, 428-442.
118. Schonhorn, H.; Ryan, F. W.; Wettability of Polyethylene Single Crystal Aggregates. *J. Phys. Chem.* **1966**, 70, 3811-3815.
119. Bartell, F. E.; Wooley, A. D. Solid-Liquid-Air Contact Angles and their Dependence upon the Surface Condition of the Solid. *J. of American Chemical Society* **1933**, 55(9), 3518-3527.
120. Jonghe, D. V.; Chatain, D. Experimental Study of Wetting Hysteresis on Surfaces with Controlled Geometrical and/or Chemical Defects. *Acta Metal. Mater.* **1995**, 43 (4), 1505-1515.
121. Dettre, R. H.; Johnson, R. E. Contact Angle Hysteresis. IV. Contact Angle Measurements on Heterogeneous Surfaces. *J. of Physical Chemistry* **1965**, 69 (5), 1507-1515.
122. Lee, Y. L. The Wettability of Solid Surfaces Modified by Vacuum Deposition of Stearic Acid *Colloids and Surfaces A* **1999**, 155, 221-229.
123. Lee, Y. L.; Chen, C. H.; Yang, Y. H. Surface Morphology and Wetting of Poly( $\alpha$ -methylstyrene) Thin Films Prepared by Vacuum Deposition. *Langmuir* **1998**, 14, 6980.
124. Rupp, F.; Scheidelet, L.; Geis, G. J. Effect of Heterogenic Surfaces on Contact Angle Hysteresis: Dynamic Contact Angle Analysis in Material Sciences. *Chem. Eng. Technol.* **2002**, 25 (9), 877-882.
125. Iwamatsu, M. Contact Angle Hysteresis of Cylindrical Drops on Chemically Heterogeneous Striped Surfaces *J. of Colloid and Interface Science* **2006**, 297, 772-777.
126. Leonard, W. S.; Stephen, G. Contact Angle Hysteresis on Heterogeneous Surfaces. *Langmuir* **1985**, 1 (2), 219-230.
127. Oner, D.; McCarthy, J. M., Ultrahydrophobic Surfaces. Effects of Topography Length Scales on Wettability. *Langmuir* **2000**, 16(20), 7777-7782.

128. Extrand, C. W. Model for Contact Angles and Hysteresis on Rough and Ultrahydrophobic Surfaces. *Langmuir* **2002**, 18(21),7991-7999.
129. Dorrer, C.; Ruhe, J. Contact Line Shape on Ultrahydrophobic Post Surfaces. *Langmuir* **2007**, 23 (6), 3179-3183.
130. Bormashenko, E.; Bormashenko, Y.; Whyman, G.; Pogreb, R.; Musin, A.; Jager, R.; Barkay, Z. Contact Angle Hysteresis on Polymer Substrates Established with Various Experimental Techniques, its Interpretation, and Quantitative Characterization. *Langmuir* **2008**, 24(8), 4020-4025.
131. Lander, L. M.; Siewierski, L. M.; Brittain, W. J.; Vogler, E. A. A Systematic Comparison of Contact Angle Methods. *Langmuir* **1993**, 9(8), 2237-2239.
132. Krishnan, A.; Liu, Y. H.; Cha, P.; Woodward, R.; Allara, D.; Vogler, E. A. An Evaluation of Methods for Contact Angle Measurement. *Colloids and Surfaces B: Biointerfaces* **2005**, 43, 95-98.
133. Kwok, D.; Neumann, A. Contact Angle Measurement and Contact Angle Interpretation. *Advances in Colloid and Interface Science* **1999**, 81, 167-249.
134. Bertrand, E. Wetting of Alkanes on Water. *J. Petrol. Sci. Eng.* **2002**, 33, 217-222.
135. Bergeron, V.; Bonn, D.; Martin, J.-Y.; Vovelle, L. Controlling Droplet Deposition with Polymer Additives. *Nature* **2000**, 405, 772-775.
136. Tabling, P. *Microfluidics* EDP Sciences: Paris, **2004**.
137. de Gennes, P. G. Wetting : Statics and Dynamics. *Rev. Mod. Phys.* **1985**, 57, 827-863.
138. Carre, A.; Gastel, J. C.; Shanahan, M. E. R. Viscoelastic Effects in the Spreading of Liquids. *Nature* **1996**, 379, 432-434.
139. Shanahan, M. E. R.; Carre, A. Anomalous Spreading of Liquid Drops on an Elastomeric Surface. *Langmuir* **1994**, 10, 1647-1649.
140. Feng, X. J.; Jiang, L. Design and Creation of Superwetting/Antiwetting Surfaces. *Adv. Mater.* **2006**, 18, 3063-3078.
141. Gau, H.; Herminghaus, S.; Lenz, P.; Lipowsky, R. Liquid Morphologies on Structured Surfaces: From Microchannels to Microchips. *Science* **1999**, 283, 46-49.
142. Bico, J.; Marzolin, C.; Quere, D. Pearl Drops. *Europhysics Letters* **1999**, 47 (2), 220-226.
143. Herminghaus, S. Roughness-Induced Non-Wetting. *Europhysics Letters*, **2000**, 52 (2), 165-170.
144. Onda, T.; Shibuichi, S.; Satoh, N.; Tshjii, K, Super-Water-Repellent Fractal Surfaces. *Langmuir* **1996**, 12, 2125-2127.
145. Herminghaus, S.; Riedel, M.; Leiderer, P.; Bastmeyer, M.; Sturmer, C. Optical Force Microscopy with Silicone Rubber Waveguides. *Applied Physics Letters* **1997**, 70 (1), 22-24.
146. Shanahan, M.E.R.; Carre, A Viscoelastic Dissipation in Wetting and Adhesion Phenomena. *Langmuir* **1995**, 11, 1396-1402.
147. Manoj, G.; Ashutosh, S. Polymer Patterns in Evaporation Droplets on Dissolving Substrates. *Langmuir*, **2004**, 20, 3456-3463.
148. Rodrigo, M. C.; Tadeusz, P. Behavior of Evaporating Droplets at Nonsoluble and Soluble Surfaces: Modeling with Molecular Resolution. *J. Phys. Chem. B* **2005**, 109, 4152.-4161.
149. Li, G.; Butt, H.J.; Graf, K.,Microstructures by Solvent Drop Evaporation on Polymer Surface: Dependence on Molar Mass. *Langmuir* **2006**, 22, 11395-11399.
150. Guangfen L.; Nobert H.; Karlheinz G. Micropologies in Polymer Surfaces by Solvent Drops in Contact and Noncontact Mode. *Applied Physics Letters* **2006**, 89, 241920-241922.

151. Head, D. A. Modeling the Elastic Deformation of Polymer Crusts Formed by Sessile Droplet Evaporation. *Physical Review E* **2006**, 74, 021601(1)- 021601(8).
152. Deegan, R. D.; Bakajin, O.; Dupont, T. F.; Huber, G.; Nagel, S. R.; Witten T. A. Contact Line Deposits in an Evaporating Drop. *Physical Review E* **2000**, 62 (1), 756-765.
153. Deegan, R.D.; Bakajin, O.; Dupont, T.F.; Huber, G.; Nagel, S. R.; Witten, T. A. Capillary Flow as the Cause of Ring Stains from Dried Liquid Drops. *Nature* **1997**, 389, 827-829.
154. Denkov, N. D.; Velev, O. D.; Kralchevsky, P. A.; Ivanov, I. B.; Yoshimurah, N.; Nagayama, K. Two-Dimensional Crystallization. *Nature* **1993**, 361, 26.
155. Denkov, N. D.; Velev, O. D.; Kralchevsky, P. A.; Ivanov, I. B.; Yoshimurah, N.; Nagayama, K. Mechanism of Formation of Two-dimensional Crystals from Latex Particels on Substrates. *Langmuir* **1992**, 8 (12), 3183-3190.
156. Ghosh, M.; Fan, F.; Stebe, K. J., Spontaneous Pattern Formation by Dip Coating of Colloidal Suspensions on Homogeneous Surface. *Langmuir* **2007**, 23, 2180-2183.
157. Kwok, D. Y.; Li, A.; Lam, C. N. C.; Wu, R.; Zschoche, S.; Poschel, K.; Gietzelt, T.; Grundke, K.; Jacobasch, H. J.; Neumann, A. W. Low-rate Dynamic Contact Angles on Poly[styrene-*alt*-(hexyl/10-carboxydecyl(90/10)maleimide)] and the Determination of Solid Surface Tensions. *Macromol. Chem. Physic.* **1999**, 200, 1121-1133.
158. Marsh, J. A.; Cazabat, A. M. Dynamics of Contact Line Depinning from a Single Defect. *Phys. Rev. Lett.* **1993**, 71, 2433-2436.
159. Yarnold, G.; Manson, B., A Theory of the Angle of Contact. *Proc. Phys. Soc. London, Sect. B* **1949**, 62, 121-125.
160. Cherry, B. W.; Holmes, C. M., Kinetics of Wetting of Surfaces by Polymers. *J. of Colloid and Interfacial Science* **1969**, 29, 174-176.
161. Blake, T. D.; Haynes J. M. Kinetics of Liquid/Liquid Displacement. *J. Colloid Interface Sci.* **1969**, 30, 421-423.
162. Golestanian, R.; Raphael, E. Dissipation in Dynamics of a Moving Contact Line. *Physical Review E* **2001**, 64, 031601(1)- 031601(7),
163. Richard, L. H. A Study of the Advancing Interface: II. Theoretical Prediction of the Dynamic Contact Angle in Liquid-Gas Systems, *J. of Colloid and Interface Science* **1983**, 94 (2), 470-486.
164. Bayber, I. S.; Megaridis, C. M. Contact Angle Dynamics in Droplets Impacting on Flat Surfaces with Different Wetting Characteristic. *J. Fluid Mech.* **2006**, 558, 415-449.
165. Yuk, S. H.; Jhon, M.S. Contact Angles on Deformable Solids. *J. of Colloid and Interface Science* **1986**, 110 (1), 252-257.
166. Shanahan, M. E. R., The influence of solid micro-deformation on contact angle equilibrium. *J. Phy. D: Appl. Phys.* **1987**, 20, 945-955.
167. Ruijter, M. J.; Charlot, M.; Voue, M.; Coninck, D. J. Experimental Evidence of Several Time Scales in Drop Spreading. *Langmuir* **2000**, 16, 2363-2368.
168. Peter, G. P.; Jordan G. P. A Combined Molecular-hydrodynamic Approach to Wetting Kinetics. *Langmuir* **1992**, 8, 1762-1767.
169. Motomu, T.; Florian, R.; Matthias, F. S.; Gerald, M.; Antero, A.; Klaus, R. N.; Oliver, P.; Erich, S. Wetting and Dewetting of Extracellular Matrix and Glycocalix Models. *J. Phys.: Condens. Matter.* **2005**, 17, S649-S663.
170. Bin, Z.; Jeffery, S. M.; David, J. B. Surface-Directed Liquid Flow Inside Microchannels. *Science* **2001**, 291, 1023-1026.

171. Hartmut, G.; Stephan, H.; Peter, L.; Reinhard, L., Liquid Morphologies on Structured Surfaces: From Microchannels to Microchips. *Science* **1999**, 283, 46-49.
172. George, M. W., The Origins and the Future of Microfluidics. *Nature* **2006**, 442, 368-373
173. Javier, A.; David, J. B. Controlled Microfluidic Interfaces. *Nature* **2005**, 437, 648-655.
174. Yang, J. L.; Tze, J. Y.; Yn, C. T. The Marching Velocity of the Capillary Meniscus in a Microchannel. *J. Micromech. Microeng.* **2004**, 14, 220-225.
175. Abraham, D. S.; Stephan, K. D.; Armand, A.; Lgor, M.; Howard, A. S.; George, M. W. Chaotic Mixer for Microchannels. *Science* **2002**, 295, 647-650.
176. Sperling, L. H. *Introduction to Physical Polymer Science*. Wiley-Interscience, New York, **2001**.
177. Gerdes, S.; Tiberg, F.; Dynamic Wetting of Silica By Aqueous Triblock Copolymer Solutions at Low Concentrations. *Langmuir* **1999**, 15, 4916-4921.
178. Morra, M.; Occhiello, E.; Garbassi, F. The Wetting Behavior of Grafted Hydrophilic Acrylic Monomers. *Colloid Polym. Sci.* **1993**, 271, 696-704.
179. Veretennikov, I.; Indeikina A.; Chang H. C. Front Dynamics and Fingering of a Driven Contact Line. *J. Fluid Mech.*, **1998**, 373,81-110.
180. Cox, R. G. The Spreading of a Liquid on a Rough Solid Surface. *J. Fluid Mech.* **1983**, 131, 1-26.
181. Frank, B.; Garoff, S. Origins of the Complex Motion of Advancing Surfactant Solutions. *Langmuir* **1995**, 11, 87-93.
182. Courrbins, L.; Denieul, E.; Dressaire, E.; Roper, M.; Ajari, A.; Stone, H. A. Imbibition by Polygonal Spreading on Microdecorated Surfaces. *Nature Materials* **2007**, 6, 661-664.
183. Saiz, E.; Tomsia, A. P.; Cannon, R.M. Ridging Effects on Wetting and Spreading of Liquids on Solids. *Acta Materialia* **1998**, 46(7), 2349-2361.
184. Kusumaatmaja, H.; Yeomans, J. M., Modeling Contact Angle Hysteresis on Chemically Patterned and Superhydrophobic Surfaces. *Langmuir* **2007**, 23, 6019 - 6032.
185. Joanny, J. F.; Robbins, M. O. Motion of a contact line on a heterogeneous surface. *J. Chem. Phys.* **1990**, 92(5), 3206-3212.
186. Zhang, J.; Kwok, D. Y., Contact Line and Contact Angle Dynamics in Superhydrophobic Channels. *Langmuir* **2006**, 22, 4998-5004.
187. Ryschenkow, G.; Arribart, H. Adhesion Failure in the Stick-Slip Regime: Optical and AFM Characterizations and Mechanical Analysis, *J. Adhesion*, **1996**, 58, 143-161.
188. Yang, H. W., Water-based Polymers as Pressure-Sensitive Adhesives – Viscoelastic Guidelines. *J. of Appl. Poly. Sci.* **1995**, 55, 645-652.
189. Benedek, I.; Heymans, L. J. *Pressure Sensitive Adhesives Technology*, Marcel Dekker Inc, New York, **1997**.
190. Voue, M.; Bioboo, R.; Bauthier, C.; Conti, J.; Charlot, M.; Coninck, D. J. Dissipation and Moving Contact Lines on Non-rigid Substrates. *J. of the European Ceramic Society* **2003**, 23(15), 2769 -2775.
191. Extrand, C. W.; Kumagai, Y. Contact Angles and Hysteresis on Soft Surfaces. *J. of Colloid and Interface Science* **1996**, 184, 191-200.
192. Roach, P.; Shirtcliffe, J. N.; Newton, I. Progress in Superhydrophobic Surface Development. *Soft Matter*. **2008**, 4, 224-240.
193. Xia, F.; Jiang, L. Bio-Inspired, Smart, Multiscale Interfacial Materials. *Adv. Mater.* **2008**, 20 (15), 2842-2858.

194. Pericet-Camara, R.; Best, A.; Butt, H. J.; Bonaccorso, E. Effect of Capillary Pressure and Surface Tension on the Deformation of Elastic Surfaces by Sessile Liquid Microdrops : An Experimental Investigation. *Langmuir* **2008**, *24*, 10565–10568.
195. Extrand, C. W.; Moon, S. Critical Meniscus Height of Liquids at the Circular Edge of Cylindrical Rods and Disks. *Langmuir* **2009**, *25*, 992-996.
196. Staicu, T.; Micutz, M.; Leca, M. Electrostatically and Electrosterically Stabilized Latices of Acrylic Copolymers used as Pressure-Sensitive Adhesives. *Prog. Org. Coat.* **2005**, *53*, 56-62.
197. Charneau, J. Y.; Berthet, R.; Gringreau, C.; Holl, Y.; Kientz, E. Effects of Film Structure on Mechanical and Adhesion Properties of Latex Films. *J Adhes. Adhes.* **1997**, *17*, 169-176.
198. Tobing, S. D.; Klein, A. Molecular Parameters and their Relation to the Adhesive Performance of Acrylic Pressure-Sensitive Adhesives. *J of Appl. Polym. Sci.* **2001**, *79*, 2230-2244.
199. Mulvihill, J.; Toussaint, A.; Wilde, M. D. Onset, Follow up and Assessment of Coalescence. *Prog. Org. Coat.* **1997**, *30*, 127-139.
200. Donkus, L. J. Solent-like Performance from Emulsion PSAs: Advances in Water-Whitening Resistance. *Adhes. Age* **1997**, *32*, 35-37.
201. Kientz, D.; Holl, Y. Distribution of Surfactants in Latex Films. *Colloids Surf. A* **1993**, *78*, 255-270.
202. Holl, Y. Distribution of Small Molecules in Latex Films. Correlation with Properties. *Macromol. Symp.*, **2000**, *151*, 473-478.
203. Guigner, D.; Fischer, C.; Holl, Y. Film Formation from Concentrated Reactive Silicone Emulsions. 2. Surfactant Distribution. *Langmuir* **2001**, *17*, 6419-6425.
204. Wheeler, O. L.; Jaffe, H. L.; Wellman, N. A Mechanism of Film Formation of Polyvinyl Acetate Emulsions. *Off. Dig.* **1954**, *26*, 1239-1241.
205. Voyutskii, S. S. Amendment to the Papers by Bradford, Brown and Co-workers: "Concerning Mechanism of Film Formation from High Polymer Dispersions" *J. Polym. Sci.* **1958**, *32*, 528-534.
206. Keddie, J. L. Structural Analysis of Organic Interfacial Layers by Ellipsometry. *Curr. Opin. Colloid Interface Sci.* **2001**, *6*(2), 102-110.
207. Zhao, C. L.; Dobler, F.; Pith, T.; Holl, Y.; Lambla, M. Surface Composition of Coalesced Acrylic Latex Films Studied by XPS and SIMS. *J. Colloid Interface Sci.* **1989**, *128*, 437-449.
208. Kunkel, J. P.; Urban, M. W. Surface and Interfacial FT-IR Spectroscopic Studies of Latexes. VIII. The Effect of Particle and Copolymer Composition on Surfactant Exudation in Styrene-n-Butyl Acrylate Copolymer Latex Films. *J. Appl. Polym. Sci.* **1993**, *50*, 1217-1223.
209. Belaroui, F.; Cabane, B.; Dorget, M.; Grohens, Y.; Marie P.; Holl, Y. Small-Angle Neutron Scattering Study of Particle Coalescence and SDS Desorption during Film Formation from Carboxylated Acrylic Latices. *J. Colloid Interface Sci.* **2003**, *262*, 409-417.
210. Belaroui, F.; Hirn, M. P.; Grohens, Y.; Marie P.; Holl, Y. Distribution of Water-soluble and Surface-active Low-molecular-weight Species in Acrylic Latex Films. *J. Colloid Interface Sci.* **2003**, *261*, 336-348.



211. Mallégol, J.; Gorce, J. -P.; Dupont, O.; Jeynes, C.; McDonald, P. J.; Keddie, J. L. Origins and Effects of a Surfactant Excess near the Surface of Waterborn Acrylic Pressure-Sensitive Adhesives. *Langmuir*, **2002**, *18*, 4478-4487.
212. Mallégol, J.; Dupont, O.; Keddie, J. L. Film Formation and Morphology of Waterborne Acrylic Pressure-Sensitive Adhesives. *Proceedings of the 28<sup>th</sup> Coating Science and Technology*; Athens: Greece, 2002.
213. Mallégol, J.; Dupont, O.; Keddie, J. L. Morphology and Elasticity of Waterborne Acrylic Pressure-Sensitive Adhesives in Investigated with Atomic Force Microscopy. *J. Adhesion Sci. Technol.* **2003**, *17*, 243-259.
214. Urban, M. W. Surfactants in Latex Films; Interactions with Latex Components and Quantitative Analysis using ATR and Step-Scan PAS FT-IR spectroscopy. *Prog. Org. Coat.* **1997**, *32*, 215-229.
215. Zhao, C.L.; Holl, Y.; Pith, T.; Lambla, M. FTIR-ATR Spectroscopic Determination of the Distribution of Surfactants in Latex Films. *Colloid & Polymer Sci.* **1987**, *265*, 823-829.
216. Tebelius, L. K.; Urban, M. W. Surface and Interfacial FTIR Spectroscopic Studies of Latexes. X. The Effect of Coalescence on Surfactant Exudation in Polystyrene and Poly(n-butyl acrylate) Latex Films. *J. Appl. Poly. Sci.* **1995**, *56*, 387-395.
217. Amalvy, J. I.; Soria, D. B. Vibrational Spectroscopic Study of Distribution of Sodium Dodecyl Sulfate in Latex Films. *Prog. Org. Coat.* **1996**, *28*, 279-283.
218. Evanson, K. W.; Thorstenson, T. A.; Urban, M. W. Surface and Interfacial FTIR Spectroscopic Studies of Latexes, II. Surfactant-Copolymer Compatibility and Mobility of Surfactants. *J. Appl. Poly. Sci.* **1991**, *42*, 2297-2307.
219. Lee, W. P.; Gundabala, V. R.; Akpa, B. S.; Johns, M. L.; Jeynes, C.; Routh, A. F. Distribution of Surfactants in Latex Films: A Rutherford Backscattering Study. *Langmuir* **2006**, *22*, 5314-5320.
220. Belaroui, F.; Grohens, Y.; Boyer, H.; Holl, Y. Depth Profiling of Small Molecules in Dry Latex Films by Confocal Raman Spectroscopy. *Polymer* **2000**, *41*, 7641-7645.
221. Schmidt, U.; Hild, S.; Ibach, W.; Hollricher, O. Characterization of Thin Polymer Films on the Nanometer Scale with Confocal Raman AFM. *Macromol. Symp.* **2005**, *230*, 133-143.
222. Leo, A.; Hansch, C.; Elkins, D. Partition Coefficients and Their Uses. *Chem Rev* **1971**, *71*, 525-616.
223. Valkó, K. Application of High-Performance Liquid Chromatography Based Measurements of Lipophilicity to Model Biological Distribution. *Chromatography. A* **2004**, *1037* (1-2): 299-310.
224. Ahel, M.; Giger, W. Partitioning of Alkylphenols and Alkylphenol Polyethoxylates between Water and Organic Solvents. *Chemosphere* **1993**, *8*, 1471-1478.
225. Ruiz-Angel, M. J.; Carda-Broch, S.; Garcia-Alvarez-Coque, M. C. ; Berthod, A. Effect of Ionization and the Nature of the Mobile Phase in Quantitative Structure-Retention Relationship Studies. *J. Chromatography A*, **2005**, *1063*, 25-34.
226. Shen, H.; Zhang, J.; Liu, S.; Liu, G.; Zhang, L. Effect of the Chain-Transfer-Agent Content on the Emulsion Polymerization Process and Adhesive Properties of Poly(n-butyl acrylate-co-acrylic acid) Latexes. *J. Appl. Poly. Sci.* **2008**, *107*, 1793-1802.
227. Gonzalez, I.; Leiza, J. R.; Asua, J. M. Exploring the Limits of Branching and Gel Content in the Emulsion Polymerization of n-BA. *Macromolecules* **2006**, *39*, 5015-5020.
228. Tzitzinou, A.; Keddie, J. L.; Geurts, J. L.; Mulder, M.; Satguru, R.; Treacher, K. E. *ACS Symposium Series, 790(Film Formation in Coatings)*, **2001**.

229. Guo, J., Severtson, S. J., Gwin, L. E., Houtman, C. J. Effect of Amphiphilic Additives on the Behavior of Water-Based Acrylic Pressure-Sensitive Adhesives during Paper Recycling. *Ind. Eng. Chem. Res.* **2008**, *47*, 2612-2617.
230. Kientz, E.; Holl, Y. Distribution of Surfactants in Latex Films. *Colloids Surf. A: Physicochem. Engng. Aspects* **1993**, *78*, 255-270.
231. Okubo, M.; Furukawa, Y.; Shiba, K.; Matoba, T. Inclusion of Nonionic Emulsifier inside Polymer Particles Produced by Emulsion Polymerization. *Colloid Polym. Sci.* **2003**, *281*, 182-186.
232. Kibbey, T. C. G.; Hayes, K. F. Effects of Surfactant Concentration and Sorbent Properties on the Sorption and Transport of Ethoxylated Nonionic Surfactant Mixtures. *J. Contam. Hydrol.* **2000**, *41*, 1-22.
233. Kibbey, T. C. G.; Hayes, K. F. A Predictive Numerical Thermodynamic Model of Mixed Nonionic Surfactant Sorption in Natural Systems: 2. Application to Broadly Distributed Mixtures. *J. Colloid Interface Sci.* **1998**, *197*, 210-220.
234. Kibbey, T. C. G.; Hayes, K. F. A predictive Numerical Thermodynamic Model of Mixed Nonionic Surfactant Sorption in Natural Systems: 1. Model Formulation and Sensitivity Analysis. *J. Colloid Interface Sci.* **1998**, *197*, 198-209.
235. Severtson, S. J.; Banerjee, S. Sorption of Chlorophenols to Wood Pulp. *Environ. Sci. Technol.* **1996**, *30*, 1961-1969.
236. Westall, J. C.; Leuenberger, C. J.; Schwarzenbach, R. P. Influence of pH and Ionic Strength on the Aqueous-nonaqueous Distribution of Chlorinated Phenols. *Environ. Sci. Technol.* **1985**, *19*, 193-198.
237. Tzitzinou, A.; Jenneson, P. M.; Clough, A. S.; Keddie, J. L.; Lu, J. R.; Zhdan, P.; Treacher, K. E.; Satguru, R. Surfactant Concentration and Morphology at the Surfaces of Acrylic Latex Films. *Prog. Org. Coat.* **1999**, *35*, 89-99.
238. Belaroui, F.; Grohens, Y.; Marie, P.; Holl, Y. Recent Results and Perspectives on some Aspects of Latex Film Formation: Drying, Coalescence and Distribution of Additives. *Prog. Colloid Polym. Sci.* **2004**, *128*, 159-162.
239. Okubo, M.; Chaiyasat, A.; Yamada, M.; Suzuki, T.; Kobayashi, H. Influence of Hydrophilic-Lipophilic Balance of Nonionic Emulsifiers on Emulsion Copolymerization of Styrene and Methacrylic Acid. *Colloid Polym. Sci.* **2007**, *285*, 1755-1761.
240. Yang, Y.; Li, H.; Wang, F. Studies on the Water Resistance of Acrylic Emulsion Pressure-Sensitive Adhesives (PSAs) *J. Adhesion Sci. Technol.* **2003**, *17*, 1741-1750.
241. Morizur, J. F.; Irvine, D. J.; Rawlins, J. J.; Mathias, L. J. Synthesis of New Acrylate-Based Nonionic Surfmers and Their Use in Heterophase Polymerization. *Macromolecules* **2007**, *40*, 8938-8946.
242. Amalvy, J. I.; Unzue, M. J.; Schoonbrood, H. A. S.; Asua, J. M. Reactive Surfactants in Heterophase Polymerization: Colloidal Properties, Films-water Absorption, and Surfactant Exudation. *J. Polym. Sci. Part A: Polym. Chem.* **2002**, *40*, 2994-3000.
243. Aramendia, E.; Barandiaran, M. J.; Grade, J.; Blease, T.; Asua, J. M. Improving Water Sensitivity in Acrylic Film Using Surfemrs. *Langmuir* **2005**, *21*, 1428-1435.
244. Evanson, K. W.; Urban, M. W. Surface and Interfacial FTIR Spectroscopic Studies of Lateses. I. Surfactant-Copolymer Interactions. *J. Appl. Polym. Sci.* **1991**, *42*, 2287-2296.
245. Juhue, D.; Wang, Y.; Lang, J.; Leung, O.-M.; Goh, M. C.; Winnik, M. A. Surfactant Exudation in Latex Films. *Polym. Mater. Sci.* **1995**, *73*, 86-87.

246. G. H. Xu, J. Dong, S. J. Severtson, C. J. Houtman, L. E. Gwin, Characterizing the Distribution of Nonylphenol Ethoxylate Surfactants in Water-Based Pressure-Sensitive Adhesive Films using Atomic-Force and Confocal Raman Microscopy. *J. Phys. Chem. B* **2008**, 112, 11907-11914.
247. Kientz, E.; Dobler, F.; Holl, Y. Desorption of the Surfactant from the Particle Surface during Latex Film Formation. *Polym. Int.* **1994**, 34, 125-134.
248. Lam, S.; Hellgren, A. C.; SjoBerg, M.; Holmberg, K.; Schoonbrood, H. A. S.; Unzue, M. J.; Asua, J. M.; Tauer, K.; Sherrington, D. C.; Montoya Goni, A. Surfactants in Heterophase Polymerization: A Study of Film Formation Using Force Microscopy. *J. Appl. Poly. Sci.* **1997**, 66, 187-198.
249. Aramendia, E.; Mallegol, J.; Jeynes, C.; Barandiaran, M. J.; Keddie, J. L.; Asua, J. M. Distribution of Surfactants near Acrylic Latex Film Surfaces: A Comparison of Conventional and Reactive Surfactants (Surfmers). *Langmuir* **2003**, 19, 3212-3221.
250. Scalarone, D.; Lazzari, M.; Castelvetro, V.; Chiantore, O. Surface Monitoring of Surfactant Phase Separation and Stability in Waterborne Acrylic Coating. *Chem. Mater.* **2007**, 19, 6107-6113.